Mass and Charge Transport in Hydrated Polymeric Membranes

A Dissertation Presented for the

Doctor of Philosophy

Degree

The University of Tennessee, Knoxville

Marshall T. McDonnell

August 2016

© by Marshall T. McDonnell, 2016
All Rights Reserved.

DEDICATION

I dedicate this to my amazing and wonderful wife, Rachel, and my beautiful daughter, Annabeth. Rachel, thank you for your patience, understanding, support, love, and sacrifice throughout this journey. I could have never done this without you. Annabeth, thank you for your copious amounts of love, laughter, and drool. I cherish you both and will for the rest of my life.

To my parents, Raymond and Janice, for loving me and helping shape me into the person I am today. To my brother, Raymond, for your help and support throughout my life and being a loving big brother. To my sister, Carol, for your love, thoughts, and prayers. To my wonderful in-laws, Marshall, Arlene, Rebecca, Matt, Luke, Renee, Sean, Ben, Josh, Trayla, John, and Whittney, for the constant love and support you give to me and to my family.

Acknowledgements

I would like to express sincere gratitude to my advisor, Prof. David J. Keffer, for his support, guidance, and encouragement throughout my graduate studies at the University of Tennessee. His guidance played a pivotal role in my research as well as my professional and personal growth. I would also like to extend thanks to Prof.. Donald Nicholson who served as a mentor in introducting me to molecular simulation techniques, to Prof. Haixuan Xu for introducing me to electronic strucuture methods used in this work, to Prof. Stephen Paddison for introducing me to statistical mechanics and modeling, and to Dr. Orland Rios who allowed me the opportunity to work hands-on with experimental characterization of materials. Also to my committee members, Prof. James Morris, Prof. Jimmy Mays, Prof. Sirus Laursen, and Prof. Donald Nicholson, thank you very much for their valuable advice and being flexible on scheduling the defense date.

Special thanks goes out to the National Science Foundation which supported this work via via Grant No. DGE-0801470 and provided me the opportunity to be a part of the Sustainable Technology through Advanced Interdisciplinary Research" (STAIR) program at UT. Thank you Jane Breder for your kindness, help and support I also appreciate the kindness, help, and support from all CBE staff (Rita Gray, Kat Forst, Amy Brewer, Jennifer Wolfenbarger, Amber Tipton, Marie Parigin). Appreciation goes out to past and present members of our research group: Dr. Qifei Wang, Dr. Nethika Suraweera, Dr. Qianping He, Nicholas McNutt, Duncan Greeley, Jedidiah Long, and Trevor Gregory.

I would also like to thank Prof. Doros Theodorou for his support by providing code from his previous work, Prof. Georgios Boulougouris for his correspondence and help in understanding particle deletion methods, and Prof. Adri van Duin, Dr. Andres Jaramillo-Botero, and Prof. Bernd Hartke for their guidance and help with developing reactive force fields.

I would also like to thank the National Institute for Computational Sciences (supported by NSF under agreement number: OCI 07-11134.5) and the Extreme Science and Engineering Discovery Environment (supported by National Science Foundation grant number ACI-1053575) for providing resources used during this work.

Abstract

Mass and charge transport through hydrated polymer membranes has significant importance for many areas of engineering and industry. Multi-scale modeling and simulation techniques were used to study transport in relation to two specific membrane applications: (1) food packaging and (2) additives for polymer electrolytes.

Chitosan/chitin films were studied due to their use as a sustainable, biodegradable food packaging film. The effects of hydration on the solvation, diffusivity, solubility, and permeability of oxygen molecules in these films were studied via molecular dynamics and confined random walk simulations. With increasing hydration, the membrane was observed to have a more homogeneous water distribution with the polymer chains being fully solvated. Insight from this work will help guide molecular modeling of chitosan/chitin membranes and experimental synthesis of these membranes, specifically highlighting efforts to chemically tailor chitosan membranes to favor discrete as opposed to continuous aqueous domains to help reduce oxygen permeability.

Additives for proton exchange membranes (PEMs) were studied to aid in the developing next-generation membrane materials for fuel cell applications. We calculate and present predictions of our analytical model that describes the fundamental relationship between the nanoscale structure of PEMs and their proton conductivity using a set of structural descriptors, accounting for nanopore size, functionalization and connectivity in order to predict proton conductivities in PEMs. The model reproduces experimentally determined conductivities in two current PEM materials. To extend the model based on structural descriptors of PEMs, we studied polyethylene glycol (PEG), a polymer used in electrochemistry applications due to it hydrophilicity and pH-dependent behavior in aqueous environments. We conducted ab initio molecular dynamics simulations of an excess proton in bulk water and aqueous triethylene glycol (TEG) solution and reactive molecular dynamics simulations of an excess proton in bulk water, aqueous TEG solution, and aqueous PEG solution. We determined differences in protonic defect structures, kinetics, thermodynamics, and hydrogen-bond networks associated with structural diffusion between systems.

Driving forces for polymeric membrane design goals include economics, efficiency, energy consumption and sustainable production. Insight from this work hopes to aid in determining key design parameters and reduce time-to-discovery for developing next-generation polymeric membranes.

Table of Contents

1 Introduction **1**

2 Molecular Dynamics Simulations of Hydration Effects on Solvation, Diffusivity, and Permeability in Chitosan/Chitin Films **16**
2.1 Simulation Details 17
2.2 Results & Discussion 26

3 Intrinsic Relationships between Proton Conductivity and Nanopore Size and Functionalization **38**
3.1 Theory 39
3.2 Results and Discussion 42

4 Ab Initio Molecular Dynamics Simulations of an Excess Proton in a Triethylene Glycol-Water Solution: Solvation Structure, Mechanism and Kinetics **51**
4.1 Simulation Details 52
4.2 Results & Discussion 55
4.3 Protonic defect species occurrence and lifetime analysis. 60

5 Reactive Molecular Dynamics Simulations of an Excess Proton in Aqueous Triethylene and Polyethylene Glycol Solutions **84**
5.1 Introduction to the Reactive Force Field: ReaxFF 84
5.2 Development of ReaxFF for H^+ in Aqueous PEG Solutions 86
5.3 Simulation Setup and Details 89
5.4 Results and Discussion 90

6 Preparation for Training a Reaction Force Field for xsPCDH/PEG Membranes **97**

7 Conclusion **100**
7.1 Summary of Work 100
7.2 Impact of Work 102
7.3 Future Work 104

Bibliography **106**

Appendix **132**

A Distribution of lifetimes in TEG-water mixtures **133**
Distribution of lifetimes in TEG-water mixtures 133

B Free energy change for H^+ to transfer from water to hydroxyl groups of TEG. **135**

C Special pairs for TEG-water mixtures with proton rattling included **136**

D Solvation shells for TEG-water mixture with proton rattling included **137**

E Probability union relation for determining concentration-dependent site occupation probabilities **138**

F Hydrogen-bond networks with proton rattling excluded **140**
F.1 Hydrogen-bond networks with proton rattling excluded for TEG-water mixtures 140

G Hydrogen-bond networks with proton rattling excluded for bulk water **143**

H Mechanistic picture for proton transfer among water molecules. **145**
H.1 Time evolution of radial distribution functions leading up to proton transfer events for bulk water 145
H.2 Time evolution of integrated coordination numbers leading up to proton transfer events for water-water proton transfer for bulk water . 149
H.3 Time evolution of radial distribution functions leading up to proton transfer events for water-water proton transfer for TEG-water mixtures 153
H.4 Time evolution of integrated coordination numbers leading up to proton transfer events for water-water proton transfer for TEG-water mixtures 156
H.5 Time evolution of integrated coordination numbers leading up to proton transfer events for water-hydroxyl proton transfer for TEG-water mixtures 158
H.6 Time evolution of integrated coordination numbers leading up to proton transfer events for hydroxyl-water proton transfer for TEG-water mixtures 161
H.7 Integrated coordination numbers during water-water proton transfer for all XC functionals 164

I Probability density functions **166**
Probability density functions 166
I.1 Probability density functions for bulk water 166
I.2 Probability density functions for water-water proton transfer in TEG-water mixtures. 170

J Hopping dynamics and mean square displacements **172**

K Hydrogen-bond networks with proton rattling included **175**
K.1 Hydrogen-bond networks with proton rattling included for bulk water 175
K.2 Hydrogen-bond networks with proton rattling included for TEG-water mixtures 178

L Hydrogen-bond networks found during proton transfer events **186**
L.1 Hydrogen-bond networks found during proton transfer events for bulk water 186
L.2 Hydrogen-bond networks found during proton transfer events for TEG-water mixtures 188

Vita **193**

List of Tables

2.1 Self-diffusivities of O_2, H_2O, and OH^- in chitosan/chitin membranes at 15% RH and 95% RH at 300 K and the self-diffusivity increase ratios. 33

2.2 $\beta\mu^{ex}$ of O_2 in chitosan/chitin membranes at 15% RH and 95% RH at 300 K using free energy perturbation, finite difference thermodynamic integration, and direct particle deletion. The $\pm\sigma$ for the direct particle deletion method gives the standard error. $N-1 \rightarrow N$ indicates the path of inserting the oxygen molecule and $N \rightarrow N-1$ indicates the path for deleting the oxygen molecule. 34

2.3 Solubility (10^{-3} mol/L/atm) of O_2 in chitosan/chitin membranes at 15% RH and 95% RH at 300 K using free energy perturbation, finite difference thermodynamic integration, and direct particle deletion. . 35

2.4 Henry's constant (atm) of O_2 in chitosan/chitin membranes at 15% RH and 95% RH at 300 K using free energy perturbation, finite difference thermodynamic integration, and direct particle deletion. 35

2.5 Permeability ($barrer$)^a of O_2 in chitosan/chitin membranes at 15% RH and 95% RH at 300 K using free energy perturbation, finite difference thermodynamic integration, direction particle deletion, experimental values at low (0% RH) and high (95% RH) humidity for comparison, and the direct particle deletion results with no Coulombic interactions ($U_{Coulombic}$) in the intermolecular potential. 36

3.1 Model parameters for percolation theory for self-diffusivity using structural descriptors for acidity (c, concentration of hydronium ions) and confinement (sa, the interfacial surface area). 41

4.1 Protonic defect species occurrences and lifetimes found in aqueous H^+ and triethylene glycol (TEG) systems. Proton rattling effects are included and excluded. 61

4.2 The occurrences and lifetimes of special pairs made up of the protonated species ($Z_{protonated}$) and the special partner of the protonated species (Z_{shared}) found in aqueous H^+ and triethylene glycol (TEG) systems. Proton rattling effects are excluded. 63

4.3 The occurrences and lifetimes of solvating shell species ($H_{A,1\text{-}3}$) around the protonated species ($Z_{protonated}$) found in aqueous H^+ and triethylene glycol (TEG) systems. Proton rattling effects are excluded. 65
4.4 The top five most occurring hydrogen-bond networks around protonic defect species and associated lifetimes for TEG-water mixtures. Protonated species (Z_{prot}), the special pair atom (Z_{shared}), the solvating atoms of the protonated species ($HB_{X,\,p}$ where x=A or D for accepting or donating a hydrogen bond, respectively), and the solvating atoms of Z_{shared} ($HB_{X,\,s}$ with the same definitions of x) are listed. Figure 4.4 provides graphical labeling. Proton rattling effects are excluded. . . 68
4.5 The occurrence percentages of a given molecule species in the total hydrogen bond network, the hydrogen bond acceptor sites (H_A) and the donor sites (H_B). The molecular groups are the ether (ROR), methylene (CH_2) and hydroxyl (ROH) groups of TEG and a "cavity". The standard deviations are reported also (SD). 70
4.6 The top five most occurring hydrogen-bond networks around reactant and product during proton transfer for TEG-water mixtures. Protonated species (Z_{prot}), the previously protonated species (Z_{prev}), the hydrogen-bond atoms of the protonated species ($HB_{X,\,p}$ where x=A or D for accepting or donating a hydrogen bond, respectively), and the solvating atoms of Z_{prev} ($HB_{X,\,r}$ with the same definitions of x) are listed. Figure 4.4 gives graphical labeling. Proton rattling effects are included. 71
4.7 Kinetics of aqueous H^+ system. Relaxation times, parameters and inverse rates (in ps) for H^+ including and excluding rattling events. . 81
4.8 Kinetics of aqueous H^+ and triethylene glycol (TEG) system. Relaxation times and inverse rates (in ps) for H^+ including and excluding rattling events. 81

B.1 The occurrence of water, W, alcohol, S, water with the excess proton ion, WH^+, and the alcohol with the excess proton, SH^+ used to calculate the change in free energy of transfer of H^+, $\Delta G(H^+, W \rightarrow S)$, for all three XC functionals and the average over all three different functionals. 135

C.1 The occurrences and lifetimes of special pairs made up of the protonated species ($Z_{protonated}$) and the special partner of the protonated species (Z_{shared}) found in aqueous H^+ and triethylene glycol (TEG) systems. Proton rattling effects are included. 136

D.1 The occurrences and lifetimes of solvating shell species ($H_{A,1\text{-}3}$)around the protonated species ($Z_{protonated}$) found in aqueous H^+ and triethylene glycol (TEG) systems. Proton rattling effects are included. 137

F.1 The occurrences and lifetimes of hydrogen-bond networks around protonated species found in TEG-water for PW91. The table lists the protonated species ($Z_{protonated}$), the atom (Z_{shared}) hydrogen bonded to the most active proton, the solvating atoms of the protonated species (HBX,p where x=A or D for accepting or donating a hydrogen bond), and the solvating atoms of Zshared (HBX,s with the same definitions of x). Figure 4.4 provides the illustration to match these labels. Proton rattling effects are excluded. 140
F.2 The occurrences and lifetimes of hydrogen-bond networks around protonated species found in TEG-water for PBE. The table lists the protonated species ($Z_{protonated}$), the atom (Z_{shared}) hydrogen bonded to the most active proton, the solvating atoms of the protonated species (HBX,p where x=A or D for accepting or donating a hydrogen bond), and the solvating atoms of Zshared (HBX,s with the same definitions of x). Figure 4.4 provides the illustration to match these labels. Proton rattling effects are excluded. 141
F.3 The occurrences and lifetimes of hydrogen-bond networks around protonated species found in TEG-water for PBE+TS-vdW. The table lists the protonated species ($Z_{protonated}$), the atom (Z_{shared}) hydrogen bonded to the most active proton, the solvating atoms of the protonated species (HBX,p where x=A or D for accepting or donating a hydrogen bond), and the solvating atoms of Zshared (HBX,s with the same definitions of x). Figure 4.4 provides the illustration to match these labels. Proton rattling effects are excluded. 142

G.1 The occurrences and lifetimes of hydrogen-bond networks around protonated species found in bulk water for PW91. The table lists the protonated species (Z_{prot}), the atom (Z_{shared}) hydrogen bonded to the most active proton, the solvating atoms of the protonated species (HBX,p where x=A or D for accepting or donating a hydrogen bond), and the solvating atoms of Zshared (HBX,s with the same definitions of x). Figure 4.4 provides the illustration to match these labels. Proton rattling effects are excluded. 143
G.2 The occurrences and lifetimes of hydrogen-bond networks around protonated species found in bulk water for BLYP. The table lists the protonated species (Z_{prot}), the atom (Z_{shared}) hydrogen bonded to the most active proton, the solvating atoms of the protonated species (HBX,p where x=A or D for accepting or donating a hydrogen bond), and the solvating atoms of Zshared (HBX,s with the same definitions of x). Figure 4.4 provides the illustration to match these labels. Proton rattling effects are excluded. 143

G.3 The occurrences and lifetimes of hydrogen-bond networks around protonated species found in bulk water for PBE. The table lists the protonated species (Z_{prot}), the atom (Z_{shared}) hydrogen bonded to the most active proton, the solvating atoms of the protonated species (HBX,p where x=A or D for accepting or donating a hydrogen bond), and the solvating atoms of Zshared (HBX,s with the same definitions of x). Figure 4.4 provides the illustration to match these labels. Proton rattling effects are excluded. 144
G.4 The occurrences and lifetimes of hydrogen-bond networks around protonated species found in bulk water for PBE+TS-vdW. The table lists the protonated species (Z_{prot}), the atom (Z_{shared}) hydrogen bonded to the most active proton, the solvating atoms of the protonated species (HBX,p where x=A or D for accepting or donating a hydrogen bond), and the solvating atoms of Zshared (HBX,s with the same definitions of x). Figure 4.4 provides the illustration to match these labels. Proton rattling effects are excluded. 144

K.1 The occurrences and lifetimes of hydrogen-bond networks around protonated species found in bulk water for PW91. The table lists the protonated species ($Z_{protonated}$), the atom (Z_{shared}) hydrogen bonded to the most active proton, the solvating atoms of the protonated species (HBX,p where x=A or D for accepting or donating a hydrogen bond), and the solvating atoms of Zshared (HBX,s with the same definitions of x). Figure 4.4 provides the illustration to match these labels. Proton rattling effects are included. 175
K.2 The occurrences and lifetimes of hydrogen-bond networks around protonated species found in bulk water for PBE. The table lists the protonated species ($Z_{protonated}$), the atom (Z_{shared}) hydrogen bonded to the most active proton, the solvating atoms of the protonated species ($HB_{X,p}$ where x=A or D for accepting or donating a hydrogen bond), and the solvating atoms of Z_{shared} ($HB_{X,s}$ with the same definitions of x). Figure 4.4 provides the illustration to match these labels. Proton rattling effects are included. 176
K.3 The occurrences and lifetimes of hydrogen-bond networks around protonated species found in bulk water for BLYP. The table lists the protonated species ($Z_{protonated}$), the atom (Z_{shared}) hydrogen bonded to the most active proton, the solvating atoms of the protonated species ($HB_{X,p}$ where x=A or D for accepting or donating a hydrogen bond), and the solvating atoms of Z_{shared} ($HB_{X,s}$ with the same definitions of x). Figure 4.4 provides the illustration to match these labels. Proton rattling effects are included. 176

K.4 The occurrences and lifetimes of hydrogen-bond networks around protonated species found in bulk water for PBE+TS-vdW. The table lists the protonated species ($Z_{protonated}$), the atom (Z_{shared}) hydrogen bonded to the most active proton, the solvating atoms of the protonated species ($HB_{X,p}$ where x=A or D for accepting or donating a hydrogen bond), and the solvating atoms of Z_{shared} ($HB_{X,s}$ with the same definitions of x). Figure 4.4 provides the illustration to match these labels. Proton rattling effects are included. 177
K.5 The occurrences and lifetimes of all hydrogen-bond networks around protonated species found in TEG-water mixture for PW91. The table lists the protonated species (Z_{prot}), the atom (Z_{shared}) hydrogen bonded to the most active proton, the solvating atoms of the protonated species ($HB_{X,p}$ where x=A or D for accepting or donating a hydrogen bond and y = 1 or 2), and the solvating atoms of Z_{shared} ($HB_{X,s}$with the same definitions of x). Figure 4.4 provides the illustration to match these labels. Proton rattling effects are included. 178
K.6 The occurrences and lifetimes of all hydrogen-bond networks around protonated species found in TEG-water mixture for PBE. The table lists the protonated species (Z_{prot}), the atom (Z_{shared}) hydrogen bonded to the most active proton, the solvating atoms of the protonated species ($HB_{X,p}$ where x=A or D for accepting or donating a hydrogen bond and y = 1 or 2), and the solvating atoms of Z_{shared} ($HB_{X,s}$ with the same definitions of x). Figure 4.4 provides the illustration to match these labels. Proton rattling effects are included. 180
K.7 The occurrences and lifetimes of all hydrogen-bond networks around protonated species found in TEG-water mixture for PBE+TS-vdW. The table lists the protonated species (Z_{prot}), the atom (Z_{shared}) hydrogen bonded to the most active proton, the solvating atoms of the protonated species ($HB_{X,p}$ where x=A or D for accepting or donating a hydrogen bond and y = 1 or 2), and the solvating atoms of Z_{shared} ($HB_{X,s}$ with the same definitions of x). Figure 4.4 provides the illustration to match these labels. Proton rattling effects are included. 183

L.1 The occurrences and lifetimes of hydrogen-bond networks around the reactant and product during proton transfer found in bulk water for PW91. The table lists the protonated species (Z_{prot}), the previously protonated species (Z_{prev}), the hydrogen-bond atoms of the protonated species ($HB_{X,p}$ where x=A or D for accepting or donating a hydrogen bond), and the solvating atoms of Z_{prev} ($HB_{X,r}$ with the same definitions of x). Figure 4.4 gives an illustration for these labels. Proton rattling effects are included. 186

L.2 The occurrences and lifetimes of hydrogen-bond networks around the reactant and product during proton transfer found in bulk water for PBE. The table lists the protonated species (Z_{prot}), the previously protonated species (Z_{prev}), the hydrogen-bond atoms of the protonated species ($HB_{X,p}$ where x=A or D for accepting or donating a hydrogen bond), and the solvating atoms of Z_{prev} ($HB_{X,r}$ with the same definitions of x). Figure 4.4 gives an illustration for these labels. Proton rattling effects are included. 187
L.3 The occurrences and lifetimes of hydrogen-bond networks around the reactant and product during proton transfer found in bulk water for BLYP. The table lists the protonated species (Z_{prot}), the previously protonated species (Z_{prev}), the hydrogen-bond atoms of the protonated species ($HB_{X,p}$ where x=A or D for accepting or donating a hydrogen bond), and the solvating atoms of Z_{prev} ($HB_{X,r}$ with the same definitions of x). Figure 4.4 gives an illustration for these labels. Proton rattling effects are included. 187
L.4 The occurrences and lifetimes of hydrogen-bond networks around the reactant and product during proton transfer found in bulk water for PBE+TS-vdW. The table lists the protonated species (Z_{prot}), the previously protonated species (Z_{prev}), the hydrogen-bond atoms of the protonated species ($HB_{X,p}$ where x=A or D for accepting or donating a hydrogen bond), and the solvating atoms of Z_{prev} ($HB_{X,r}$ with the same definitions of x). Figure 4.4 gives an illustration for these labels. Proton rattling effects are included. 187
L.5 The occurrences and lifetimes of hydrogen-bond networks around the reactant and product during proton transfer found in TEG-water mixture for PW91. The table lists the protonated species (Z_{prot}), the previously protonated species (Z_{prev}), the hydrogen-bond atoms of the protonated species ($HB_{X,p}$ where x=A or D for accepting or donating a hydrogen bond), and the solvating atoms of Z_{prev} ($HB_{X,r}$ with the same definitions of x). Figure 4.4 gives an illustration for these labels. Proton rattling effects are included. 188
L.6 The occurrences and lifetimes of hydrogen-bond networks around the reactant and product during proton transfer found in TEG-water mixture for PBE. The table lists the protonated species (Z_{prot}), the previously protonated species (Z_{prev}), the hydrogen-bond atoms of the protonated species ($HB_{X,p}$ where x=A or D for accepting or donating a hydrogen bond), and the solvating atoms of Z_{prev} ($HB_{X,r}$ with the same definitions of x). Figure 4.4 gives an illustration for these labels. Proton rattling effects are included. 189

L.7 The occurrences and lifetimes of hydrogen-bond networks around the reactant and product during proton transfer found in TEG-water mixture for PBE+TS-vdW. The table lists the protonated species (Z_{prot}), the previously protonated species (Z_{prev}), the hydrogen-bond atoms of the protonated species ($HB_{X,p}$ where x=A or D for accepting or donating a hydrogen bond), and the solvating atoms of Z_{prev} ($HB_{X,r}$ with the same definitions of x). Figure 4.4 gives an illustration for these labels. Proton rattling effects are included. 191

List of Figures

1.1 Food Packaging Schematic 2
1.2 Model for Fuel Cell Cost 5
1.3 Fuel Cell Targets versus Status for 2013. 6
1.4 PEMFC Cost Breakdown - 2012. 7
1.5 Protonic Structures 9
1.6 Presolvation Concept 10
1.7 Conductivity vs. Relative Humidity of Nafion, xsPCHD, and xsPCHD/PEG Membranes 12
1.8 Protonic Structures 12
1.9 PEG in Aqueous Domains of xsPCHD/PEG Blend and Block Copolymer 14

2.1 Schematic of infinitely dilute oxygen molecule permeability in chitosan/chitin film, with change in diffusivity for increasing humidity levels. 16
2.2 Saccharide monomers of a) chitin b) chitosan and c) chitosan with a protonated amine group. Oxygens are displayed as red, hydrogens as white, carbon as cyan, and nitrogen as blue. A double-bond is present for the N-acetyl group of the chitin monomer but not shown. 17
2.3 Radial distribution functions for the O of H_2O with solute O_2, OH^- and specific N atoms for polymer monomers at 300 K for both humidity levels: (a) 15% RH and (b) 95% RH. See Figure 2.2 for graphic of monomers. 27
2.4 Water distributions for (a) 15% RH and (a) 95% RHfor chitosan/chitin membranes. Polymers and other solute molecules are not show for clarity. Graphics were created using VMD [1, 2] and Tachyon. [3] . . 28
2.5 Radial distribution functions for O of OH^- with O_2, H_2O and the N of the cation for the chitosan monomer at 300 K for both humidity levels: (a) 15% RH and (b) 95% RH. See Figure 2.2 for the monomer group graphic. 29
2.6 Radial distribution functions for O of O_2 with H_2O, OH^- and specific N atoms for polymer monomers at 300 K for both humidity levels: (a) 15% RH and (b) 95% RH. See Figure 2.2 for graphic of monomers. . 30

2.7 Mean square displacements for H_2O, OH^-, and O_2 using both molecular dynamics (MD) simulations and confined random walk (CRW) simulations at 300 K for both (a) 15% RH and (b) 95% RH. The log-log plot of the MSD vs. time is unity for the CRW simulations, satisfying the long, linear regime requirement for calculating accurate self-diffusivities. Note the difference in the y-axis scale from (a) to (b). 32
2.8 Reduced excess chemical potential ($\beta\mu^{ex}$) vs. d for (a) 15% RH and (b) 95% RH with error bars shown to determine optimal d value. . . . 34

3.1 Schematic of transfer from molecular-level detail of membrane (with polymer/aqueous domain overlay) to a percolation theory model for giving an connected aqueous domain that spans a membrane. 38
3.2 Self-diffusivity of charge and sources of transport losses as a function of water content. Experimental data is taken from refs. [4] & [5]. . . 43
3.3 Self-diffusivities as a function of surface coverage for a range of pore radii. (a) water, (b) structural component of charge, (c) vehicular component of charge, (d) total charge. 46
3.4 Conductivity as a function of surface coverage for a range of pore radii. 46
3.5 Self-diffusivities as a function of pore radii for a range of surface coverages. (a) water, (b) structural component of charge, (c) vehicular component of charge, (d) total charge. 47
3.6 Conductivity as a function of pore radius for a range of surface coverages. 47
3.7 Conductivity as a function of surface coverage across a range of pore radii. (a) The excluded volume of the anion group is accounted for but the surface area is not. (b) The maximum surface area of the anion group is accounted for but the volume is not. (c) Both the excluded volume and the maximum surface area of the anion group are accounted for. 49

4.1 Image of excess H^+ as hydronium ion (highlighted in yellow) with hydrogen bond network formed to water and triethylene glycol polymer and graph of change in integrated coordination number of protonated oxygen of water leading up to a proton transfer event. 51
4.2 The radial distribution functions of oxygen and hydrogen of water and hydronium ion in bulk water and TEG-water mixtures at 300 K. The different figures are as follows: (a) O (water)-O (water), (b) O (water)-H (all hydrogens), (c) O (hydronium)-O (water), and (d) O (hydronium)-H (all hydrogens). 56
4.3 The radial distribution functions of oxygen for water and hydronium ion in TEG-water mixtures with the oxygens of TEG chain at 300 K. The different figures are as follows: (a) O (water)-O (ether of TEG), (b) O (water)-O (hydroxyl of TEG), (c) O (hydronium)-O (ether of TEG), and (d) O (hydronium)-O (hydroxyl of TEG). 59

4.4 Hydrogen-bond network around a water-water special pair. Labels the protonated species ($Z_{protonated}$ / Z_{prot}), the atom (Z_{shared}) hydrogen bonded to the most active proton, the hydrogen-bond acceptors (HB_A) and the hydrogen-bond donors (HB_D). 68
4.5 The ICNs using the PBE+TS-vdW XC functional for protonated oxygen in water (O* in (a)) and the next water oxygen to be protonated (O_{next} in (b)) averaged over 20 fs intervals long before proton transfer (500-480 fs) and leading up to proton transfer (200-180 fs, 100-80 fs, 60-40 fs, and 20-0 fs) at 300 K . The integration is over the RDF in Figure H.11 in the Appendix. Specific regions are marked for the proton transfer process and the change in the HB network. Proton rattling events are excluded. 73
4.6 Probability density function of proton transfer for PBE+TS-vdW XC between water molecules in TEG-water mixture at 300 K. R_{O^*O} is the oxygen-oxygen distance and δ is the asymmetric reaction coordinate. The surface has been smoothed and z-axis made arbitrary. 75
4.7 Free energy profile of proton transfer between water molecules in bulk water and TEG-water mixtures at 300 K using different XC functionals. The reaction coordinate δ is the difference of the HB distances for the shared proton (H^*) between the two oxygen atoms of the water molecules. 76
4.8 Intermittent time correlation functions for protonic defects in bulk water and TEG-water mixtures. (a) Proton rattling included. (b) Proton rattling excluded. 78
4.9 Continuous time correlation functions for protonic defects in bulk water and TEG-water mixtures. (a) Proton rattling included. (b) Proton rattling excluded. Note the difference in the scale of the x-axis from (a) to (b). 79
4.10 The distance for the atom (O*) that has the protonic defect relative to the initial position of the first protonated atom in TEG-water mixture for selected simulation trajectories for each of the XC functionals (a) PW91, (b) PBE, and (c) PBE+TS-vdW at 300 K. The trajectories were selected based on the red trajectory being an example of a trajectory that mostly contains "rest" dynamics and the blue trajectory displaying both "burst-and-rest" dynamics. The horizontal lines and labels for burst and rest sections annotate only the blue trajectory and are to help guide the reader and highlight each section. 82
4.11 The average mean squared displacements (MSDs) of the protonated atom (O*) versus time in TEG-water mixture for each XC functional at 300 K. The average MSDs were averaged out to the longest time length simulated for the XC functional set but with averaging over only a subset of all MSDs after 10 ps. 83

5.1 Snapshot of excess proton in aqueous polyethylene glycol solution with infinite chain (linked across periodic boundary), where water molecule with excess proton has a yellow oxygen atom. 84
5.2 The polymers (a) ethylene glycol and (b) diethylene glycol used for the quantum mechanical calculations to generate the training and validation sets. 86
5.3 Energy profile for deprotonation of hydroxyl group for hydrated diethylene glycol (5 H_2O). Comparison to B3LYP/6-311++G(2d,2p), previous ReaxFF from work of Monti et al., [6] and our current re-parameterized ReaxFF. Energy difference is compared to optimized geometry for the final protonation of the distant water molecule. . . . 88
5.4 Energy profile for proton transfer to ether group for hydrated diethylene glycol (3 H_2O). Comparison between B3LYP/6-311++G(2d,2p) and our current re-parameterized ReaxFF. Energy difference is compared to equilibrium proton bond to water molecule. 89
5.5 The ReaxFF and experimental results from van Duin et al. [7], the results from our own simulations using the Monti et al. ReaxFF parameterization and our current re-parameterized ReaxFF results for both (a)Oxygen-Oxygen, and (b) Oxygen-Hydrogen RDFs for bulk water. The van Duin ReaxFF RDFs were obtained for an 800-water system for 100 ps simulations. Our ReaxFF RDFs were from a 100-water system with one excess $H^+$from 200 ps simulations. Both were simulated using the NVE ensemble and a temperature of 300 K . . . 91
5.6 The radial distribution functions of the water oxygen in bulk water, aqueous TEG and PEG solutions at 300 K. The different figures are as follows: (a) O (water)-O (water), (b) O (water)-O(ether), (c) O (water)-C(CH_2), and (d) O (water)-O(hydroxyl. 92
5.7 The radial distribution functions of the protonated water oxygen in bulk water, aqueous TEG and PEG solutions at 300 K. The different figures are as follows: (a) O (hydronium)-O (water), (b) O (hydronium)-O(ether), (c) O (hydronium)-C(CH_2), and (d) O (hydronium)-O(hydroxyl. 92
5.8 Free energy profile of proton transfer between water molecules in bulk water, aqueous TEG, and aqueous PEG solutions at 300 K. The reaction coordinate δ is the difference of the HB distances for the shared proton (H^*) between the two oxygen atoms of the water molecules. . 93
5.9 The distance for the atom (O*) that has H^+ relative to the initial position of the first protonated atom for bulk water, aqueous TEG and aqueous PEG solution at 300 K 94
5.10 The mean squared displacements (MSDs) of the protonated atom (O*) versus time in bulk, aqueous TEG and aqueous PEG solution at 300 K. 95

5.11 The decomposition of the aqueous PEG mean squared displacement of the protonated atom (O*) versus time for each axis of the simulation box at 300 K. The PEG chain is oriented along the X-axis. 96

6.1 The polymers (a) methanesulfonic acid (b) dithionic aicd (c) sulfonated cyclohexadiene monomer (d) 1,2-cyclohexanol sulfonate and (e) a three monmer chain of sPCHD. These are the structures used for the quantum mechanical calculations to build a xsPCHD/PEG ReaxFF training and validation set. 98
6.2 The polymers (a) chloromethane (b) dichloroethane (c) chlorocyclohexane (d) chlorocyclohexane disulfide and (e) the disulfide crosslinked chlorocyclohexane monomers structure. These are the structures used for the quantum mechanical calculations to build a xsPCHD/PEG ReaxFF training and validation set. 98

A.1 Normalized distribution of H_3O^+lifetimes in TEG-water mixture for PW91 XC functional. 133
A.2 Normalized distribution of H_3O^+lifetimes in TEG-water mixture for PBE XC functional. 134
A.3 Normalized distribution of H_3O^+lifetimes in TEG-water mixture for PBE+TS-vdW XC functional. 134

H.1 The RDFs for bulk water using the PW91 XC functional for protonated oxygen in water (O* in (a)) and the next water oxygen to be protonated (O_{next} in (b)) averaged over 20 fs intervals long before proton transfer (500-480 fs) and leading up to proton transfer (200-180 fs, 100-80 fs, 60-40 fs, and 20-0 fs) at 300 K . Specific regions are marked for the proton transfer process and the change in the HB network. Proton rattling events are excluded. 145
H.2 The RDFs for bulk water using the BLYP XC functional for protonated oxygen in water (O* in (a)) and the next water oxygen to be protonated (O_{next} in (b)) averaged over 20 fs intervals long before proton transfer (500-480 fs) and leading up to proton transfer (200-180 fs, 100-80 fs, 60-40 fs, and 20-0 fs) at 300 K . Specific regions are marked for the proton transfer process and the change in the HB network. Proton rattling events are excluded. 146
H.3 The RDFs for bulk water using the PBE XC functional for protonated oxygen in water (O* in (a)) and the next water oxygen to be protonated (O_{next} in (b)) averaged over 20 fs intervals long before proton transfer (500-480 fs) and leading up to proton transfer (200-180 fs, 100-80 fs, 60-40 fs, and 20-0 fs) at 300 K . Specific regions are marked for the proton transfer process and the change in the HB network. Proton rattling events are excluded. 147

H.4 The RDFs for bulk water using the PBE+TS-vdW XC functional for protonated oxygen in water (O* in (a)) and the next water oxygen to be protonated (O_{next} in (b)) averaged over 20 fs intervals long before proton transfer (500-480 fs) and leading up to proton transfer (200-180 fs, 100-80 fs, 60-40 fs, and 20-0 fs) at 300 K . Specific regions are marked for the proton transfer process and the change in the HB network. Proton rattling events are excluded 148
H.5 The ICNs for bulk water using the PW91 XC functional for protonated oxygen in water (O* in (a)) and the next water oxygen to be protonated (O_{next} in (b)) averaged over 20 fs intervals long before proton transfer (500-480 fs) and leading up to proton transfer (200-180 fs, 100-80 fs, 60-40 fs, and 20-0 fs) at 300 K . The integration is over the RDF in Figure S5. Specific regions are marked for the proton transfer process and the change in the HB network. Proton rattling events are excluded. 149
H.6 The ICNs for bulk water using the BLYP XC functional for protonated oxygen in water (O* in (a)) and the next water oxygen to be protonated (O_{next} in (b)) averaged over 20 fs intervals long before proton transfer (500-480 fs) and leading up to proton transfer (200-180 fs, 100-80 fs, 60-40 fs, and 20-0 fs) at 300 K . The integration is over the RDF in Figure S6. Specific regions are marked for the proton transfer process and the change in the HB network. Proton rattling events are excluded. 150
H.7 The ICNs for bulk water using the PBE XC functional for protonated oxygen in water (O* in (a)) and the next water oxygen to be protonated (O_{next} in (b)) averaged over 20 fs intervals long before proton transfer (500-480 fs) and leading up to proton transfer (200-180 fs, 100-80 fs, 60-40 fs, and 20-0 fs) at 300 K . The integration is over the RDF in Figure S7. Specific regions are marked for the proton transfer process and the change in the HB network. Proton rattling events are excluded. 151
H.8 The ICNs for bulk water using the PBE+TS-vdW XC functional for protonated oxygen in water (O* in (a)) and the next water oxygen to be protonated (O_{next} in (b)) averaged over 20 fs intervals long before proton transfer (500-480 fs) and leading up to proton transfer (200-180 fs, 100-80 fs, 60-40 fs, and 20-0 fs) at 300 K. The integration is over the RDF in Figure S8. Specific regions are marked for the proton transfer process and the change in the HB network. Proton rattling events are excluded. 152
H.9 The RDFs for TEG-water mixtures using the PW91 XC functional for protonated oxygen in water (O* in (a)) and the next water oxygen to be protonated (O_{next} in (b)) averaged over 20 fs intervals long before proton transfer (500-480 fs) and leading up to proton transfer (200-180 fs, 100-80 fs, 60-40 fs, and 20-0 fs) at 300 K . Specific regions are marked for the proton transfer process and the change in the HB network. Proton rattling events are excluded. 153

H.10 The RDFs for TEG-water using the PBE XC functional for protonated oxygen in water (O* in (a)) and the next water oxygen to be protonated (O_{next} in (b)) averaged over 20 fs intervals long before proton transfer (500-480 fs) and leading up to proton transfer (200-180 fs, 100-80 fs, 60-40 fs, and 20-0 fs) at 300 K . Specific regions are marked for the proton transfer process and the change in the HB network. Proton rattling events are excluded. 154
H.11 The RDFs for TEG-water using the PBE+TS-vdW XC functional for protonated oxygen in water (O* in (a)) and the next water oxygen to be protonated (O_{next} in (b)) averaged over 20 fs intervals long before proton transfer (500-480 fs) and leading up to proton transfer (200-180 fs, 100-80 fs, 60-40 fs, and 20-0 fs) at 300 K . Specific regions are marked for the proton transfer process and the change in the HB network. Proton rattling events are excluded. 155
H.12 The ICNs using the PW91 XC functional for protonated oxygen in water (O* in (a)) and the next water oxygen to be protonated (O_{next} in (b)) averaged over 20 fs intervals long before proton transfer (500-480 fs) and leading up to proton transfer (200-180 fs, 100-80 fs, 60-40 fs, and 20-0 fs) at 300 K . The integration is over the RDF in Figure S13. Specific regions are marked for the proton transfer process and the change in the HB network. Proton rattling events are excluded. . 156
H.13 The ICNs using the PBE XC functional for protonated oxygen in water (O* in (a)) and the next water oxygen to be protonated (O_{next} in (b)) averaged over 20 fs intervals long before proton transfer (500-480 fs) and leading up to proton transfer (200-180 fs, 100-80 fs, 60-40 fs, and 20-0 fs) at 300 K . The integration is over the RDF in Figure S14. Specific regions are marked for the proton transfer process and the change in the HB network. Proton rattling events are excluded. . . . 157
H.14 The ICNs for TEG-water mixtures using the PW91 XC functional for protonated oxygen in water (O* in (a)) and the next hydroxyl oxygen of TEG to be protonated (O_{next} in (b)) averaged over 20 fs intervals leading up to proton transfer (60-40 fs, and 20-0 fs) at 300 K. Specific regions are marked for the proton transfer process and the change in the HB network. Proton rattling events are included. 158
H.15 The ICNs for TEG-water mixtures using the PBE XC functional for protonated oxygen in water (O* in (a)) and the next hydroxyl oxygen of TEG to be protonated (O_{next} in (b)) averaged over 20 fs intervals leading up to proton transfer (100-80 fs, 60-40 fs, and 20-0 fs) at 300 K . Specific regions are marked for the proton transfer process and the change in the HB network. Proton rattling events are included. . . . 159

H.16 The ICNs for TEG-water mixtures using the PBE+TS-vdW XC functional for protonated oxygen in water (O* in (a)) and the next hydroxyl oxygen of TEG to be protonated (O_{next} in (b)) averaged over 20 fs intervals long before proton transfer (500-480 fs) and leading up to proton transfer (200-180 fs, 100-80 fs, 60-40 fs, and 20-0 fs) at 300 K. Specific regions are marked for the proton transfer process and the change in the HB network. Proton rattling events are included. . . . 160
H.17 The ICNs for TEG-water mixtures using the PW91 XC functional for protonated oxygen in the hydroxyl group of TEG (O* in (a)) and the next water oxygen to be protonated (O_{next} in (b)) averaged over 20 fs intervals leading up to proton transfer (100-80 fs, 60-40 fs, and 20-0 fs) at 300 K . Specific regions are marked for the proton transfer process and the change in the HB network. Proton rattling events are included. 161
H.18 The ICNs for TEG-water mixtures using the PBE XC functional for protonated oxygen in the hydroxyl group of TEG (O* in (a)) and the next water oxygen to be protonated (O_{next} in (b)) averaged over 20 fs intervals leading up to proton transfer (100-80 fs, 60-40 fs, and 20-0 fs) at 300 K . Specific regions are marked for the proton transfer process and the change in the HB network. Proton rattling events are included. 162
H.19 The ICNs for TEG-water mixtures using the PBE+TS-vdW XC functional for protonated oxygen in the hydroxyl group of TEG (O* in (a)) and the next water oxygen to be protonated (O_{next} in (b)) averaged over 20 fs intervals leading up to proton transfer (200-180 fs, 100-80 fs, 60-40 fs, and 20-0 fs) at 300 K . Specific regions are marked for the proton transfer process and the change in the HB network. Proton rattling events are included. 163
H.20 The ICNs for all four XC functionals in bulk water for protonated oxygen in water (O* in (a)) and the next water oxygen to be protonated (O_{next} in (b)) averaged over 20 fs intervals leading up to proton transfer at 300 K. Specific regions are marked for the proton transfer process and the HBs. Proton rattling events are excluded. 164
H.21 The ICNs for all three XC functionals in TEG-water mixtures for protonated oxygen in water (O* in (a)) and the next water oxygen to be protonated (O_{next} in (b)) averaged over 20 fs intervals leading up to proton transfer at 300 K. Specific regions are marked for the proton transfer process and the HBs. Proton rattling events are excluded. . . 165

I.1 Probability density function of proton transfer between water molecules in bulk water for the PW91 XC functional simulations at 300 K. The reaction coordinate δ is the difference of the HB distances for the shared proton (H^*) between the two oxygen atoms of the water molecules and R_{O^*O} is the oxygen-oxygen distance. The surface has been smoothed and z-axis made arbitrary. 166

I.2 Probability density function of proton transfer between water molecules in bulk water for the BLYP XC functional simulations at 300 K. The reaction coordinate δ is the difference of the HB distances for the shared proton (H^*) between the two oxygen atoms of the water molecules and R_{O^*O} is the oxygen-oxygen distance. The surface has been smoothed and z-axis made arbitrary. 167
I.3 Probability density function of proton transfer between water molecules in bulk water for the PBE XC functional simulations at 300 K. The reaction coordinate δ is the difference of the HB distances for the shared proton (H^*) between the two oxygen atoms of the water molecules and R_{O^*O} is the oxygen-oxygen distance. The surface has been smoothed and z-axis made arbitrary. 168
I.4 Probability density function of proton transfer between water molecules in bulk water for the PBE+TS-vdW XC functional simulations at 300 K. The reaction coordinate δ is the difference of the HB distances for the shared proton (H^*) between the two oxygen atoms of the water molecules and R_{O^*O} is the oxygen-oxygen distance. The surface has been smoothed and z-axis made arbitrary. 169
I.5 Probability density function of proton transfer between water molecules for the TEG-water mixture for one of the PW91 functional simulations at 300 K. The reaction coordinate δ is the difference of the HB distances for the shared proton (H^*) between the two oxygen atoms of the water molecules and R_{O^*O} is the oxygen-oxygen distance. The surface has been smoothed and z-axis made arbitrary. 170
I.6 Probability density function of proton transfer between water molecules for the TEG-water mixture for one of the PBE functional simulations at 300 K. The reaction coordinate δ is the difference of the HB distances for the shared proton (H^*) between the two oxygen atoms of the water molecules and R_{O^*O} is the oxygen-oxygen distance. The surface has been smoothed and z-axis made arbitrary. 171

J.1 The distance for the protonated atom (O*) that has the excess proton H^+ relative to the initial position of the first protonated atom in TEG-water mixture for all individual simulation trajectories for each of the XC functionals (a) PW91, (b) PBE, and (c) PBE+TS-vdW. 172
J.2 The distance for the hydronium oxygen (O*) relative to the initial position vs. time in bulk water for the XC functionals (a) PW91, (b) BLYP, (c) PBE, and (d) PBE+TS-vdW. 173

J.3 The mean squared displacements (MSDs) of the protonated atom (O*) versus time in TEG-water mixture for each individual trajectory and their average (a-c) and the average MSDs for each XC functional (d). The graphs show the XC functionals (a) PW91, (b) PBE, and (c) PBE+TS-vdW and then the average for all three XC functionals in in graph (d). The average MSDs in (a-c) were truncated at 10 ps where the MSDs in (d) were averaged out to the longest time length but with averaging over only a subset of all MSDs. 174
J.4 The mean squared displacements of the hydronium oxygen (O*) versus time in bulk water for all XC functionals. 174

Chapter 1

Introduction

Transport of small molecules through polymer membranes has significant importance for many areas of engineering and industry. Applications include additives, membrane separations, bio-sensors, protective coatings, food and beverage packaging, and polymer electrolytes [8–10]. A better understanding of transport through membranes by a small molecular species is key to membrane design goals. Driving forces for design goals include economics, efficiency, energy consumption and sustainable production. [8, 11]

The objective of this work is to study and understand the transport mechanism of small molecules through polymeric membranes to help improve future membrane design with applications directly related to sustainability science. In this work, two specific applications, (i) food packaging and (ii) additives for polymer electrolytes, are studied. Comparing these two applications, the small molecule species of interest for mass transport studies are very different in that they have inverse effects on design goals for permeability through the membrane. For food packaging, the goal is a barrier membrane that has a low permeability of gas and moisture. For polymer electrolytes, the goal is a conductive membrane that has high permeability of ions. The transport mechanisms differ between these two systems but both show that their transport properties are a function of polymer chemistry and membrane morphology. The specific systems of interest are (i) chitosan/chitin membranes for oxygen and water transport in edible food packaging films derived from naturally-occurring, sustainable waste materials and (ii) different variants of cross-linked, sulfonated poly-cyclohexadiene with polyethylene glycol PEMs for studying transport through polymer electrolytes with PEMFC applications.

Chitosan/Chitin Membranes

Polysaccharides are a sub-class of polymer, specifically a carbohydrate whose monomer units are sugars. The biodegradable and non-toxic properties of polysaccharides and the ability to be prepared as edible membranes make them attractive

materials for edible food packaging films [12, 13]. A successful polysaccharide membrane should be a barrier for a range of small molecular species and exhibit good water transfer control. Without these properties, food preservation will be unsuccessful either due to high oxidation rates from high oxygen permeability, high water activity, or from loss of antimicrobial food additives at the surface due to absorption [13]. The food packaging schematic in Figure 1.1 highlights these effects.

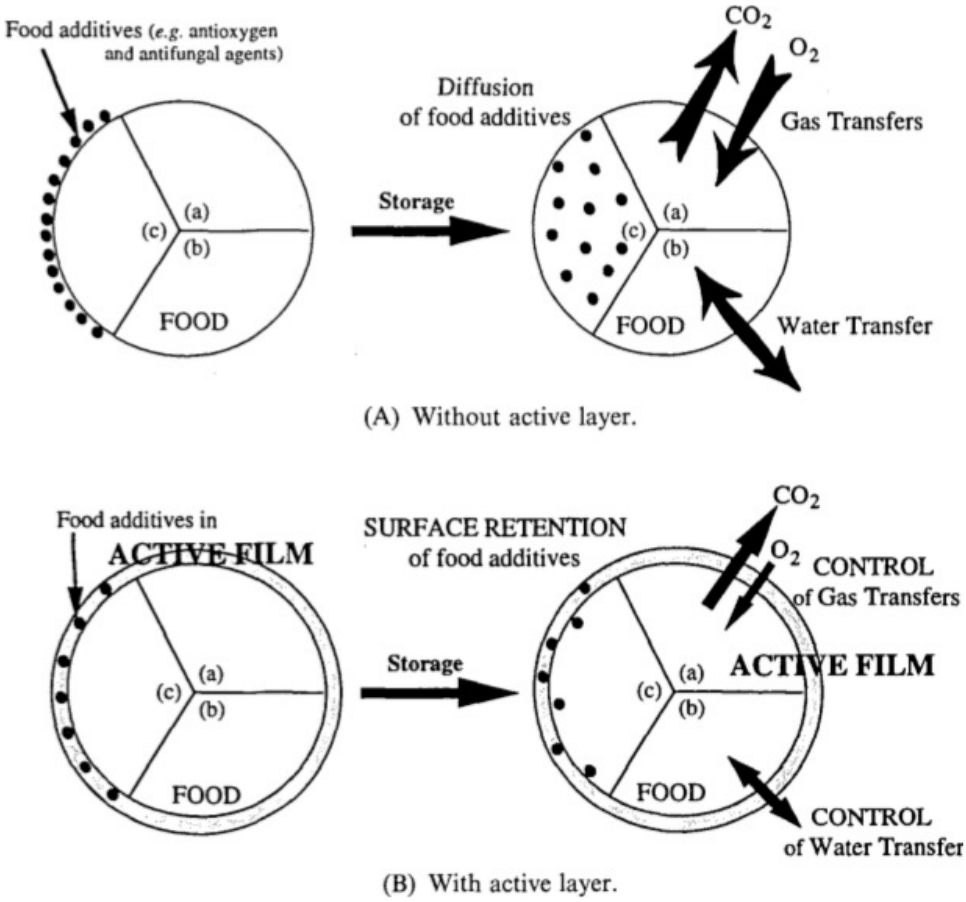


Figure 1.1: Food Packaging Schematic: Representation of food preservation with or without edible films and coatings as active layers, when the first mode of deterioration results from respiration (a), from dehydration (b), or from surface microbial development or oxidation (c). Figure from [13]

Chitosan/chitin polymeric films (membranes) are attractive in a variety of applications including drug delivery [10, 12, 14, 15], medical applications [14, 16–19], air and water filtration [20, 21], and food science [18, 19, 22–26]. These polysaccharide polymers are non-toxic, biodegradable, biocompatible, water-soluble, bacteriostatic [17, 27], and fungistatic [25, 28], desirable properties giving rise to their wide range of application. Chitosan, the second most abundant polymer in the world, makes up the exoskeleton of a vast majority of arthropods which includes insects, arachnids

and crustaceans. The majority of commercial chitosan comes from the exoskeleton of marine crustaceans, mainly, shrimp shells. [29–32] Upon treating the exoskeleton waste product with sodium hydroxide, and undergoing deacetylation, chitosan and chitin can be formed into a variety of films, fibres, and hydrogels. Also, chitosan is classified by the Food and Drug Administration (FDA) as GRAS (Generally Recognized as Safe). [9] These numerous attractive qualities and natural, sustainable abundance have given rise to the appeal of chitosan/chitin polymers compared to that of synthetic polymers in industry.

Specific to food science, an ideal food packaging material should possess three major characteristics: be derived from renewable resources, be biodegradable, and meet essential structural and chemical requirements for functioning. The structural and chemical requirements refer to being a barrier for a range of small molecular species, mainly oxygen, and exhibit good water transfer control, both of which are required for food preservation. The biodegradable and non-toxic properties of chitin and chitosan make these polysaccharides attractive materials for food packaging films. Under dry conditions, chitosan/chitin films have the attractive property of low oxygen permeability, however under increasingly humid conditions, the films absorb water and become proportionally more permeable to oxygen. [9] Possible solutions to reduce this permeability at high humidity is either by chemical modification of chitosan [9, 14, 18, 33] or by creating composite films incorporating chitosan with other materials. [27, 34–38] Chitosan is amenable to chemical modification due to favorable hydroxyl and amino groups along its backbone and many means of modification have been reported. [33, 38] Yet, it is not well understood how the change in polymer chemistry will dictate the chitosan and chitin membrane morphology at differing hydration levels and how these together will influence the permeability for gas, moisture, and other small molecules. This understanding would greatly benefit future membrane design for food packaging.

Molecular simulations have been used as a tool to probe the atomistic-level detail of chitosan and chitin materials. Siraleartmukul el al. [39] used Monte Carlo (MC) simulations to determine detailed analysis of solvation structures of single glucosamine monomers of chitosan in aqueous solution. Prathab and Aminabhav [40] used molecular mechanics calculations and molecular dynamics (MD) simulations to study structure, thermal properties, and diffusivity of N_2, O_2, and CO_2 gas molecules with a 50 monomer chitosan polysaccharide as both a bulk and a thin film at 0% relative humidity (RH). Franca et al. [41] performed MD simulations to understand the chitosan and chitin structure, hydrogen-bonding and solvation with varying NaCl concentration and pH in aqueous solution with an explicit solvent. Chitosan and chitin were modeled as polymer chains, made infinite by connection across periodic boundaries, and with chitin also modeled as an α-chitin nanoparticle. Recently, Franca et al. also extended their study to include varying the degree of acetylation [42] and to examine nanoparticles of chitosan and chitin. [43] Yin et al. [44] also performed MD simulations of chitosan with similar analysis, varying temperature, NaCl concentration, and pH in an aqueous solution with an explicit

solvent, with specific focus on the polyampholytic character of the carboxyethyl group of chitosan. Skovstrup et al. [45] analyzed the configurations and hydrogen-bonding of a wide range of different oligosaccharides with varying degrees of acetylation and methoxy substitution for terminal hydroxyl groups in an aqueous solution with an implicit solvent using mixed Monte Carlo and stochastic dynamics simulations. Stelcov et al. performed MD simulations of multiple structural arrangements of 10 chitin chain nanofibrils to elucidate the structure and mechanism of nanofibril self-assembly in aqueous solution with explicit solvent. Petrov et al. [46] employed density functional theory (DFT) and DFT-based tight-binding to determine crystal structure configurations and hydrogen-bonding of chitin from a first principles approach. On the other end of the multiscale methods, Yu and Lau [47] have developed a coarse-grained model for chitin, allowing the simulation of 300 nm long chitin chains, while Kossovich et al. [48, 49] have developed a hybrid atomistic/coarse-grained model for chitosan, allowing simulations of 200 nm long chitosan chains. Recent studies [50–52] have also performed conformational and interaction analysis of chitosan with carbon nanotubes in aqueous solution for applications in drug delivery and structural reinforcement.

From the preceding, we see that molecular simulation has proven to be a valuable tool for determining atomistic origins for conformational structures of chitosan and chitin in aqueous environments for a range of varying conditions. In relation to food packaging materials, in this work we employ molecular dynamics simulations to provide atomic-level detail of how altering moisture content in the chitosan/chitin membranes can affect oxygen permeability, dictated by both the mechanisms of oxygen diffusivity throughout the bulk of the membrane and soluble amounts of oxygen within the membrane. Results of these simulations can provide guidance for chemical modifications of this material to enhance oxygen impermeability under humid conditions. This atomic-level understanding can provide insight into design principles and help in high-throughput screening to determine optimal polymer candidates for synthesis, reduce costs from exhaustive experimental studies, and reduce time-of-discovery for next-generation chitosan/chitin films.

Proton Exchange Membranes

Polymer electrolyte membranes are commonly used in portable and stationary power fuel cell applications. Fuel cells are electrochemical cells that convert the chemical energy of a fuel into electrical energy via a chemical reaction with an oxidizing agent. There are many types of fuel cells that cover a broad range of operating conditions but all have the same three main components: (i) an anode, (ii) a cathode, and (iii) an electrolyte. The fuel enters the fuel cell at the anode side of the cell where it undergoes mass transport, possibly through a gas diffusion layer, to a catalyst embedded in the anode material, usually the electrolyte, where the fuel is oxidized. Electrons produced are passed through an external circuit for electrical energy production while the ions produced undergo charge transport through the electrolyte. The ions and electrons

are recombined at the cathode along with an oxidizing agent where the ionic species is reduced to form the waste products, which then leave the cell. Polymer electrolyte membrane fuel cells have found uses from one-watt scale chargers to one megawatt stationary power generators [53].

Proton exchange membranes (PEMs) are a specific type of polymer electrolyte membrane used in polymer electrolyte membrane hydrogen fuel cells, or PEMFCs. PEMFCs use hydrogen as the fuel source, the anode and cathode are mainly comprised of platinum (Pt) nanoparticles with a carbon support as the catalyst layer, and a proton exchange membrane as the electrolyte. PEMFCs are an attractive candidate for transportation applications in light duty vehicles due to their potential as a clean, reliable, and efficient means of electrical power [54]. Approximately ten years ago, two major issues of PEMFCs were the durability and the cost [55]. The durability issues were due to loss of catalytic activity upon operational cycling due to Pt catalyst poisoning from carbon monoxide, weakened Pt-carbon interaction from electrochemical oxidization of the carbon support, loss of catalytic surface area from sintering Pt nanoparticles, and membrane breakdown from swelling and contracting upon water uptake. The cost issues were central to the large amounts of Pt loading in the catalyst layers.

According to DOE Annual Report for 2013 [54], the cost of the entire fuel cell has been reduced by half since 2006, highlighted in Figure 1.2. This is mainly attributed



Figure 1.2: Modeled cost of an 80-kW automotive fuel cell system based on projection to high-volume manufacturing (500,000 units/year). Figure from: [54]

to reducing the amount of Pt loading by five fold since 2005 [56].

The commercialization of hydrogen-powered fuel cell vehicles continues with major car companies creating technology-sharing alliances in 2013 and many planned fuel

cell vehicle releases from now till 2020 [53]. Daimler and Ford created one of the first joint ventures in 2007 under the name of the Automotive Fuel Cell Cooperation (AFCC). Within the first seven months of 2013, three new joint alliances were formed: (i)Renault-Nissan joined the AFCC, (ii) BMW formed an alliance with Toyota, and (iii) General Motors joined with Honda. Daimler has already shipped the last of its pre-commercial B-Class F-CELL vehicle and now looks to 2017 to begin its next vehicle launch. BMW will be co-developing a vehicle platform with Toyota by 2020, while Toyota released its latest fuel cell vehicle, the Mirai, in the the USA for $57,500 in 2016, [57] with a new fuel cell stack that has twice the power density of its 2008 model. Approximately 210 Toyota Mirais have been sold as of May 2016. [58] Hyundai took its ix35 Fuel Cell into production with a small release of 1,000 vehicles from 2013 to 2015 before a mass production of 10,000 per year, based on demand. For future plans to 2025, eight states have committed to putting 3.3 million fuel cell cars on the road by 2025 and California has provided $20 million to fund 100 new hydrogen filling stations by 2024. Yet, we still face the same two technological challenges for PEMFCs today as we did ten years ago, shown in Figure 1.3.

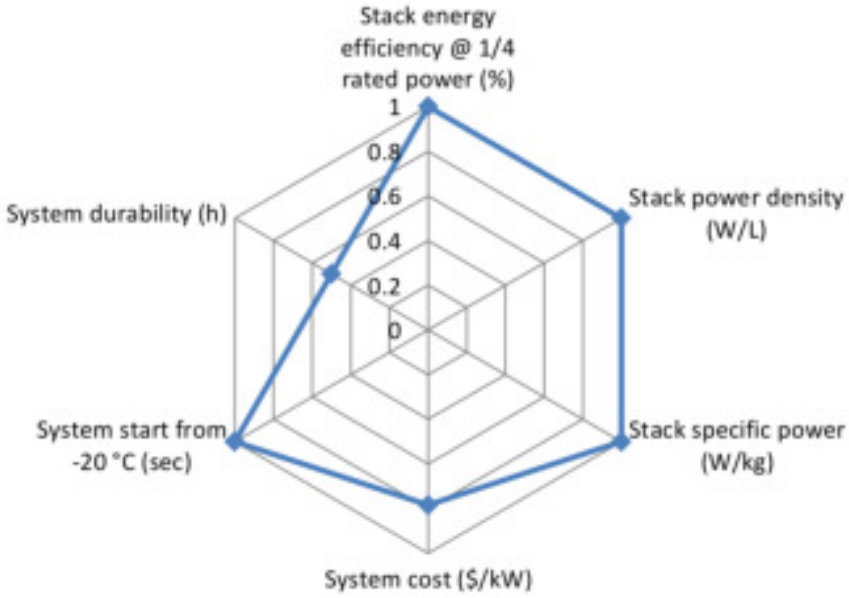


Figure 1.3: Fuel Cell Issues and Challenges - Technical Targets vs. Current Status for 2013. Figure from: [54]

A potential solution for further reducing the cost and improving durability is to operate the PEMFC at an elevated temperature, in the range of 120 °C. Increasing operational temperature of the PEMFC increases the catalytic activity and reduces the susceptibility of catalyst poisoning, specifically carbon monoxide [59]. Currently and for the past 10 years, the industry standard proton exchange membrane has

been DuPont's Nafion, a perflurosulfonic acid (PFSA) polymer membrane [60]. Upon hydration, Nafion has shown to nanosegregate into both a hydrophobic region consisting of polymer backbone and also into an aqueous region of water. The PFSA polymer side chains extend into the aqueous domains, terminated by the sulfonate group and hydronium ions. Nafion is a class of membrane where the charge transport is highly correlated with water transport. The operating conditions are optimal at about 80 °C and the membrane typically dehydrates at about 100 °C, causing major loss in charge and operating functionality [61]. Thus, the extensive research has been performed and reported for a membrane that can maintain charge transport at elevated temperatures [62,63]. This can either be by retention of water at the elevated temperatures or by decoupling the charge transport from water transport so the drop in conductivity from hydration is less pronounced.

An optimal PEM material would be inexpensive, durable, and highly-conductive at elevated temperatures. Figure 1.4 highlights that this ideal PEM material would drive down the main costs of the hydrogen fuel cell, independent of market size. The inexpensive nature of the membrane would reduce the cost in small markets while the high-operating temperature capability would alleviate the amount of catalyst and reduce the cost for large markets.

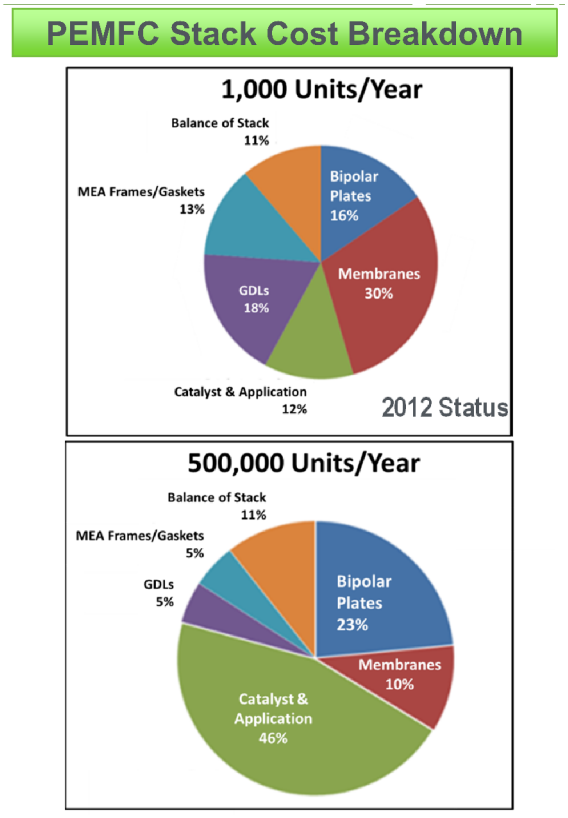


Figure 1.4: PEMFC Stack Cost Breakdown for 2012. Figure from: [64]

Materials discovery can be accelerated by guidance based on a fundamental understanding of the relationship between molecular-level structure and macroscopic properties. [65] The abundance of data produced by molecular simulations, positions and velocities of every atom as a function of time, must be distilled into a set of structural descriptors that characterize the material. The structural descriptors are chosen to comprise a necessary and sufficient set from which the properties of interest can be functionalized. Once generated, these functions which provide the value of the property at a given set of structural descriptors should be able to reproduce experimental measurements for known materials and predictively estimate values for new materials.

In the work of Esai-Sevlan and others, a set of three structural descriptors were postulated from which the self-diffusivity of water and the proton conductivity in this class of PEMs, where water and charge transport are correlated, could be estimated. [66] The descriptors include (1) acidity, a measure of the number of excess protons per unit volume of the aqueous domain, (2) confinement, a measure of the interfacial surface area between the polymer and aqueous domains per unit volume of the aqueous domain and (3) connectivity, a measure of the nature of the network of aqueous clusters through which transport of water and charge occurs. These three structural descriptors, while themselves coarse-grained, require a molecular model of the hydrated membrane in order to estimate the volume, surface area and distribution of the aqueous domain within the polymer. These three structural descriptors are again invoked in this work to provide an approximate characterization of the structure from which transport properties can be estimated.

In studying the transport through proton exchange membranes, we must understand the atomistic-level of transport of protons, or hydronium ions. Proton, or charge, transport is more complicated than simple translational movement through the membrane. Proton transport occurs via a combination of two mechanisms, the vehicular (center-of-mass translational motion) mechanism and the structural (proton hopping) diffusion mechanism, also known as the Grotthuss mechanism. [61, 67–69] Thus, the total self-diffusion of protons/charge is a combination of vehicular and structural diffusion. The latter mechanism has been the elusive mechanism in understanding the anomalously high proton conductivity in aqueous solutions. Structural diffusion has been shown to make up 60% - 70% of the total diffusion of charge in the temperature range of 280 K to 320 K [70]. Common experimental techniques for studying microscopic proton transport include nuclear magnetic resonance [61,67,68] and quasi-elastic neutron scattering [71], yet nanoscale-level resolution results beyond a qualitative level are difficult to extract due to the atomic origin of proton transport. [69] Yet, over the last two decades, computer simulations of liquids have given a quantitative understanding of the general hydrogen transfer reaction. Ab initio molecular dynamics (AIMD) simulations, [72] specifically the "Car-Parrinello" techniques for liquids, [73, 74] allow one to compute the forces on nuclei of atoms “on-the-fly” via electronic structure calculations. This gives a

technique that allows the study of systems free of parameter fitting, gives an atomic-level description of the structure and dynamics as the system evolves through time, and forces on nuclei that allow for the reactions (i.e. bond breaking and creation) to occur. This last advantageous quality of the Car-Parrinello AIMD (CPMD) scheme is of central importance in proton transport in aqueous solutions. Some of the pioneering CPMD simulations [75,76] determined that an excess proton in aqueous solution exists in two previously postulated structures, the Zundel [77] and Eigen [78] ion complexes, with the latter being the dominant species. Both structures are shown in Figure 1.5, with (a) the Zundel ion and (b) the Eigen ion. Understanding the fundamental details of proton transport through aqueous medium continues to be a challenging research topic, both for experimental spectroscopic [79–81] and computer simulation [74,82–85] studies.

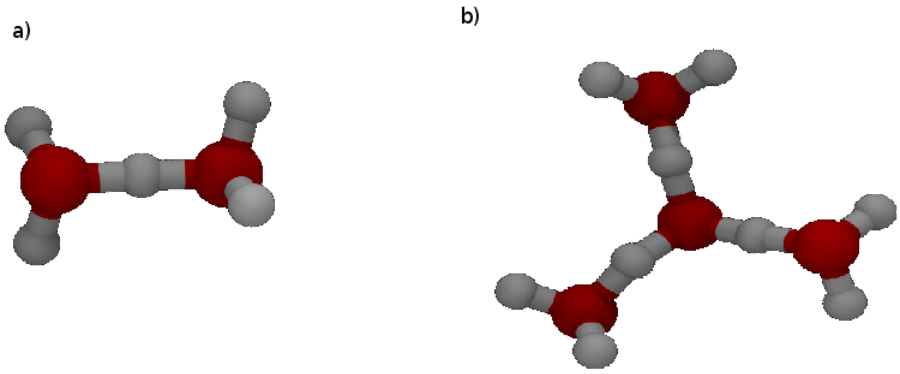


Figure 1.5: The (a) Zundel ion and (b) the Eigen ion.

Computational studies using AIMD have shown that proton transport is both a multi-dynamic and multi-timescale process that does not consist of a single proton hopping mechanism but a coupling of multiple molecular mechanisms. [82, 85–87] The chemical bonding formation is coupled to the dynamic rearrangement of the hydrogen bonding network, which is coupled to larger-scale motions that determine conditions for long-range proton transport. [85] In the work of Berkelbach et al., [82] the structural diffusion mechanism for proton transport is studied by observing the change in solvation structure of the hydronium and the proton-receiving water, [76,88] only for proton hops that then transfer to a different water molecule, thus not undergoing a reverse proton transfer reaction between the oxygen atoms. This stepwise, concerted mechanism for long-range proton transport is described as a weak hydrogen bond formation mechanism, where the hydronium begins to accept a weak, donating hydrogen bond from a water molecule while, simultaneously, the proton-receiving water loses an accepting hydrogen bond, giving an exchange of solvation structure between the hydronium and the water. This exchange of solvation

structure between the hydronium and the proton-receiving water is referred to as the "presolvation" concept [69, 82, 83, 89] and is shown in Figure 1.6. In a recent work of Hassanali et al., [86] they observed that long-range proton transport occurs via periods of "burst" dynamics where the excess proton hops across multiple water molecules for a larger distance on a short timescale, followed by periods of long-lived "rest" (>5ps) where it is stabilized by the local solvation structure on the picosecond (ps) timescale, still undergoing local proton hopping. To further clarify the role of both the weak hydrogen bond formation to the hydronium ion and proton hopping over multiple waters simultaneously to the molecular mechanism that gives rise to long-range proton transport, Tse et al. [85] showed that concerted hops over multiple water molecules occur during both burst and rest periods and that the weak hydrogen bond formation to the hydronium was the stronger correlation to the burst behavior. Thus, long range proton transport occurs via single and multiple hops and is mostly coupled to a favorable hydrogen bond network paired with a weak hydrogen bond formation to the hydronium to initiate the forward hopping, burst dynamics.

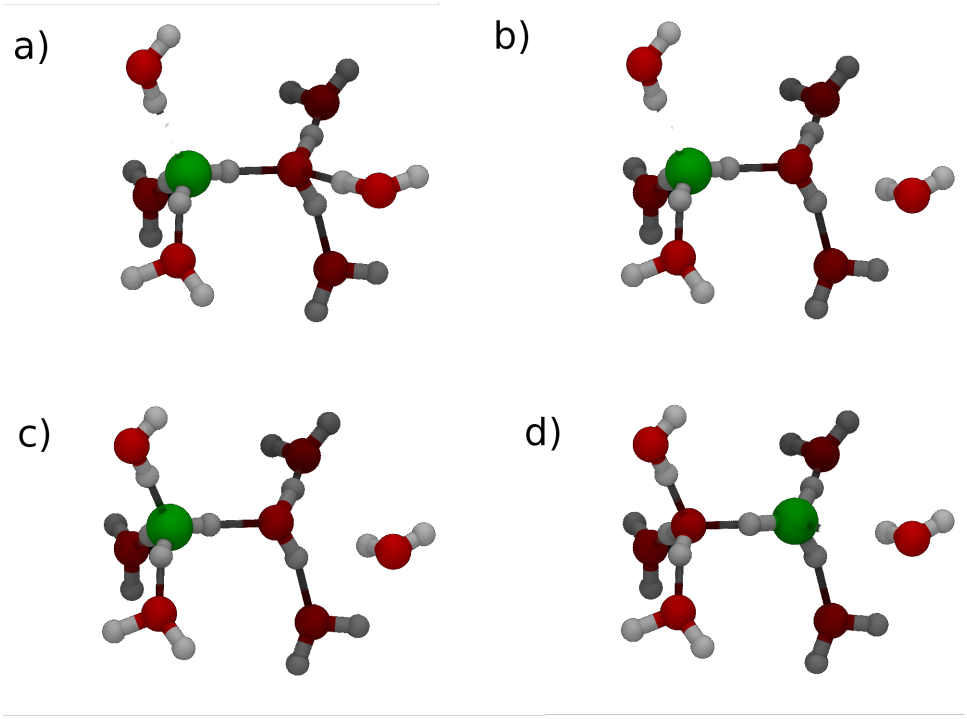


Figure 1.6: Presolvation concept for proton transport between water molecules where (a) the protonated water lacks a hydrogen-bond and the receiving water is fully solvated by 4 waters, (b) the receiving water begins to lose a hydrogen-bond donor, (c) the protonated water begins to accept a hydrogen-bond donor, exchanging solvation structures, and (d) the proton transfer occurs, leaving a "mirror-image" of solvation shell structures from beginning to end (comparing (a) to (d)).

Cross-linked, sulfonated poly-cyclohexadiene, or xsPCHD, are a recent class of PEM materials that have been studied and show a higher proton conductivity than Nafion membranes at high temperatures [90–97]. Atomic force microscopy has provided potential explanation of this enhanced conductivity from observing connected water channels at the nanoscale at elevated temperatures ($> 100\,^{\circ}C$) [92, 93, 97]. The homopolymer xsPCHD retains proton transport due to water retention at elevated temperatures [93, 95]. xsPCHD was also studied as a block copolymer and blend with polyethylene glycol (PEG) [92, 96, 97]. Both of these two types of xsPCHD/PEG membranes were shown to greatly exceed the conductivities than that of Nafion and also the current DOE target for 2020 from 20% to 100% relative humidity (RH) levels at $120\,^{\circ}C$. The xsPCHD/PEG blend membranes have displayed the highest conductivities of the two types of xsPCHD/PEG PEMs. Experimentally measured conductivities have been reported for 1499.60 mS/cm and 322.44 mS/cm for 100% and 50% RH, respectively [92], which is more than ten times that of Nafion [92, 97]. This is shown in Figure 1.7. High conductivity at a low RH level at $120\,^{\circ}C$ points to the potential of decoupling proton transport from water transport in the membrane. The polymer morphology has been studied extensively for xsPCHD/PEG membranes via experimental characterization and computational studies but the transport mechanism has only been studied indirectly. Better understanding of this mechanism could lead to directing future proton exchange membrane synthesis design to realize an ideal PEM material and thus optimize performance for high-temperature, low-humidity PEMFC operation.

PEG is a water soluble polymer that has been widely studied for its interesting properties in aqueous environments. In our work, we study both PEG and triethylene glycol (TEG), a PEG oligomer of 3 monomer units. The chemical structures of PEG and TEG are shown in Figure 1.8. The interesting properties of PEG include interactions of its ethylene oxide (EO) chains in aqueous solutions, [98–101] the ability to adsorb on surfaces and interfaces, [102] and proton conductivity in polymer electrolytes. [95, 97, 103–113] The interaction of water with the PEG chain backbone has been widely studied to date, both by experiment [98, 99, 114] and simulation [96, 101, 115–120] due to the interesting ability of PEG to form bridged hydrogen bonds (HBs) from EO monomer units to water molecules to other EO monomer units within the same chain. [101]

These properties give PEG a wide variety of applications such as biphasic (two-phase) liquid-liquid catalysis, [121] in drug delivery via modification of therapeutic molecules (known as PEGylation), [122–124], and electrochemical energy conversion as a proton exchange membrane additive as already discussed. [97, 104, 108, 110–113, 125] The conductivity of various ions with PEG in aqueous solution has also been of research interest in past years. In pharmaceutical applications, Capuano et el. [126] studied the transport properties of NaCl in PEG-water mixtures to understand the combined effect of PEG and salt interactions in aqueous solution for extension to PEGylated proteins for drug delivery. Consta and Chung [127, 128] used hybrid Monte Carlo and classical molecular dynamics (MD) simulations to

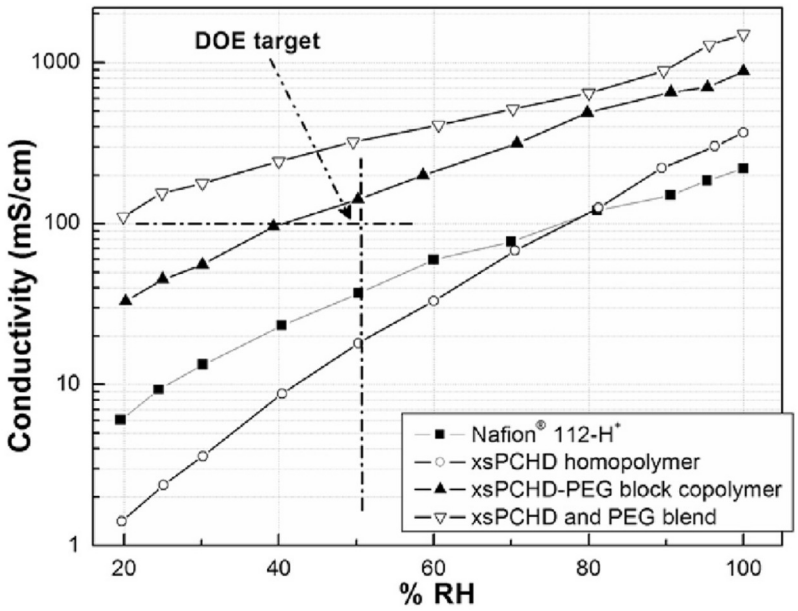


Figure 1.7: Proton conductivity vs. relative humidty for Nafion, xsPCHD homopolymer, xsPCHD/PEG block copolymer, and xsPCHD/PEG blend proton exchange membranes. **NOTE**: Reprinted from *Polymer*, **77**, S. Deng, M. K. Hassan, A. Nalawade, K. A. Perry, K. L. More, K. A. Mauritz, M. T. McDonnell, D. J. Keffer, J. W. Mays, "High temperature proton exchange membranes with enhanced proton conductivities at low humidity and high temperature based on polymer blends and block copolymers of poly(1,3- cyclohexadiene) and poly(ethylene glycol)", pgs. 208-217, DOI: 10.1016/j.polymer.2015.09.033, Copyright 2015 with permission from Elsevier.

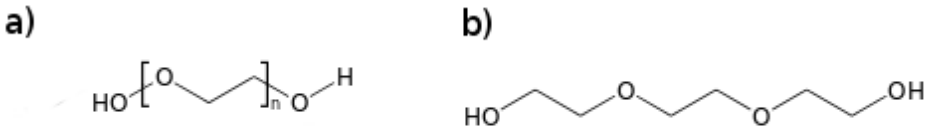


Figure 1.8: The polymers (a) polyethylene glycol (PEG) and (b) triethylene glycol (TEG).

determine charge-induced conformational changes and ion release mechanisms of PEG chains in aqueous charged nanodroplets for applications in atmospheric aerosols and electrospray mass spectroscopy experiments. In fuel cell applications, Honma et al. [105–107] synthesized organic/inorganic nanocomposite hybrid polymer electrolyte membranes of SiO_2/PEO via sol-gel processes. Sundholm et al. [129, 130] synthesized

and characterized PEO sulfonic acids as a polymer electrolyte material. Ennari et al. [131–134] performed computational studies of acidic aqueous PEO and PEO sulfonic acid solutions of the similar molecular weight as those of Sundholm et al. [129, 130] Classical MD simulations were used to study the structure, solvation and proton diffusion to determine the atomic-level effect of the PEO chains and the sulfonic acid groups on the proton conductivity with varying water content. Ennari et al. [131, 134–136] used classical MD simulations with an empirical force field that does not explicitly contain the electronic degrees of freedom in its definition. This implies that bond breaking and formation required for structural diffusion of proton transport could not be simulated in such a way that is available in CPMD simulations. To overcome this limitation, the systems simulated included both a hydronium ion to model the vehicular diffusion and a particle with the mass and charge of a proton that, interacting via electrostatics, could move freely from surrounding water molecules to model the structural diffusion. This decomposition makes MD simulations of larger systems such as that required for long polymer chains viable but such simplification deviates from the real picture of structural diffusion. Mainly, it is not a single excess proton that hops from one water molecule to another but a much larger, multi-dynamic and multi-timescale molecular mechanism that is still a current research challenge.

Research Hypothesis

We hypothesis that PEG has an enhancement effect on proton transport in PEMs given that it is located in the aqueous domain and that it has an optimum configuration to re-structure the hydrogen-bond network to facilitate directed structural diffusion. We base this on the following observations. The xsPCHD/PEG membranes show greatly enhanced conductivity over that of the homopolymer xsPCHD and Nafion. Specifically, the blend xsPCHD/PEG PEM has a higher conductivity than that of the block copolymer xsPCHD/PEG PEM. Previous computational work attributes this to the PEG chain being incorporated fully into the aqueous domains for the blend relative to the PEG in the block copolymer, that has the tail end of the PEG chain extending into the aqueous domain while "tethered" to the polymer domain. [95] This is shown in Figure 1.9.

Yet, this only gives a correlation but not a mechanism for the enhanced conductivity when incorporating PEG into the PEM. Work by Ennari et al. [134] has shown that PEG reduces water diffusion in aqueous solution. This would imply that the vehicular component of proton transport is not the mechanism for enhancing proton transport. Thus, we believe PEG must increase the structural diffusion for proton transport when incorporated into the aqueous domain. We believe, due to the strong correlation of burst dynamics of proton transport to the hydrogen-bond network in bulk water, [74, 82, 85] that PEG is able to create a directed hydrogen-bond network to enhance structural diffusion. We undertake fundamental studies

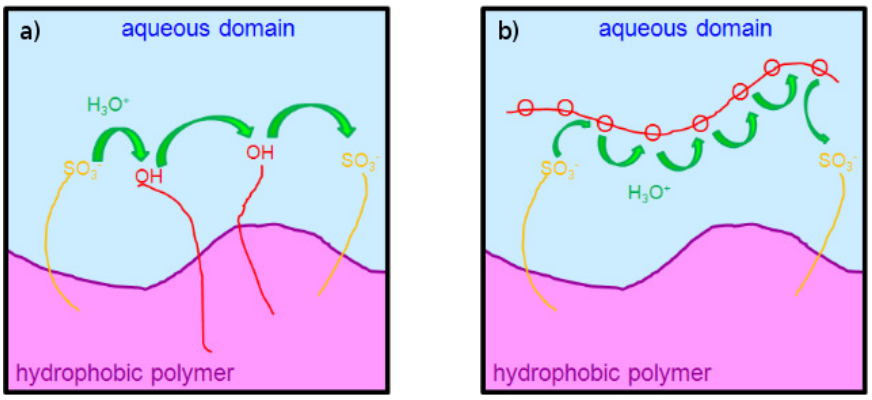


Figure 1.9: Hypothesized effect of PEG on proton transport in (a) block copolymer and (b) blend of xsPCHD/PEG PEMs.

to determine the key effects of PEG on proton transport in aqueous solution using multi-scale modeling and simulation.

Chapters Overview

We utilize multi-scale computational modeling and simulation to provide basic understanding of these membrane materials, specifically their nanoscale structure, membrane morphology, thermodynamic and dynamic properties. We undertake ab initio molecular dynamics, classical molecular dynamics, reactive molecular dynamics, confined random-walk, and continuum-level simulation work to aid in future membrane design of these materials.

In Chapter 2, we combine classical molecular dynamics and confined random walk simulations to study chitosan/chitin membranes at the lower (15% RH) and upper (95% RH) limits of hydration with infinitely- dilute oxygen molecule concentrations. We determine the change in solvation around oxygen, water, and specific chitosan and chitin polymer groups with this change in hydration. Utilizing parallel data analysis tools and confined random walk simulations, we calculate the mean square displacements and diffusivities of oxygen, water, and hydroxide ions with change in hydration. We find that the oxygen diffusivity increases by four-fold while the water and hydroxide diffusivities increase by approximately an order of magnitude. We use multiple free energy calculation techniques to determine the chemical potential, Henry's constant, and solubility of oxygen in the system with change in hydration. Combining the diffusivity and solubility, we calculate the permeability of oxygen for the modeled chitosan/chitin membranes.

In Chapter 3, we utilize our analytical model based on the three structural descriptors of a PEM, accounting for nanopore size, functionalization and connectivity, in order to predict proton conductivities. The model reproduces experimentally determined conductivities in two current PEM materials. The model was applied

to water-filled cylindrical nanopores functionalized on their interior surface with acid groups. The model predicts a theoretical maximum conductivity through a cylindrical nanopore to be 0.70 S/cm at 300 K.

In Chapter 4, we undertake fundamental AIMD simulations to determine the effects on charge transport with the presence of PEG for PEMs. This work is to try and extend the model based on structural descriptors of PEMs, utilized in chapter 3. We conducted Car-Parrinello (*ab initio*) molecular dynamics simulations of an excess proton in both bulk water and an excess proton in an aqueous solution of triethylene glycol (TEG) to investigate differences in the solvation shell structures, the distribution of protonic defects, mechanistic details, kinetics and dynamics of proton transfer with varying levels theory. We determined similarities in the time scales, mechanisms, and kinetics for structural diffusion and differences in the free energy for proton transfer, burst-rest dynamics, protonic defect structures, and hydrogen-bond networks associated with structural diffusion between the two systems. The results of this work impact general topics of research outside PEMs. PEG is used extensively in drug delivery and other electrochemistry applications due to it hydrophilicity and pH-dependent behavior in aqueous environments. These results give the first molecular-level detailed differences between proton transport in bulk water and in the presence of PEG.

In Chapter 5, we multiscale our previous work in Chapter 4 by developing a reactive force field potential, ReaxFF, [137] parameter set that can describe the effect of PEG on charge transport. We first create a quantum mechanical dataset of structures and energies, split into a training set and a validation set. We then use a genetic-algorithm-based force field optimization software [138, 139] with the training dataset to create an optimized parameter set of the ReaxFF that better describes the interaction of H^+ with PEG in an aqueous environment. With our ReaxFF parameterization, we then undertake classical molecular dynamics simulations of H^+ in bulk water, aqueous TEG solution, and aqueous PEG solution, where the PEG chain is made infinite by connection across the periodic boundaries of the simulation box. We find that the self-diffusivity of charge in the PEG chain simulation does increase the self-diffusivity by two-fold compared to that of bulk water, specifically along the axis of the box that is parallel to the PEG chain. The results of this work expand on the molecular-level details of the difference in proton transport in bulk water and aqueous PEG solution that are discussed in 4 by a multiscale approach and provide a necessary step in performing reactive molecular dynamics of xsPCHD/PEG membranes.

In Chapter 6, we describe our current progress in developing the quantum mechanical data set of structures relevant to xsPCHD, specifically the sulfonate anions, the disulfide crosslink, and C/Cl group of the polymer. The are the calculations necessary for the development of a ReaxFF parameter set that can accurately describe H^+ in xsPCHD/PEG membranes. This work is the preliminary work to perform the final step of performing reactive molecular dynamics of xsPCHD/PEG membranes.

Chapter 2

Molecular Dynamics Simulations of Hydration Effects on Solvation, Diffusivity, and Permeability in Chitosan/Chitin Films

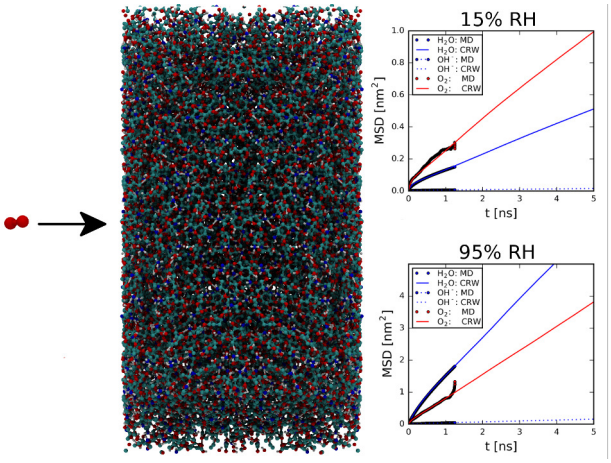


Figure 2.1: Schematic of infinitely dilute oxygen molecule permeability in chitosan/chitin film, with change in diffusivity for increasing humidity levels.

NOTE: Reproduced with permission from *J. Phys. Chem. B*, in press, Unpublished work copyright 2016 American Chemical Society.

2.1 Simulation Details

2.1.1 System Setup and Molecular Dynamics Simulations.

The chitosan/chitin membranes were modeled via 15 monomer unit chains, with three different types of monomer incorporated into the chain. The three types of monomer are (a) chitin, (b) chitosan, and (iii) chitosan with a protonated amine group, all shown in Figure 2.2. The presence of chitin monomers in the chain is to represent the degree of deacetylation. Various properties are a function of the degree of deacetylation, which is controlled during the conversion of chitin to chitosan. Typical deacetylation ranges from 60 - 80% for barrier applications. [32]

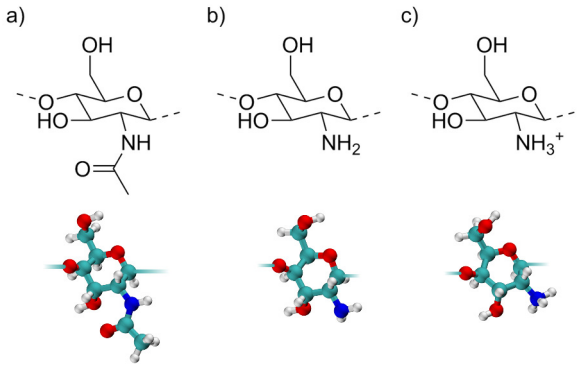


Figure 2.2: Saccharide monomers of a) chitin b) chitosan and c) chitosan with a protonated amine group. Oxygens are displayed as red, hydrogens as white, carbon as cyan, and nitrogen as blue. A double-bond is present for the N-acetyl group of the chitin monomer but not shown.

Therefore, a 1:3 ratio of chitin to chitosan monomers was chosen to represent a 66% degree of deacetylation, well within barrier application range, giving 5 chitin monomers and 10 chitosan monomers to make up the polymer chain. The degree of protonation via protonated amine groups of the chitosan monomer can be controlled during the chitin-to-chitosan conversion and is a function of the degree of deacetylation and also solution pH via the Henderson-Hasselbalch equation:

$$pH = pK_a + log\frac{[A^-]}{[HA]} \tag{2.1}$$

For our amine group, this translates to

$$pH = pK_a + log\frac{[NH_2]}{[NH_3^+]} \tag{2.2}$$

Experimentally for chitosan/chitin films, the pKa for chitosan based on the degree of deacetylation ranges from 6.3 to 7.2. [140] Thus, for our model system, we assume

an average pH of 7. Thus, we have that approximately one in six amine groups of chitosan are protonated (17%). This was rounded to 20% for the 15 monomer chain so that out of the 10 chitosan monomer units, 2 monomers have protonated amine groups. To give an overall charge neutral system, compliment hydroxide ions were introduced for every protonated amine group. The chitosan polymer chain is modeled via the Optimized Potential for Liquid Simulations United-Atom (OPLS-UA) force field, [141–145] along with the TIP4P water model, [146, 147] the hydroxide ions modeled using the rigid Wick and Dang model, [148] and oxygen modeled using the rigid Hansen, Agbor, and Keil model. [149]

The simulation of the chitosan/chitin membrane consists of a cubic 10 nm box with periodic boundaries to represent the bulk membrane. The lower and upper limit of relative humidity (RH) was chosen based on previously reported moisture sorption isotherms for chitosan films. [150, 151] The lower humidity level chosen was 15% RH, giving one water molecule per monomer unit, and an upper limit of 95% RH, giving four water molecules per monomer unit. Hydroxide ions were included in the number of water molecules included in each system. The 15% RH system consisted of 277 polymer chains, 3601 water molecules, and 554 hydroxide ions. The 95% RH system consisted of 217 polymer chains, 12,586 water molecules and 434 hydroxide ions.

The long-range Coulombic interactions were computed using the k-space style, long-range particle-particle particle-mesh solver [152] with a relative error in the force tolerance of 10^{-6} kcal/mol. Geometric mixing rules were used for computing pair-style force field parameters of different atom types. The pair-wise and Coulombic forces used a cutoff of 15.0 . The Large-Scale Atomistic/Molecular Massively Parallel Simulator (LAMMPS) open-source code was used to perform all MD simulations. [153, 154] The reversible reference system propagator algorithm (rRESPA) by Tuckerman et al. [155] was used for integrating the equations of motion. The largest time step was 0.5 fs for pairwise interactions and a smallest time step was 0.06 fs for bonding interactions. Prior testing using small NVE simulations showed these time step sizes to provide good energy conservation, required because of the fixed degrees of freedom. The water molecules and hydroxide ions were made rigid via the SHAKE algorithm [156, 157] while the oxygen molecules were held rigid via the method of Kaberaj et al. [158] Two different schemes for rigid molecules were implemented since the implementation of SHAKE in LAMMPS did not apply to linear molecules. The system was initialized by first performing energy minimization with an energy convergence tolerance of 10^{-5} kcal/mol and a force convergence tolerance of 10^{-7} kcal/mol. After minimization, the system was run in the isobaric-isothermal ensemble (NPT) for 250 ps using the Nosé-Hoover-style [159, 160] thermostat and barostat. [161–164] The thermostat was set at 300 K with a relaxation timelength of 0.1 ps. The barostat was set at 1 atmosphere with a relaxation timelength of 1 ps.

To ensure valid equilibration of the system, different initial conditions were used for the hydroxide ions and thermal annealing was employed to ensure crossing of possible high energy barriers that may not be overcome at low temperatures. Initially, oxygen was not introduced into the system during equilibration. To ensure that the

initial conditions were not sensitive to hydroxide-cation positioning, two different initial conditions were setup per hydration level. For each hydration level, one initial condition located the hydroxide ions in close proximity to the protonated amine groups of chitosan while the other initial condition had the hydroxide ions randomly distributed throughout the system. The equilibration of the systems consisted of the following simulation steps: energy minimization, 15 ps NVT (fixed density, isothermal) with velocity rescaling, 0.2 ns NVE (fixed density and adiabatic), then thermal annealing via 0.2 ns NVT ramping from 300 K to 600 K, 1 ns for NVT at 600 K, 0.2 ns for NVT quenched to 300 K, and 2.4 ns of NPT (fixed number of molecules, isobaric, isothermal). The system gave the same energy convergence for both sets of initial conditions per hydration level, implying that initial conditions of the hydroxide-protonated were not a strong factor and the systems were well equilibrated.

From the equilibrated simulations, molecular oxygen was introduced via insertion into the systems. We simulated infinitely dilute oxygen systems via inserting a single oxygen molecule into the system. We repeated this for 20 random oxygen molecule insertions, each with unique coordinates in the system, to create 20 different initial conditions for data production. This allowed for isolated oxygen trajectories to better understand molecular mechanisms for solubility and transport across the chitosan/chitin membranes. Multiple trajectories were realized to ensure adequate sample size and exploration of possible phase space relative to oxygen molecules. These initially oxygenated systems were then run using NPT for 100 ps of equilibration, followed by 1.25 ns of data production.

2.1.2 Parallel MapReduce-MPI Mean Square Displacement Calculation.

With advances in high-performance molecular dynamics simulations, longer (millisecond) [165] and larger (trillions of atoms) [166] simulations are possible. Yet, with larger and longer simulations comes larger datasets, specifically tera-scale MD simulation trajectories. Currently, a majority of post-processing data analysis of these trajectories is performed in a sequential manner, not taking advantage of large advances in parallel data processing algorithms and software. Recently, MapReduce algorithms [167–169], Google's programming model for performing large dataset processing and computation, have made their way into parallel post-processing of massive MD trajectories. D. E. Shaw and coworkers have created HiMach, [170] a scalable, parallel analysis framework that uses MapReduce to do just such analysis such as analyzing ion permeation through membrane channels, generating electron density maps, and calculating root mean squared deviations between frames in MD trajectories. Plimpton and coworkers have also implemented a parallel C++ library that utilizes message-passing (MPI) calls to help develop algorithms using the MapReduce programming model, called MapReduce-MPI. [171–173]

The MapReduce programming model consists of the following steps: 1) Splitting data to be processed into chunks (usually in a parallel fashion using MPI-IO.) 2) Send

the data chunks to processes with a "key" assigned to the data chunk to uniquely identify the data and "values" that are the data to be evaluated, called the "key-value pair". 3) Performing parallel analysis/evaluation of the data on each process with no inter-process communication. 4) Create a new key-value pair and aggregate the results. 5) Upon aggregating the results, we reduce the data to the new key-value pair, giving a smaller dataset. 6) Repeat steps 2-5 until we reach the desired output from the data.

We have utilized the MapReduce-MPI library [171–173] to create a parallel, post-processing mean square displacement (MSD) code to handle the collectively terascale-size dataset generated from the MD trajectories in this work. Testing, validation, and scalability measurements were performed on bulk water utilizing the TIP4P-Ew model by reproducing diffusivity data found in Table 7 of the work by Horn et al. [146] Data-to-knowledge time was reduced from days of sequential computation to hours/minutes for the entire dataset utilizing up to 128 processors per MSD calculation.

2.1.3 Confined Random Walk Simulations.

Confined random walk theory [174] (CRW) describes diffusion in the presence of nanoscale confinement. CRW theory allows for a multiscale approach to accurately determine MSDs from simulations long enough to reach the linear regime, as required by the Einstein relation to determine accurate diffusivities. Due to its simplicity, CRW simulations can alleviate the large computational expense of long MD simulations (months on a supercomputer) to reach the linear regime with a much smaller computational effort (minutes on a laptop computer). Previously, CRW simulations have successfully been applied to small molecules in metal-organic frameworks, [174] water in proton exchange membranes, [93, 174, 175] and liquid and glassy iron. [174]

CRW simulations augment traditional unconfined random walk theory by introduction of two parameters to describe the nanoscale confinement: 1) a cluster size and 2) a cluster-to-cluster to hopping probability. The CRW simulations are fit to short-time MD simulation MSDs to find the optimized parameters. These optimized CRW parameters are then used to run much longer, infinite time limit CRW simulations to extend the MSDs for accurate diffusivity calculations. For further information, the reader is directed to the original work by Calvo-Munoz et al. [174]

2.1.4 Solubility Calculations.

To calculate the solubility, S , of a solute at infinite dilution, we utilize the following relation:

$$S = \frac{1}{V_m K_H} = \frac{\rho}{M}\frac{1}{K_M} = \frac{1}{RT}\exp\left(-\frac{1}{RT}\mu^{ex}\right) = \beta\exp\left(-\beta\mu^{ex}\right) \tag{2.3}$$

where V_M , ρ , and M are the molar volume, the density, and the molar weight of the pure solvent, R is the gas constant, T is the temperature, μ^{ex} is the excess chemical

potential of the solute, and K_H is the Henry's constant for a solute at infinite dilution given as:

$$K_H = \frac{\rho RT}{M} \exp\left(\frac{1}{RT}\mu^{ex}\right) = \frac{\rho}{\beta M} \exp\left(\beta\mu^{ex}\right) \tag{2.4}$$

Therefore, the solubility is reduced to calculating the excess chemical potential of the solute molecule, or the free energy of solvation. The excess chemical potential of the solute is the difference between the chemical potential in solution and the chemical potential of the solute as a pure ideal gas for the same temperature, pressure and density between both phases. Many methods have been developed for calculating the chemical potential, [176, 177] including particle insertion methods, [178] particle deletion methods, [179–184] particle reinsertion methods, [185, 186] alchemical free energy perturbation, [187–189] thermodynamic integration, [187, 188, 190] Gibbs ensemble Monte Carlo, [191, 192] Gibbs-Duhem integration, [193] and the Bennet acceptance ratio method, [194] to name only a few. For more discussion about free energy calculations, the reader is directed to texts available on the subject. [176, 177] For our current work, we employ free energy perturbation, [187–189] finite-difference thermodynamic integration [190] and particle deletion methods [179–182, 184] to calculate the excess chemical potential of the oxygen solute molecule at infinite dilution in the aqueous polymer solvent.

Free Energy Perturbation and Thermodynamic Integration.

For the free energy perturbation (FEP) method, the change in the free energy for the solute from the pure ideal gas (G_0) to the solvent (G_1), otherwise known as the free energy of solvation, can be calculated using a two-state free energy difference:

$$\begin{aligned} G_1 - G_0 = &\quad \Delta G_0^1 \\ = &\quad -k_B T \ln\left[Q_1/Q_0\right] \\ = &\quad -k_B T \ln\left[\frac{\int \ldots \int d\mathbf{r}^N d\mathbf{p}^N \exp\left(-\beta \Delta H_0^1\right) \exp(-\beta H_0)}{\int \ldots \int d\mathbf{r}^N d\mathbf{p}^N N \exp\left(-\beta H_0\right)}\right] \\ = &\quad -k_B T \ln\left\langle \exp\left(-\beta \Delta H_0^1\right)\right\rangle_0 \end{aligned} \tag{2.5}$$

where ΔG_0^1 is the free energy of solvation, k_B is Boltzmann's constant, Q_i is the partition function of the i$^{\text{th}}$-state, $\mathbf{r}^N$ and $\mathbf{p}^N$ are the position and momenta of the N particles of the system, respectively, H_i is the Hamiltonian for the i$^{\text{th}}$-state, and $\langle \ldots \rangle_i$ denotes an ensemble average of the given property, sampled in the i$^{\text{th}}$-state. For the chemical potential, the states represent the oxygen solute as a pure ideal gas particle at state 0 and a solute molecule that fully interacts with the solvent at state 1. As long as temperature and mass are held constant during the simulation, we can integrate out the kinetic energy component of the Hamiltonians in Eq. (2.5), leaving

only the change in the potential energy (U):

$$\Delta G_0^1 = -k_B T \ln \left\langle \exp\left(-\beta \Delta U_0^1\right) \right\rangle_0 \tag{2.6}$$

To link the two states together, we construct intermediate states via a coupling parameter (λ), giving:

$$\Delta U_0^1 = (1-\lambda)U_0 + \lambda U_1 = U_0 + \lambda \Delta U_0^1 \tag{2.7}$$

we can then express the free energy of solvation as:

$$\Delta G_0^1 = \sum_{i=0}^{n-1} \Delta_{\lambda_i}^{\lambda_{i+1}} G = -k_B T \sum_{i=0}^{n-1} \ln \left\langle \exp\left(-\beta \Delta U_{\lambda_i}^{\lambda_{i+1}}\right) \right\rangle_{\lambda_i} \tag{2.8}$$

Eq. (2.8) indicates we can obtain the free energy difference between two states via computing energy differences. Thus, we can compute the excess chemical potential via a coupling parameter to the potential interaction of the oxygen molecule with the rest of the polymer solvent, and slowly "grow" the interaction at each λ_i -state. For our work, we have used $\lambda = 0.1$ as our coupling parameter, with 100 ps of equilibration at each λ_i -state followed by 500 ps of production for the λ_i -state to collect the average annotated in Eq. (2.8). In order to avoid the singularity problem of linear scaling, a soft-core potential was used. [195, 196]

For finite difference thermodynamic integration (FDTI), the change in the free energy for the solute from the pure ideal gas to the solvent is not computed via energy differences as in FEP but instead using the energy derivative with respect to the coupling parameter λ :

$$\begin{aligned} \frac{\partial G(\lambda)}{\partial \lambda} &= -k_B T \frac{\partial}{\partial \lambda} \ln\left[Q(\lambda)\right] \\ &= \frac{\int \ldots \int d\mathbf{r}^N d\mathbf{p}^N \frac{\partial H(\lambda)}{\partial \lambda} \exp(-\beta H(\lambda))}{\int \ldots \int d\mathbf{r}^N d\mathbf{p}^N \exp\left(-\beta H(\lambda)\right)} \\ &= \left\langle \frac{\partial H(\lambda)}{\partial \lambda} \right\rangle_\lambda \end{aligned} \tag{2.9}$$

Upon integration with respect to λ and giving each state an equal weighting, we have:

$$\begin{aligned} \Delta G_0^1 &= \int_{\lambda=0}^{\lambda=1} \left\langle \frac{\partial H(\lambda)}{\partial \lambda} \right\rangle_\lambda d\lambda \\ &= \sum_{i=0}^{n-1} \left\langle \frac{H(\lambda_{i+1}) - H(\lambda_i)}{\lambda_{i+1} - \lambda_i} \right\rangle \end{aligned} \tag{2.10}$$

By choosing a very small difference in $\lambda_{i+1} - \lambda_i$, we can numerically solve for the free energy of solvation/excess chemical potential. Although $\lambda = 0.1$ is relatively large for

FDTI, we use this to give an additional method for calculating the excess chemical potential, discussed more in section 2.2.3.

Particle Deletion Methods.

The pioneering work for the particle deletion method (inverse Widom method) is attributed to Shing and Gubbins. [183] Kofke and Cummings gave a critical evaluation and comparison to various free energy methods for the hard-sphere model, specifically showing that compared to Widom's particle insertion method, [178] the particle deletion method was inferior and prone to systematic error. [197] However, Boulougouris and co-workers have since re-visited the particle deletion method, developing both the staged [179–181] and direct [182, 184] particle deletion methods and have been able to calculate accurate chemical potentials and solubilities for a number of systems, [179–182, 184] including infinitely dilute benzene in polyethylene melts. [182] Development for direct particle deletion has also been carried out separately by Siegert et al. [198] with applications to solubilities of O_2, N_2, and benzene in poly (dimethyl siloxane). The driving force for developing particle deletion methods is the ability to calculate chemical potentials and solubilities for dense systems and large solute molecules, key limitations to the particle insertion method.

We have implemented the direct particle deletion method in our work as another method to calculate the excess chemical potential for oxygen in the chitosan/chitin membranes and supplementing with the staged particle deletion method calculations also, for reasons given below. Below, Eqs. 2.11 and 2.12 are the excess chemical potential using the staged and direct particle deletion methods, respectively, for the NPT ensemble. The reader is directed elsewhere for the derivation of these methods. [179, 180, 184] Note that in the NVT ensemble the volume is constant and this term will cancel out in the calculation.

$$\begin{aligned} \mu^{ex} = & - k_B T \ln \left[\left\langle \frac{1}{V} \right\rangle_N \left\langle \theta(\mathbf{r}_{solute}, d) \frac{\exp(\beta U^{\text{int}\,er}_{solute})}{V} \right\rangle_N^{-1} \right] \\ & - k_B T \ln \left[\left\langle \int \theta(\mathbf{s}_{solute}, d/L) d\mathbf{s}_{solute} \right\rangle_{N-1} \right] \\ = & \quad \mu^{ex}_{energy} + \mu^{ex}_{volume} \end{aligned} \tag{2.11}$$

$$\begin{aligned} \mu^{ex} = & \, k_B T \\ & \ln \left[\left\langle \frac{1}{V} \right\rangle_N^{-1} \left\langle \frac{1}{\int \theta(\mathbf{s}_{solute}, d/L) d\mathbf{s}_{solute}} \theta(\mathbf{r}_{solute}, d) \frac{\exp(\beta U^{\text{int}\,er}_{solute})}{V} \right\rangle_N \right] \end{aligned} \tag{2.12}$$

where d is the hard sphere diameter to represent the deleted particle as an ideal gas particle that creates a cavity, or a "hard solute molecule", $\mathbf{r}_{solute}$ is the coordinates of the solute molecule, $\theta(\mathbf{r}_{solute}, d)$ is the Heaviside function (=0 when the hard sphere

molecule overlaps with another atom in the system and =1 otherwise), U_{solute}^{inter} is the intermolecular potential energy of the solute molecule, L is the length of the simulation box, $\mathbf{s}_{solute}$ is the scale solute coordinates, and $\int \theta(\mathbf{s}_{solute}, d/L) d\mathbf{s}_{solute}$ is the accessible volume fraction of the hard solute molecule. The staged particle deletion expression of the excess chemical potential is composed of a sum of an energetic term and a volume term, where the volume term is the free energy for creating a cavity to accommodate the solute molecule in the solvent and the energetic term is the free energy to change from a "hard solute molecule" to a fully interacting solute molecule with the solvent. Note that the averages for the staged particle deletion method differ in that the volume term is computed in an N-1 particle system while the energetic term is computed in an N particle system. To use the staged particle deletion method rigorously, one must run two simulations, one with the solute interacting with the system to calculate the energetic term and another without the solute to calculate the volume term. However, one can make the assumption that the volume term will be relatively equal for the N and N-1 particle systems and one simulation is run. This assumption breaks down for larger molecules. The direct particle deletion method in Eq. (2.12) only requires a single simulation but does not have the decomposition of the excess chemical potential into an energetic and a volume term. However, one can instead use energetic term of the staged particle deletion method to determine the energetic term for the direct particle deletion method and then use the total and energetic term to back-calculate the volume term. We employ this method in our current work to determine the decomposition of excess chemical potential and solubility.

The two key components to using the stage and direct particle deletion methods are in calculating the U_{solute}^{inter} term and the $\int \theta(\mathbf{s}_{solute}, d/L) d\mathbf{s}_{solute}$ term. The U_{solute}^{inter} term was computed by post-processing the MD trajectory using the LAMMPS MD engine [153, 154] to compute only the intermolecular potential energy term of the oxygen molecule with the aqueous polymer system. Accuracy is an issue with chemical potential calculations, thus, to compute the accessible volume fraction, $\int \theta(\mathbf{s}_{solute}, d/L) d\mathbf{s}_{solute}$, we use the analytical method developed previously by Dodd and Theodorou, which calculates the volume of a body of fused spheres with intersecting planes. [199] The excluded volume of a single atom/sphere is calculated by adding its radius to the spheres in the system and then performing the body-volume calculation. Then, the difference in this body-volume and the system volume gives the accessible volume. Extension to accessible volume of chain molecules is discussed further in other works. [180,198] When performing chain molecule deletions, the number of spheres in the body-volume calculation increases as the number of atoms in the system times the number of atoms in the chain molecule. For larger systems of over 10,000 spheres, this analytical calculation of the accessible volume can be very computationally demanding and also very memory intensive, limiting serial implementations. Since we have upwards of 100,000 atoms in our systems, a serial implementation was not an option. The original, serial Fortran code for volume analysis was parallelized by implementing the spatial decomposition method

and additional load balancing algorithms were used to ensure equal distribution of work among processes. Data-to-knowledge time was reduced from days of sequential computation (if the computation was possible at all) to hours utilizing 64 to 128 processors. The parallel, post-processing calculations were carried out on two separate platforms 1) the Gordon cluster and 2) the Google Compute Engine (GCE) using virtual machines. Gordon is an Extreme Science and Engineering Discovery Environment (XSEDE) cluster housed at the San Diego Supercomputer Center (SDSC). The GCE is part of the Google Cloud Platform. The parallel computation does not require strong inter-process communication and tightly-coupled process interconnect (like that required for HPC applications such as MD), allowing for the cloud computing platform to perform with almost equal performance as that of the Gordon cluster.

To determine an accurate value of d for the particle deletion methods, one must perform a parametric sensitivity analysis, involving multiple accessible volume calculations as a function of d . At values of d that are too small, the accessible volume fraction is over approximated and the Heaviside function does not "delete" the high energy configurations not accessible to the N-1 system. At too large values of d , the accessible volume fraction is under approximated and statistical sampling decreases due to the Heaviside function deleting important configuration accessible to both N and N-1 particle systems. Upon evaluating the standard error of the excess chemical potential with varying d , one will observe both a plateau and a decrease in the error of the calculation for a range of d where accurate excess chemical potentials can be calculated. We employed this method in our own calculations and then compared to excess chemical potentials to the FEP and FDTI methods to ensure accuracy. We validated our own volume analysis and excess chemical potential calculation software by reproducing both the Lennard-Jones system [179, 184] and benzene in polyethylene [182] data of the previous work by Boulougouris and coworkers.

2.1.5 Permeability Calculations.

With the diffusivity available via MSD vs. observation time slope discussed in section 2.1.2 and 2.1.3 and the solubility available via the excess chemical potential calculations discussed in section 2.1.4, we can readily calculate the permeability (P) of the solute oxygen molecule via the solution-diffusion mechanism:

$$P = S * D \tag{2.13}$$

At low concentration of the solute molecule, the transport diffusivity of the solute can be approximated by its self-diffusivity.

2.2 Results & Discussion

2.2.1 Radial Distribution Functions and Distribution of Water Molecules.

To understand the interactions of solute molecules (H_2O, OH^-, and O_2) with each other and the chitosan/chitin chain monomers and possible changes with humidity, we calculated the radial distribution functions (RDFs) for solute molecules with various other atoms in the system. The RDFs for H_2O, OH^-, and O_2 are shown in Figures 2.3, 2.5, and 2.6, respectively.

In Figure 2.3, we show the RDFs of the O of H_2O with other H_2O, O_2, OH^- and the N of the chitosan and chitin monomers observed during the MD simulations of 15% RH in (a) and 95% RH in (b). The first peak occurs at 2.75-2.80 across all RDFs, indicating solute molecules and both N-containing side groups of the chain are fully immersed in an aqueous, hydrophilic phase. The H_2O-H_2O and H_2O-O_2 RDFs lay directly on top of one another for both humidity levels, implying that the O_2 has strong interaction with water and follows its dynamic behavior throughout the membrane with increasing humidity. For all three monomer groups, the protonated amine/cation group has the strongest attraction to the water molecules, most likely due to the strong positive charge attracting the electronegative lone electron pairs of the water molecule. Relative to the chitosan monomer, the chitin monomers interact to a higher degree with the water molecules of the system. In increasing humidity, we see that the peaks are reduced for all but the chitin monomer groups and the peaks all have relatively the same peak height. This indicates that with increasing humidity, we see a more homogeneous water distribution throughout the entire membrane, with solute and polymer being equally solvated.

In our force fields used to model the system, fixed point charges are used for all atoms and bonding is modeled via harmonic springs. Thus, polarizability and also proton dissociation are not possible with the current model. The strong interaction of the cation with water molecules indicates that these effects could be very important to further accurately describe the system, discussed more below.

In Figure 2.4, we show snapshots of the water distribution for both the (a) 15% RH and (b) 95% RH systems to visualize the difference in polymer hydration. All polymer chains and other solute molecules are not show for clarity. We see that with increasing humidity, there is a larger connection of the aqueous domains and a homogeneous distribution at 95% RH. Comparing both Figure 2.3 and Figure 2.4, we can visualize the full solvation of the polymer chains and realize the aqueous domain that solute molecules use for transport pathways across the chitosan/chitin membrane.

In Figure 2.5, we show the RDFs for O of OH^- with other OH^-, O_2, H_2O, and the N of the protonated amine/cation group of the chitosan monomer group for both 15% RH in (a) and 95% RH in (b). We first note the large peak associated with the cation

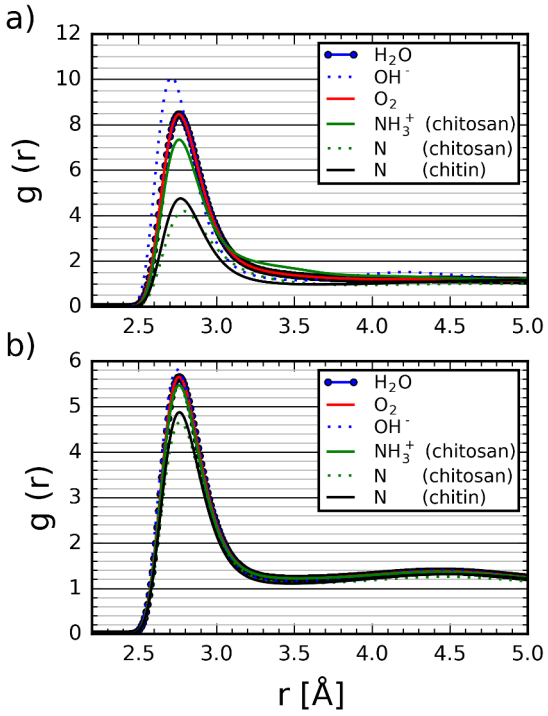


Figure 2.3: Radial distribution functions for the O of H_2O with solute O_2, OH^- and specific N atoms for polymer monomers at 300 K for both humidity levels: (a) 15% RH and (b) 95% RH. See Figure 2.2 for graphic of monomers.

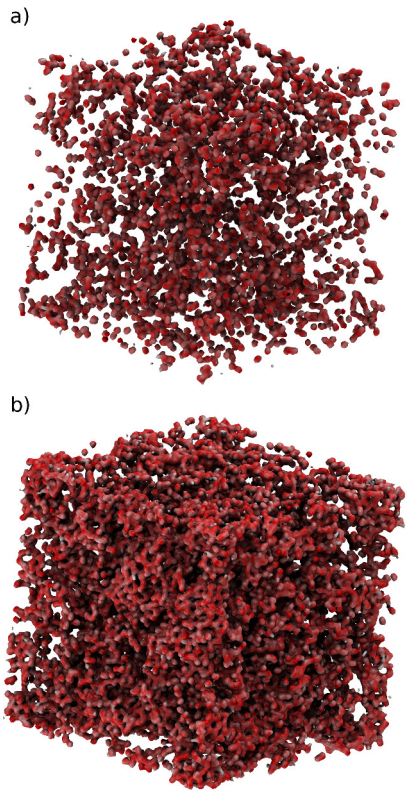


Figure 2.4: Water distributions for (a) 15% RH and (a) 95% RHfor chitosan/chitin membranes. Polymers and other solute molecules are not show for clarity. Graphics were created using VMD [1, 2] and Tachyon. [3]

group. There is a very strong anion-cation correlation in the system, implying that the anion groups are always located proximal to these protonated amine groups. Our current force field implementation does not allow for modeling proton dissociation.

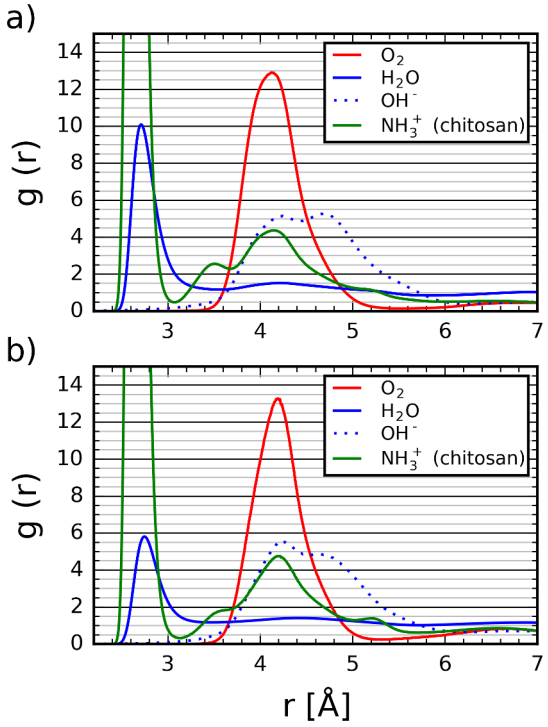


Figure 2.5: Radial distribution functions for O of OH^- with O_2, H_2O and the N of the cation for the chitosan monomer at 300 K for both humidity levels: (a) 15% RH and (b) 95% RH. See Figure 2.2 for the monomer group graphic.

With a higher computational cost, using a reactive force field [137,200] could allow for the amine group to de-protonate or a polarizable force field [95, 201, 202] could better describe the charge distribution, both potentially removing the bias of the anion to always be located proximal to the cation. The first peak with the O of H_2O at 2.75 shows that the rest of the first solvation shell around OH^- is populated by water molecules. The second and third peak of the OH^- RDF with the cation is correlated to the other protonated amine groups located along the chitosan/chitin chain. Thus, the anion is associated with one of the protonated chitosan monomers and is kept a fixed distance away from the other protonated monomers of the same chain. We see that the OH^--OH^- RDF peaks line up with the second nearest protonated amine group peaks at 4.0-4.2 for both RH levels. The O of O_2 also has a strong peak located at this distance. Thus, the OH^- stays proximal to the protonated chitosan monomer, solvated by other water molecules, and located 4.0-4.5 from O_2 that are strongly attracted to the protonated chitosan monomers along the polymer chain backbone.

In Figure 2.6, we show the RDFs for O of O_2 with other O_2, OH^-, H_2O, and the N of the chitosan and chitin monomers for both 15% RH in (a) and 95% RH in (b). In the O_2-H_2O RDF, we see again that the O_2 is strongly correlated to the water of the system by the first peak occurrence. This leads to the expectation that O_2 dynamic behavior will be also strongly correlated to water in the system. The O_2-N(chitosan) and O_2-N(chitin) RDF comparison shows that the O_2 favor the chitosan monomers of the polymer chain relative to the chitin monomers. The O_2-NH_3^+ RDF is consistent with the previous discussion, specifically, that the O_2 are attracted to the cation group. The O_2-OH^- RDF peak is also consistent with the previous discussion, in that the O_2 and OH^- are both attracted to the protonated chitosan monomer group, proximal to the protonated groups located laterally along the polymer chain and giving rise to the correlated peaks at similar distances of protonated chitosan monomers along the backbone.

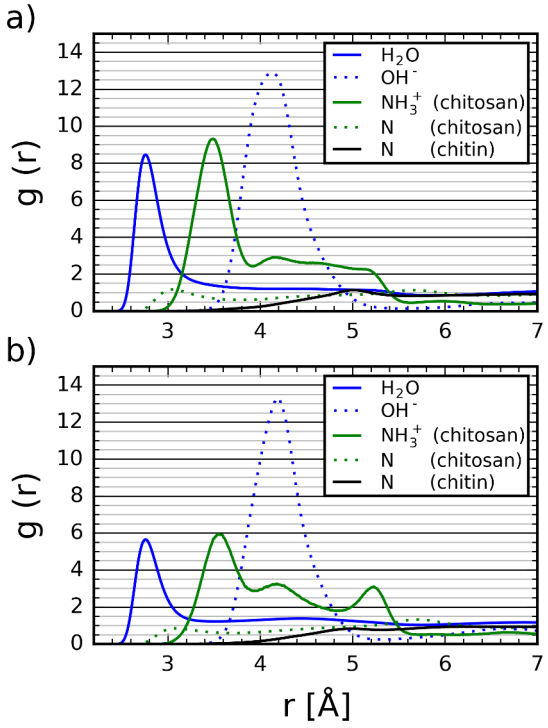


Figure 2.6: Radial distribution functions for O of O_2 with H_2O, OH^- and specific N atoms for polymer monomers at 300 K for both humidity levels: (a) 15% RH and (b) 95% RH. See Figure 2.2 for graphic of monomers.

For all RDFs, we observe the strong interactions of the groups mainly with the chitosan monomer groups of the chain and also the effects of increasing humidity. The water RDFs show the largest difference with increasing humidity. Mainly, the peaks lose distinction at higher humidity, giving rise to a more homogenous aqueous phase with polymer chains becoming fully solvated. There is little change in the O_2

and OH^- RDFs with increasing humidity, mainly due to having full water solvation at both humidity levels and the strong attraction to specific groups in the system that is not hindered upon increased humidity.

2.2.2 Mean Square Displacements and Self-Diffusivities.

To understand the dynamic behavior of oxygen and water in the chitosan/chitin membranes, we have computed the MSDs for both 15% RH and 95% RH levels, utilizing our in-house MapReduce-MPI-based parallel MSD code, previously described in section 2.1.2. Then, using the Einstein relation, self-diffusivities are calculated from the slope of the MSD vs. time in the long-time, linear limit. Upon plotting the log-log MSD vs time relation, the MD simulation MSDs have not reached the long-time, linear regime. Using the CRW simulations to fit the short-time MSDs of the MD simulations, we were able to extend the MSDs to the long-time, linear regime to satisfy the requirement for calculating accurate self-diffusivities. In Figure 2.7, we have plotted the MSDs for both the MD and CRW simulations for both 15% RH and 95% RH.

From Figure 2.7, we see interesting dynamic behavior for O_2 and H_2O at different humidity levels. We see that O_2 has a higher diffusivity relative to H_2O at 15% RH. Using our previous results from the RDFs, we know that the OH^- and O_2 are attracted to the protonated chitosan monomers throughout the membrane. We see that the OH^- stays relatively immobile but, in contrast, the O_2 is very mobile at this RH level. Thus, we believe the O_2 is "hopping" from one protonated chitosan monomer to another, traveling through water domains shown in Figure 2.4. At low humidity, the water mobility is suppressed and instead mainly solvates the polymer chains. As we increase the humidity to 95% RH, we see that the MSDs all greatly increase, specifically the O_2 and H_2O MSDs. Also, the H_2O MSD slope becomes greater than the O_2 at 95% RH. Again, we know from the RDF results that the O_2 is still strongly attracted to the protonated chitosan monomers of the polymer chains. Thus, the O_2 dynamics at higher humidity mimic the water dynamics due to the correlated increase but, attraction to the polymer chain cations restricts the dynamics O_2 relative to water. We can also observe that in Figure 2.4, the aqueous domain has increased for 95% RH, causing separation between chains. This could further reduce the O_2 "hopping" dynamics from cation groups between different polymer chains, causing the attraction of O_2 to these cation groups to suppress its mobility as opposed to increasing it at lower humidity.

In Table 2.1, we show the self-diffusivities calculated from the CRW simulation MSDs for both 15% RH and 95% RH and also the ratio of the 95% RH self-diffusivity over the 15% RH self-diffusivity to display the increase of the given diffusivity with increasing humidity. We see that the O_2 shows almost a four-fold increase in diffusivity, a small change relative to the 11-fold and 12-fold increase for OH^- and H_2O, respectively, with increasing humidity. Overall, there is an order of magnitude increase in the diffusivity for the water of the system. This is shown to

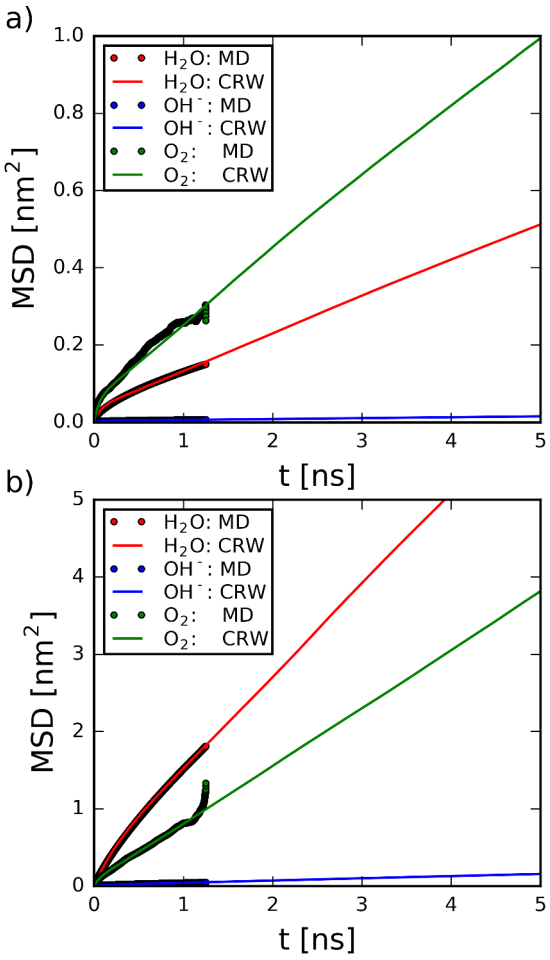


Figure 2.7: Mean square displacements for H_2O, OH^-, and O_2 using both molecular dynamics (MD) simulations and confined random walk (CRW) simulations at 300 K for both (a) 15% RH and (b) 95% RH. The log-log plot of the MSD vs. time is unity for the CRW simulations, satisfying the long, linear regime requirement for calculating accurate self-diffusivities. Note the difference in the y-axis scale from (a) to (b).

be correlated to the oxygen diffusivity increase at higher humidity. The attraction of O_2 to protonated chitosan groups is believed to be the reason we do not also observe an order of magnitude increase in diffusivity for the O_2. Since oxygen permeability is directly related to oxygen diffusivity, we determine that reducing the connectivity and homogeneous aqueous domain could provide means to reduce both the water and O_2 diffusivities. The strong attraction of O_2 to protonated amine groups is overcome by the strong increase in water diffusivity at higher humidity, implying that efforts that focus on reducing the water diffusivity will inevitably also reduce oxygen diffusivity and have a larger impact on reducing the overall oxygen permeability.

Table 2.1: Self-diffusivities of O_2, H_2O, and OH^- in chitosan/chitin membranes at 15% RH and 95% RH at 300 K and the self-diffusivity increase ratios.

	D(10^{-10} m^2/s)		
RH	O_2	H_2O	OH^-
15%	0.31	0.15	0.0045
95%	1.20	1.85	0.0500
$\frac{D_{95\%}}{D_{15\%}}$	3.9	12.3	11.1

2.2.3 Solubility of Oxygen in Chitosan/Chitin Membranes.

We have carried out FEP, FDTI, and direct particle deletion (DPD) calculations to determine the solvation free energy/excess chemical potential of the solute oxygen molecule at infinite dilution in the chitosan/chitin membranes at both 15% RH and 95% RH. Table 2.2 shows $\beta\mu^{ex}$ for all three methods. For the FEP calculations, we performed both deletion of the oxygen molecule from the system, using one of the final snapshots of the data production equilibrium MD trajectories as the initial condition for the FEP deletion, and also an addition of an oxygen molecule into the system, using one of the final snapshots from the equilibration MD trajectories as the initial condition for the FEP insertion. The FDTI was calculated from the same output of these FEP MD simulations. For the DPD method, we analyzed 1 of the 20 MD simulation trajectories for each RH level for a range of d values. We found that $d = 0.700$ for 15% RH and $d = 0.850$ for 95% RH gave the best criteria (smallest standard error) for computing excess chemical potentials. Figure 2.8 shows the reduced excess chemical potential ($\beta\mu^{ex}$) vs. d for (a) 15% RH and 95% RH, respectively, for clarity. With these values of d , we then calculated $\beta\mu^{ex}$ for all 20 simulations of each RH level to get an average value and standard error (reported with $\pm$ in Table 2.2). The energy term, $\beta\mu^{ex}_{energy}$, and volume, $\beta\mu^{ex}_{volume}$, terms are also included in Table 2.2 for the particle deletion method. The total $\beta\mu^{ex}$ was computed using the direct particle deletion method (Eq. (2.12) of section 2.1.4), the energy

term $\beta\mu^{ex}_{energy}$ was computed using Eq. (2.11) in section 2.1.4 for the staged particle deletion method, and the volume term, $\beta\mu^{ex}_{volume}$, was computer via the relation $\beta\mu^{ex}_{volume} = \beta\mu^{ex} - \beta\mu^{ex}_{energy}$.

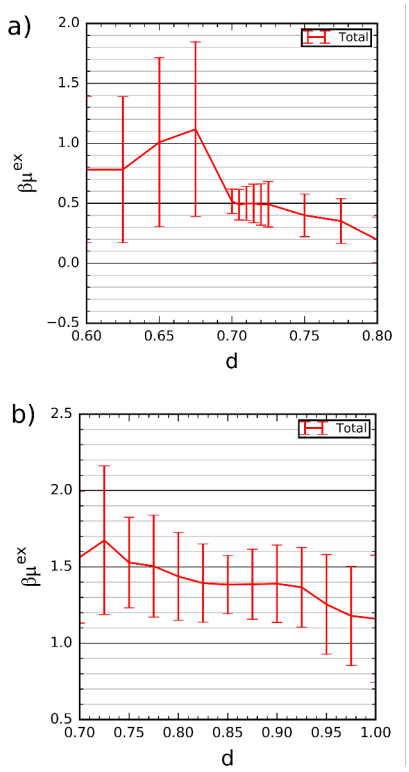


Figure 2.8: Reduced excess chemical potential ($\beta\mu^{ex}$) vs. d for (a) 15% RH and (b) 95% RH with error bars shown to determine optimal d value.

Table 2.2: $\beta\mu^{ex}$ of O_2 in chitosan/chitin membranes at 15% RH and 95% RH at 300 K using free energy perturbation, finite difference thermodynamic integration, and direct particle deletion. The $\pm\sigma$ for the direct particle deletion method gives the standard error. $N-1 \rightarrow N$ indicates the path of inserting the oxygen molecule and $N \rightarrow N-1$ indicates the path for deleting the oxygen molecule.

	FEP		FDTI		DPD		
RH	$\beta\mu^{ex}_{N-1\rightarrow N}$	$\beta\mu^{ex}_{N\rightarrow N-1}$	$\beta\mu^{ex}_{N-1\rightarrow N}$	$\beta\mu^{ex}_{N\rightarrow N-1}$	$\langle\beta\mu ex\rangle$	$\langle\beta\mu^{ex}_{volume}\rangle$	$\langle\beta\mu^{ex}_{energy}\rangle$
15%	2.20	0.26	2.50	0.56	1.12(±0.75)	7.73(±0.12)	-6.62(±0.74)
95%	4.14	2.88	4.61	3.20	2.84(±0.92)	10.98(±0.05)	-8.14(±0.93)

We see that the FEP and FDTI values are approximately equal to each other for both humidity levels and directions of coupling the free energy, indicating that the coupling parameter, λ , is small enough. The DPD values lie between the FEP and FDTI values for 15% RH and tends toward the lower end of the 95% RH FEP and

FDTI values. The standard error in the DPD values is attributed to the standard error associated with the energy term, $\beta\mu^{ex}_{energy}$, calculated using the staged particle deletion (SPD) method. There is very little variance in the volume term, $\beta\mu^{ex}_{volume}$.

For the benefit of readers who are unfamiliar with the computation of chemical potential from MD simulation, we note that the range of the values within a given RH in Table 2.2 are characteristic of the challenges associated with the evaluation of the chemical potential. [176, 197, 203–205] Unlike other thermodynamic properties, e.g. pressure or heat capacity, the estimation of free energy and chemical potential from MD remains a challenge. [204] From a thermodynamic point of view, we observe that the excess chemical potential increases with increasing RH. In other words, oxygen molecules experience a more favorable thermodynamic environment in a less hydrated membrane.

In Table 2.3 and Table 2.4, we use the $\beta\mu ex$ values from Table 2.2 to compute the solubility, S , and Henry's constant, K_H , using equations (2.3) and (2.4), respectively. For the K_H calculation, the molar volume of the solvent, V_M , term was computed using the average value of the 2.4 ns equilibration simulation period before the oxygen molecules were inserted into the system.

Table 2.3: Solubility (10^{-3} mol/L/atm) of O_2 in chitosan/chitin membranes at 15% RH and 95% RH at 300 K using free energy perturbation, finite difference thermodynamic integration, and direct particle deletion.

	FEP		FDTI		DPD		
RH	$S\left(\beta\mu^{ex}_{N-1\to N}\right)$	$S\left(\beta\mu^{ex}_{N\to N-1}\right)$	$S\left(\beta\mu^{ex}_{N-1\to N}\right)$	$S\left(\beta\mu^{ex}_{N\to N-1}\right)$	$S\left(\langle\beta\mu ex\rangle\right)$	$S\left(\langle\beta\mu ex\rangle-\sigma\right)$	$S\left(\langle\beta\mu ex\rangle+\sigma\right)$
15%	4.51	31.23	3.32	23.25	13.31	28.06	6.31
95%	0.64	2.29	0.40	1.65	2.37	5.93	0.95

Table 2.4: Henry's constant (atm) of O_2 in chitosan/chitin membranes at 15% RH and 95% RH at 300 K using free energy perturbation, finite difference thermodynamic integration, and direct particle deletion.

	FEP		FDTI		DPD		
RH	$K_H\left(\beta\mu^{ex}_{N-1\to N}\right)$	$K_H\left(\beta\mu^{ex}_{N\to N-1}\right)$	$K_H\left(\beta\mu^{ex}_{N-1\to N}\right)$	$K_H\left(\beta\mu^{ex}_{N\to N-1}\right)$	$K_H\left(\langle\beta\mu ex\rangle\right)$	$K_H\left(\langle\beta\mu ex\rangle-\sigma\right)$	$K_H\left(\langle\beta\mu ex\rangle+\sigma\right)$
15%	1,707.40	246.68	2,321.39	331.26	578.77	274.6	1220.0
95%	33,826.61	9,515.87	54,045.45	13,177.83	9,194.03	3,672.4	23,019.8

Interestingly, we see that the MD simulations predict O_2 to be more soluble in the lower, 15% RH level relative to the 95% RH level for all three free energy methods. From the previous discussion of the RDFs, the most likely group to cause this favorable solubility is the protonated chitosan monomer group of the polymer chain. This further emphasizes the importance for the description of the O_2-NH_3^+ interaction in the system since it appears to have a large impact on the solubility of the O_2 in the aqueous chitosan/chitin membranes, specifically at low membrane hydration.

2.2.4 Permeability of Oxygen in Chitosan/Chitin Membranes.

With the diffusivity and solubility readily available, we can calculate the oxygen permeability in the chitosan/chitin membranes, shown in Table 2.5 along with experimental results from previously studied chitosan membranes. We see that the lower values of permeability at 95% RH level are in relatively good agreement with the experimental values. However, the 15% RH do not agree well with experiment. Moreover, the predicted trend from simulation of permeability with respect to RH is in disagreement with experiment. Since the permeability is the product of the diffusivity and the solubility, we can directly identify which factor is responsible for the trend. The O_2 diffusivity increases with RH but the solubility decreases with RH. Therefore, the disagreement with experiment is due to the calculated solubility.

Table 2.5: Permeability (*barrer*)[a] of O_2 in chitosan/chitin membranes at 15% RH and 95% RH at 300 K using free energy perturbation, finite difference thermodynamic integration, direction particle deletion, experimental values at low (0% RH) and high (95% RH) humidity for comparison, and the direct particle deletion results with no Coulombic interactions ($U_{Coulombic}$) in the intermolecular potential.

	FEP		FDTI		DPD		
RH	$P\left(\beta\mu^{ex}_{N-1\to N}\right)$	$P\left(\beta\mu^{ex}_{N\to N-1}\right)$	$P\left(\beta\mu^{ex}_{N-1\to N}\right)$	$P\left(\beta\mu^{ex}_{N\to N-1}\right)$	$P\left(\langle\beta\mu ex\rangle\right)$	$P\left(\langle\beta\mu ex\rangle-\sigma\right)$	$P\left(\langle\beta\mu ex\rangle+\sigma\right)$
15%	4.05	28.04	2.98	20.88	11.95	5.67	25.19
95%	2.26	8.02	1.41	5.79	8.31	3.32	20.79

RH	Experimental		RH	DPD (without $U_{Coulombic}$)[e]		
0%	0.0017[b]	0.024[c]	15%	3.95	1.22	12.82
1%	0.31[c]		95%	4.88	1.96	12.09
93%	1.41[d]					

[a] $barrer = 10 - 10\frac{cm^3_{STP}\cdot cm}{cm2\cdot s\cdot cm - Hg} = \frac{1}{3.348\cdot 10-16}\frac{mol}{m\cdot s\cdot Pa}$.
[b]From Pavlath et al. for chitosan membranes @ 298K. [206]
[c]From Despond et al. for chitosan membranes @ 293K. [151]
[d]From Gontard et al. for chitosan membranes @ 298K. [207]
[e]No Coulombic terms included in intermolecular potential.

Given the disagreement between experiment and simulation, in this case we have no reason to doubt the experimental results. Moreover, experimental studies of O_2 permeability in other similar hydrated systems indicate that solubility and permeability should increase with hydration. [207] Therefore, we turn our investigation toward seeking an explanation for the discrepancy in the MD simulations. In classical MD, there is either an error in the method or in the interaction potential. The consistency of three different free energy methods in predicting an increase in the excess chemical potential (and a corresponding decrease in solubility) with increasing RH leads us to believe the issue is not in the method. Instead we speculate that

the simulations indicate an overly strong association of O_2 with NH_3^+. The strength of this association limits the ability of O_2 to "dissociate" and move further into the aqueous domain. From a mechanistic point of view, O_2 must explore a more fully solvated state in order for the solubility to be enhanced by the addition of more water to the membrane. Thus we suspect that the O_2-NH_3^+ association is overly represented, leading us to believe that the force field is the likely culprit for the inaccuracy in the solubilities and permeabilities. There are other instances in the literature where the manner in which the charge description is mapped from continuous electron distributions of quantum mechanical calculations to point charges can have a dramatic effect on adsorption properties. For example, in the simulation of a polar organic molecule in a metal organic framework the adsorption isotherm in the Henry's Law regime varied by seven orders of magnitude depending upon the selection of (ostensibly reasonable) methods for the generation of point charges. [208] Recent work of modeling permeability in 1,2-dimyristoyl-sn-glycero-3-phosphorylcholine (DMPC) lipid bilayer membranes also highlight the issues of force fields and specifically not including explicit polarizability. [204] However, with this inclusion comes a 2-6 times increase in computational cost. [95, 201, 202]

To test this hypothesis, we can use the DPD method to do post-processing calculations of the excess chemical potential while varying the intermolecular potential calculation. Since the most obvious reason that there is too strong of an interaction is probably due to the positive charge on the cation, we remove all charges from the system, thus removing all Coulombic interactions. Upon removing the electrostatic terms, the DPD predicts the O_2 permeability for the 15% RH to be 3.95 barrer and for the 95% RH to be 4.88 barrer. These values are reported in Table 2.5 with the $P\pm$ also reported. Thus, the correct trend is observed and the 95% RH O_2 permeability is brought in closer agreement with the experimental values of Gontard et al. [207] Note that this is not a rigorous test to determine that the O_2-NH_3^+ interaction is the definitive issue. However, weakening the O_2-NH_3^+ interaction would result in O_2 preferentially exploring volume in the aqueous domain, which could more closely tie the mobility of O_2 to that of H_2O and would further increase the permeability with increasing RH. This evidence, coupled with the O_2-NH_3^+ RDFs in Figure 2.6, points toward the interaction potential as the source of the discrepancy between simulation and experiment. It also clearly highlights the importance of the additional work done to evaluate the chemical potential, which made the estimation of the solubility and permeability possible. These calculations ultimately allowed comparison with experiment, which revealed a shortcoming, likely traced to the strength of the Coulombic interaction. Subsequent efforts should be focused on the Coulombic contribution to the potential in order to address the accuracy of the O_2 solubility and permeability predictions.

Chapter 3

Intrinsic Relationships between Proton Conductivity and Nanopore Size and Functionalization

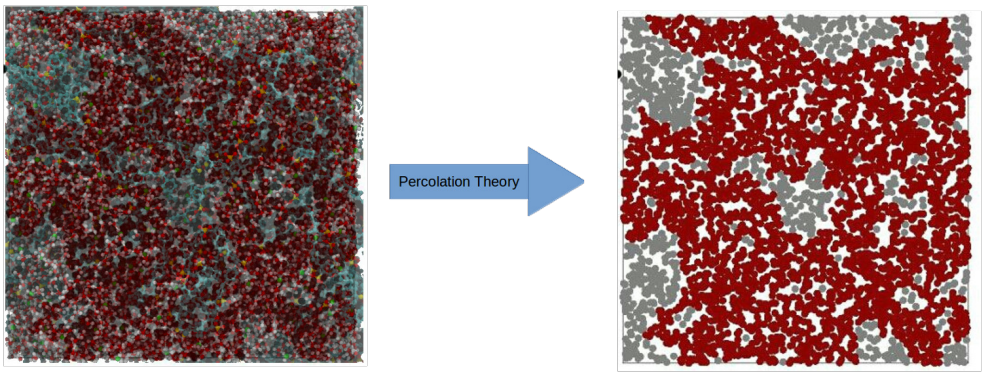


Figure 3.1: Schematic of transfer from molecular-level detail of membrane (with polymer/aqueous domain overlay) to a percolation theory model for giving an connected aqueous domain that spans a membrane.

NOTE: Reprinted from *Microporous Mesoporous Mater.*, **177**, M. T. McDonnell and D. J. Keffer, "Intrinsic relationships between proton conductivity and nanopore size and functionalization", pgs. 17-24, DOI:10.1016/j.micromeso.2013.04.007, Copyright 2013 with permission from Elsevier.

3.1 Theory

Percolation theory describes the relationship between a transport property through a network, the connectivity and fraction of defects within the network. Analytical models of percolation, such as the effective medium approximation (EMA), [209, 210] take as input the coordination (connectivity) of the network, z, the fraction of pathways that are blocked to transport, p_{EMA}, and the diffusivity through open (o) and blocked (b) paths, D_o and D_b respectively. From these inputs, one obtains the effective diffusivity, D_{eff} , from EMA. Given a bimodal distribution of open and blocked windows, we have

$$g(D) = p_{EMA}\delta(D - D_b) + (1 - p_{EMA})\delta(D - D_o) \tag{3.1}$$

where δ is the Dirac delta function, defined as:

$$\int_{-\infty}^{\infty} \delta(D - D_b)dD = 1 \tag{3.2}$$

EMA yields,

$$\int_0^{\infty} \frac{g(D)(D_{eff} - D)}{D + (\frac{z}{2} - 1)D_{eff}} dD = 0 \tag{3.3}$$

Upon integration and solving for the relevant root of, we have

$$\frac{D_{eff}}{D_o} = \frac{1}{2}\left[A + \sqrt{A^2 + \frac{4f}{\frac{z}{2} - 1}}\ \right] \tag{3.4}$$

where $f = D_b/D_o$ and

$$A = 1 - p_{EMA} + f\ p_{EMA} - \frac{f + p_{EMA} - f\ p_{EMA}}{\frac{z}{2} - 1} \tag{3.5}$$

When applied to water (w), EMA yields the effective diffusivity of water. To obtain the conductivity, EMA is applied to charge (chg) and coupled with the relation, [211]

$$D_{eff}^{chg} = \left(\frac{RT}{|z|^2F^2}\frac{\sigma}{c}\right) \tag{3.6}$$

where σ is the conductivity, R is the gas constant, F is Faraday's constant, and T is the temperature.

The challenge lies in parameterizing percolation theory in terms of the structural descriptors. We begin with water and then proceed to charge. The self-diffusivity of water through an open pathway can be made a function of acidity and confinement by accounting for the concentration of hydronium ions, c, and the interfacial surface area, sa, (where f_c is the concentration component)

$$D_\alpha(c, sa) = f_c \; f_{sa} \; D_\alpha(c = 0, sa = 0) \tag{3.7}$$

$$f_c = \frac{D_\alpha(c, sa = 0)}{D_\alpha(c = 0, sa = 0)} = \begin{cases} 1 & for \; c \leq \tau_c^\alpha \\ e^{k_c(c - \tau_c^\alpha)} & for \; c > \tau_c^\alpha \end{cases} \tag{3.8}$$

and the surface area component, f_{sa} , has a completely analogous form to f_c, where the c and sa subscripts are switched. The subscript α is set to w for water. These functional forms of an exponential decay with a rate constant, k_c^α , and a lag, τ_c^α , are suggested by both experimental observation [212] and simulation [70, 213] of bulk acids and water in carbon nanotubes.

To use exponential decay functional forms for diffusivities of both water and charge for change in acidity is motivated by the experimental evidence from the work of Dippel and Kreuer[12]. The explanation of the decay is attributed to addition of anions breaking up the hydrogen-bond network, increasing water disorder and thus decreasing the entropic change for vehicular diffusion for Dippel and Kreuer's pre-exponential factor. Interestingly, the activation enthalpy decreases simultaneously with anion addition. One can infer that their entropic, exponential pre-factor is the dominate term in the decay.

To use exponential decay functional forms for the change in confinement has been motivated by simulation of water in carbon nanotubes[13]. The simulations were validated based on experimental and other simulation data available. Confinement also has a negative effect on the diffusivity where the mobility of the water decreases with decreases in the tube size. The behavior of the decrease in diffusivity motivated the use of an exponential fit.

For the self-diffusivity of charge, the total charge diffusivity must be decomposed into two separate mechanisms for diffusivity, structural and vehicular diffusivities. More detail on the difference in the vehicular and structural components of self-diffusivity of charge will be discussed later.

The values of experimentally determined diffusivities, the factor of contribution of each type of diffusivity, the prefactor determined from the two previous values and the parameters for the rate constants and lag used in equation (3.8) are given in Table 3.1.By multiplying the experimental bulk water self-diffusivity and the factor given in Table 3.1, we compute the exponential pre-factor. The pre-factor is incorporated into the $D_\alpha\,(c = 0, sa = 0)$ term in equation (3.6). Importantly, no information on transport in PEMs was used in the generative of Table 3.1. The values of the concentration and interfacial surface area require a molecular model from which the volume and surface area of the aqueous domain can be determined. Values for Nafion are published. [214] For percolation theory, $D_o = D_\alpha\,(c, sa)$.

The MD simulations that provide the volume and surface area also provide short-time mean square displacements (MSDs) of water. By fitting these MSDs to confined random walk simulations, one obtains the probability of a successful cluster-to-cluster hop, p_c. [174, 217] The diffusivity of water through a blocked pore is thus $D_b = p_c D_o$.

Table 3.1: Model parameters for percolation theory for self-diffusivity using structural descriptors for acidity (c, concentration of hydronium ions) and confinement (sa, the interfacial surface area).

		water	charge-struct	charge-veh
Experiment	(m^2/sec)	2.26E-09[a]	9.7E-09[b,*]	9.7E-09[b,*]
factor		1	0.621	0.379
pre-factor	(m^2/sec)	2.26E-09	6.0237E-09	3.6763E-09
k_c (acidity)	(L/mol)	-0.00543	-0.459	-0.191
τ_c (acidity)	(mol/L)	...	...	4.7
k_{sa} (confinement)	(water molecules/Å^2)	-0.00103	-0.00715	-0.002
τ_{sa} (confinement)	(Å^2)	...	...	29.5

[a] From work [215]
[b] From work [216]
[*] Experimental measures total charge self-diffusivity.

In all this work, the connectivity is set to z=6 and is not an adjustable parameter. The CRW simulations also provide the effective diffusivity for water. Thus percolation theory can be fit to water data and solved for the connectivity, p_{EMA}. Thus percolation theory for water transport is completely parameterized.

The application of percolation theory to charge is analogous but has two significant differences. First, water molecules diffuse through only one mechanism, a vehicular mechanism, corresponding to translation of the center of mass. Thus modeling the mobility of water in aqueous solutions requires only that this vehicular mechanism be incorporated. In contrast, charge carried by protons in aqueous solution, can diffuse via two mechanisms. The first is a vehicular mechanism, corresponding to translation of the center of mass of the hydronium ion. The second is a structural mechanism, corresponding to "proton hopping", first proposed by Grotthuss, [218] and well-described in bulk solution by *ab initio* studies. [75] Experimentally, only the total (*tot*) self-diffusivity of charge (*chg*) is directly measurable. Various simulation techniques, such as Reactive Molecular Dynamics (RMD), simulations allow one to measure the structural (*struct*) and vehicular (*veh*) contributions (and any correlation (*corr*) between them) independently. [66, 70, 213, 219]

$$D_{tot}^{chg} = D_{veh}^{chg} + D_{struct}^{chg} + D_{corr}^{chg} \tag{3.9}$$

In this work we assume that the vehicular and structural components of charge diffusivity must be independently functionalized with respect to acidity and confinement. To fit the diffusivities with as few parameters as possible yet also capture the behavior accurately, an exponential was used for both. We observed a separate

exponential between the vehicular and structural diffusivities due to the vehicular diffusivity appearing constant up to a given concentration limit before decay set in. Thus, to empirically fit the data accurately with few parameters as possible, a lag was introduced into the vehicular diffusivity exponential. While more parameters could be introduced to provide a better fit, noise in the data could not justify this approach. Thus equations 3.7 and 3.8 are implemented for $\alpha = veh$ and *struct*. The correlation term has been shown to be zero in bulk acids and in dilute solutions in carbon nanotubes and is neglected here. [213, 219, 220] It is noted that a negative correlation has been observed in Nafion, which is not accounted for in this model. [66, 220]

The second difference between water and charge is that we used the effective diffusivity of water, based on the MD & CRW simulations, to set the value of p_{EMA}. For charge, we do not make that assumption. Rather we simply use the values of p_c and p_{EMA} obtained from the water simulations for charge transport. This assumption requires that water and charge transport be highly correlated, which is valid in Nafion. If water and charge transport are decoupled by, for example the addition of dopants, then separate values of p_c and p_{EMA} are required. In this work we limit ourselves to systems in which water and charge transport are correlated.

3.2 Results and Discussion

The estimation of water self-diffusivity and proton conductivity described above provides accurate results for a variety of systems, including bulk hydrochloric acid solutions [219] and dilute solutions in carbon nanotubes [213] because those systems were used to generate the parameters in Table 3.1. It also reproduces the self-diffusivity (or conductivity via equation (3.6)) in Nafion [217] and crosslinked and sulfonated polycyclohexadiene [93] membranes. In order to both validate this model and to motivate the work that follows, we revisit the predictions of the model for charge transport in Nafion with an equivalent weight of 1144 at a temperature of 300 K. A summary of the results are shown in Figure 3.2. The x-axis spans water content from a minimally hydrated Nafion membrane ($\lambda = 3$ H_2O/HSO_3) to the fully saturated membrane (λ =22). Bulk water at pH = 7 is included for comparison. The plot includes experimentally determined values of the total self-diffusivity of charge. [4,5] In this plot one observes that the predictions of a model that incorporates the effect of three factors - acidity, confinement and connectivity of charge transport, agrees very well with experimental observations.

The agreement between the model and experiment is encouraging because it suggests that of the many ways to characterize the disordered structure of a hydrated polymer membrane, accounting for only three structural descriptors—acidity, confinement and connectivity—is sufficient to establish a reliable relationship between nanostructure and the relevant transport properties. Other effects, such as the immobility of anions, that lead to theoretical observations of non-zero correlations between the vehicular and structural components of the diffusivity, [66, 220] seem to

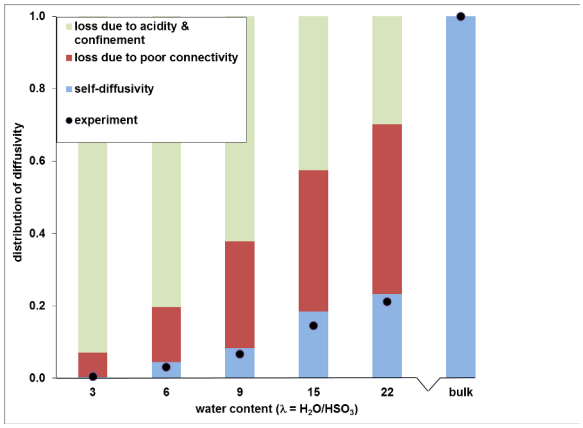


Figure 3.2: Self-diffusivity of charge and sources of transport losses as a function of water content. Experimental data is taken from refs. [4] & [5].

be of secondary importance. More importantly, this model, validated by experiment, allows us a relatively straightforward path to optimizing membranes in terms of acidity, confinement and connectivity.

It should be clear that all three factors - acidity, confinement and connectivity - monotonically decrease the self-diffusivity of water and both the vehicular and structural components of the self-diffusivity of charge from their values in bulk water. By equations 3.7 and 3.8, the acidity and confinement are characterized by exponentials of concentration of hydronium ions and surface area, respectively, which obviously decay. The effective medium approximation also allows only a monotonic decrease in transport as the connectivity diminishes. (Here we think of a bulk system as having perfect connectivity.) In Figure 3.2, the reduction of the bulk water diffusivity due to the combined impacts of acidity and confinement is illustrated. Acidity and confinement result in a 30% decrease in diffusivity in the fully saturated membrane and a 93% decrease in the minimally hydrated membrane. Poor connectivity in the aqueous domain further reduces the diffusivity an additional 47% and 6.7% in the fully saturated membrane and minimally hydrated membrane respectively. It may seem counter-intuitive that poor connectivity has a bigger percentage impact at high water contents (where connectivity is relatively better) than at low water contents (where connectivity is relatively worse), however this can be explained based on the fact that the intrinsic diffusivity (after acidity and confinement had been taken into account) was already much smaller in the minimally hydrated membrane. The effect of poor connectivity reduced the intrinsic diffusivity by an additional factor of 20 in the minimally hydrated case but only by an additional factor of three in the fully saturated membrane.

The message from this model is that acidity, confinement and poor connectivity all negatively impact the self-diffusivity of water and charge. Thus, if the goal is to maximize the self diffusivity of water and charge, bulk water, which has low acidity, no confinement and perfect connectivity is the ideal media. However, this premise

is false on two counts. First, the mechanical strength of the medium is important. Even if we ignore mechanical issues and focus solely on optimizing transport, it is not the self-diffusivity of charge that is important but rather the conductivity. Since the concentration appears in the expression for conductivity, equation (3.6), minimizing the acidity will not result in maximizing the conductivity.

Thus in order to maximize the conductivity, one must strike a balance in terms of acidity, in which the concentration is sufficiently high to provide significant charge carriers, but not so high that the presence of so many charge carriers results in a negligible diffusivity. The extent of confinement in the system also impacts conductivity because, most obviously, it changes the diffusivity. However, confinement is a measure of surface area per volume. In a material in which the anions are fixed to the surface, for a given surface coverage of anions, an increase in confinement results in an increase in the surface area to volume ratio, which corresponds to an increase in concentration of protons distributed in the volume. Thus confinement, for a given surface coverage of anions, indirectly impacts concentration as well. Connectivity impacts conductivity only through the diffusivity.

One can take this insight on the effects of acidity, confinement and connectivity and translate them into an optimal membrane design. From a conceptual point of view, the membrane could be composed of an array on parallel cylindrical channels. If the channels are full of water and defect free, then there are no blockages and thus no decrease in the diffusivity due to poor connectivity. In this highly idealized conceptual case, the pore is filled with water and the interior surface area is functionalized with acid groups. The anion is tethered to the surface. The proton is free to dissociate and enter the aqueous domain. The only two additional characteristics of this membrane are the pore size and the surface coverage of the interior pore space with acid groups. The surface coverage of acid groups has an obvious impact on acidity. The pore size dictates confinement. In the case of a water-filled, defect free pore, there are no connectivity issues. In the case of a partially water-filled (still defect free) pore, issues of connectivity will arise.

This remaining discussion is organized into three sections. First results are presented for idealized cylindrical nanopores with full water occupancy. Next, results are presented for idealized cylindrical nanopores with partial water occupancy. Finally, we compare the predictions of this theory with published conductivity measurements taken from acid-functionalized MCM-41 materials.

The channels studied first are defect free cylinders filled with water. The acidity in the system is determined based on the surface coverage of acid groups. The acid is a strong acid that fully dissociates. So, it is straightforward to calculate the number of hydronium ions per unit of pore volume, based on a nominal pore radius, which is the necessary characterization of acidity required by the theory. The confinement is based on the nominal radius of the pore with a surface roughness factor of 2 to mimic atomistic detail. The theory requires surface area per water molecule. To determine the number of water molecules in a water-filled pore, we approximate the density as that of bulk water and use the nominal volume. In a defect free cylinder filled with

water, there are no blockages and no dead ends in the pores. Since the pore is filled with water, there is a continuous aqueous domain. Therefore, there is no negative impact of connectivity in these cases. The self-diffusivities of water and charge are determined strictly from the effects of acidity and confinement. Additionally, in Figures 3.3 through 3.6, the presence of the acid group is considered not to change the accessible volume or the interfacial surface area. This assumption is later relaxed.

In Figure 3.3, the self-diffusivities are plotted as a function of surface coverage over a range of pore radii for (a) water, (b) structural component of charge, (c) vehicular component of charge and (d) total charge self-diffusivity. All four self-diffusivities decrease as the surface coverage increases, simply because diffusivities decrease as the ion concentration increases, as experimentally observed. [221] It is also observed that all four self-diffusivities decrease with decreasing pore size, in line with simulation observations. [213] (The theoretically predicted defect-free nanowire of water that gives rise to anomously high water conductivity lies well below the pore sizes investigated here. [222]) The impact of acidity and confinement is most strongly felt on the structural component of charge diffusivity. (The discontinuity in the slope of the total self-diffusivity of charge is not physically meaningfully and is a feature that lies within the uncertainty of the theory. It is strictly a consequence of the discontinuity in the slope of the vehicular component due to the presence of a lag. While a model with a continuous slope is easily conceived, it would require additional parameters. Moreover, the uncertainty in the data itself is such that a lag followed by a decay is all that is justifiable.)

In Figure 3.4, the proton conductivity is plotted as a function of surface coverage for a range of pore radii. For any given pore size, there is a relatively sharp peak in the conductivity, followed by steep drops on either side. It is clear that the conductivity in a pore can vary dramatically as a function of surface coverage. The two competing factors in this optimization are as follows. At very low surface concentrations, there are few charge carriers. At very high surface concentrations, the negative impact of acidity on charge self-diffusivity dominates. Clearly the position of the optimum surface coverage is a function of pore radii, as will be discussed in greater depth below.

In Figure 3.5, the self-diffusivities are now plotted as a function of pore radius over a range of surface coverages for (a) water, (b) structural component of charge, (c) vehicular component of charge and (d) total charge self-diffusivity. Again all four self-diffusivities decrease as the pore radius decreases. It is also observed that all four self-diffusivities decrease with increasing surface coverage, as was the case with Figure 3.3. In Figure 3.6, the proton conductivity is plotted as a function of pore radius across a range of surface coverages. For all surface coverages except the lowest one, there is an optimal pore radius in terms of maximizing conductivity. The maximum is a result of two competing effects. For a given surface coverage of acid groups, changing the pore size changes both the confinement and acidity. The change in confinement is obvious since the interfacial surface area to pore volume ratio increases as the pores become smaller. The acidity changes as well since there are a fixed number of acid groups per surface area but the change in the surface area/volume ratio results in

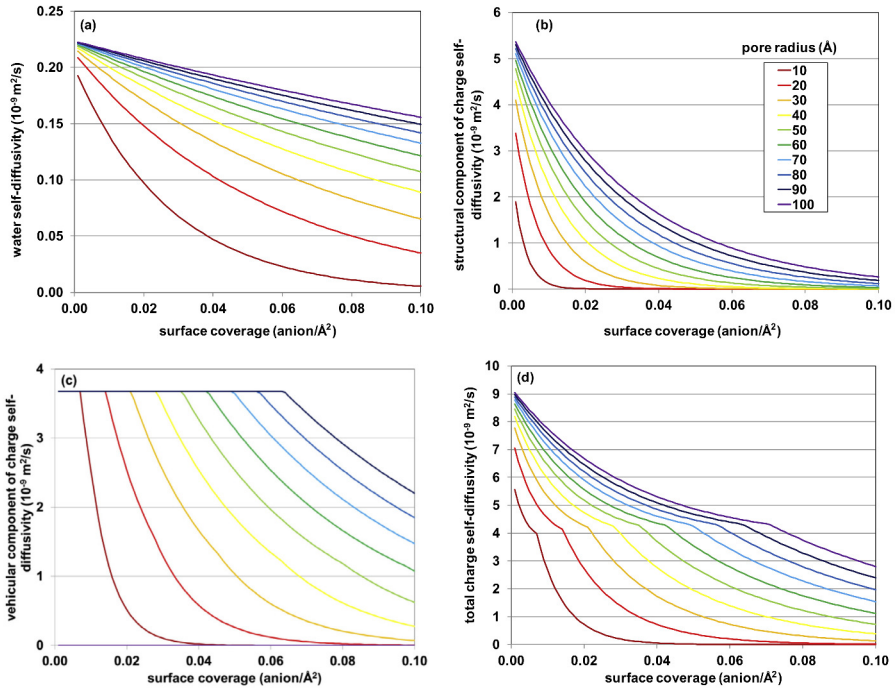


Figure 3.3: Self-diffusivities as a function of surface coverage for a range of pore radii. (a) water, (b) structural component of charge, (c) vehicular component of charge, (d) total charge.

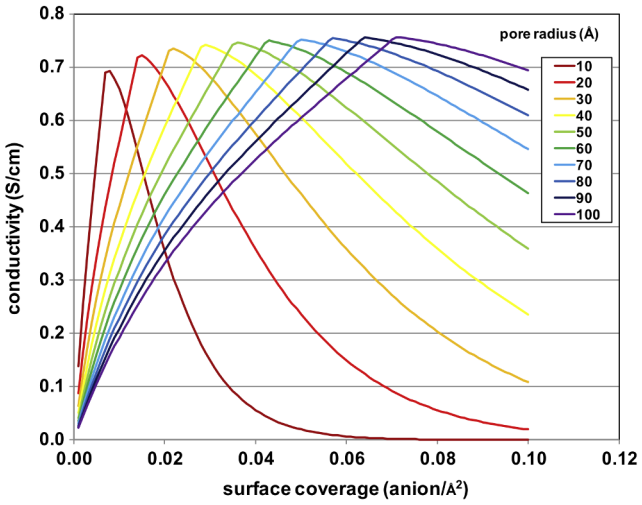


Figure 3.4: Conductivity as a function of surface coverage for a range of pore radii.

less volume per acid group, or higher acidity as the pores become smaller. Thus in the limit of very large pores, there is very little acidity, resulting in fewer charge carriers. At the other limit of very small pores, the negative impact of both acidity and confinement lower the self-diffusivity of the charge. Between these limits, there is an optimal value.

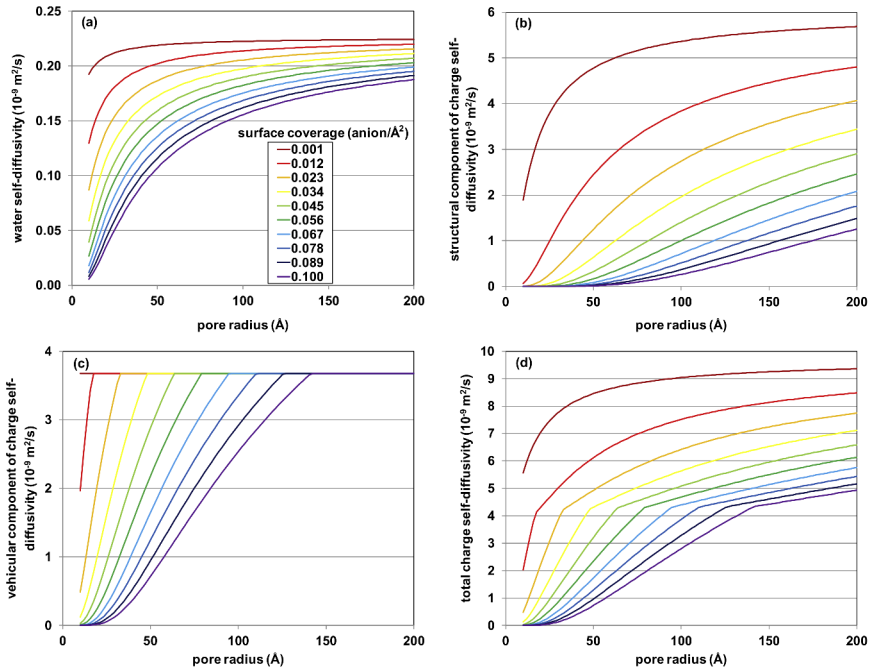


Figure 3.5: Self-diffusivities as a function of pore radii for a range of surface coverages. (a) water, (b) structural component of charge, (c) vehicular component of charge, (d) total charge.

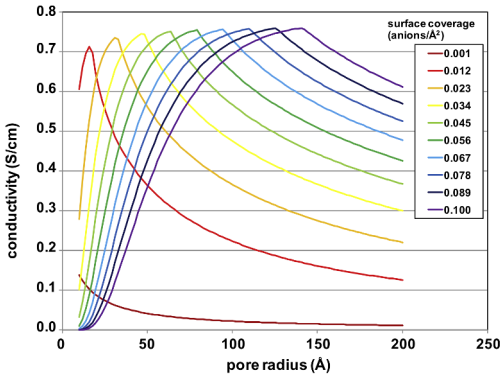


Figure 3.6: Conductivity as a function of pore radius for a range of surface coverages.

We note that the maximum conductivity has very little variation between the entire range of pore size and surface coverage. The proton transport in the direction parallel to the pore wall is highly dependent on its structural diffusivity and that the structural diffusivity of the proton is highly dependent on the hydrogen-bond network present. In order to maximize the transport parallel to the wall, we can imagine that want the most directed lines of connectivity in the hydrogen-bond network to be parallel in the direction of desired conductivity and to reduce transport in any other direction. Once the network is optimized (via optimal pore size and surface coverage), then the limit of the proton transport (and the conductivity) is only limited to small, molecular-level mechanisms and no longer the larger-scale nano-structure of the pore. Using our model, we calculated the maximum conductivity through bulk water (no confinement) by varying the acidic concentration and found it to be 0.076 S/cm. This is our molecular-level limit for conductivity based on the model. Therefore, we claim the robust conductivity over a range of pore size or surface coverage is due to reaching this limit.

Figures 3.4 and 3.6 demonstrate that there is an inherent relationship between conductivity and pore size and surface functionalization even in the most ideal case of water-filled, defect free pores. While these results are intended to be qualitative and illustrate the nature of the structure/property relationship, we should point out that the maximum conductivity for each pore size is greater than 0.7 S/cm at 300 K. This number is important because as can be seen from Figure 3.2, approximately 78% of the mobility that charge possesses in bulk solution is lost in Nafion even under fully saturated conditions. A goal of replacement membranes should be to avoid this up-front loss of charge mobility under the wettest conditions.

The results shown in Figures 3.3 through 3.6 neglected the fact that the presence of acid groups attached to the interior wall could impact the interfacial surface area or pore volume. Certainly, each acid group and the tether to the pore wall occupies some volume. One can imagine in the case of a relatively low surface coverage the functional groups increase interfacial surface area. On the other hand, at very high surface coverages, a monolayer of functional groups could effectively provide a smaller pore diameter with smaller surface area. In order to capture the effects of functional groups on interfacial surface area and pore volume and the resulting impact on conductivity, we included those effects in the analytical theory. In Figure 3.7, the conductivity is shown as a function of surface coverage for a case where the functional groups are modeled as cylinders with diameter of 3 Å and length of 6 Å. Of course, more sophisticate modeling of the surface area and the volume of the functional groups could be done (as was done in the case of Nafion [214]) but the fact of the matter is the inherent relationship between pore geometry, functionalization and conductivity holds regardless of the finer details. We observe that including the effects of the functional groups surface area and volume results in much narrower peaks of slightly lower height. With a narrower peak, the identification of the optimum relationship between pore size and surface coverage becomes more important as well as more difficult to identify. The conclusion is that the general form of the plots provided in

Figures 3.3-3.6 are not altered by including the effect of the functional group to the surface area and accessible volume.

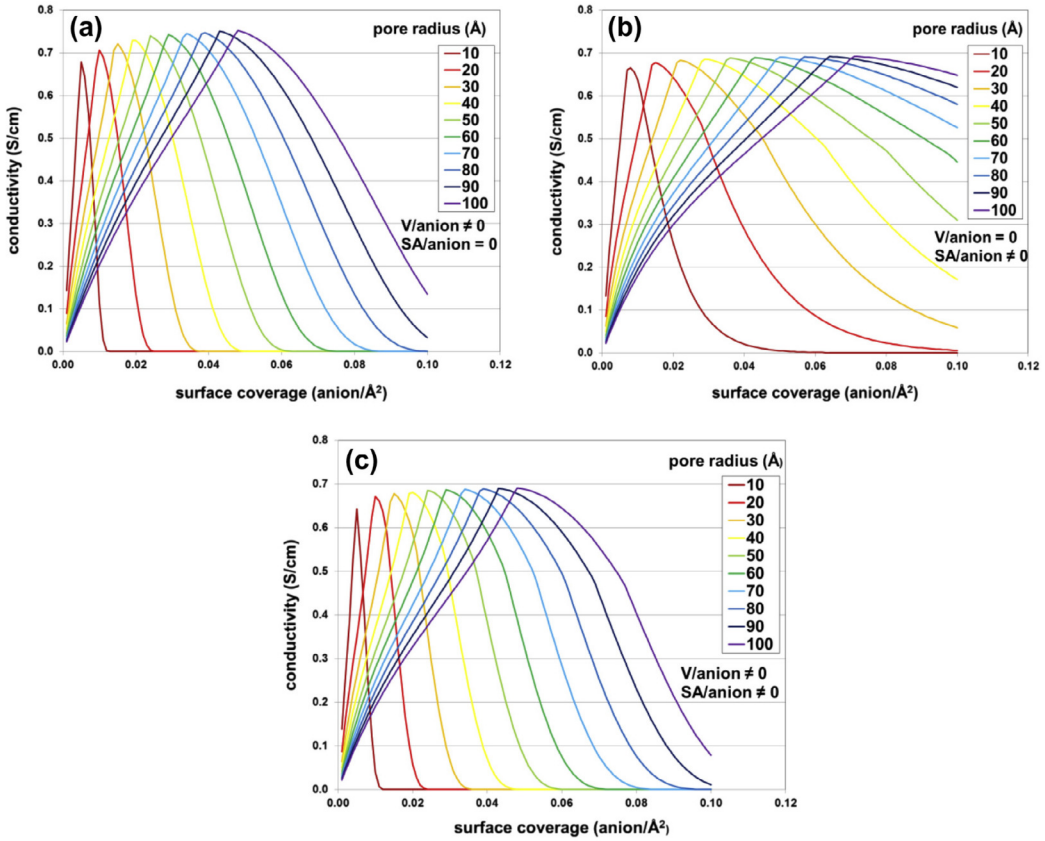


Figure 3.7: Conductivity as a function of surface coverage across a range of pore radii. (a) The excluded volume of the anion group is accounted for but the surface area is not. (b) The maximum surface area of the anion group is accounted for but the volume is not. (c) Both the excluded volume and the maximum surface area of the anion group are accounted for.

When the pore is filled with water, the protons can be transported via either vehicular or structural diffusion through the aqueous phase without disruption. If the aqueous phase within the pore is discontinuous, there is loss of connectivity in the transport network. In Nafion, it is well understood that the polar sulfonic acid groups at the end of the side chains act as anchors around which water clusters can form. Given the limited mobility of the acid groups tethered to the backbone, they aggregate in aqueous clusters to whatever extent is possible based on the details of the polymer chemistry (separation along the backbone between side chains and length of the side chain). In poorly hydrated systems, net diffusion of either water or protons involves moving from one cluster to another. There is a significant amount of work reported in examining the impact of spacing of functional groups within the pore

on the transport of water and charge. [214, 223–225] The percolation theory used to describe connectivity in Nafion could be used equally well to describe transport in partially filled cylindrical pores. However, that work requires a further understanding of the distribution of aqueous clusters in these nanopores.

There is a body of work from the research group of Wark investigating proton conductivity in the cylindrical pores of Si-MCM-41 functionalized by sulfonic acid groups tethered to the wall by MPMS (3-mercaptopropyl-trimethoxysilane) groups. [226] In this section of the work, we compare the predictions of the analytical theory with the experimental measurements.

These materials have a number of attractive characteristics. The Si-MCM-41 PEMs have increased proton conductivity and high water storage with increased temperature, even above 100 °C. Where Nafion has decreased proton conductivity due to loss of water storage after 80 °C, Si-MCM-41 increases its proton conductivity up to 140 °C. [227] Recently, these functionalized Si-MCM-41 PEMs were able to achieve conductivities of 0.19 S cm^{-1} at 140 °C and 100% relative humidity, comparable to Nafion's 0.2 S cm^{-1} at 80 °C and 100% relative humidity, proving functionalized Si-MCM-41 to be a good candidate for high-temperature proton-conducting PEMs. [227]

Comparing to the body of work from Wark's research group, the conductivities that we present in Figure 3.4 and 3.6 are significantly higher than those reported from the experimental methods. This can be explained that our analytical theory uses an ideal system of exact, cylindrical pore size and distribution of anions for surface coverage. The experimental synthesis relies on the presence of the MPMS groups after co-condensation of solution that are functionalized by thiol oxidation using hydrogen peroxide to produce sulfonic acid groups. The solid produced is then washed with ethanol and water. The experimental work was able to determine that the functional groups were in fact present using cross-polarization magic-angle spinning NMR spectroscopy, but even the authors notes that incomplete oxidation is present due to strong signals for thiol groups in the spectra and also that further quantitative evaluation is needed to determine the amounts of each group type, including the sulfonic acid groups. Thus, the surface coverage of anions is not clear. Even with such high conductivity comparable to Nafion and operation at a temperature of 140 °C, from the analytical theory, conductivities much higher than those reported could be realized with selectivity of the pore size and surface coverage of anion. With further advances in experimental synthesis guided by theory, an optimized PEM design could be set as a target that would achieve even higher proton conductivities.

Chapter 4

Ab Initio Molecular Dynamics Simulations of an Excess Proton in a Triethylene Glycol-Water Solution: Solvation Structure, Mechanism and Kinetics

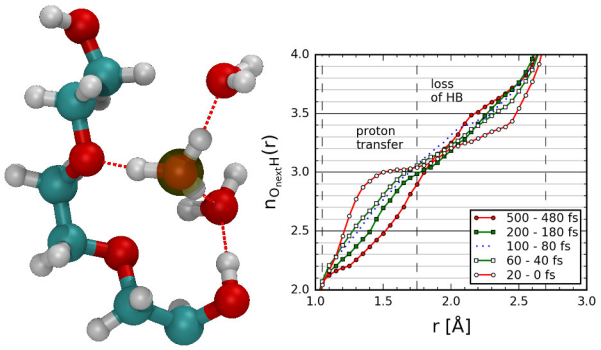


Figure 4.1: Image of excess H^+ as hydronium ion (highlighted in yellow) with hydrogen bond network formed to water and triethylene glycol polymer and graph of change in integrated coordination number of protonated oxygen of water leading up to a proton transfer event.

NOTE: Reproduced with permission from *J. Phys. Chem. B*, **120**(23), M. T. McDonnell, H. Xu, and D. J. Keffer, "Ab Initio Molecular Dynamics Simulations of an Excess Proton in a Triethylene Glycol-Water Solution: Solvation Structure, Mechanism and Kinetics", pgs. 5523-5524, DOI: 10.1021/acs.jpcb.6b02445, Copyright 2016 American Chemical Society.

4.1 Simulation Details

4.1.1 Simulation Size and Cell Setups.

Density functional theory [228] (DFT) based ab initio (AIMD) simulations, specifically Car-Parrinello (CPMD) simulations, were performed in the micro-canonical ensemble (NVE) using the Quantum ESPRESSO (opEn-Source Package for Research in Electronic Structure, Simulation, and Optimization) software suite [229] for an excess proton in bulk water and a TEG-water mixture. For the bulk water simulations, the system consisted of 32 water molecules and one excess proton in a cubic simulation cell of length 9.8652 Å, taken from previous studies. [230] The TEG-water mixture consisted of 27 water molecules, an excess proton and one TEG chain in a cubic simulation cell of length 10.0 Å. Both systems were subject to periodic boundary conditions for both classical and ab initio MD simulations.

The system size was chosen to ensure strong interaction and observable effect of the TEG chain with the excess proton. For a larger system, the aqueous TEG solution becomes more dilute, decreasing the observation of the TEG effect on proton transport. Thus, our system size helps increase interaction sampling of possible proton transport effects induced by the TEG chain. The simulation cell sizes were determined after classical MD simulations were used for rough equilibration and generation of the initial nuclear coordinates in the system, to be discussed further below. Using this system cell size, multiple AIMD simulations with different initial nuclear coordinates, were carried out to sample different phase space trajectories in order to increase the probability of seeing TEG interactions with the excess proton and also to increase the statistical sampling of structure and transport of the excess proton.

4.1.2 Classical MD for Generating Initial Conditions for AIMD

Classical MD simulations using the Optimized Potentials for Liquid Simulations - All Atom (OPLS-AA) empirical force field [142, 143, 231] for the TEG molecule and the Transferable Inter-molecular Potential - Three Point (TIP3P) water model [147] with flexible OH bonds [232] for the water molecule and the hydronium molecules were performed prior to the AIMD simulations to generate initial nuclear coordinates for initialization of the AIMD systems. For the classical MD simulations, the hydronium charges were taken from the work of Urata et al. [233] The long-range coulombic interactions were computed using the k-space style, long-range particle-particle particle-mesh solver [152] with a relative error in the force tolerance of 10^{-4} kcal/mole. Geometric mixing rules were used for computing pair-style force field parameters of different atom types. The simulation cell was +1 charged due to the hydronium ion (not a charge neutral system). The pair-wise and coulombic forces used a cutoff of 10.0 Å. To initialize the system, the TEG chain, water molecule and hydronium ion were put on a simple cubic lattice arrangement of very low density (0.3 g/cm^3)

initially to reduce aphysical initial configurations of high energy using the open-source Moltemplate molecule building and force field database code. [234] The Large-Scale Atomistic/Molecular Massively Parallel Simulator (LAMMPS) open-source code was used to perform all classical MD simulations. [153,154] The reversible reference system propagator algorithm (rRESPA) by Tuckerman et al. [155] was used for integrating the equations of motion. The largest timestep was 1 femtosecond (fs) for pairwise interactions and a smallest timestep was 0.2 fs for bonding interactions. The system was initialized by first performing energy minimization with an energy convergence tolerance of 10^{-5} kcal/mole and a force convergence tolerance of 10^{-7} kcal/mole. After minimization, the system was run in the isobaric-isothermal ensemble (NPT) for 250 ps using the Nosé-Hoover thermostat and barostat [159, 160] with the equations of motion formalism from the work of Shinoda et al. [163], the hydrostatic equations of Martyna et al. [161], the strain energy proposed by Parrinello and Rahman [162] and the time integrator closely following the one from Tuckerman et al. [164] The thermostat was set at 300 K with a relaxation timelength of 0.1 ps. The barostat was set at 1 atmosphere with a relaxation timelength of 1 ps with a drag applied to the Nosé-Hoover equations to dampen the large pressure oscillations that can occur in going from low density to high density. This protocol gave a converged density of 1.05 g/cm^3 for the system. This density appears to be within reasonable agreement with experiment, lying between the density of pure water (0.99 g/cm^3) and the density of pure TEG (1.12 g/cm^3) at STP. With a TEG mole fraction of 0.0357 and at 300 K, we are in relatively good agreement with the recent work of Begum et al., [235] who report a density of 1.0412 g/cm^3 for a mole fraction of TEG equal to 0.05023 and at 303.15 K for TEG-water mixtures. Keeping the density fixed, the system then underwent thermal annealing via temperature ramping from 300 K to 900 K within 250 ps and then run in the canonical ensemble for a fixed temperature of 900 K for 500 ps and then quenched back to 300 K for 500 ps. This allowed the system to cross possible high energy barriers that may not be overcome at low temperatures and to explore more of the phase space within the simulation time. The initial configurations for AIMD simulations were taken from the final 500 ps at 300 K of the classical MD simulations at one of the five equally spaced (100 ps) configurations.

4.1.3 Ab Initio Molecular Dynamics

For the TEG-water mixture, three different DFT conditions were set up, each with either a different exchange-correlation (XC) functional used in the quantum mechanical treatment of the electronic degrees of freedom, a different pseudopotential used to describe the interaction between the valence electrons and the ions (nuclei and their core electrons), or the inclusion of non-local electron correlation effects that are responsible for the van der Waals (vdW)/dispersion interactions, or vdW-inclusion/dispersion DFT. The first set of conditions, deemed the PW91 set, used the Perdew-Wang 91 (PW91), generalized-gradient approximation (GGA) XC functional, [236, 237] Vanderbilt ultrasoft pseudopotentials for core electron-valence

electron interactions, [238, 239] and no vdW/dispersion interactions. The second set of conditions, deemed the PBE set, used the Perdew, Burke, and Ernzerhof (PBE) GGA-type XC functional, [240, 241] Martin-Troullier (MT) norm-conserving pseudopotentials, [242] and no vdW/dispersion interactions. The third set of conditions, deemed the PBE+TS-vdW set, used were the same as the PBE set but included the Tkatchenko-Scheffler density-dependent vdW/dispersion functional (TS-vdW). [243, 244] For the bulk water simulations, four sets of DFT XC functionals were used: the PW91 XC functional with Vanderbilt ultrasoft pseudopotentials, the Beck, Lee, Yang, Parr (BLYP) [245, 246] XC functional with MT pseudopotentials, the PBE XC functional with MT pseudopotentials, and the PBE XC functional with the Tkatchenko-Scheffler density-dependent vdW/dispersion functional (TS-vdW). [243, 244] The choice of including the BLYP functional for the bulk water simulations was made to allow for comparison with results in the literature. [247, 248]

For each set of DFT conditions, four to five independent AIMD simulations of the TEG-water mixture were run, totaling thirteen different simulations across all XC functionals. Since the system is positively charged due to the hydronium ion, a negatively charged jellium/background charge [249] was applied to the system to give a charge-neutral cell. The Kohn-Sham orbitals were expanded in plane waves with a kinetic energy cutoff 80 Ry for all three sets of DFT conditions. This cutoff is also consistent with previous work for determining accurate cutoffs for pure water CPMD simulations. [250–253] The charge density was expanded in plane waves with an energy cutoff of 320 Ry for the PBE and vdW-PBE setups and 960 Ry cutoff for the PW91 setup since ultrasoft pseudopotentials trade-off a smaller Kohn-Sham orbital cutoff for a larger charge density cutoff. The electronic subsystem was sampled at the Γ-point at the first Brillouin zone. This is also consistent with previous literature, specifically in the work of Galli et al. [251, 253] where electronic structure calculations of both a 64 water molecule cell and, by repeating the 64 molecule cell periodically twice in each direction, a 512 water molecule cell, showed energy per molecule changes were less than 0.01 kcal/mole and the force was equivalent per atom within 10^{-5} a.u. between both systems.

For the all the CPMD simulations, a timestep of 0.075 fs and a fictitious electronic mass of 300 a.u. was chosen due to testing from previous studies [250–253] of CPMD for water simulations. The small timestep and electronic mass are due to the light hydrogen nucleus within the system. To ensure adiabaticity between the ions and the electrons, the fictitious kinetic energy of the orbitals was monitored and showed to be constant and remained close to zero. This test is a measure of how close the system stays to the ground-state Born-Oppenheimer (BO) energy surface. [72] If incorrect parameters are used, the electrons will exchange energy with the ions (destroying adiabaticity) and this kinetic energy will increase, undermining the integrity of the CPMD simulation.

For the bulk water AIMD simulations, the simulations were first run with 10 ps in the canonical (NVT) ensemble and followed by 50 ps of NVE for data production for each XC functional. The TEG-water mixture AIMD simulations were first carried out

in the NVT ensemble for 13 ps of equilibration and then run in the NVE ensemble for a minimum of 10 ps for data production for each of the simulations. The length of each simulation varied but it was ensured that 50 ps of data production per XC functional set were obtained. The collective total for each XC functional were 95 ps for the PBE set, 68 ps for the PW91 set, and 52 ps for the PBE+TS-vdW set. The system was initialized by first relaxing the electronic wave function by relaxing the electronic degrees of freedom with frozen, immobile ions. Then, the system wave function was relaxed by mobilizing the ions, allowing the ionic and electronic dynamical degrees of freedom to converge on the ground-state energy simultaneously. This was performed via geometry optimization using dampened dynamics with a total energy convergence tolerance and a fictitious electronic kinetic energy convergence tolerance of 10^{-7} Hartree a.u. and 10^{-4} Hartree a.u., respectively. For the equilibration stage of the TEG-water mixtures in the NVT ensemble, Nosé-Hoover chain thermostats were implemented, [254] each with a chain length of four. To achieve rapid equipartition of the thermal energy, one Nosé-Hoover chain was applied per atom ("massive" Nosé-Hoover thermostat). Four different thermostat frequencies were used to stimulate both the slow and fast intra-molecular, oxygen-hydrogen vibrational motions. The ionic temperature was monitored and was found to be well-averaged around 300 K after 3 ps. This was the followed by an additional 10 ps of NVT equilibration and then switched to the NVE ensemble for a minimum of 10 ps for data production.

4.2 Results & Discussion

4.2.1 Comparative analysis of solvation structure via radial distribution functions.

Our analysis begins with a description of the solvation structure found around H_2O and H_3O^+ molecules for both the bulk water and TEG-water mixture systems using radial distribution functions (RDF), $g(r)$. We present a subset of all RDFs calculated from the simulations to illustrate key differences in local liquid structure between the bulk water system and the TEG-water mixture, and also to highlight affinity of H_2O and H_3O^+ for specific groups along the TEG polymer chain specific to the TEG-water mixture. In Fig. 4.2, the RDFs for oxygen and hydrogen atoms of H_2O and H_3O^+ with different species are shown.

For understanding the solvation structure around water molecules, we first analyze the correlation between the O of H_2O, annotated O (H_2O), with other O (H_2O) RDF, or $g_{O(H_2O)-O(H_2O)}(r)$, in Fig. 4.2(a). The oxygen-oxygen RDF in Fig. 4.2(a) shows that the first peak around 2.75 Å is the same for the bulk water and the TEG-water mixture and all density functionals. The first minimum occurs around 3.2-3.3 Å with the location being found at greater distance from the oxygen with an increasing level of theory for the XC functional. The second peak occurs at around 4.2-4.3 Å, appears to vary less for the XC functional in the TEG-water mixture.

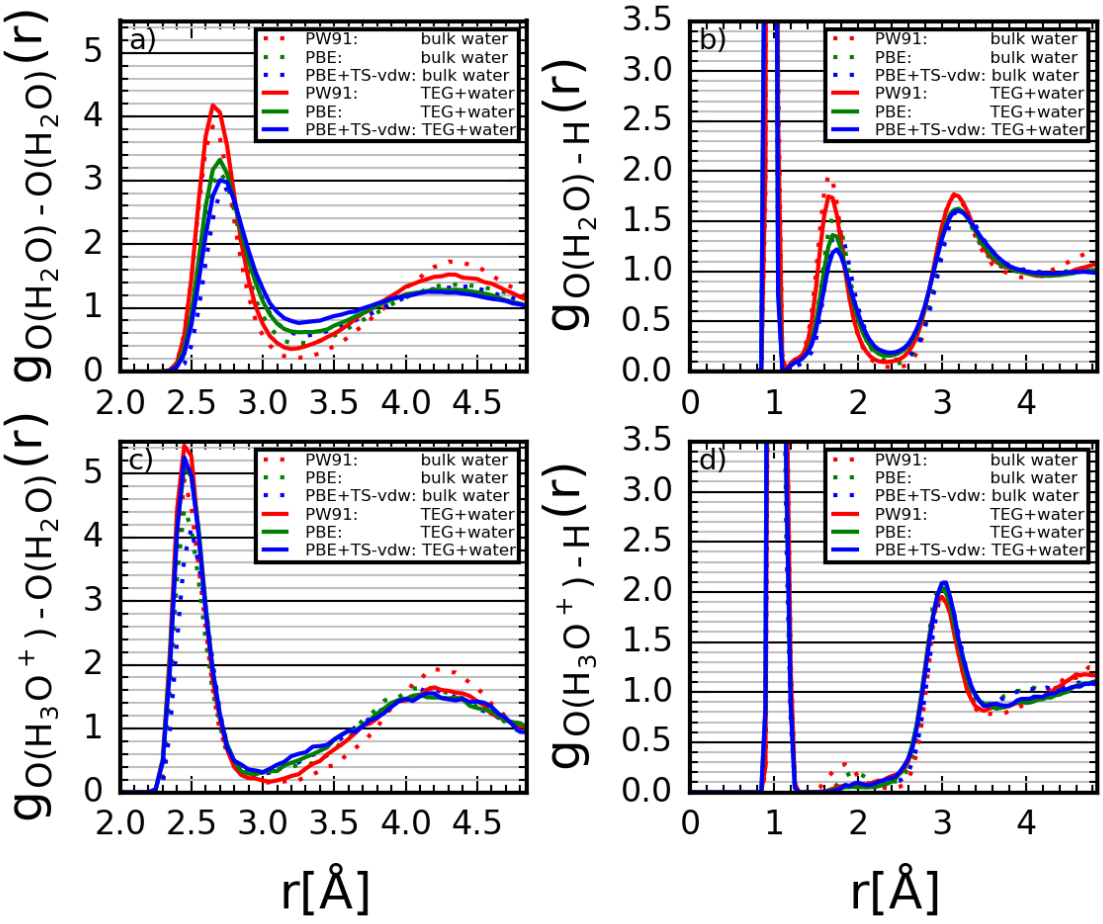


Figure 4.2: The radial distribution functions of oxygen and hydrogen of water and hydronium ion in bulk water and TEG-water mixtures at 300 K. The different figures are as follows: (a) O (water)-O (water), (b) O (water)-H (all hydrogens), (c) O (hydronium)-O (water), and (d) O (hydronium)-H (all hydrogens).

In Fig. 4.2(b), the RDF between the oxygen of water, O (H_2O), and surrounding H, $g_{O(H_2O)-H}(r)$ is shown. The first peak occurs due to covalently bonded hydrogen atoms. We see that the second and third peaks occur around 1.75 Å and 3.2 Å, respectively, for both bulk and TEG-water mixture, regardless of the XC functional. The peak height decreases with increasing level of theory and from bulk water to the TEG-water mixture, indicating a weakening of the HB network.

Based on the RDFs for oxygen atoms of water, the presence of TEG shows an overall reduction in RDF peak height and softening of the local water structure. This occurs most likely due to the TEG chain species being located in the first solvation shell, causing softening of the first solvation structure and disrupting the HB network. This disruption is best shown in the reduction of the second peak of the O of H_2O and any H, signifying that H atoms are less likely to be locked into hydrogen bonds with oxygen of water molecules. Also, we see that inclusion of vdW/dispersion interactions also reduce the peak height, indicating a further softening of the water structure. [250] It has become well-known that the PBE level of theory gives an over-structured oxygen-oxygen RDF for water due to the key limitations in GGA-DFT. These limitations manifest in theoretical descriptions of water as over-structuring, giving a representation of super-cooled liquid water at ambient conditions. Recently, DiStasio et al. determined that including vdW/dispersion interactions strengthen the interaction between a given water molecule and those found in its first and second solvation shells. [250] The stronger interaction with second solvation shell water molecules allow them to move inward to interstitial regions, weakening the HBs in the first solvation shell and allowing first solvation shell water molecules to move outward. Thus, we attribute this softening of structure with the dispersion-included PBE+TS-vdW level of theory due to weakened HBs and stronger interaction with second solvation shell species, displacing first solvation shell water molecules compared to the PBE level of theory. The most evident feature is the increase in the RDF value for the first minimum in the $g_{O(H_2O)-O(H_2O)}(r)$ in Fig. 4.2(a). This is due to interstitial water molecules between the first and second solvation shell, i.e. the water molecules migration outward, from first to second solvation shells, and inward, from second to first solvation shells.

For the solvation structure around H_3O^+, we analyze the RDF of O in H_3O^+ with O in H_2O, $g_{O(H_3O^+)-O(H_2O)}(r)$ (Fig. 4.2(c)), and with H atoms, $g_{O(H_3O^+)-H}(r)$ (Fig. 4.2(d)). In $g_{O(H_3O^+)-O(H_2O)}(r)$, we observe the first peak around 2.5 Å for both systems and all levels of theory. The first minimum occurs at approximately 2.9-3.0 Å with increasing peak height for the TEG-water mixture and increasing level of theory. The second peak occurs at around 4.2-4.3 Å. In Fig. 4.2(d), the O of H_3O^+ and any hydrogen RDF has a first peak for covalently bonded hydrogen atoms. Comparing to the O of H_2O and any hydrogen RDF in Fig. 4.2(b), we observe a broadening of the first peak farther from the oxygen atom. The second peak for the bulk water systems occur at 1.80 Å. This peak is the hydrogen of a HB donor. Comparing Fig. 4.2(b) to Fig. 4.2(d), we see the expected reduction in the second peak height for bulk water

due to H_2O accepting two HBs while H_3O^+ can only accept one HB. For the TEG-water mixture, no strong peak is observed at 1.80 Å across all levels of theory but instead shows an increasing slope starting around 1.6 Å. Thus, the hydrogen of the HB donor is less localized than that for bulk water and is located within any range from 1.6 Å to 2.6 Å.

In Fig. 4.3, we show the RDFs for oxygen atoms of H_2O and H_3O^+ with oxygen atoms of the TEG chain, specifically the ether (ROR) oxygen and hydroxyl (ROH) oxygen. We begin with the RDFs of the O of H_2O with the TEG atoms to better understand the direct interaction of water molecules with the TEG chain and the effects of TEG on the solvation structure around water molecules. In Fig. 4.3(a), $g_{O(H_2O)-O(ROR)}(r)$ shows the first peak at around 2.70 to 2.75 Å. The first peak of the PW91 XC functional occurs closer to the oxygen of water, indication a stronger attraction between ether and water compared to the PBE and PBE+TS-vdW functionals. Also, the minimum between the water and ether is farther away for the PBE and PBE+TS-vdW XC functionals, indicating that the PW91 has a more rigid structure between the water molecules and the ether backbone compared to the other XC functionals.

In Fig. 4.3(b), we examine the correlation of O of H_2O with the O of the ROH group. We observe that $g_{O(H_2O)-O(ROH)}(r)$ has a first peak located around 2.7 Å and that there is a decrease in the peak height. The highest peak belongs to PBE, the next highest belongs to PW91, and the PBE+TS-vdW with the lowest peak. The trend that we observe is that the ultrasoft pseudopotential used for PW91 could effect this interaction and thus the RDF. Also, that the inclusion of dispersion effects seem to have a drastic decrease in RDF size, going from the PBE to the PBE+TS-vdW XC functionals, indicating the importance of including dispersion for this system. This shows overall there is a softening of the second solvation shell structure around H_2O via including dispersion.

For Fig. 4.3(c) and Fig. 4.3(d), we show the RDF for O of H_3O^+ with the ether O and hydroxyl O of TEG, respectively. In Fig. 4.3(c), the ether O of TEG is shown to be in the first solvation shell of H_3O^+ for the PBE+TS-vdW XC functional but not for the PW91 and PBE levels of theory. There appears to be a strong interaction between the ether oxygen of TEG and H_3O^+ that is not captured by modeling without dispersion effects. In Fig. 4.3(d), the hydroxyl O of TEG is in the first solvation shell of H_3O^+ for the PW91 and PBE levels of theory but not for the PBE+TS-vdW XC functional. Interestingly, the PBE+TS-vdW XC functional gives an almost featureless RDF between a H_3O^+ and the hydroxyl group of TEG, whereas, the PW91 and PBE RDFs have apparent peaks at 2.5 Å and 4.5 Å. The strongest interaction of H_3O^+ with the hydroxyl group occurs with the PW91 level of theory. Overall, for H_3O^+, the PW91 and PBE XC functionals give a H_3O^+ solvated mostly by H_2O but also by hydroxyl O of TEG in the first solvation shell and PBE+TS-vdW gives H_3O^+ solvated by H_2O and ether groups of TEG.

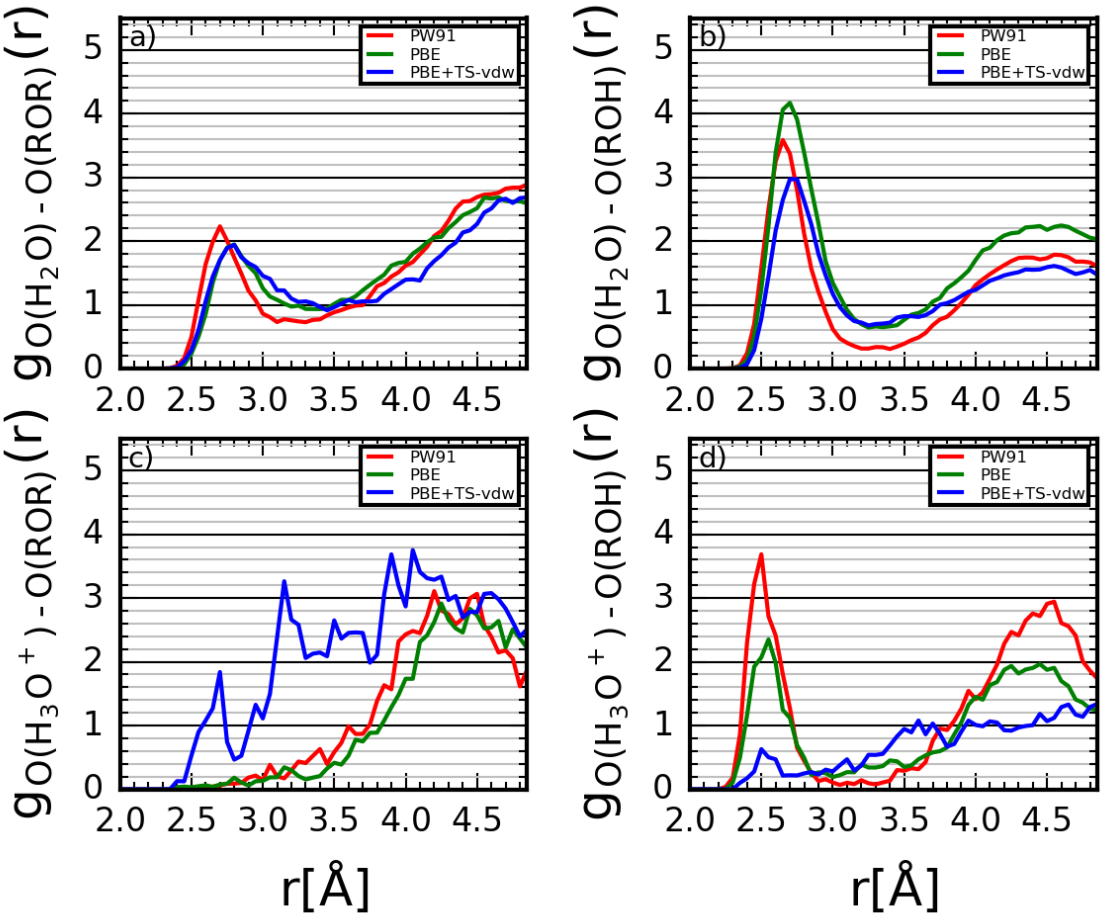


Figure 4.3: The radial distribution functions of oxygen for water and hydronium ion in TEG-water mixtures with the oxygens of TEG chain at 300 K. The different figures are as follows: (a) O (water)-O (ether of TEG), (b) O (water)-O (hydroxyl of TEG), (c) O (hydronium)-O (ether of TEG), and (d) O (hydronium)-O (hydroxyl of TEG).

4.3 Protonic defect species occurrence and lifetime analysis.

One interesting effect that TEG has on proton transfer in aqueous solution is the different protonated and de-protonated species, or protonic defect species, that can occur and their associated lifetimes. We analyze the trajectory for these species by, first, assigning every hydrogen atom to the geometrically closest oxygen or carbon atom for every frame to identify it as a water molecule or a molecular group of the TEG chain (i.e. ether, hydroxyl, or methylene). Then, the molecule/molecular group is identified as having either an excess or lack of a hydrogen atom, indicating a protonic defect species.

In Table 4.1, we show the different species that occur over all simulations of the aqueous TEG solutions with occurrence percentages, cumulative occurrence percentages, and lifetimes of each species. For the lifetimes, the mean value is reported with one standard deviation being noted as ($\pm\sigma$). Proton rattling, where upon two consecutive proton transfer events, the protonic defect is returned to the original species, is both included and excluded. The reasoning for excluding proton rattling is, if one includes the proton rattling events in analysis, the transient protonic defect species and surrounding solvation take over the recorded observations. One can exclude these proton rattling events, recording only those where two consecutive proton transfer events lead to a different protonated atom to determine structures that are associated with long-range, structural diffusion.

For all three XC functionals used, we note three common trends for the protonic defect species occurrences. First, H_3O^+ is the dominant species that occurs for more than 99% of the simulation time. Second, the second most likely protonated species to be found is the protonated hydroxyl group of the TEG. It is also the only other protonated species besides H_3O^+ to not exist simply as a proton rattling species, implying it has a role in proton transfer events that correlate to structural diffusion. Third, the OH^- ion and RO^- occur with only a small fraction of a percent and only exist in proton rattling occurrences.

For the lifetimes of these species that occur, we point out a few key notes in Table 4.1. First, the H_3O^+ lifetime occurs well within one standard deviation for all three XC functionals, signifying no strong change among levels of theory, for both cases of proton rattling. Yet, the mean and the standard deviation of the lifetimes do increase with increasing the level of theory, pointing to longer lifetimes of H_3O^+ in the system. Note, the standard deviation is larger than the mean of the lifetime. A lifetime cannot be negative, thus putting a lower bound on the lifetime and implying a larger standard deviation implies longer lifetimes. Distributions of the H_3O^+ lifetimes in TEG-water mixtures with proton rattling included are shown in Appendix Section A in Figures A.1-A.3 for the three functionals for clarity.

Next, we observe that for the protonated hydroxyl group of TEG, the occurrences and lifetimes are lower for the inclusion of dispersion effects when proton rattling

Table 4.1: Protonic defect species occurrences and lifetimes found in aqueous H^+ and triethylene glycol (TEG) systems. Proton rattling effects are included and excluded.

Functional	Proton Rattling	Protonic Defect Species	%	$\sum$ %	Lifetime (fs)
PW91	Included	H_3O^+	99.46	99.46	34.6 (±55.5)
		ROH_2^+, [a]	0.43	99.89	34.6 (±39.4)
		OH^-	0.07	99.96	15.6 (±13.4)
		RO^-, [b]	0.04	100	7.6 (±3.9)
	Excluded	H_3O^+	99.57	99.57	700 (±1380)
		ROH_2^+, [a]	0.43	100	475[c]
PBE	Included	H_3O^+	99.85	99.85	47.6 (±94.0)
		ROH_2^+, [a]	0.13	99.98	42.7 (±96.2)
		OH^-	0.01	99.99	14.8 (±12.77)
		RO^-, [b]	0.01	100	7.6 (±3.9)
	Excluded	H_3O^+	99.87	99.87	1290 (±2430)
		ROH_2^+, [a]	0.13	100	110 [c]
PBE+TS-vdW	Included	H_3O^+	99.97	99.97	45.9 (±81.1)
		ROH_2^+, [a]	0.03	100	8.2 (±1.5)
		OH^-	0.00	100	1.6 [c]
	Excluded	H_3O^+	99.97	99.97	1300 (±2100)
		ROH_2^+, [a]	0.03	100	126.61 [c]

[a] Protonated hydroxyl group of the TEG chain

[b] De-protonated hydroxyl group of the TEG chain

[c] Single lifetime measurement.

is included but approximately equal when proton rattling is excluded. This implies that for the PBE XC functional, the proton reside on the hydroxyl group longer during proton rattling events compared to the PBE+TS-vdW XC simulations. Yet, overall, the proton rattling occurs for the same length of time before the proton travels to another atom, undergoing structural diffusion. Interestingly, we also see more occurrences and shorter lifetimes of the protonated hydroxyl group of TEG with the PW91 level of theory for both including and excluding proton rattling. This indicates a much stronger interaction between the H_3O^+ and the hydroxyl group for PW91, consistent with Figure 4.2(d).

The OH^- ion and RO^- ion show a very short lifetime among all levels of theory. Upon further analysis of the trajectory, the majority of the occurrences of the OH^- and RO^- ion have the OH bond lengths (the receiving O atom to H^+ bond length and the O atom of H_3O^+ to H^+ bond length) are approximately equal during these event, implying these are proton sharing event versus proton transfer event.

Using our values for the probability of H^+ to reside on water or the hydroxyl/ROH of TEG in Table 4.1, we calculate the change in the free energy of transfer for H^+ from water to ROH to be 7.2, 10.2, and 13.8 in kJ/mol for the PW91, PBE, and PBE+TS-vdW levels of theory, respectively, with an average value of 10.4 kJ/mol over all three XC functionals. This gives excellent agreement compared to the experimental values for both 10.4 kJ/mol for methanol and 10.5 kJ/mol for ethanol, in Table 2 and Table 3, respectively, from the work of Marcus [255] that reports the standard Gibbs free energy for the transfer of ions from water to aqueous alcohol mixtures for varying mass fraction of the alcohol content using the extra-thermodynamic assumption. Note, we used the assumption that we can mimic the ROHs of TEG as methanol and ethanol. Discussion and tabulation of the reported values in Table C.1 can be found in Appedix Section B.

4.3.1 Special pair occurrence and lifetime analysis.

Another effect of introducing TEG is the different special pairs that can form between atoms, helping identify the most active protons of the system. The term special pair originally referred to the protonated H_3O^+ and its hydrogen-bonded water molecule in the first solvation shell that was under-coordinated with similar hydration, [76] yet this identity has changed with time. [256] For further detail and insight, the reader is directed to the work of Markotvitch et al. [88] where, using the multi-state empirical valence bond (MS-EVB) approach, [87, 88, 256–259] they investigated the role of the special pair in the proton transport process and its dynamics throughout the system, termed the "special pair dance".

For the present work, we begin by expanding on the previous section analysis, in that once the protonic defect species is determined, the "most-active" proton of the system is identified using the asymmetric stretch coordinate [230, 260], given as $\delta = R_{aH^*} - R_{bH^*}$, where R_{aH^*} and R_{bH^*} are the HB distances for the shared proton (H^*) between two atoms, a and b. The hydrogen atom which gives the smallest value

δ between the protonic defect species atom and the HB acceptor atom is identified as H^+ and these two atoms form the special pair.

In Table 4.2, the different special pair types that occur over all simulations of the aqueous TEG solutions are listed with occurrence percentages, cumulative occurrence percentages, and lifetimes of each species. For the lifetimes, the mean value is reported with one standard deviation being noted as ($\pm\sigma$). Proton rattling events have been excluded to highlight special pairs relevant to structural diffusion. For all special pairs that occur with proton rattling events included, the reader is directed to Table C.1 in the Appendix Section C.

Table 4.2: The occurrences and lifetimes of special pairs made up of the protonated species ($Z_{protonated}$) and the special partner of the protonated species (Z_{shared}) found in aqueous H^+ and triethylene glycol (TEG) systems. Proton rattling effects are excluded.

Functional	Proton Rattling	$Z_{protonated}$	Z_{shared}	%	$\sum$ %	Lifetime (ps)
PW91	Excluded	H_3O^+	H_2O	97.32	97.32	1.16 $\pm$1.57
		H_3O^+	ROH	2.18	99.50	2.45 $\pm$2.42
		ROH_2^+	H_2O	0.50	100	0.06 [a]
PBE	Excluded	H_3O^+	H_2O	98.76	98.79	1.85 $\pm$3.06
		H_3O^+	ROH	1.07	99.86	0.08 $\pm$1.16
		ROH_2^+	H_2O	0.14	100	0.02 [a]
PBE+TS-vdW	Excluded	H_3O^+	H_2O	99.51	99.51	1.53$\pm$2.51
		H_3O^+	ROH	0.46	99.97	0.01 [a]
		ROH_2^+	H_2O	0.03	100	0.01 [a]

[a] Single lifetime measurement.

The trends of the special pairs follows closely with those of the protonic defect species analysis, as expected. First, the special pair between two water molecules (H_3O^+ and H_2O) occurs more than 97% for the entire simulation time over all levels of theory. The second and third highest occurring special pairs are direct results from proton transfer between a water molecule and a hydroxyl group of TEG (H_3O^+ with ROH and ROH_2^+ with H_2O). These are expected since the second highest occurring protonic defect species across all levels of theory was the protonated hydroxyl group of TEG and the only other protonated species that occurs when proton rattling is excluded for structural diffusion events.

The lifetimes of the H_3O^+ - H_2O special pairs appear to be in the range of 1-2 ps across all levels of theory. These lifetimes have a very wide spread over the simulations, shown by the PBE having lifetimes up to 5 ps within one standard deviation. For the H_3O^+ - ROH and ROH_2^+ - H_2O complexes, the general trend is a decrease in the occurrences with increasing level of theory. For the lifetimes of

the H_3O^+ - ROH, the same general trend is observed with decreasing lifetimes for increasing level of theory. The occurrence of a special pair and the lifetime of that pair are correlated, most likely due to favorable stability of the structure for the given XC functional. The ROH_2^+ - H_2O complex does not show a strong trend due to only a single occurrence for all XC functionals when proton rattling events have been excluded.

4.3.2 Solvation shell occurrence and lifetime analysis.

The results for analysis of the molecular groups that populate the hydrogen-bond acceptors, also called the ligand sites for the Eigen cation for protonated water molecules, are presented and discussed below to expand on the understanding of the solvation shells that are present around the given protonated species. Similar to the previous analysis of protonated species and special pairs, Table 4.3 shows all of the occurrences of solvation shells and their lifetimes for all levels of theory with proton rattling events excluded to highlight solvation likely present during structural diffusion events. We observe that the dominant species is the Eigen cation, occurring more than 85% of the simulation time sampled for all levels of theory. The lifetimes of this solvation shell seem to be dependent on the XC functional used but independent of dispersion inclusion.

Consistent with the RDFs of Figure 4.3(d) and the special pair analysis in Table 4.2, we see that the second dominant solvation shell structure is one that contains the hydroxyl group for the PW91 and PBE XC functionals but not for the PBE+TS-vdW XC functional. Instead, the second dominant solvation shell structure for the PBE+TS-vdW XC functional simulations is one with a vacant ligand site. The fact that this occurs for the dispersion inclusion functional leads one to conclude that the over-structuring of water that has been discussed for GGA XC functionals (PW91 and PBE) suppresses this solvation structure due to overly strong hydrogen bonding interactions for this given temperature. It appears that including dispersion increases the probability of observing a vacancy in the solvation structure, most likely due to stronger interactions with more distant molecular groups that can help stabilize this structure. Yet, the GGA XC functionals do have this as the third dominant solvation shell, implying that this solvation pattern is only suppressed but not prohibited.

Interestingly, the methylene group is present in the PW91 and PBE+TS-vdW solvation shell structures but only as a minority species. Yet, the lifetimes are very high for this solvation shell. Upon analyzing the solvation shell structures including proton rattling, it is observed that these may be long lived proton rattling events, where the protonic defect resides on another atom with a different solvation shell for an extended amount of time before returning back to this solvation shell. The lifetime reported is therefore the collective lifetime of this solvation shell and all others observed during proton rattling events, which is not reflected in the occurrence of this solvation shell. The fact that this lifetime is long lived (1 ps for PBE+TS-vdW and 4 ps for PW91) indicates that this is a solvation shell structure that can lead to

Table 4.3: The occurrences and lifetimes of solvating shell species ($H_{A,1\text{-}3}$) around the protonated species ($Z_{protonated}$) found in aqueous H^+ and triethylene glycol (TEG) systems. Proton rattling effects are excluded.

Functional	$Z_{protonated}$	$H_{A,1}$	$H_{A,2}$	$H_{A,3}$	%	$\sum$ %	Lifetime (ps)	
PW91 [d]	H_3O^+	H_2O	H_2O	H_2O	86.40	86.40	0.81	± 1.46
	H_3O^+	ROH	H_2O	H_2O	9.76	96.16	0.82	± 1.34
	H_3O^+	H_2O	H_2O	...	3.06	99.22	0.62	± 0.01
	ROH_2^+	H_2O	H_2O	...	0.50	99.72	0.03	± 0.02
	H_3O^+	H_2O	H_2O	CH_2	0.28	100	4.09[b]	
PBE [b]	H_3O^+	H_2O	H_2O	H_2O	85.75	85.75	1.52	± 2.84
	H_3O^+	ROH	H_2O	H_2O	8.00	93.75	1.10	± 1.42
	H_3O^+	H_2O	H_2O	...	6.11	99.86	0.49	± 0
	ROH_2^+	H_2O	H_2O	...	0.14	100	0.01[b]	
PBE+TS-vdW [d]	H_3O^+	H_2O	H_2O	H_2O	90.12	90.12	1.52	± 2.32
	H_3O^+	H_2O	H_2O	...	5.95	96.07	0.72[b]	
	H_3O^+	ROH	H_2O	H_2O	2.21	98.28	0.21	± 0.20
	H_3O^+	H_2O	H_2O	CH_2	1.70	99.98	1.36[b]	
	ROH_2^+	H_2O	H_2O	...	0.02	100	1.27[d]	

[a] 12 different solvation shells found when proton rattling included.
[b] Single lifetime measurement.
[c] 12 different solvation shells found when proton rattling included.
[d] 13 different solvation shells found when proton rattling included.

proton "traps", giving rise to rest periods and reduce overall structural diffusion. One explanation could be that when this solvation shell occurs, the excess proton has a reduced amount of paths along the hydrogen bond network to escape. An analysis of the hydrogen bond ring statistics, as in similar work, [85,86] relative to this structure could determine the validity of this hypothesis but is not explored in the current work. All solvation shells present when proton rattling is included is shown in Table D.1 in the Appendix Section D.

Agmon et al. [261, 262] have interpreted the free energy of proton transfer from water to methanol, concluding that the solvation shell around the hydronium ion does not show preference to water or methanol and that either are likely candidates for hydrogen-bond acceptors. [88] For our simulations, to determine if the hydroxyl group is also equally likely to populate the solvation shell relative to water, we determine what the probability is for hydroxyl to be on either of the three sites based on its concentration. We then compare this concentration-based probability to the observed probability during the simulation for the hydroxyl to be found in the solvation shell. Using a probability union relation and the assumption that there are 36 molecular groups that could possibly populate the solvation shell sites (2 hydroxyl groups, 2 ether groups, 6 methylene groups, and 26 water molecules, not including the centrally protonated water), we determine that there is a 16% chance that the hydroxyl group will populate the solvation shell ligand sites based on solely on concentration. For a discussion of the probability union relation used to calculate this probability, the reader is referred to Appendix Section E. From our simulations for each XC functional, we find that for PW91, PBE, and PBE+TS-vdW that the mean and standard deviation occurrence percentage of ROH on the ligand sites are 9.5% ±12.2, 8.2% ±4.2, and 2.1% ±4.0, respectively, where the averaging was performed over the simulations that make up each XC functional set. Note, that the above values where obtained from analyzing all solvation shells, thus, include proton rattling, and lead to slight differences in values reported in Table 4.3. We see that PW91 is within $\pm\sigma$, PBE slightly decreases this occurrence, interestingly, and the inclusion of dispersion effects for PBE+TS-vdW reduces this occurrence. Possibly, the long-range dispersion effects could allow the hydrophilic hydrogens of hydronium and the hydrophobic methylene groups bonded to the hydroxyl groups to feel a stronger repulsion, reducing the attraction between the hydronium and the hydroxyl group. Also, our assumptions have an effect on this concentration-based probability prediction. First, the assumption that the hydroxyl group of TEG can be mimicked by methanol is ignoring the fact that the rest of the chain can both sterically hinder interaction with the hydroxyl group from other molecules in the system and also that the additional methylene groups in the chain could invoke repulsive behavior, already discussed. These effects would suppress the probability of finding ROH on the ligand sites to varying degree. Second, in determining the target probability, we have assumed that all the sites will be occupied by one of the 36 molecular groups specified. Yet, we know this is not the case since we can have vacant sites as seen in Table 4.3 where there is no hydrogen bond acceptor present. Including this observance would

further reduce the likelihood of observing the hydroxyl group in the solvation shell based solely on concentration since we introduce a species that can populate the site, a vacancy or "cavity". Yet, only at above 90% of the total solvation shell occurrences do we see the vacancies, indicating that the assumption that only one of the 36 molecular groups will populate the site is within reason. Reducing the concentration-dependent probability would bring the observed probabilities from simulation into closer agreement. For this discussion of hydroxyl groups populating the solvation shells, we conclude that our simulations show that for GGA XC functionals, PW91 and PBE, it is equally likely to observe methanol / hydroxyl on the ligand sites but when including important dispersion effects, there is a preference for water to occupy the ligand sites relative to the hydroxyls of TEG.

4.3.3 Hydrogen-bond network occurrence and lifetime analysis.

In line with the three previously discussed analysis of protonated species, special pairs, and solvation shells, the HB network that exists around protonic defect species have been investigated in a similar manner. This analysis is similar to recent work for studying HB networks for the excess proton in water such as that of Lapid et al. [263] that used bond-order analysis to analyze HB dynamics in larger water clusters (second-solvation shell) around the Zundel ion and, the work of Shevchuk et al. [264] that use complex network analysis to track several coordinates of interest of the HB network relevant to proton transport. We determine the hydrogen bonded atoms that surround the special pair complex based on the criteria that the distance between HB acceptor (A) and donor (B) is less $R_{ab} < 3.5$ Åand the angle between the HB acceptor, hydrogen of the HB, and the HB donor $\alpha(A...H...B) < 30°$. Using a tree-structure data type, we "grow" the tree for the HBs surrounding the special pair by levels where the levels indicate the solvation shells. We can then compare tree-structures to determine equality, i.e. equivalent HB networks around the same special pair. We report the occurrences of each HB network around a given special pair and its associated lifetimes, shown in Table 4.4, only including HB networks that occur when proton rattling has been excluded. Only the five highest occurring of these HB networks are listed for brevity in the Table 4.4, with the total number of HB networks found listed in the footnotes for both excluding and including proton rattling. All of the HB networks found for TEG-water mixtures with proton rattling excluded are listed in the Appedix Tables F.1-F.3 in Section F.1. In Figure 4.4, we give an illustration for the labels found in Table 4.4. Since most HB networks surround a water-water special pair, this is the species shown in Fig. 4.4.

From Table 4.4, we can determine the most significant HB networks present for structural diffusion proton transfer events. The H_3O^+ - H_2O special pair dominates the center of the HB networks found due to the high occurrence of this complex listed in Table 4.2 for all XC functionals. It is observed that the most likely hydrogen-bond donor for the hydronium, $HB_{D,p,}$ is either a vacancy or $CH_{2.}$ This observation

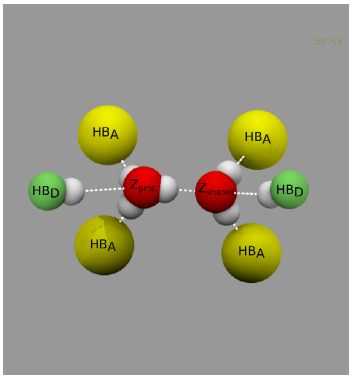


Figure 4.4: Hydrogen-bond network around a water-water special pair. Labels the protonated species ($Z_{protonated}$ / Z_{prot}), the atom (Z_{shared}) hydrogen bonded to the most active proton, the hydrogen-bond acceptors (HB_A) and the hydrogen-bond donors (HB_D).

Table 4.4: The top five most occurring hydrogen-bond networks around protonic defect species and associated lifetimes for TEG-water mixtures. Protonated species (Z_{prot}), the special pair atom (Z_{shared}), the solvating atoms of the protonated species ($HB_{X,\,p}$ where x=A or D for accepting or donating a hydrogen bond, respectively), and the solvating atoms of Z_{shared} ($HB_{X,\,s}$ with the same definitions of x) are listed. Figure 4.4 provides graphical labeling. Proton rattling effects are excluded.

Functional	Z_{prot}	Z_{shared}	$HB_{A,p}$	$HB_{A,p}$	$HB_{D,p}$	$HB_{A,s}$	$HB_{A,s}$	$HB_{D,s}$	%	$\sum$ %	Lifetime (ps)
PW91[a]	H_3O^+	H_2O	H_2O	H_2O	...	H_2O	H_2O	H_2O	17.60	17.60	2.3 ± 1.1
	H_3O^+	H_2O	H_2O	H_2O	CH_2	H_2O	H_2O	...	16.14	33.75	0.6
	H_3O^+	H_2O	H_2O	H_2O	...	H_2O	H_2O	...	15.61	49.36	0.3
	H_3O^+	H_2O	H_2O	H_2O	CH_2	H_2O	H_2O	H_2O	6.52	55.87	0.01 ± 0.004)
	H_3O^+	H_2O	H_2O	H_2O	...	H_2O	H_2O	CH_2	6.29	62.16	1.4 ± 1.3
PBE[b]	H_3O^+	H_2O	H_2O	H_2O	...	H_2O	H_2O	H_2O	21.35	21.35	1.3 ± 2.5
	H_3O^+	H_2O	H_2O	H_2O	...	H_2O	H_2O	...	19.71	41.06	0.5 ± 0.4
	H_3O^+	H_2O	H_2O	H_2O	...	H_2O	H_2O	CH_2	6.45	47.51	1.8
	H_3O^+	H_2O	H_2O	H_2O	...	ROH	H_2O	...	5.26	52.78	0.1
	H_3O^+	H_2O	H_2O	H_2O	...	ROH	H_2O	H_2O	4.85	57.63	0.7
PBE+TS-vdW[c]	H_3O^+	H_2O	H_2O	H_2O	...	H_2O	H_2O	H_2O	20.56	20.56	0.8 ± 0.04
	H_3O^+	H_2O	H_2O	H_2O	...	H_2O	H_2O	...	14.09	34.65	0.8 ± 0.1
	H_3O^+	H_2O	H_2O	H_2O	CH_2	H_2O	H_2O	H_2O	6.22	40.87	0.05
	H_3O^+	H_2O	H_2O	H_2O	...	H_2O	H_2O	CH_2	4.62	45.49	4.3
	H_3O^+	H_2O	H_2O	H_2O	H_2O	H_2O	H_2O	H_2O	3.89	49.38	2.4 ± 4.0

[a] 23 (excluded) and 160 (included) different hydrogen-bond networks found.
[b] 19 (excluded) and 196 (included) different hydrogen-bond network found.
[c] 16 (excluded) and 176 (included) different hydrogen-bond networks found.

is in line with previous literature, [220, 265–267] that the hydronium ion has an "amphiphilic" nature, due to possessing both hydrophilic character via HBs formed with water molecules and also a hydrophobic character due to the lone pair of oxygen not forming a HB with water molecules due to the overall positive charge on the cation. Thus, instead of forming HBs with water at the HB donor site, the hydronium ion orients such that the hydrophobic lone electron pair either remains vacant or creates a HB to the hydrophobic CH_2 of TEG and the hydrophilic hydrogens form HBs with other hydrophilic molecules and monomers (water molecules, ethers, and hydroxyls). Note, for this HB network analysis, the tree-structure has initially been setup to only capture "water-like" hydrogen-bond networks based on H_3O^+ - H_2O being the most likely observed special pair, seen in Table 4.2. This was to allow for easier comparison of similar hydrogen-bond networks and to reduce the already high number of entities identified. Relaxation of this constraint could be easily implemented but is not pursued in the current work. We report the HB networks for the bulk water simulations where proton rattling has been excluded (Tables G.1 - G.4), included (Tables K.1-K.4) and all HB networks found in TEG-water mixtures where proton rattling has been included (Tables K.5-K.7) in the Appendix Sections G and K.

Following similar analysis used for the solvation shell ligand sites, we examine the relative probability of a molecule/molecular group to occupy HB network sites. Table 4.5 gives the percentage of occurrence of a given species on any of the 6 sites in the HB network, on any of the 4 HB acceptor sites, and on either of the 2 HB donor sites. Table 4.5 should be understood as follows. From the first row, for the PW91 XC functional, 49% of the hydrogen bond networks around a special pair have at least one methylene group in one of the six sites shown in Figure 4.4. 0.6% of the hydrogen bond networks have at least one methylene group in one of the four acceptor sites shown in Figure 4.4. 48.5% of the hydrogen bond networks have at least one methylene group in one of the two donor sites shown in Figure 4.4. We note that water occurs in at least one acceptor site for all HB networks (thus a 100% occurrence for the total and acceptor columns of Table 4.5) and occurs at the donor site with 45% probability for all functionals.

Focusing on the preference for methylene in the HB network, we first determine that there is a 70% probability for CH_2 to occur in the HB network based solely on concentration. Again, for discussion of the concentration-based probability union relation used, the reader is referred to Appedix Section E. We see that based on the simulations, the CH_2 group occurrence is XC functional-dependent, varies over the different simulation runs for each XC functional set seen in the large standard deviations, and that it does not appear to have an equal probability to occur when we compare to our probability to see it in any of the HB network sites. Yet, we notice that CH_2 groups mainly sit on donor sites. Thus, if we reformulate our above analysis to only look at the donor sites instead, the probability for CH_2 groups to be at either site based on concentration is 31%. From previously discussed assumptions of this analysis, if we look at the "cavity" occurrence, there is an overwhelmingly high chance of having no hydrogen bond donor present. This implies that our assumption

Table 4.5: The occurrence percentages of a given molecule species in the total hydrogen bond network, the hydrogen bond acceptor sites (H_A) and the donor sites (H_B). The molecular groups are the ether (ROR), methylene (CH_2) and hydroxyl (ROH) groups of TEG and a "cavity". The standard deviations are reported also (SD).

Molecule Group	Functional	Total		H_A		H_D	
		%	SD	%	SD	%	SD
CH_2	PW91	49.0	(± 22)	0.6	(± 1.1)	48.5	(± 23)
	PBE	27.1	(± 10)	0.6	(± 0.6)	26.6	(± 9)
	PBE+TS-vdW	31.5	(± 4)	3.3	(± 5)	28.5	(± 7)
ROH	PW91	19.2	(± 15)	18.8	(± 15)	0.4	(± 0.5)
	PBE	25.4	(± 12)	20.0	(± 10)	5.3	(± 7)
	PBE+TS-vdW	10.3	(± 15)	8.2	(± 13)	2.2	(± 2)
ROR	PW91	1.5	(± 2)	1.5	(± 2)	...	...
	PBE	0.9	(± 1)	0.9	(± 1)	...	...
	PBE+TS-vdW	20.2	(± 16)	20.2	(± 16)	...	...
...	PW91	81.9	(± 1)	10.6	(± 5)	80.3	(± 2)
	PBE	88.4	(± 3)	17.0	(± 4)	86.1	(± 4)
	PBE+TS-vdW	86.6	(± 2)	16.2	(± 4)	84.1	(± 3)

for computing the probability based on concentration over-estimates the probability for the HB donor site since we do not take into account the lack of a hydrogen bonded species at these sites. Therefore, CH_2 groups have preference to be located at the HB donor sites relative to other molecule groups, observed previously in Table 4.4. Similarly, for the ROR or ROH to occupy any of the HB acceptor sites based on concentration is 22%. Thus, we can say ROH has a preferential probability be in the HB acceptor sites relative to other molecules. Surprisingly, the ether ROR has almost no probability for the PW91 and PBE XC functionals but a 20% probability when dispersion effects are included. This can also be seen in Fig. 4.3c. Yet, we see that ROR actually has a relatively high preference over other molecules to be in the HB acceptor sites for only the PBE+TS-vdW XC functional. Therefore, we conclude that ROH has preference over other molecule groups to be at the acceptor sites, CH_2 groups have preference over other molecule groups to be in the donor sites, and ROR has a XC functional-dependence that ranges from very low probability to preference when dispersion effects are included.

In Table 4.6, we report the HB networks that occur during proton transfer events. This helps determine how TEG is incorporated into the HB network to facilitate proton transport. Only the top five highest occurring HB networks are listed for brevity. Only the number of occurrences are listed for these HB networks since they are only captured at the instance of a proton transfer event. The CH_2 of TEG is again in the top three most observed the HB networks, consistent with a similar

observation in Table 4.4. This implies that proton transfer could possibly take place along the axis parallel to the TEG chain with the chain CH_2 groups being HB donors, providing the necessary solvation around the special pair for proton transfer. This observation appears to be in line with the high proton mobility that is found at oil-water interfaces, shown in the work of Zhang et al. [268] They showed via experiment and AIMD simulations of an interface of n-decane and water with an excess proton that the amphiphilic hydronium was attracted to the interface and retained high lateral mobility along the interface that exceed the bulk mobility for proton carriers.

Table 4.6: The top five most occurring hydrogen-bond networks around reactant and product during proton transfer for TEG-water mixtures. Protonated species (Z_{prot}), the previously protonated species (Z_{prev}), the hydrogen-bond atoms of the protonated species ($HB_{X,\,p}$ where x=A or D for accepting or donating a hydrogen bond, respectively), and the solvating atoms of Z_{prev} ($HB_{X,\,r}$ with the same definitions of x) are listed. Figure 4.4 gives graphical labeling. Proton rattling effects are included.

Functional	Z_{prot}	Z_{prev}	$HB_{A,p}$	$HB_{A,p}$	$HB_{D,p}$	$HB_{A,r}$	$HB_{A,r}$	$HB_{D,r}$	%	$\sum$ %
PW91[a]	H_3O^+	H_2O	H_2O	H_2O	...	H_2O	H_2O	...	15.19	15.19
	H_3O^+	H_2O	H_2O	H_2O	...	H_2O	H_2O	CH_2	14.82	30.02
	H_3O^+	H_2O	H_2O	H_2O	H_2O	H_2O	H_2O	...	14.25	44.26
	H_3O^+	H_2O	H_2O	H_2O	CH_2	H_2O	H_2O	...	11.52	55.79
	H_3O^+	H_2O	H_2O	H_2O	CH_2	H_2O	H_2O	H_2O	4.45	60.24
PBE[b]	H_3O^+	H_2O	H_2O	H_2O	...	H_2O	H_2O	...	21.12	21.12
	H_3O^+	H_2O	H_2O	H_2O	H_2O	H_2O	H_2O	...	15.96	37.08
	H_3O^+	H_2O	H_2O	H_2O	...	H_2O	H_2O	CH_2	7.55	44.63
	H_3O^+	H_2O	ROH	H_2O	...	H_2O	H_2O	...	7.40	52.03
	H_3O^+	H_2O	ROH	H_2O	H_2O	H_2O	H_2O	...	4.36	56.38
PBE+TS-vdW[c]	H_3O^+	H_2O	H_2O	H_2O	...	H_2O	H_2O	...	16.07	16.07
	H_3O^+	H_2O	H_2O	H_2O	H_2O	H_2O	H_2O	...	11.36	27.42
	H_3O^+	H_2O	H_2O	H_2O	CH_2	H_2O	H_2O	...	7.94	35.36
	H_3O^+	H_2O	ROR	H_2O	...	H_2O	H_2O	...	6.37	41.74
	H_3O^+	H_2O	H_2O	H_2O	...	H_2O	H_2O	H_2O	6.00	47.74

[a] 90 different hydrogen-bond networks found
[b] 99 different hydrogen-bond networks found
[c] 87 different hydrogen-bond networks found

The hydroxyl of TEG is present for PBE in Table 4.6 but not PW91. From Fig 2(d), it appears that PW91 would also have HB networks that contain hydroxyls. Yet, Tables 4.1 and 4.2 and Fig 2(d) together give the picture that when the excess proton is located on a water and approaches the hydroxyl group, the hydroxyl group has a higher probability to become protonated for the PW91 as opposed to only occupying the solvation shell for the PBE case. The ether of TEG shows a high probability for occupying the solvation shell for PBE+TS-vdW, seen previously in Table 4.5. However, since this species does not appear in Table 4.3, we believe this HB network to be present for proton rattling events and not for longer range, structural diffusion

proton transfer events. In the Appendix, we show all HB networks during proton transfer events for the bulk water (Tables L.1-L.4) and TEG-water mixtures (Tables L.5-L.7).

4.3.4 Mechanistic picture for proton transfer among water molecules.

One would also like to know the effect of TEG on the mechanistic picture of proton transfer for water-to-water hops. Previous studies [230, 247, 248] have shown that for proton transport in bulk water that, using the asymmetric stretch reaction coordinate (δ) to identify the most likely oxygen to receive a transferring proton, the hydrogen-bonding patterns of this oxygen and the protonated oxygen had great similarity, termed the "presolvation" concept, previously discussed. [69, 82, 83, 89] This analysis was further refined in a recent study [82] where, having knowledge of the entire trajectory, the focus was shifted from the atom most likely to receive a transferring proton instead to the atom that will receive the next transferring proton. In the work of Berkelbach et al. [82], the RDF of atom A relative to atom B, $g_{AB}(r)$, and corresponding integrated coordination number (ICN), $n_{AB}(r) = 4\pi\rho_B \int_0^r R^2 g_{AB}(R)dR$, where ρ_B is the number density of atom B, were sampled at intervals to give a time progression of these functions leading up to a proton transfer event. They showed that the presolvation concept retained validity under this refined analysis for the concerted mechanism of proton transfer. In bulk water, the importance of the hydronium ion accepting a hydrogen bond to initiate long range structural diffusion has been demonstrated in the work described by Berkelbach et al. [82] and again in recent work by Tse et al. [85] We employ this analysis for our system, comparing across different XC functionals and both for the bulk water and TEG-water mixtures. Figure 4.5 highlights the results using the PBE+TS-vdW XC functional for the TEG-water mixtures. The RDFs (Figures H.1-H.1 in Section H.1) and the ICNs (Figures H.5-H.8 and H.20) for proton transfer from water to water for bulk water, the RDFs for proton transfer from water to water (Figures H.9-H.11) and the ICNs for proton transfer from water to water (Figures H.12-H.13 and Figure H.21), from water to hydroxyl (Figures H.14-H.16), and from hydroxyl to water (Figures H.17-H.19) are provided in the Appendix Section H using all XC functionals. For all XC functionals, the water-to-water ICNs for bulk water show evidence of the "presolvation" concept.

In Fig. 4.5, we show the ICNs when proton rattling is excluded for the donating (Fig. 4.5(a)) and receiving (Fig. 4.5(b)) entities with the PBE+TS-vdW XC functional prior to the proton transfer event. Presolvation is captured in Fig. 4.5 by noting the similarity between the ICNs in the range associated with HBs of the donating and receiving entities in the time immediately preceding (20-0 fs) the proton transfer event. For the PW91 and PBE levels of theory, shown in Figures H.12 and H.12 in the Appedix Section H, respectively, the protonated oxygen clearly

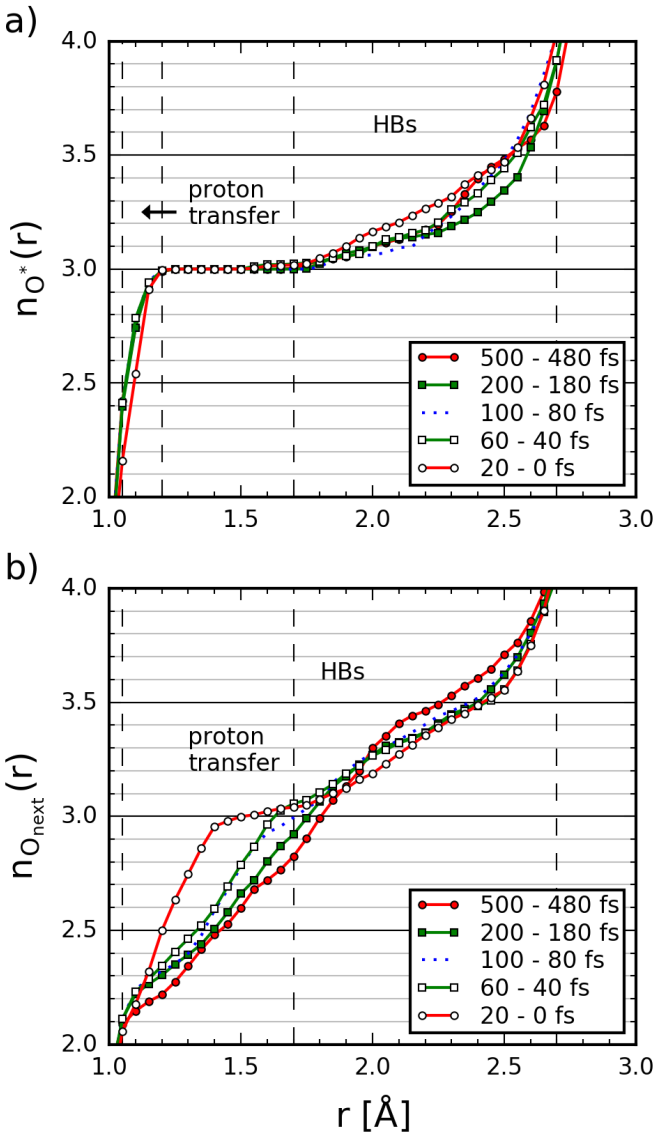


Figure 4.5: The ICNs using the PBE+TS-vdW XC functional for protonated oxygen in water (O* in (a)) and the next water oxygen to be protonated (O_{next} in (b)) averaged over 20 fs intervals long before proton transfer (500-480 fs) and leading up to proton transfer (200-180 fs, 100-80 fs, 60-40 fs, and 20-0 fs) at 300 K . The integration is over the RDF in Figure H.11 in the Appendix. Specific regions are marked for the proton transfer process and the change in the HB network. Proton rattling events are excluded.

gains a HB and the receiving oxygen clearly loses a HB. However, at the PBE+TS-vdW level of theory, we observe smaller changes in ICN in Fig. 4.5(a) for the protonated species and even less for the receiving oxygen in Fig. 4.5(b), indicating little difference in the solvation leading up to the proton transfer event. To explain the difference in solvation, we compared the ICNs in the range of 20-0 fs for PBE (Fig. fig:icnsTEGpbe) and for PBE+TS-vdW (Fig. 4.5). An explicit comparison of 20-0 fs ICNs for different XC functionals is given in Figure H.20 and Figure H.21 for bulk water and TEG-water mixtures, respectively, in Appendix Section H. We observe that the ICNs for PBE and PBE+TS-vdW are roughly equivalent at 20-0 fs prior to proton transport. Thus, for PBE+TS-vdW simulations, prior to the proton transfer the HB is already partially broken for the receiving oxygen and the HB that must be present for the protonated oxygen is already partially formed. This can be attributed to the softening of the HB network due to inclusion of dispersion effects for PBE+TS-vdW XC functional. The PW91 and PBE XC functionals over-structure the oxygen-hydrogen bond in H_2O, as seen previously in Fig. 4.2(b), compared to the PBE+TS-vdW XC functional, allowing the latter to have a persistent HB network that provides the necessary HB for the donating entity. Using the GGA-type XC functionals, we see that there is a larger dynamic change of the hydrogen bond network to either form or break a HB prior to the proton transfer event. Thus, an equivalent solvation is required for proton transfer, but the dynamics of the HB network leading up to this event are different due to including dispersion effects that soften the HB structures.

Overall, the ICNs for both the protonated water molecule and the protonated receiving water molecule were lower than the bulk water ICNs. This further supports the fact that the HB networks are different in the TEG-water mixture compared to bulk water, which we also observed in the analysis of the HB networks during reaction in Table 4.6. The reduction in the ICNs is consistent with Table 4.6 in that the most common HB networks found during reaction for any XC functional did not find a HB donor for either the protonated or previously protonated species.

4.3.5 Free energy profiles of proton transfer.

The free energy barriers for proton transfer between two water molecules have been calculated to determine the effects of TEG in the TEG-water mixtures. We first calculate the two-dimensional probability density functions, $P(R_{O^*O}, \delta)$, using the oxygen-oxygen distance (R_{O^*O}) between the oxygens of a water-water special pair and the asymmetric stretch (δ) as reaction coordinates to describe proton transport. An example of $P(R_{O^*O}, \delta)$ for proton transport between water molecules for a single PBE+TS-vdW XC functional simulation is shown in Fig. 4.6. In the Appendix, the plots for $P(R_{O^*O}, \delta)$ are shown for both bulk water (Figures I.1-I.4) and PW91 and PBE XC functional TEG-water mixtures (Figures I.5-I.5). Upon integrating over the R_{O^*O} coordinate, we have the one-dimensional probability density function of the

asymmetric stretch reaction coordinate, $P'(\delta)$. Since δ is the reaction coordinate that describes proton transport, we can calculate the free energy barrier as

$$\begin{aligned} \Delta F(\delta) = & -k_B T \ln \left[\int P(R_{O^*O}, \delta) dR_{O^*O} \right] \\ = & -k_B T \ln P'(\delta) \end{aligned} \tag{4.1}$$

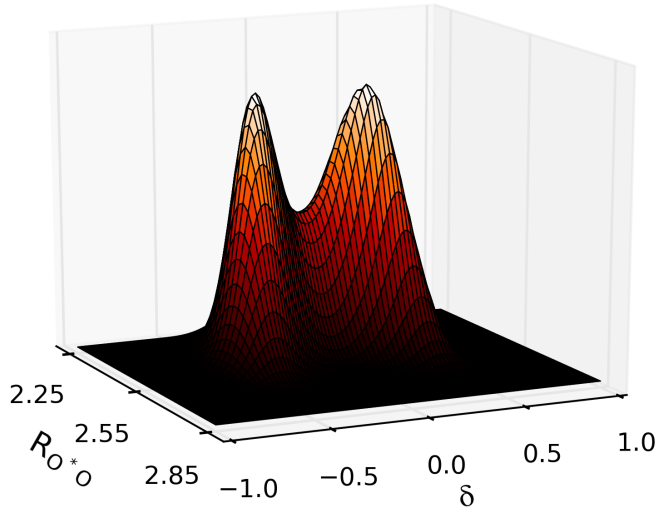


Figure 4.6: Probability density function of proton transfer for PBE+TS-vdW XC between water molecules in TEG-water mixture at 300 K. R_{O^*O} is the oxygen-oxygen distance and δ is the asymmetric reaction coordinate. The surface has been smoothed and z-axis made arbitrary.

The free energy barrier averages and standard deviations ($\pm\sigma$) were calculated to be 0.21 ($\pm$0.08), 0.38 ($\pm$0.07), and 0.42 ($\pm$0.13) kcal/mol for PW91, PBE, and PBE+TS-vdW, respectively. These averages and standard deviations were calculated using the 4-5 simulations for a given XC functional set. For our bulk water simulations, we found the free energy barriers of the single 50 ps simulations to be 0.26, 0.59, 0.40, and 0.64 kcal/mol for PW91, BLYP, PBE, and PBE+TS-vdW, respectively. The BLYP XC functional for bulk water was chosen to compare with previous results in the literature. [247,248] Thus, the free energy barriers of the TEG-water mixtures for the PW91 and PBE XC functional are equal to that of bulk water (within one σ) and the PBE+TS-vdW gives a lower free energy barrier in TEG-water mixtures compared to bulk water. In Fig. 4.7, we show the free energy profiles for visual comparison of bulk water to TEG-water mixture. Interestingly, by comparing the PBE and PBE+TS-vdW free energy profiles for TEG-water mixture in Fig. 4.7, the inclusion of dispersion effects are observed to increase the free energy barrier for

both TEG-water mixtures and bulk water. Yet, the PBE and PBE+TS-vdW free energy barriers for TEG-water mixtures do fall with one standard deviation of each other.

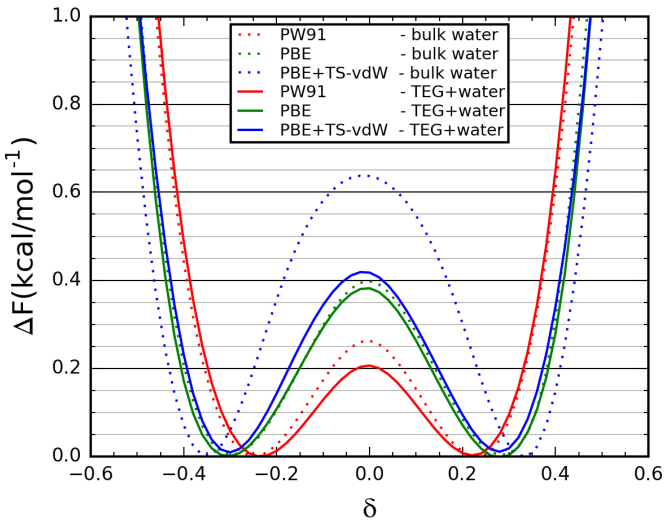


Figure 4.7: Free energy profile of proton transfer between water molecules in bulk water and TEG-water mixtures at 300 K using different XC functionals. The reaction coordinate δ is the difference of the HB distances for the shared proton (H^*) between the two oxygen atoms of the water molecules.

4.3.6 Kinetics of proton transfer among water molecules.

We investigate the effects of TEG on the kinetics of proton transport between water molecules by utilizing the population time correlation function (TCF) approach from the recent work of Chandra et al. [247,248] The formulation of these population TCFs is analogous to that of the previously derived hydrogen bond correlation functions and kinetics. [269,270] This approach has proven to be advantageous for a variety of proton transport mechanisms in hydrogen-bonded systems such as an excess proton and a hydroxide ion in water [247, 248, 271], an excess proton and a hydroxide ion in water-ammonia mixtures [272], and an excess proton in water-HCl mixtures. [273] Time scales of proton transfer and proton transfer rate constants are determined using both the history-independent, or intermittent, time correlation function, $C_i(t)$, and the history-dependent, or continuous, time correlation function, $C_c(t)$. To construct these time correlation functions (TCFs), we define the population functions $h(t)$ and $H(t)$. We denote the protonic defect species atom as O^*. Then, we define $h(t) = 1$ if a specific oxygen atom is O^* at time and $h(t) = 0$ otherwise. $H(t) = 1$ if an atom is O^* for a time interval t, given that the atom was initially O^* at the beginning of

the interval. Then, using these population functions, we can define our intermittent TCF as

$$C_i(t) = \frac{\langle h(0)h(t)\rangle}{h} \tag{4.2}$$

Thus, $C_i(t)$ gives us the probability that an atom that was O^* at $t = 0$ will be O^* at t, without regard to proton transfer events in the interval t. The continuous TCF is defined as

$$C_c(t) = \frac{\langle h(0)H(t)\rangle}{h} \tag{4.3}$$

which gives the probability that an atom that was O^* at $t = 0$ will remain O^* on the time interval t. Importantly, from $C_c(t)$, we can directly calculate the average exchange time of O^*, τ_{exch}, as

$$\tau_{exch} = \int_0^\infty C_c(t)dt \tag{4.4}$$

In Fig. 4.8(a) and (b), we show $C_i(t)$ including and excluding proton rattling events, respectively, for all XC functionals used for both bulk water and TEG-water mixture. Similarly, in Fig. 4.9(a) and (b), we show the same plots for $C_c(t)$. When rattling is included in $C_c(t)$, such as in Fig. 4.9(a), ultrafast processes are accessible such as short lived complexes that exist in bulk water measured by femtosecond vibrational spectroscopy. [81] However, experimental research continues [80] to determine what complexes are short-lived and what are metastable, discussed more below. By excluding proton rattling, we analyze the time scale for true charge displacements via structural diffusion in the system. The difference between including and excluding proton rattling is less for $C_i(t)$ compared to $C_c(t)$ due to the continuous-time-independence of $C_i(t)$.

Previously, it has been thought that the interconversion from Zundel to Eigen configurations was an ultrafast process on the sub-100 fs timescale. [81] However, in recent experimental work by Thämer et al., [80] ultrafast two-dimensional (2D) IR spectroscopy was used to probe the lifetime of the Zundel proton complex and suggested that the Zundel configuration is not merely a transition state between Eigen configurations but a metastable configuration that has a lower limit lifetime of 480 fs. The reader is encouraged to consult a recent article [79]for further discussion of the impact of the work by Thämer et al., its contrast to theoretical results, and the future role of 2D infrared spectroscopy in further unraveling the elusive proton complexes in water. From the current work, our analysis of TCFs is consistent with ultrafast processes on the sub-100 fs timescale. [81]

The slow and fast decay times, τ_{slow} and τ_{fast}, respectively, associated with proton transfer can be well defined by a biexponential function fit of $C_c(t)$.

$$C_c(t) = \alpha_{slow} \mathrm{e}^{\frac{-t}{\tau_{slow}}} + \alpha_{fast} \mathrm{e}^{\frac{-t}{\tau_{fast}}} \tag{4.5}$$

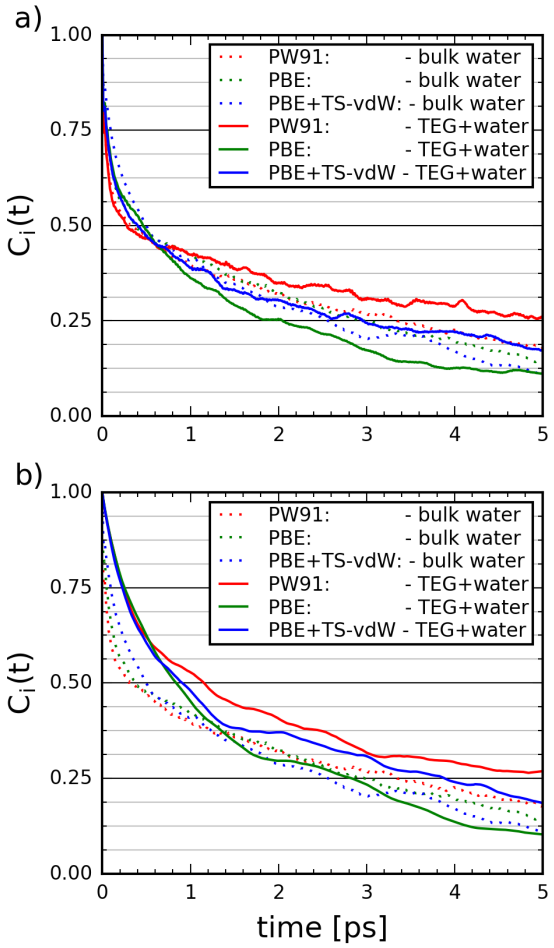


Figure 4.8: Intermittent time correlation functions for protonic defects in bulk water and TEG-water mixtures. (a) Proton rattling included. (b) Proton rattling excluded.

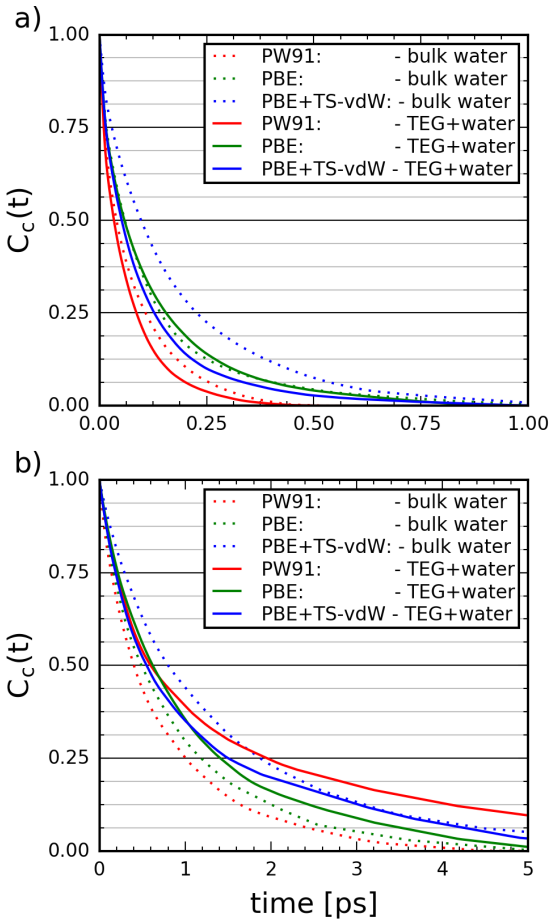


Figure 4.9: Continuous time correlation functions for protonic defects in bulk water and TEG-water mixtures. (a) Proton rattling included. (b) Proton rattling excluded. Note the difference in the scale of the x-axis from (a) to (b).

with $\alpha_{slow}+\alpha_{fast} = 1$. Similarly, from Eq. (16) and (17) of the work by Tuckerman et al. [248], we can also fit a bi-exponential to $C_i(t)$ to determine parameters a_0, a_1, and a_2 in Eq. (4.6) below to then determine the forward rate constant for proton transfer, k_1^{PT}, in Eq. (4.7) below.

$$C_i(t) = \alpha_0 \mathrm{e}^{-\alpha_1 t} + (1-\alpha_0)\mathrm{e}^{-\alpha_2 t} \tag{4.6}$$

$$k_1^{PT} = \alpha_0\alpha_1 + \alpha_2(1-\alpha_0) \tag{4.7}$$

This bi-exponential decay model for $C_i(t)$ of proton transport in water has shown to be in good agreement up to approximately 30 ps. [247, 248, 271] However, the work of Chen et al. [271] showed that approaching the long-time limit, $C_i(t)$ initially displays an exponential decay (t < 30 ps), then transitions to slower, non-exponential decay (30 ps < t < 100 ps), and finally reaching power law decay at the asymptotic limit (t > 100 ps). Yet, the simulations in the work presented here are far from reaching this power law asymptotic limit and well within the exponential decay regime.

In Table 4.7 and Table 4.8, the kinetics for proton transfer are presented for bulk water and TEG-water mixtures, respectively. We have computed τ_{exch} via Eq. (4.4), τ_{fast}, τ_{slow}, and α_{slow} via eq (4.5), and $\frac{1}{k_1^{PT}}$ via Eq. (4.6) and (4.7) (including parameters for fitting α_0, α_1, and α_2). For bulk water in Table 4.7, the fast time scale associated with including proton rattling events gives lifetimes, τ_{fast}, < 100 fs for XC functionals that display bi-exponential decay behavior, in agreement with experiment [81] and previous simulation [82, 248] results. The only outlier that had exhibited simple exponential decay was the PBE+TS-vdW, which still displayed decay lifetimes of 160 fs. The exchange lifetimes qualitatively agree with previous simulation results. [248] The difference is most likely due to the lighter mass of the hydrogen atom used in the present simulations (here, using the mass of hydrogen instead of deuterium). The exchange lifetime appears to be $\tau_{exch} \approx 1$ ps for all four XC functionals when analyzing the kinetics associated with structural diffusion via excluding proton rattling. The shortest lifetime appears to be for PW91, with $\tau_{exch} = 0.73$ ps and the longest lifetime is for PBE+TS-vdW, with $\tau_{exch} = 1.39$ ps. These lifetimes are consistent with those in Table 4.1 and the free energy barriers observed in Fig. 4.7 for PW91 and PBE+TS-vdW in bulk water.

From Table 4.8, there is a noticeable effect when incorporating TEG, specifically in the exchange lifetimes for excluded proton rattling, thus time scales for structural diffusion. For the PW91 XC functional, there is an increase in exchange lifetime from bulk to TEG-water mixtures. This is caused by an increase in the slow process lifetime. The PBE XC functional lifetimes also increase going from bulk water to TEG-water mixtures but with a much smaller change in the lifetime, being 1 ps for both bulk water and TEG-water mixtures. The PBE+TS-vdW functional lifetimes decrease going from the bulk water to the TEG-water mixtures. However, we see that this is due to contamination of the fast process since α_{slow} decreases to 60%, implying an increase in the effect of the fast dynamic processes associated with τ_{fast}. Overall,

Table 4.7: Kinetics of aqueous H^+ system. Relaxation times, parameters and inverse rates (in ps) for H^+ including and excluding rattling events.

Functional	Rattling	τ_{exch}	α_{slow}	τ_{fast}	τ_{slow}	$\frac{1}{k_1^{PT}}$	α_0	$\frac{1}{\alpha_1}$	$\frac{1}{\alpha_2}$
PW91	Included	0.08	0.71	0.01	0.10	0.40	0.32	13.77	0.27
	Excluded	0.73	0.71	0.18	0.96	0.98	0.22	15.67	0.76
BLYP	Included	0.17	0.24	0.09	0.42	0.26	0.57	2.37	0.11
	Excluded	0.94	0.96	...	1.00	1.05	0.09	14.58	0.96
PBE	Included	0.12	0.43	0.05	0.21	0.16	0.56	3.59	0.07
	Excluded	0.89	1.00	...	0.83	0.50	0.70	3.09	0.15
PBE+TS-vdW	Included	0.17	1.00	...	0.16	0.36	0.53	3.53	0.17
	Excluded	1.39	0.70	0.46	1.82	1.30	0.65	3.20	0.46

the TEG-water mixture shows an increased lifetime for proton transfer using the PW91 XC functional due to an increase in slow processes associated with structural diffusion and shows relatively little change in the lifetimes for PBE and PBE+TS-vdW XC functionals, with only slight decrease being accounted to the decrease of the fast processes associated with proton rattling events for PBE+TS-vdW.

Table 4.8: Kinetics of aqueous H^+ and triethylene glycol (TEG) system. Relaxation times and inverse rates (in ps) for H^+ including and excluding rattling events.

Functional	Rattling	τ_{exch}	α_{slow}	τ_{fast}	τ_{slow}	$\frac{1}{k_1^{PT}}$	α_0	$\frac{1}{\alpha_1}$	$\frac{1}{\alpha_2}$
PW91	Included	0.06	0.74	0.01	0.08	0.10	0.51	6.81	0.05
	Excluded	1.71	0.43	0.43	3.50	1.01	-2.08	3.12	3.12
PBE	Included	0.12	0.64	0.02	0.17	0.35	0.55	0.20	3.61
	Excluded	1.05	1.00	...	1.02	1.01	0.50	0.50	3.53
PBE+TS-vdW	Included	0.10	0.56	0.03	0.15	0.19	0.52	4.00	0.09
	Excluded	1.17	0.60	0.30	1.84	0.68	0.62	3.90	0.26

4.3.7 Hopping dynamics and mean square displacements for proton transport

The displacement of the protonic defect throughout the trajectories was extracted to determine 1) the observation of burst-rest dynamics previously discussed and 2) the mean square displacements (MSDs) for the protonated atom. For all TEG-water mixture MSDs of the protonated atom, we have not yet reached the linear regime where reliable self-diffusion coefficients based on the Einstein relation can be calculated. We reserve this for a future effort where reliable values can be reported.

Figure 4.10 shows the proton hopping dynamics via displacement of the protonated atom relative to the initial position of the first protonated atom in the trajectory for selected trajectories of the XC functional simulation sets. The red line indicates trajectories that display an overall "rest" behavior during the simulation while the

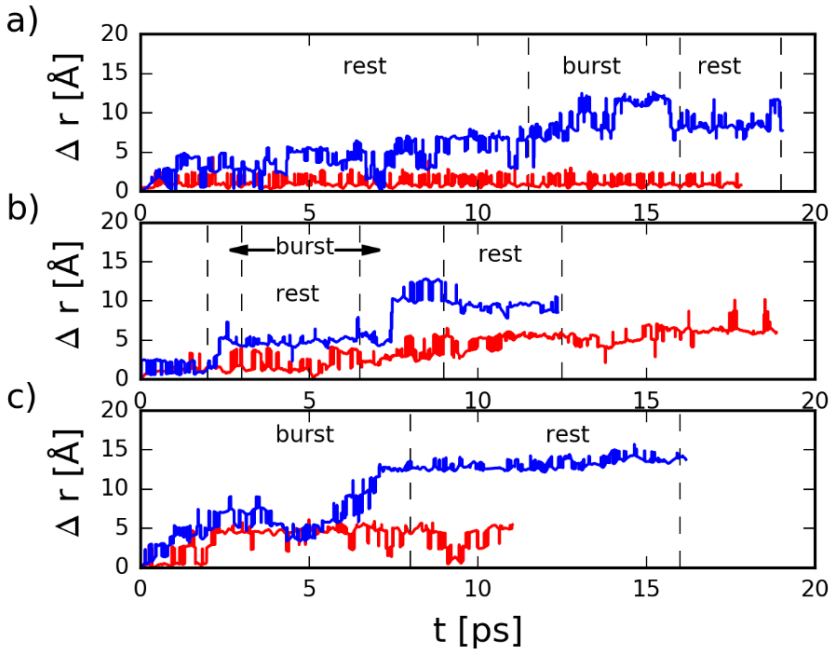


Figure 4.10: The distance for the atom (O*) that has the protonic defect relative to the initial position of the first protonated atom in TEG-water mixture for selected simulation trajectories for each of the XC functionals (a) PW91, (b) PBE, and (c) PBE+TS-vdW at 300 K. The trajectories were selected based on the red trajectory being an example of a trajectory that mostly contains "rest" dynamics and the blue trajectory displaying both "burst-and-rest" dynamics. The horizontal lines and labels for burst and rest sections annotate only the blue trajectory and are to help guide the reader and highlight each section.

blue line indicates trajectories that show burst-rest dynamics, similar to recent simulation work of an excess proton in bulk water. [85, 86] Previous work showed that rest periods consisted of long-lived proton traps, being > 5 ps. [86] We do observe such long rest dynamic period in our simulations, specifically in the PW91 functional simulations in Fig. 4.10. The length of burst periods and rest periods seem to be shorter for our protonated atom in TEG-water mixtures compared to the displacements of the hydronium oxygen in bulk water in Fig. 2 of Tse et al. [85] Yet, our simulation lengths are almost an order of magnitude shorter, in exchange for increasing number of trajectories per XC functional. We believe extended simulations of the present trajectories would be required before a conclusion on whether the TEG-water mixture could shorten these burst and rest periods relative to those observed in bulk water. The observance of trajectories with either a long-lived rest period or that have occurrences of burst and rest periods seems overall to be less dependent of the XC functional used and more dependent on initial conditions of the trajectory and simulation length. Emphasis is placed on using a number of trajectories for these types

of analysis due to the variety of burst-rest dynamic behavior that can be observed during a simulation and the long length that these periods can have, such as rest periods for 100 ps of the excess proton in bulk water simulation observed in Fig. 2 of Tse et al. [85] The Appendix Section J presents all trajectories for all XC functionals of TEG-water mixtures (Figure J.1) and bulk water (Figure J.2) for comparison of burst-rest dynamics in different simulation trajectories and XC functionals used. Similar burst-rest behavior is displayed for all XC functionals tested for bulk water.

In Figure 4.11, the average MSDs over all trajectories for a given XC functional set are shown. The MSDs are extended to the longest time length simulated for a given XC functional set, implying that average over all the simulations was guaranteed up to 10 ps, since this was a minimum for simulated time length. Yet, past 10 ps, only a subset of all trajectories were used for the averaging. We note that the PW91 XC functional set has the MSD with the smallest slope, which can be attributed to the long rest behavior seen in the trajectories shown in Figure 4.10 and Figure J.1. Included in Appendix Section J are the MSDs of each individual simulation trajectory and the corresponding average MSDs using only 10 ps of each trajectory in Figure J.3 and the bulk water MSDs in Figure J.4.

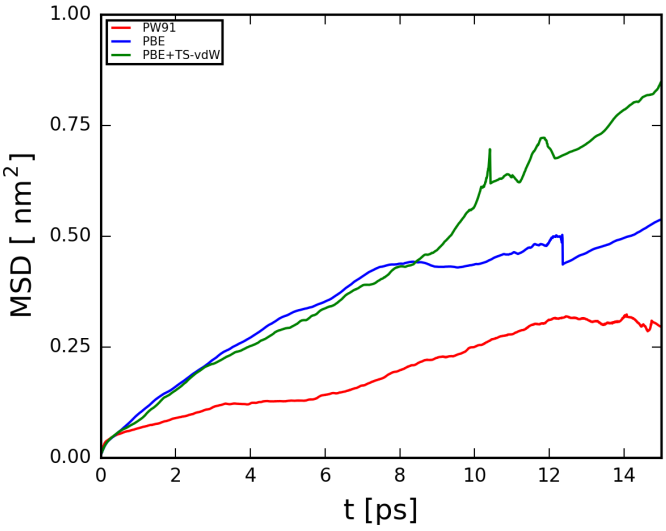


Figure 4.11: The average mean squared displacements (MSDs) of the protonated atom (O*) versus time in TEG-water mixture for each XC functional at 300 K. The average MSDs were averaged out to the longest time length simulated for the XC functional set but with averaging over only a subset of all MSDs after 10 ps.

Chapter 5

Reactive Molecular Dynamics Simulations of an Excess Proton in Aqueous Triethylene and Polyethylene Glycol Solutions

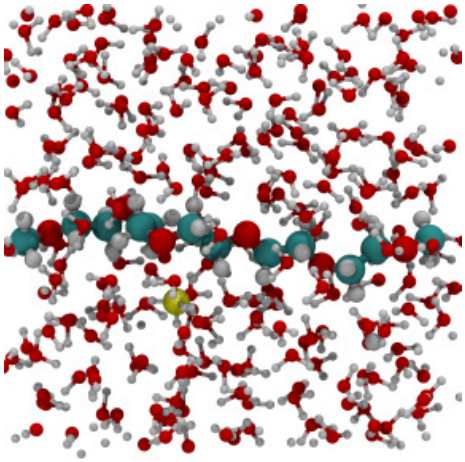


Figure 5.1: Snapshot of excess proton in aqueous polyethylene glycol solution with infinite chain (linked across periodic boundary), where water molecule with excess proton has a yellow oxygen atom.

5.1 Introduction to the Reactive Force Field: ReaxFF

The reactive force field (ReaxFF) platform contains all essential ingredients to accurately to model various dissociation pathways and the formation of chemical bonds in molecular simulations without the need for a quantum treatment of the

system. ReaxFF is similar to AIMD in that it is able to model bond breaking and formation but, unlike AIMD, uses classical mechanics as opposed to quantum mechanics for calculating the potential energy surface. The former quality allows it to describe a variety of chemical reactions of interest that can take place during the simulation and the latter quality allows it to do so for larger spatial and temporal scales than those computationally possible for AIMD simulations. Specifically, ReaxFF has been used extensively to describe proton transfer dynamics across a wide range of materials, including an excess proton in water. [200] The force field combines a bond order/bond distance relationship with a polarizable charge description and many-body interactions (also, with bond-order dependence). The combination of covalent and Coulomb interactions has made ReaxFF applicable to a wide range of materials, including covalent and metallic systems in an aqueous environment.

The key to the accuarcy of the ReaxFF force field is in its parameterization/optimization for properties of interest. One begins by first constructing a dataset from either experimentally available data, from ab initio/quantum mechanical (QM) calculations, or a combination of both. The dataset is then split into two parts, one used for training the force field (the training set) and the other part is left to validate the force field (the validation set) to ensure its transferability and that one does not over-fit the parameters. Then, one uses the training set to adjust given parameters of the ReaxFF force field to reproduce the QM or experimental data. The parameterized force field is then used to calculate the valdiation dataset to detemine its accuracy. The ReaxFF methodology has previously been used to parameterize force fields able to describe liquid water and reactions involving proton transfer in small H_2O clusters and the water phase. [7] Since the ReaxFF water potential is fully compatible with previous parametrizations, reactive MD simulations of a wide range of complex chemical processes in the aqueous phase are possible. The van Duin group are a central repository for current ReaxFF force fields due to their continuous work to derive, develop and update ReaxFF parameterizations for different classes of materials.

From correspondence with the van Duin group, it was determined that the optimal intitial ReaxFF force field for our xsPCHD/PEG system would be the Monti et al. [6] ReaxFF force field for glycine. We have used this force field to carry out initial reactive MD simulations of H^+ in bulk water, aqueous TEG solutions, and aqeuous PEG solution with the PEG chain made infinite by connection across the periodic boudary conditions. We found that H^+ tightly bound to the hydroxyl and ether groups, in contrast to experiment and our previous work described in Chapter 4. Thus, the Monti et al. ReaxFF force field did not appear to accurately describe H^+ in aqueous TEG or PEG solutions without parameterization. In order to do so, we have carried out development to update this ReaxFF force field to accurately describe H^+ in aqueous PEG solutions as a necessary step to perform reactive MD modeling and simulation of xsPCHD/PEG PEM membranes.

5.2 Development of ReaxFF for H^+ in Aqueous PEG Solutions

5.2.1 Quantum Mechanical Calculations on Model Systems

To generate the training and validation sets, we carried out quantum mechanical calculations for ethylene glycol and diethylene glycol, show in Figure 5.2, as single molecules and hydrated with water clusters of $n H_2Os = 1-5$, both with and without protonation. The protonated structures have the H^+ located on the hydroxyl groups of ethylene glycol and both the hydroxyls and ether of diethylene glycol to focus the training to accurately describe the correct binding strength to these groups. All quantum mechanical calculations were carried out using the NWChem software suite, [274] launched inside the Atomic Simulation Environment, [275, 276] a set of Python-based tools and modules used to help create a workflow for automated calculation and training set file generation for our parameterization/optimization steps. Geometry optimizations, bond dissocation energies and proton transfer calculations were carried out in the gas phase using DFT with the B3LYP exchange-correlation hybrid functional [277] using the Pople 6-311++G(2d,2p) basis set. [278] The B3LYP/6-311++G(2d,2p) was used due to providing accurate energies for the ion hydration reactions found in previous work on evaluation of density functionals for neutral, protonated and deprotonated water clusters. [279] An ultrafine numerical integration grid was used for all QM calculations, corresponding to a target accuracy of 10^{-8} hartree. Approximately 800 QM calculations were completed in total. This gave a sufficient dataset to train the ReaxFF force field to describe H^+ in aqueous PEG solution and also provide a robust validation set.

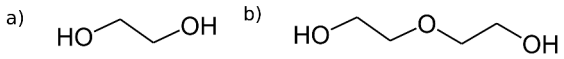


Figure 5.2: The polymers (a) ethylene glycol and (b) diethylene glycol used for the quantum mechanical calculations to generate the training and validation sets.

5.2.2 Parameterization and Validation

The van Duin group currently performs ReaxFF parameter development using a straightforward, single-parameter parabolic search method. [280] This method has a high level of transparency, allowing one to determine sensitivity of a single parameter against the entire training set fitting. However, given the complex force-field energy landscape and possible implicit parameter correlations, this method risks convergence to a local energy minima versus a global energy minima. [200] Recent research has focused on developing more sophisticated parameter sampling methods, specifically making use of evolutionary algorithms. In particular, genetic algorithms (GA) have

shown to be advantageous in developing a parameterization method that is capable of performing global optimization in a scalable, parallel fashion. [138, 281–283] They show promise for reducing force-field development time, as well as for making the process more accessible to nonexpert users. [200]

For our current work, we have utilized the Genetic Algorithm based Reactive Force Field optimizer (GARFfield) code developed from the work of Jaramillo-Botero. [138, 139] GARFfield is a multi-platform, multi-objective parallel hybrid genetic algorithm (GA) / conjugate-gradient (CG) based force field optimization framework. It uses the LAMMPS MD engine [153, 154] at its core for force field calculations and is able to parameterize multiple types of potentials for simulations, including embedded-atom methods (EAM), [284] charge-optimized many-body (COMB) potentials, [285] ReaxFF potentials, general coarse-grained potentials, and also pseudopotentials for describing core electrons in AIMD methods, previously used in Chapter 4. It uses an evolutionary algorithm to optimize the force field parameter sets, with user-defined limits and options to guide the force field parameterization given physical reasoning and insight to the system.

The previous version of the ReaxFF force field has been well parameterized against an extensive set of DFT and coupled-cluster theory calculations and is capable of accurately describing the oxygen-oxygen and oxygen-hydrogen RDF of water and reproduce the experimentally measured self-diffusivity of H^+ in water. [7] To narrow the search space and not compromise the previous force field parameterization for water, a subset of parameters was refitted against our current DFT calculations. Specifically, the C/O bond and C/O/H angle parameters were varied in order to accurately describe the strength of interaction between the acidic protons and the ether/hydroxyl groups of the PEG chains. A similar approach has been used previously to develop an accurate ReaxFF force field of glycine on TiO_2 surfaces for the Ti/O/H and Ti/N/H interactions. [286] None of the parameters associated with the water part of the force-field were changed, discussed more in section 5.3. Initially, 23 parameters that describe the C/O bond and C/O/H angle were used with only a $1 - 2\%$ margin of change allowed for each optimization iteration. Each iteration consisted of 25 steps where the force field parameters were evolved at each step to generate new force field parameters. A force field is selected for reproduction based on its fitness, or reduction in the overall error for comparison against the training set. At each iteration, crossover occurs where bits are taken from parent force field parameters and they are combined to create sibling force fields, where the crossover rate was taken to be 0.85. A total of 20 iterations were carried out, giving a total of 500 evolutionary steps. The force field parameters were monitored during each optimization process to ensure the reduction in training set error proceeded as expected. Each force field produced after each optimization iteration was used to run a separate water MD simulation simultaneously with the training development to ensure the oxygen-oxygen and oxygen-hydrogen RDFs were not affected. The best force field based on the above optimization process was then used to calculate against the energies and structures of the QM validation set.

For part of our training, we calculated the deprotonation minimum energy pathway of the hydroxyl group of diethylene glycol in the presence of 5 water molecules. The energy profile of transfer from the hydroxyl group to a second water is shown in Figure 5.3. The comparison is made between the current ReaxFF and both the QM data and the previous Monti et al. [6] ReaxFF parameterization. It is apparent that the previous ReaxFF implementation predicts a preferential binding in the figure, contrary to experiment [255] and our previous work in Chapter 4. We see that we have corrected this overly-bound interaction in our current parameterization.

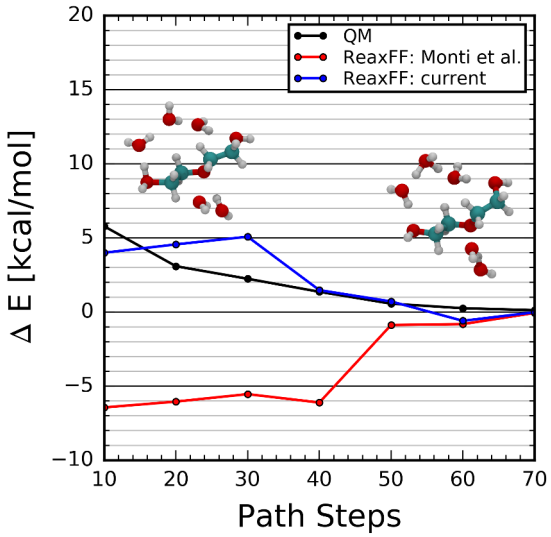


Figure 5.3: Energy profile for deprotonation of hydroxyl group for hydrated diethylene glycol (5 H_2O). Comparison to B3LYP/6-311++G(2d,2p), previous ReaxFF from work of Monti et al., [6] and our current re-parameterized ReaxFF. Energy difference is compared to optimized geometry for the final protonation of the distant water molecule.

We also show in Figure 5.4 our comparison to the validation dataset for the proton transfer pathways from the ether and hydroxyl group of diethylene glycol in the presence of 3 water molecules. We have the transfer from both hydroxyl groups in Figure 5.4(a-b) and the proton transfer for the ether group in (c). We observe that the ReaxFF is in good agreement with the QM validation dataset, implying that we have re-parameterized the ReaxFF in a transferable manner such that we can accurately calculate other proton transfer pathways not explicitly trained against.

With our ReaxFF force field re-parameterized, we are able to perform reactive MD simulations of H^+ in aqueous PEG at larger temporal and spatial dimensions than those accessible to the AIMD simulations of Chapter 4.

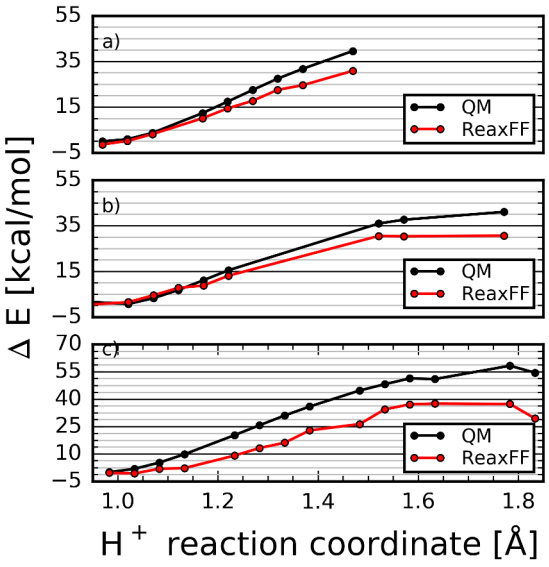


Figure 5.4: Energy profile for proton transfer to ether group for hydrated diethylene glycol (3 H_2O). Comparison between B3LYP/6-311++G(2d,2p) and our current re-parameterized ReaxFF. Energy difference is compared to equilibrium proton bond to water molecule.

5.3 Simulation Setup and Details

We carry out reactive MD simulations of three different systems: 1) H^+ in bulk water to determine that we can still accurately calculate the RDFs and H^+ diffusivity, 2) H^+ in aqeuous TEG solution to make parallel comparisons to our previous work and 3) H^+ in an aqueous PEG solution where the PEG chain is made infinite by connecting a six monomer chain across the periodic boundary conditions. The chain is oriented such that the backbone is parallel to the x-axis of the simulation box. For the bulk water simulations, we perform both a simulation with our current ReaxFF force field and also a small simulation with the Monti et al. [6] ReaxFF force field for comparison. The bulk water for the previous ReaxFF was performed in a small simulation of 32 water molecules with one excess H^+. Our current ReaxFF force field implementation uses 100 water molecules with one excess H^+. The volume for both was made so that the density was 1.0 g/cm^3. The aqueous TEG solution was modeled by replacing 8 of the water molecules in the bulk water simulation with the TEG chain, giving 92 water molecules, one TEG chain, and one excess H^+. The box length was increased slightly to accommodate the TEG chain, giving a density of 0.985 g/cm^3. The infinite chain PEG system was make up of 250 water molecules, one six monomer chain, and one excess H^+. We used a timestep of 0.20 fs and a cubic simulation box for all simulation setups. The initial cordinates of the system were prepared using using the PackMol packing optimization software. [287]

For equilibration, the systems were first subject to energy minimization, followed by 100 ps of NVT ensemble MD. For the minimization, an energy convergence threshold of 10^{-6} kcal/mol was used. The Berendensen thermostat [288] was used for the NVT equilibration with a 100 fs relaxation timelength. After the NVT equilibration, the total linear momentum of all atoms in the system was set to zero. This was followed by data production using the NVE ensemble for 100-200 ps.

5.4 Results and Discussion

We first began by determining how well our parameter set can model water in our system. In Figure 5.5, we have the RDFs for both the (a) oxygen-oxygen and (b) oxygen-hydrogen for the bulk water simulations. We compare our outcome to the results from previous work of van Duin et al. [7] for bulk water simulations of 800 water molecules in the NVE ensemble at 300 K for 100 ps simulations. In the same reference, comparison is made to experimental RDFs, also shown here. Finally, we show the results from our smaller 32 water molecule system using the Monti et al. parameters and our current re-parameterized ReaxFF force field results for the 100 water molecule system. Our simulations include the excess H^+ in the system also. This does not appear to have a large impact on the results. We see that our current ReaxFF parameter set still accurately reproduces the correct oxygen-oxygen and oxygen-hydrogen distances.

We have also calculated the RDFs for the oxygen of water with the oxygen of other water molecules in the aqueous TEG and PEG solutions. In Figure 5.6(a), we show both of these with the bulk water simulation, also. We can see that there is no strong change in the water structure for incorporating TEG or PEG into solution. This is mostly due to the strong hydrophilic character of PEG and is similar to the RDFs we calculated previously for the AIMD simulations in Figure 4.2. Figure 5.6(b), we have the RDFs for the oxygen of water with the oxygen of the ether groups of TEG and PEG. Interestingly, we see that the TEG solution has two distinct solvation shells occuring at $\approx 3\mathring{A}$ and at $\approx 4\mathring{A}$, respectively, while the PEG solution only has a single, larger solvation shell at $\approx 4\mathring{A}$. In Figure 5.6(c), the carbon of the TEG and PEG chains both show no strong change between the two solutions and have a similar peak height to that of the ether group of TEG in Figure 5.6(b). The oxygen of the hydroxyl group of TEG is shown in Figure 5.6(d), with a peak height closer to the water-water RDF but with the characteristic solvation peaks comparable to the ether and carbon RDFs.

In Figure 5.7(a), we show the oxygen of the protonated water with the oxygen of other water molecules. Comparing to Figure 4.2(c), our peaks incicating solvation shells occur at similar distances ($\approx 2.5\ \mathring{A}$ and $\approx 4.0\ \mathring{A}$, respectively). Yet, our first solvation shell peak is approximatly two-fold the peak height of the most structured AIMD result. The second peak has a similar peak height compared to the DFT results. Another interesting feature is the intermediate, shoulder peak that occurs at

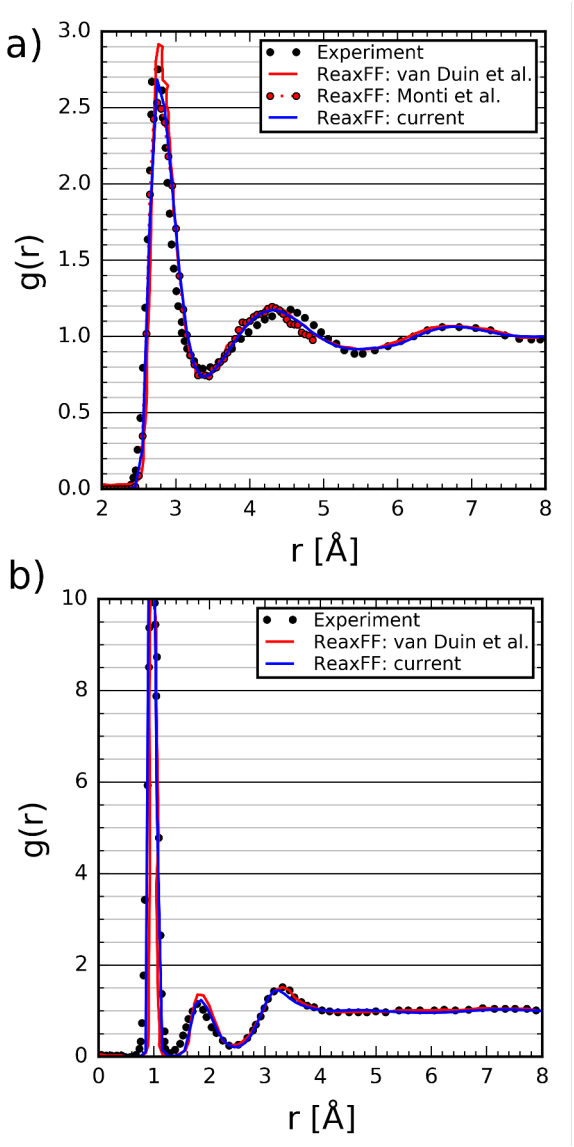


Figure 5.5: The ReaxFF and experimental results from van Duin et al. [7], the results from our own simulations using the Monti et al. ReaxFF parameterization and our current re-parameterized ReaxFF results for both (a)Oxygen-Oxygen, and (b) Oxygen-Hydrogen RDFs for bulk water. The van Duin ReaxFF RDFs were obtained for an 800-water system for 100 ps simulations. Our ReaxFF RDFs were from a 100-water system with one excess $H^+$from 200 ps simulations. Both were simulated using the NVE ensemble and a temperature of 300 K

≈ 3.0 $\mathring{A}$. This may be correlated to the larger first peak height, indicating that there is a separation, or splitting, of the first peak. This may be over-structuring aroud the hydronium ion and causing intermediate to outer-first peak waters to be pushed farther out to a secondary, intermediate peak height. This may be an aphysical

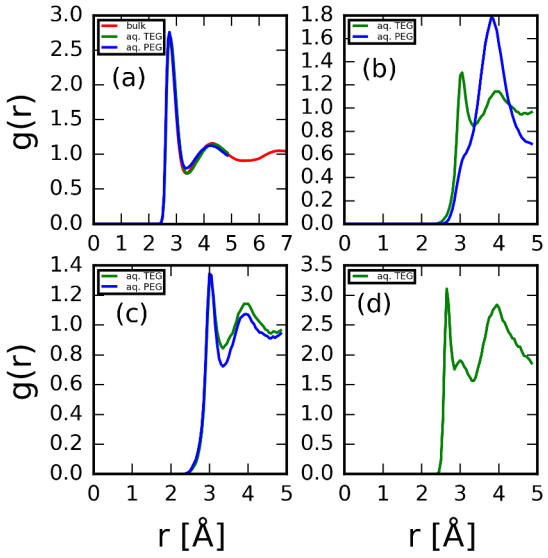


Figure 5.6: The radial distribution functions of the water oxygen in bulk water, aqueous TEG and PEG solutions at 300 K. The different figures are as follows: (a) O (water)-O (water), (b) O (water)-O(ether), (c) O (water)-C(CH_2), and (d) O (water)-O(hydroxyl.

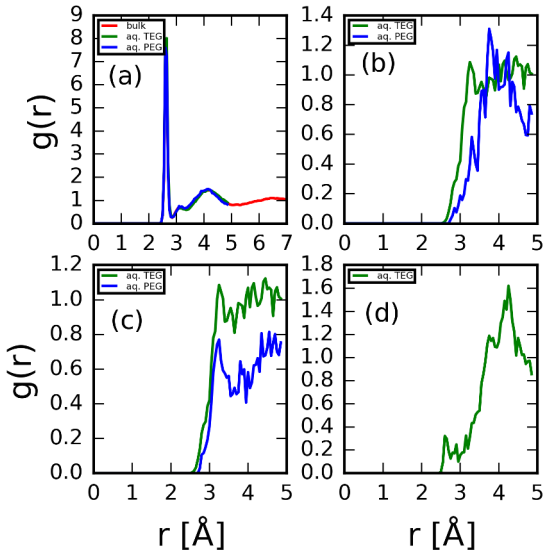


Figure 5.7: The radial distribution functions of the protonated water oxygen in bulk water, aqueous TEG and PEG solutions at 300 K. The different figures are as follows: (a) O (hydronium)-O (water), (b) O (hydronium)-O(ether), (c) O (hydronium)-C(CH_2), and (d) O (hydronium)-O(hydroxyl.

feature of the model that requires a higher level of theory or experimental spectra to compare against. We see that for the oxygen of the ether, the carbon backbone, and the hydroxyl group of TEG and PEG, in Figures 5.7(b)-(d), respectively, that the protonated oxygen does not show strong preference to any of these groups due to the small peak height. Interestingly, from Figure 5.7(b) and (c), there is no strong change in the distance of the protonated oxygen to the ether and carbon backbone of TEG or PEG.

Similar to our previous work, we have determined the free energy barrier of proton transfer between water molecules based on Equation 4.1. We see that there is no correlation to change in the free energy of proton transfer with the presence of TEG or PEG in the system, with all free energy barrier ≈0.80 kcal/mol. Compared to Figure 4.7, we see that our ReaxFF parameterization predicts a larger free energy barrier than that from the AIMD simulations. We note that it has been show that including nuclear quantum effects in the modeling of proton transport in water causes a large reduction in the free energy barrier calculated using QM methods, making it essentially barrier-less at room temperature. [230] We can determine that any increase in proton mobility due to the presence of PEG is not from a reduction in the free energy barrier based on Figure 5.8.

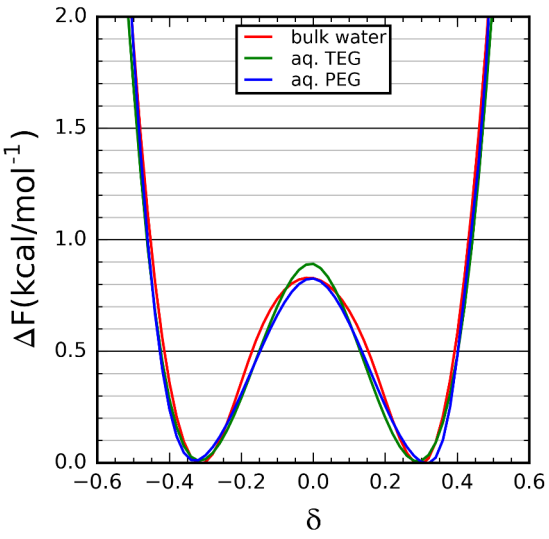


Figure 5.8: Free energy profile of proton transfer between water molecules in bulk water, aqueous TEG, and aqueous PEG solutions at 300 K. The reaction coordinate δ is the difference of the HB distances for the shared proton (H^*) between the two oxygen atoms of the water molecules.

We explore the differecne in proton hopping dynamics via displacement of the protonated atom relative to the initial position of the first protonated atom in the trajectory in Figure 5.9. We see that the characteristics of burst-rest dynamics are still present in the hopping displacements. Burst behavior is shown in the bulk water

trajectory for the range of 120 ps to the end of the trajectory. Rest behavior is observed for the aqueous TEG trajectory in the range of 80 ps to approximately 120 ps, giving a long-lived 40 ps proton trap, similar to the work of [85]. Interestingly, the aqueous PEG solution does not display any strong rest behavior and has the largest slope up to the first 100 ps of trajectory for all systems. It appears that the aqueous TEG solution has more rest behavior compared to the bulk water or the aqueous PEG solution, where the PEG solution has similar burst behavior to bulk water, if not more.

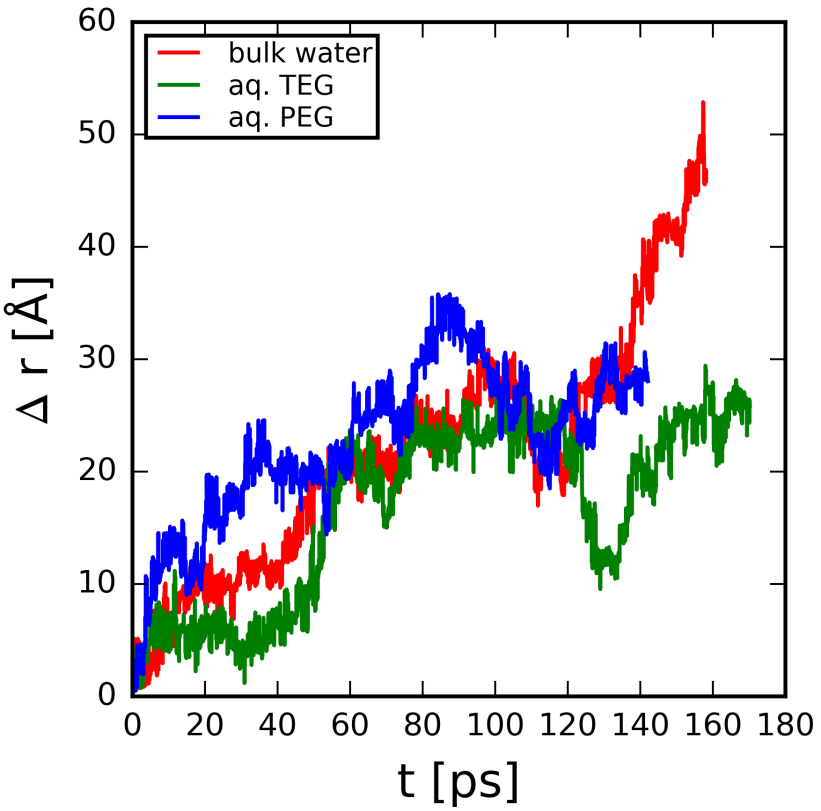


Figure 5.9: The distance for the atom (O*) that has H^+ relative to the initial position of the first protonated atom for bulk water, aqueous TEG and aqueous PEG solution at 300 K

In Figure 5.10, we have plotted the mean square displacement versus observation time of the protonated water molecule during the trajectories. It is very apparent that the aqueous PEG solution has the greatest mobility compared to the bulk water and aqueous TEG solutions. This makes it clear that PEG does have an effect on the proton mobility. The aqueous TEG solution shows little to no change for the proton mobility in the first 60 ps simulated. Using the MSD versus time slope and the Einstein Diffusion Equation, we can determine the total self-diffusivity for the

positive charge in the systems. The self-diffusivity for bulk water, aqueous TEG, and aqueous PEG are 0.75 $\mathring{A}^2/ps^{-1}$, 0.70 $\mathring{A}^2/ps^{-1}$, and 1.80 $\mathring{A}^2/ps^{-1}$, respectively. Plotting the MSD vs. time on a log-log scale and calculating the slope, we determine the the linearity of the relationship, a test to determine if we have reached the linear regime where accurate self-diffusivities can be calculated. We have a log-log linearity of 0.90, 0.99, and 1.10 for bulk water, aqueous TEG and aqueous PEG solutions, respectively. The experimental value for bulk water is 0.93 $\mathring{A}^2/ps^{-1}$ [289], implying that the aqueous PEG solution has almost a doubling of the self-diffusivity. To further assess the accuracy of this result a collection of simulations will need to be performed to determine a statistical mean. We know that long-term rest and long-term burst dynamics can cause large change to the MSD and calculated diffusivity from our own results, shown in Figure J.3 in the Appedix for our AIMD TEG solutions results.

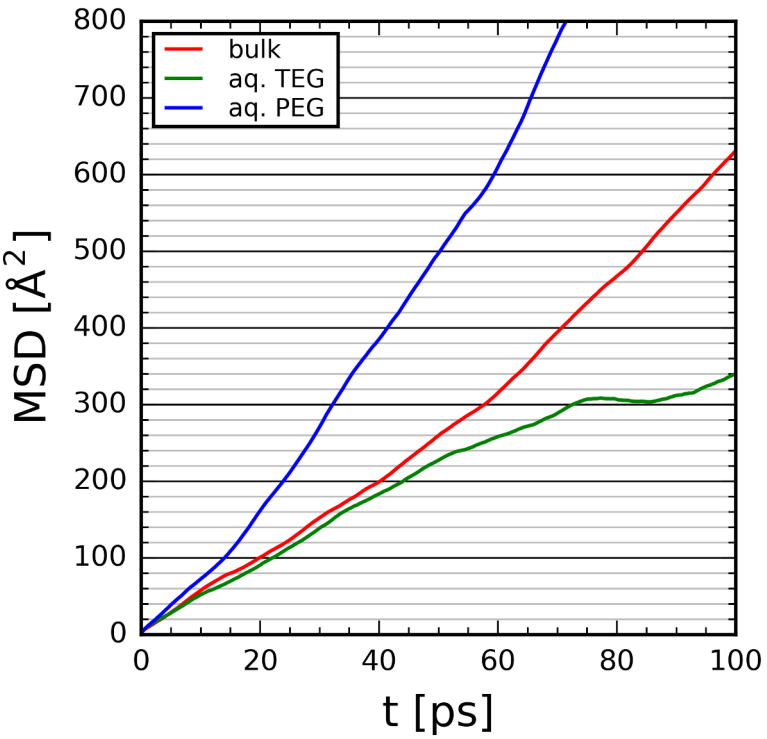


Figure 5.10: The mean squared displacements (MSDs) of the protonated atom (O*) versus time in bulk, aqueous TEG and aqueous PEG solution at 300 K.

In Figure 5.11, we show the decomposition of the MSD in Figure 5.10 into its X, Y, and Z components. This is to determine if the proton mobility is aligned to the PEG chain, as hypothesized in Chapter 4. We do see that the largest component is the X-axis self-diffusivity, the axis which the PEG chain backbone is parallel. We believe that the amphiphilic nature of the hydronium causes attraction to the PEG chain. Yet, due to the hydrophilic nature of PEG, the water is still able to structure

favorable hydrogen-bond networks that can orient along the backbone. The aqueous TEG solution most likely restructures the hydrogen bond network in such a way that well-structured networks are dirupted that the proton would be able to transfer along if it were in bulk water. We believe the PEG chain has an entropically favorable effect on protont mobility, given the correct orientation. In nanopores that are present in PEMs, this optimal geometry could be realized to enhance the proton mobility. This concept is similar to the high proton mobility found at oil-water interfaces. [268]

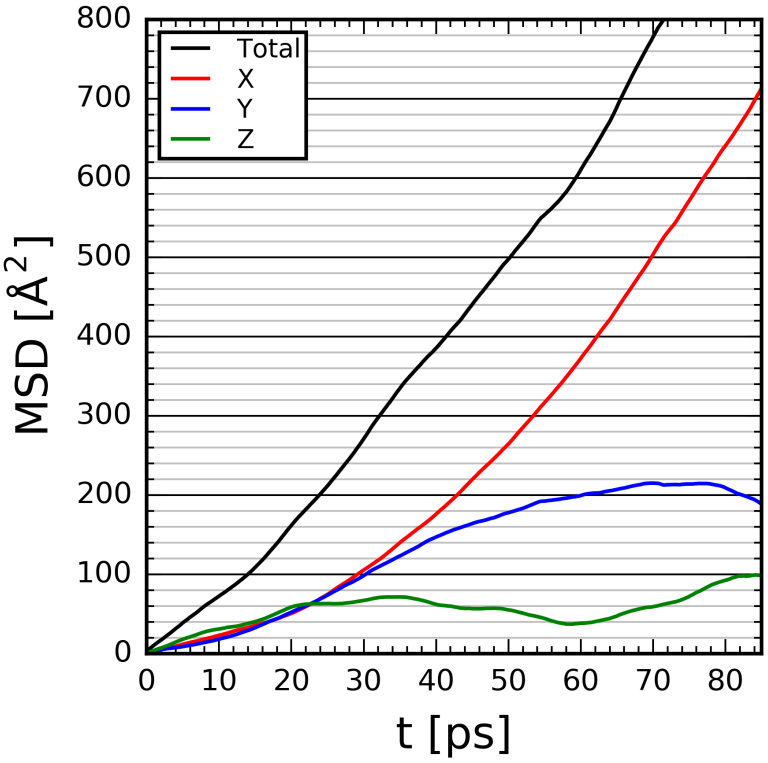


Figure 5.11: The decomposition of the aqueous PEG mean squared displacement of the protonated atom (O*) versus time for each axis of the simulation box at 300 K. The PEG chain is oriented along the X-axis.

Chapter 6

Preparation for Training a Reaction Force Field for xsPCDH/PEG Membranes

We have began work to create a ReaxFF force field to accurately describe xsPCHD and PEG proton exchange membranes. Chapter 5 provided necessary work to accurately describe H^+ in PEG solutions. The next step is to determine what is required to accurately describe xsPHD using the ReaxFF force field. From correspondence with the van Duin group, we know that there are two key molecular groups that must be trained and parameterized for the current ReaxFF force field: 1) the sulfonate groups and 2) the C/Cl groups. We have take the ReaxFF S/O/H bond and angle parameters from the recent work of Shin et al. [290] to give an initial parameter set to perform further training for the sulfonate groups. The first necessary step is to develop a dataset to begin training our xsPCHD ReaxFF force field.

We have again used NWChem [274] to generate a QM data set for training our next ReaxFF parameter set. We also used the Atomic Simulation Environment [275, 276] as a framework again due to its flexibility and means for a workflow. We have also again used DFT with the B3LYP exchange-correlation hybrid functional [277] and the 6-311++G(2d,2p) basis set for consistency. [278] The QM dataset consists of small molecules such as methanesulfonic acid and dithionic acid and also larger molecules to resemble the monomers of xsPCHD, shown in Figure 6.1. We have performed geometry optimizations of these structures as isolated molecules and also bond dissocation calculations for the H of the sulfonic acid groups. We have also performed geometry optimizations for these structures hydrated with water clusters of $n\mathrm{H_2Os} = 1-5$. The water molecules were place close to the sulfonic acid groups to form hydrogen bonds and as a means to provide proton transfer pathways. From the optimized geometries, we have calculated proton transfer pathways using restricted calculations where the closest water forming a hydrogen bond with the hydrogen of the sulfonic acid group is used as a protonation species. The oxygen of the water and the sulfonic acid oxygen are kept at a fixed distance and the rest of the structure is

relaxed. Then the proton is held fixed at positions transferring from one oxygen to another with geometry relaxations for the rest of the atoms at each fixed distance. Then, the oxygen distance is increase by 0.2 $\mathring{A}$ and the process is repeated. This is to devlep free energy profiles similar to the ones calculated in Chapter 4 and 5. Thus, we have created a robust training and validation set that accurately models the xsPCHD polymer chain.

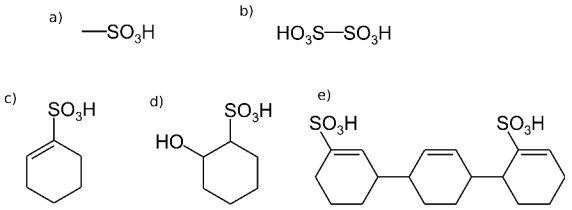


Figure 6.1: The polymers (a) methanesulfonic acid (b) dithionic aicd (c) sulfonated cyclohexadiene monomer (d) 1,2-cyclohexanol sulfonate and (e) a three monmer chain of sPCHD. These are the structures used for the quantum mechanical calculations to build a xsPCHD/PEG ReaxFF training and validation set.

We have also created a training set to address parameterization of the C/Cl bonds and angles. In Figure 6.2, we have the small molecules and larger, representative molecules for accurately modeling the disulfide crosslink in the xsPCHD/PEG membranes. We have again calculated bond dissociation energies, only for the Cl from the C for these molecules. We have also performed geometry optimizations as gas phase molecules and as hydrated cluster with $n\mathrm{H_2O}$s $= 1 - 5$. No proton transfer pathways were carried out for these structures.

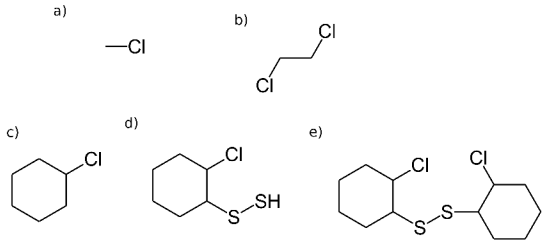


Figure 6.2: The polymers (a) chloromethane (b) dichloroethane (c) chlorocyclohexane (d) chlorocyclohexane disulfide and (e) the disulfide crosslinked chlorocyclohexane monomers structure. These are the structures used for the quantum mechanical calculations to build a xsPCHD/PEG ReaxFF training and validation set.

This work provides the necessary steps to begin training from the ReaxFF parameter set of Chapter 5, specifically the generation of a QM data set. The larger molecules of each set are reserved as the validation structures. Currently, at this stage, the future work would first train the parameter set to accurately describe xsPCHD,

specifically the sulfonate groups. Then, validation of the new parameter set against the previous QM dataset in Chapter 5 could determine that the description of H^+ with PEG has not been compromised. From there, reactive molecular dynamics of xsPCHD/PEG membranes can be carried out to give insight into the atomistic level details of proton conductivity in these PEMs.

Chapter 7

Conclusion

In this section of the disseration, we provide (i) summaries of the works presented in each chapter, (ii) a forward-looking statement on the significance and impact of this work and (iii) a description of promising future-work.

7.1 Summary of Work

To summarize, we have performed molecular modeling and simulations across multiple length and timescales (ab initio molecular dynamics, classical molecular dynamics, confined random walk simulations, and continuum modeling) of two different applications for hydrated polymeric membranes.

In Chapter 2, we modeled chitosan/chitin membranes for sustainable, biodegradable food packaging applications at low (15%) and high (95%) relative humidity (RH) levels to provide atomistic-level detail of the mechanisms that cause increased oxygen permeability across these membranes with increasing humidity. We have simulated the oxygen at infinite dilution. Utilizing radial distribution functions (RDFs), we find that only the H_2O RDFs change with increasing RH level and mainly signifies that the water distribution becomes more homogenous and the polymer chains become fully solvated. This was further emphasized by observing water distribution snapshots of the MD simulation at both RH levels. The O_2 and OH^- molecules show preference for the protonated chitosan monomer groups at both RH levels. However, this cation may have too strong of an interaction with these molecules and be the reason for our disagreement with experimental solubility and permeability trends. We have calculated the self-diffusivities of these three molecules (H_2O, O_2 and OH^-) with increasing RH level. We see order of magnitude changes for H_2O and OH^- but only a four-fold increase in diffusivity for O_2 with increasing humidity. The O_2 has the highest diffusivity at low humidity but H_2O has the highest diffusivity at higher humidity. We calculated the free energy of solvation/excess chemical potential of the oxygen using free energy perturbation, thermodynamic integration, and direct particle deletion methods. Similar values and trends are observed for all three methods.

We use the chemical potential to then compute the solubility and Henry's constant of oxygen in the system. We observe that the simulations predict that oxygen is more soluble at lower humidity, opposite of what one would expect from experimental results. Using the diffusivity and solubility, we calculate the oxygen permeability at both humidity levels and do see an opposite trend compared to experiment, giving a higher permeability at lower humidity levels. Based on the three free energy methods giving the same results, we suspect the Coulombic component of the force field interaction of the protonated chitosan monomer to be the culprit of this disagreement. Using the direct particle deletion method to re-calculate the excess chemical potential, we manipulate the intermolecular potential of the O_2 by "turning off" the electrostatic interactions. We do recover the correct trend compared to experiment (increasing permeability with increasing humidity) and our direct particle deletion calculation comes into closer agreement with experimental values at the higher RH level. However, the lower humidity level is still far from agreeing with experimental values, showing little change in permeability from the high RH level.

In Chapter 3, we present a model for characterizing the conductivity of proton exchange membranes in which the water and charge transport are strongly correlated. By determining three nanoscale structural descriptors, 1) acidity 2) confinement and 3) connectivity, we provide a prescription to determine the optimal membrane design to maximize performance, taking into account operational temperature, polymer chemistry, morphology, and hydration. This approach is advantageous since only the three structural descriptors are needed to functionally determine the complex relationship between nanostructure and important transport properties, such as the optimal conductivity for a given operating temperature.

In Chapter 4, we investigated the effects of TEG on the distribution of protonic defect structures, special pair formation, solvation structure around water and protonic defect structures, hydrogen-bond network patterns, mechanistic details for proton transfer, proton transfer kinetics and proton dynamics via ab initio molecular dynamics simulations using a variety of exchange-correlation functionals, including dispersion effects. For the structural effects of TEG associated proton transport, we observe the following. The protonic defect structure that occurs most is found to be the protonated water molecule, H_3O^+, with the hydroxyl group of TEG being the second highest occurring species. The TEG chain disrupts the hydrogen-bond network, causing the solvation shell around water to be populated by TEG chain groups instead of other waters, reducing the rigidity of the HB network. The predominant special pair is water-water special with the water-hydroxyl special pair being the second most common. The solvation shell analysis showed that the hydroxyl groups of TEG populate the hydrogen-bond acceptor sites with decreasing probability with increasing level of theory. The hydrogen-bond network analysis around the special pair showed that hydroxyl groups populate the hydrogen-bond acceptor sites with relatively equal probability to other molecules/molecular groups and the methylene groups populate the hydrogen-bond donor sites preferentially compared to other molecules. A myriad of hydrogen-bonding networks were found, showing

that methylene groups of TEG are hydrogen-bond donors in hydrogen bond networks that are associated with long range structural diffusion. This observation leads to the hypothesis that proton transport could possibly occur along the axis parallel to the PEG backbone with methylene groups providing as hydrogen-bond donors in the solvation around special pairs.

For the mechanistic and dynamical effects of TEG on proton transport, we observe the following. All three functionals studied support the presolvation requirement for structural diffusion in the presence of TEG, even with very different hydrogen-bond networks. The detailed mechanistic dynamics of presolvation appear to differ when dispersion effects are included due to softening of the hydrogen bonding structure with increasing level of theory. A favorable reduction in the free energy barrier for proton transfer was observed for the PBE+TS-vdW level of theory for TEG-water mixture compared to bulk water, while not including dispersion effects for PW91 and PBE gives equal barriers between TEG-water mixtures and bulk water. The kinetics show that the structural diffusion time scale differences for TEG-water mixtures to bulk water are relatively equal for both PBE and PBE+TS-vdW levels of theory but unfavorably increase for the PW91 level of theory. The excess proton displays burst-rest dynamic behavior, similar to that observed in bulk water.

In Chapter 5, we multiscale our work from Chapter 4 by developing a ReaxFF parameter set that can describe H^+ in aqueous PEG solution. We undertook three separate simulations using our currently developed parameter set: H^+ in 1) bulk water 2) aqueous TEG solution and 3) aqueous PEG solution with an infinite chain across periodic boudaries of the simulation box. We determine the solvation structures aroud the water molecles and hydronium ion, the free energy of proton transfer between water molecules, and the charge diffusivity. We see that there is a two-fold increase in the diffusivity in the PEG system compared to bulk water. Upon decomposing the mean-square displacements into the x, y, and z components, we see that the increase is along the axis parallel to the PEG chain.

In Chapter 6, we describe our work to create a quantum mechanical dataset of molecules specific to xsPCHD. We undertake this work a necessary step towards our goal to parameterize a ReaxFF potential that can accurately describe the xsPCHD/PEG membranes.

7.2 Impact of Work

In Chapter 2, we provide insight into the transport of small molecules in chitosan/chitin membranes by showing that the water/polymer distribution develops to a well-connected, continuous aqueous domain distributed through-out the membrane with increasing humidity. To the extent that small molecules are located in the aqueous domain, this sample-spanning network is ideal for transport. In fuel cells membranes, where proton transport is desirable, polymer chemistry is manipulated to encourage the development of well-connected aqueous domains. [4, 61, 291] When

sample-spanning aqueous domains are not present, a percolation threshold appears, resulting in virtually no transport. [217] This same knowledge can be applied to chitosan/chitin membranes for the opposite effect. Manipulation of polymer chemistry leading to isolated and disconnected aqueous domains in the membrane would result in lower oxygen permeability.

In Chapter 3, our goal is to apply the analytical theory to a range of proton exchange membranes and help guide experimental synthesis to determine optimal design of membranes. We recognize that potential performance for proton exchange membranes could far exceed current performance. A key result from this work is that there exists an optimal surface coverage for a given pore size in terms of maximizing proton conductivity.

In Chapter 4 , we believe that for systems where there is a strong correlation to hydration and proton migration, PEG monomers can take the place of water molecules in necessary solvation shell structures and potentially have modestly favorable effects on proton transport. This would imply that in systems whose proton conductivity suffers due to low hydration, PEG can have an enhancement effect on the structural diffusion of protons. Also, as a polymer, given an optimal orientation of the PEG chain, the structural diffusion could show directional preference along the polymer backbone.

In Chapter 5, we show how, given an optimum polymer chain orientation, the PEG polymer chain does have an impact on the diffusivity of H^+ in an aqueous environment. This can impact the design of materials that aim to control charge transport in aqueous domains. This could possibly be achieved by confining the space the polymer is in such that it orients in an elongated fashion, possibly by confinement in a nanpore. Yet, the confinement may have a strong impact on the charge transport and requires further study to validate this approach. This work has provided the molecular-level detail that can aid in material designs that involve PEG.

In Chapter 6, we describe our development of a quantum mechanical dataset for training a ReaxFF parameter set for xsPCHD. The impact of this work is in direct relation to performing reactive molecular dynamics of xsPCHD/PEG. The results of these simulations would provide the larger impact for giving atomistic insight into transport processes in these materials and overall membrane design.

The focus of Chapters 4, 5, and 6 is to describe the subtle effects that PEG has on proton transport in trying to understand the enhanced conductivity in xsPCHD/PEG membranes. In Chapter 4, we observed the effects of incorporating the PEG oligomer, TEG, into aqueous solution and the differences from proton transport in bulk water. We observed that the free energy of proton transfer between water molecules and the incorporation of TEG chain molecular groups in the hydrogen-bond network were the largest differences. Specifically, we found that the inclusion of methylene as a hydrogen-bond donor was associated with hydrogen-bond networks that where correlated to structural diffusion. This was attributed to the fact that the hydronium ion has an amphiphilic nature, with the lone electron pair attracted to the hydrophobic methylene group. The work in Chapter 5 showed that the orientation

of the PEG chain was the strongest indication for enhanced proton transport and that the free energy of proton transfer between water does not share a correlation to enhanced proton transport. From the observations in Chapter 4 and 5, we believe that the elongated chain, showing preference for proton transport parallel to the polymer backbone, attracts the amphiphilic hydronium ion. The chain also rearranges the hydrogen-bond network to local structures that favor structural diffusion along the axis parallel to the chain backbone. Thus, the mechanistic picture for PEG to enhance proton transport is a coupling of attraction of the hydronium ion to the polymer backbone and the rearrangement of the local hydrogen-bond network surrounding the polymer chain. In the xsPCHD/PEG membranes, the water structures and local environment will certainly be different than in the bulk due to confinement and the inclusion of anion groups. The work in Chapter 6 is the first step to seeing what effect the confinement and anion groups will have on proton transport and how it is coupled to the PEG orientation in the xsPCHD/PEG blend and block copolymer PEMs. From this work, the natural extension would be to revise the analytical model used in Chapter 3 to incorporate hydrophilic polymers that can have an effect on proton transport and decouple water and charge transport in PEMs.

7.3 Future Work

For our permeability work on chitosan/chitin membranes, we have identified the need of a more robust force field to accurately predict the solubility and permeability of oxygen in the chitosan/chitin membranes. A polarizable force field [95,201,202] should alleviate some of the issues of the current model but, a reactive force field, such as the ReaxFF force field, [137,200] would naturally allow the protonated chitosan monomers to become deprotonated and remove the requirement to explicitly model hydroxide ions in the system. For future work, developing a training and validation set of ab initio calculation relative to the chitosan and chitin monomers and training a reactive force field currently appears to be the best route for future progress of accurately modeling chitosan/chitin membranes with increasing humidity. From this, modeling chemically modified chitosan/chitin membranes could help identify a promising group of membrane materials, reducing the cost and time to synthesis and characterize new materials.

For our theoretical work on PEM conductivity based on key structural descriptors, our analytical theory would provide a means to rapidly screen a range of nanostructured proton exchange membranes to expedite material discovery and optimize the design of current PEMs.

For our ab initio molecular dynamics studies of TEG-water mixtures, we note that increasing chain length and varying TEG composition in the TEG-mixture would be of interest to determine chain-dependent and compositional effects. No quantum nuclear effects were treated in the simulations. This quantum treatment of the nuclei has been shown [230] to flatten out the free energy barrier for proton transfer in

bulk water, making it effectively "barrier-less". Including these nuclear quantum effects via path-integral molecular dynamics would be interesting due to possibly more protonic defect structures that could become more energetically favorable at ambient temperature.

For our ReaxFF work, we hope to continuously develop and further validate this ReaxFF parameter set. The benefit would be to have a transferable potential to describe a variety of materials that incorporate PEG. Specifically, drug delivery and bi-phasic catalysis are two potential applications that could greatly benefit from having large-scale, reactive molecular simulation work applied. This shows that our work can have a larger impact than just for the xsPCHD/PEG membranes that we have targeted thus far.

Our computational modeling and simulation work has provided atomistic-level understanding of the chitosan/chitin membranes and polyethylene glycol additives to xsPCHD/PEG membranes that hopes to aid in the future of membrane design and synthesis.

Bibliography

[1] W. Humphrey, A. Dalke, and K. Schulten. Vmd: Visual molecular dynamics. *Journal of Molecular Graphics*, 14(1):33–38, 1996. xvi, 28

[2] A. Varshney, F. P. Brooks, and W. V. Wright. Linearly scalable computation of smooth molecular surfaces. *IEEE Computer Graphics and Applications*, 14:19–25, 1994. xvi, 28

[3] John Stone. *an efficient library for parallel ray tracing and animation. Master's thesis, Computer Science Department, University of Missouri-Rolla, April 1998. xvi, 28*

[4] K. D. Kreuer. On the development of proton conducting materials for technological applications. Solid State Ionics, *97(1-4):1–15, 1997. xvii, 42, 43, 102*

[5] R. A. Robison and R. H. Stokes. Electrolyte solutions. *Butterworths, London, 1959. xvii, 42, 43*

[6] Susanna Monti, Alessandro Corozzi, Peter Fristrup, Kaushik L. Joshi, Yun Kyung Shin, Peter Oelschlaeger, Adri C. T. van Duin, and Vincenzo Barone. Exploring the conformational and reactive dynamics of biomolecules in solution using an extended version of the glycine reactive force field. Phys. Chem. Chem. Phys., *15:15062–15077, 2013. xix, 85, 88, 89*

[7] Adri C. T. van Duin, Chenyu Zou, Kaushik Joshi, Vyascheslav Bryantsev, and William A. Goddard. Chapter 6 a reaxff reactive force-field for proton transfer reactions in bulk water and its applications to heterogeneous catalysis. In Computational Catalysis, *pages 223–243. The Royal Society of Chemistry, 2014. xix, 85, 87, 90, 91*

[8] Soney C George and Sabu Thomas. Transport phenomena through polymeric systems. Progress in Polymer Science, *26(6):985 – 1017, 2001. 1*

[9] Y. Luo and Q. Wang. Recent advances of chitosan and its derivatives for novel applications in food science. Journal of Food Processing & Beverages, *1(1):1–13, 2013. 1, 3*

[10] Yangchao Luo and Qin Wang. Recent development of chitosan-based polyelectrolyte complexes with natural polysaccharides for drug delivery. International Journal of Biological Macromolecules, *64(0):353 – 367, 2014. 1, 2*

[11] Florian Mller-Plathe. Permeation of polymers a computational approach. Acta Polymerica, *45(4):259–293, 1994. 1*

[12] *Marguerite Rinaudo. Main properties and current applications of some polysaccharides as biomaterials.* Polymer International, *57(3):397–430, 2008.* 2

[13] *Stphane Guilbert, Bernard Cuq, and Nathalie Gontard. Recent innovations in edible and/or biodegradable packaging materials.* Food Additives ; Contaminants, *14(6-7):741–751, 1997. PMID: 9373537.* 2

[14] *M. Kumar, R. A. A. Muzzarelli, C. Muzzarelli, H. Sashiwa, and A. J. Domb. Chitosan chemistry and pharmaceutical perspectives.* Chemical Reviews, *104(12):6017–6084, 2004.* 2, 3

[15] *F. L. Mi, Y. C. Tan, H. F. Liang, and H. W. Sung. In vivo biocompatibility and degradability of a novel injectable-chitosan-based implant.* Biomaterials, *23(1):181–191, 2002.* 2

[16] *I. M. Helander, E. L. Nurmiaho-Lassila, R. Ahvenainen, J. Rhoades, and S. Roller. Chitosan disrupts the barrier properties of the outer membrane of gram-negative bacteria.* International Journal of Food Microbiology, *71(2-3):235–244, 2001.* 2

[17] *H. K. No, N. Y. Park, S. H. Lee, and S. P. Meyers. Antibacterial activity of chitosans and chitosan oligomers with different molecular weights.* International Journal of Food Microbiology, *74(1-2):65–72, 2002.* 2

[18] *K. V. H. Prashanth and R. N. Tharanathan. Chitin/chitosan: modifications and their unlimited application potential - an overview.* Trends in Food Science & Technology, *18(3):117–131, 2007.* 2, 3

[19] *S. Wongsasulak, K. M. Kit, D. J. McClements, T. Yoovidhya, and J. Weiss. The effect of solution properties on the morphology of ultrafine electrospun egg albumen-peo composite fibers.* Polymer, *48(2):448–457, 2007.* 2

[20] *K. Desai, K. Kit, J. Li, and S. Zivanovic. Morphological and surface properties of electrospun chitosan nanofibers.* Biomacromolecules, *9(3):1000–1006, 2008.* 2

[21] *Marguerite Rinaudo. Chitin and chitosan: Properties and applications.* Progress in Polymer Science, *31(7):603 – 632, 2006.* 2

[22] *S. S. Koide. Chitin-chitosan: Properties, benefits and risks.* Nutrition Research, *18(6):1091–1101, 1998.* 2

[23] *C. Kriegel, A. Arrechi, K. Kit, D. J. McClements, and J. Weiss. Fabrication, functionalization, and application of electrospun biopolymer nanofibers.* Critical Reviews in Food Science and Nutrition, *48(8):775–797, 2008.* 2

[24] *R. A. A. Muzzarelli. Chitosan-based dietary foods.* Carbohydrate Polymers, *29(4):309–316, 1996.* 2

[25] *S. Roller and N. Covill. The antifungal properties of chitosan in laboratory media and apple juice.* International Journal of Food Microbiology, *47(1-2):67–77, 1999.* 2

[26] *F. Shahidi, J. K. V. Arachchi, and Y. J. Jeon. Food applications of chitin and chitosans.* Trends in Food Science & Technology, *10(2):37–51, 1999.* 2

[27] *S. Zivanovic, J. J. Li, P. M. Davidson, and K. Kit. Physical, mechanical, and antibacterial properties of chitosan/peo blend films.* Biomacromolecules, *8(5):1505–1510, 2007.* 2, 3

[28] *R. A. A. Muzzarelli, J. Boudrant, D. Meyer, N. Manno, M. DeMarchis, and M. G. Paoletti. Current views on fungal chitin/chitosan, human chitinases, food preservation, glucans, pectins and inulin: A tribute to henri braconnot, precursor of the carbohydrate polymers science, on the chitin bicentennial.* Carbohydrate Polymers, *87(2):995–1012, 2012.* 2

[29] *S. Hajji, I. Younes, O. Ghorbel-Bellaaj, R. Hajji, M. Rinaudo, M. Nasri, and K. Jellouli. Structural differences between chitin and chitosan extracted from three different marine sources.* International Journal of Biological Macromolecules, *65:298–306, 2014.* 3

[30] *I. Younes, O. Ghorbel-Bellaaj, R. Nasri, M. Chaabouni, M. Rinaudo, and M. Nasri. Chitin and chitosan preparation from shrimp shells using optimized enzymatic deproteinization.* Process Biochemistry, *47(12):2032–2039, 2012.* 3

[31] *I. Younes, S. Hajji, V. Frachet, M. Rinaudo, K. Jellouli, and M. Nasri. Chitin extraction from shrimp shell using enzymatic treatment. antitumor, antioxidant and antimicrobial activities of chitosan.* International Journal of Biological Macromolecules, *69:489–498, 2014.* 3

[32] *I. Younes and M. Rinaudo. Chitin and chitosan preparation from marine sources. structure, properties and applications.* Marine Drugs, *13(3):1133–1174, 2015.* 3, 17

[33] *N. M. Alves and J. F. Mano. Chitosan derivatives obtained by chemical modifications for biomedical and environmental applications.* International Journal of Biological Macromolecules, *43(5):401–414, 2008.* 3

[34] *K. Desai and K. Kit. Effect of spinning temperature and blend ratios on electrospun chitosan/poly(acrylamide) blends fibers.* Polymer, *49(19):4046–4050, 2008.* 3

[35] *C. Kriegel, K. M. Kit, D. J. McClements, and J. Weiss. Electrospinning of chitosan-poly(ethylene oxide) blend nanofibers in the presence of micellar surfactant solutions.* Polymer, *50(1):189–200, 2009.* 3

[36] *J. Li, S. Zivanovic, P. M. Davidson, and K. Kit. Characterization and comparison of chitosan/pvp and chitosan/peo blend films.* Carbohydrate Polymers, *79(3):786–791, 2010.* 3

[37] *J. Li, S. Zivanovic, P. M. Davidson, and K. Kit. Production and characterization of thick, thin and ultra-thin chitosan/peo films.* Carbohydrate Polymers, *83(2):375–382, 2011.* 3

[38] *V.K. Mourya and Nazma N. Inamdar. Chitosan-modifications and applications: Opportunities galore.* Reactive and Functional Polymers, *68(6):1013 – 1051, 2008.* 3

[39] *K. Siraleartmukul, K. Siriwong, T. Remsungnen, N. Muangsin, W. Udomkichdecha, and S. Hannongbua. Solvation structure of glucosamine in aqueous solution as studied by monte carlo simulation using ab initio fitted potential.* Chemical Physics Letters, *395(4-6):233–238, 2004.* 3

[40] *B. Prathab and T. M. Aminabhavi. Molecular modeling study on surface, thermal, mechanical and gas diffusion properties of chitosan.* Journal of Polymer Science Part B: Polymer Physics, *45(11):1260–1270, 2007.* 3

[41] *E. F. Franca, R. D. Lins, L. C. G. Freitas, and T. P. Straatsma. Characterization of chitin and chitosan molecular structure in aqueous solution.* Journal of Chemical Theory and Computation, *4(12):2141–2149, 2008.* 3

[42] *E. F. Franca, L. C. G. Freitas, and R. D. Lins. Chitosan molecular structure as a function of n-acetylation.* Biopolymers, *95(7):448–460, 2011.* 3

[43] *R. R. Faria, R. F. Guerra, L. R. de Sousa Neto, L. F. Motta, and E. d. F. Franca. Computational study of polymorphic structures of alpha- and beta-chitin and chitosan in aqueous solution.* Journal of Molecular Graphics and Modelling, *63:78–84, 2016.* 3

[44] *Q. Yin, G. Zhou, Y. Y. Liu, Q. J. Yin, J. H. Luo, and B. Jiang. Molecular dynamic simulation of carbonxyethyl chitosan: Effect of temperature, salt concentration and ph.* Journal of Theoretical & Computational Chemistry, *9:167–176, 2010.* 3

[45] *S. Skovstrup, S. G. Hansen, T. Skrydstrup, and B. Schiott. Conformational flexibility of chitosan: A molecular modeling study.* Biomacromolecules, *11(11):3196–3207, 2010.* 4

[46] *M. Petrov, L. Lymperakis, M. Friak, and J. Neugebauer. Ab initio based conformational study of the crystalline alpha-chitin.* Biopolymers, *99(1):22–34, 2013.* 4

[47] *Z. Yu and D. Lau. Development of a coarse-grained alpha-chitin model on the basis of martini forcefield.* Journal of Molecular Modeling, *21(5), 2015.* 4

[48] *E. L. Kossovich, I. V. Kirillova, L. Y. Kossovich, R. A. Safonov, D. V. Ukrainskiy, and S. A. Apshtein. Hybrid coarse-grained/atomistic model of "chitosan plus carbon nanostructures" composites.* Journal of Molecular Modeling, *20(10), 2014.* 4

[49] *E. L. Kossovich and R. A. Safonov. Predictive analysis of chitosan-based nanocomposite biopolymers elastic properties at nano- and microscale.* Journal of Molecular Modeling, *22(4), 2016.* 4

[50] *D. Aztatzi-Pluma, E. O. Castrejon-Gonzalez, A. Almendarez-Camarillo, J. F. J. Alvarado, and Y. Duran-Morales. Study of the molecular interactions between functionalized carbon nanotubes and chitosan.* Journal of Physical Chemistry C, *120(4):2371–2378, 2016.* 4

[51] *Y. Liu, C. Chipot, X. Shao, and W. Cai. Free-energy landscape of the helical wrapping of a carbon nanotube by a polysaccharide.* Journal of Physical Chemistry C, *115(5):1851–1856, 2011.* 4

[52] *S. Piovesan, P. A. Cox, J. R. Smith, D. G. Fatouros, and M. Roldo. Novel biocompatible chitosan decorated single-walled carbon nanotubes (swnts) for biomedical applications: theoretical and experimental investigations.* Physical Chemistry Chemical Physics, *12(48):15636–15643, 2010.* 4

[53] *Dan Carter and Jonathan Wing. The fuel cell industry review 2013. Industry review report, Fuel Cell Today - Johnson Matthey PLC, 2013.* 5, 6

[54] *Dimitrios Papageorgopoulos. Fuel cells program overview - 2013. Annual progress report, Department of Energy, 2013.* 5, 6

[55] *Qingfeng Li, Ronghuan He, Jens Oluf Jensen, and Niels J. Bjerrum. Approaches and recent development of polymer electrolyte membranes for fuel cells operating above 100 c.* Chemistry of Materials, *15(26):4896–4915, 2003.* 5

[56] *Steven Chu and Arun Majumdar. Opportunities and challenges for a sustainable energy future.* Nature, *488(7411):294 – 303, 2012.* 5

[57] *John Voelcker. 2016 toyota mirai priced at* $57,500, *with499 monthly lease.* Green Car Reports, *2014.* 6

[58] *John Voelcker. Smaller, cheaper toyota mirai fuel-cell car coming in 2019, company says.* Green Car Reports, *2016.* 6

[59] *High Temperature Membrane Working Group. R and d plan for the high temperature membrane working group. R and d plan report, US Department of Energy EERE Fuel Cell Technologies, 2012.* 6

[60] *Kenneth A. Mauritz and Robert B. Moore. State of understanding of nafion.* Chemical Reviews, *104(10):4535–4586, 2004.* 7

[61] *K. D. Kreuer, S. J. Paddison, E. Spohr, and M. Schuster. Transport in proton conductors for fuel-cell applications: Simulations, elementary reactions, and phenomenology.* Chemical Reviews, *104(10):4637–4678, 2004.* 7, 8, 102

[62] *B. Smitha, S. Sridhar, and A.A. Khan. Solid polymer electrolyte membranes for fuel cell applicationsa review.* Journal of Membrane Science, *259(12):10 – 26, 2005.* 7

[63] *Martin F.H. Schuster and Wolfgang H. Meyer. Anhydrous proton-conducting polymers.* Annual Review of Materials Research, *33(1):233–261, 2003.* 7

[64] *Dimitrios Papageorgopoulos. U.s. department of energy hydrogen and fuel cells overview - 2013. H2fc-fair conference presentation, Department of Energy, 2013.* 7

[65] *Tom Kalil and Cyrus Wadia. Materials genome initiative for global competitiveness. Technical report, Executive Office of the President, National Science and Technology Council, 2011.* 8

[66] *Myvizhi Esai Selvan, Elisa Calvo-Munoz, and David J. Keffer. Toward a predictive understanding of water and charge transport in proton exchange membranes.* The Journal of Physical Chemistry B, *115(12):3052–3061, 2011.* 8, 41, 42

[67] *Noam Agmon. The grotthuss mechanism.* Chemical Physics Letters, *244(56):456 – 462, 1995.* 8

[68] *K.-D. Kreuer. Proton conductivity: Materials and applications.* Chemistry of Materials, *8(3):610–641, 1996.* 8

[69] *D. Marx. Proton transfer 200 years after von grotthuss: Insights from ab initio simulations.* ChemPhysChem, *7(9):1848–1870, 2006.* 8, 10, 72

[70] *M. Esai Selvan and D. J. Keffer.* Molecular-Level Modeling of the Structure and Proton Transport within the Membrane Electrode Assembly of Hydrogen Proton Exchange Membrane Fuel Cells, *volume 46. Springer, New York, 2010.* 8, 40, 41

[71] *M. L. Hoarfrost, M. S. Tyagi, R. A. Segalman, and J. A. Reimer. Effect of confinement on proton transport mechanisms in block copolymer/ionic liquid membranes.* Macromolecules, *45(7):3112–3120, 2012.* 8

[72] *D. Marx and J. Hutter.* Ab Initio Molecular Dynamics: Basic Theory and Advanced Methods. *Cambridge University Press, 2009.* 8, 54

[73] *R. Car and M. Parrinello. Unified approach for molecular dynamics and density-functional theory.* Physical Review Letters, *55(22):2471–2474, 1985.* 8

[74] *A. A. Hassanali, J. Cuny, V. Verdolino, and M. Parrinello. Aqueous solutions: state of the art in ab initio molecular dynamics.* Philosophical Transactions of the Royal Society of London A: Mathematical, Physical and Engineering Sciences, *372(2011), 2014.* 8, 9, 13

[75] *M. Tuckerman, K. Laasonen, M. Sprik, and M. Parrinello. Ab initio molecular dynamics simulation of the solvation and transport of h3o+ and oh- ions in water.* The Journal of Physical Chemistry, *99(16):5749–5752, 1995.* 9, 41

[76] *M. Tuckerman, K. Laasonen, M. Sprik, and M. Parrinello. Abinitio molecular dynamics simulation of the solvation and transport of hydronium and hydroxyl ions in water.* The Journal of Chemical Physics, *103(1):150–161, 1995.* 9, 62

[77] *G. Zundel and H. Metzger. Energiebänder der tunnelnden Überschuß-protonen in flüssigen säuren - eine ir-spektroskopische untersuchung der natur der gruppierungen h5o2+.* Z. Physik. Chem., *58:225, 1968.* 9

[78] *M. Eigen. Proton transfer, acid-base catalysis, and enzymatic hydrolysis. part i: Elementary processes.* Angewandte Chemie International Edition in English, *3(1):1–19, 1964.* 9

[79] *N. Agmon. Infrared spectroscopy: The acid test for water structure.* Nat Chem, *8(3):206–207, 2016.* 9, 77

[80] *M. Thämer, L. De Marco, K. Ramasesha, A. Mandal, and A. Tokmakoff. Ultrafast 2d ir spectroscopy of the excess proton in liquid water.* Science, *350(6256):78–82, 2015.* 9, 77

[81] *S. Woutersen and H. J. Bakker. Ultrafast vibrational and structural dynamics of the proton in liquid water.* Physical Review Letters, *96(13):138305, 2006.* 9, 77, 80

[82] *T. C. Berkelbach, H.-S. Lee, and M. E. Tuckerman. Concerted hydrogen-bond dynamics in the transport mechanism of the hydrated proton: A first-principles molecular dynamics study.* Physical Review Letters, *103(23):238302, 2009.* 9, 10, 13, 72, 80

[83] *R. Biswas, Y.-L. S. Tse, A. Tokmakoff, and G. A. Voth. Role of presolvation and anharmonicity in aqueous phase hydrated proton solvation and transport.* The Journal of Physical Chemistry B, *120(8):1793–1804, 2016.* 9, 10, 72

[84] *F. Giberti, A. A. Hassanali, M. Ceriotti, and M. Parrinello. The role of quantum effects on structural and electronic fluctuations in neat and charged water.* The Journal of Physical Chemistry B, *118(46):13226–13235, 2014.* 9

[85] *Y.-L. S. Tse, C. Knight, and G. A. Voth. An analysis of hydrated proton diffusion in ab initio molecular dynamics.* The Journal of Chemical Physics, *142(1):014104, 2015.* 9, 10, 13, 66, 72, 82, 83, 94

[86] *A. Hassanali, F. Giberti, J. Cuny, T. D. Khne, and M. Parrinello. Proton transfer through the water gossamer.* Proceedings of the National Academy of Sciences, *110(34):13723–13728, 2013.* 9, 10, 66, 82

[87] *Y. Wu, H. Chen, F. Wang, F. Paesani, and G. A. Voth. An improved multistate empirical valence bond model for aqueous proton solvation and transport.* The Journal of Physical Chemistry B, *112(2):467–482, 2008.* 9, 62

[88] *O. Markovitch, H. Chen, S. Izvekov, F. Paesani, G. A. Voth, and N. Agmon. Special pair dance and partner selection: Elementary steps in proton transport in liquid water.* The Journal of Physical Chemistry B, *112(31):9456–9466, 2008.* 9, 62, 66

[89] *M. E. Tuckerman, D. Marx, and M. Parrinello. The nature and transport mechanism of hydrated hydroxide ions in aqueous solution.* Nature, *417(6892):925–929, 2002.* 10, 72

[90] *Jimmy Mays and Kenneth A Mauritz. Poly(cyclohexadiene)-based polymer electrolyte membranes for fuel cell applications. Final technical report, University of Tennessee and University of Southern Mississippi, March 2011.* 11

[91] *Jimmy Mays and Kenneth A Mauritz. Poly(cyclohexadiene)-based polymer electrolyte membranes for fuel cell applications. Annual progress report, University of Tennessee and University of Southern Mississippi, 2009.* 11

[92] *J.W. Mays, S. Deng, K.A. Mauritz, M.K. Hassan, and S.P. Gido. Materials comprising polydienes and hydrophilic polymers and related methods, November 22 2011. US Patent 8,061,533.* 11

[93] *Qifei Wang, Nethika S. Suraweera, David J. Keffer, Suxiang Deng, and Jimmy Mays. Atomistic and coarse-grained molecular dynamics simulation of a cross-linked sulfonated poly(1,3-cyclohexadiene)-based proton exchange membrane.* Macromolecules, *45(16):6669–6685, 2012.* 11, 20, 42

[94] *Qifei Wang, David J. Keffer, Suxiang Deng, and Jimmy Mays. Multi-scale models for cross-linked sulfonated poly (1, 3-cyclohexadiene) polymer.* Polymer, *53(7):1517 – 1528, 2012.* 11

[95] *Qifei Wang, David J. Keffer, Suxiang Deng, and Jimmy Mays. Structure and diffusion in cross-linked and sulfonated poly(1,3-cyclohexadiene)/polyethylene glycol-based proton exchange membranes.* The Journal of Physical Chemistry C, *117(10):4901–4912, 2013.* 11, 13, 29, 37, 104

[96] *Qifei Wang, David J. Keffer, Suxiang Deng, and Jimmy Mays. Structure and proton transport in proton exchange membranes based on cross-linked sulfonated poly (1, 3-cyclohexadiene) with varying local acid environment.* Polymer, *54(9):2299 – 2307, 2013.* 11

[97] *S. Deng, M. K. Hassan, A. Nalawade, K. A. Perry, K. L. More, K. A. Mauritz, M. T. McDonnell, D. J. Keffer, and J. W. Mays. High temperature proton exchange membranes with enhanced proton conductivities at low humidity and high temperature based on polymer blends and block copolymers of poly(1,3-cyclohexadiene) and poly(ethylene glycol).* Polymer, *77:208–217, 2015.* 11

[98] *A. C. Barnes, T. W. N. Bieze, J. E. Enderby, and J. C. Leyte. Dynamics of water in the poly(ethylene oxide) hydration shell: A quasi elastic neutron-scattering study.* The Journal of Physical Chemistry, *98(44):11527–11532, 1994.* 11

[99] *T. W. N. Bieze, A. C. Barnes, C. J. M. Huige, J. E. Enderby, and J. C. Leyte. Distribution of water around poly(ethylene oxide): A neutron diffraction study.* The Journal of Physical Chemistry, *98(26):6568–6576, 1994.* 11

[100] *R. Kjellander and E. Florin. Water structure and changes in thermal stability of the system poly(ethylene oxide)-water.* Journal of the Chemical Society, Faraday Transactions 1: Physical Chemistry in Condensed Phases, *77(9):2053–2077, 1981.* 11

[101] *K. Tasaki. Poly(oxyethylene)-water interactions: A molecular dynamics study.* Journal of the American Chemical Society, *118(35):8459–8469, 1996.* 11

[102] *J. M. Harris.* Poly(Ethylene Glycol) Chemistry: Biotechnical and Biomedical Applications. *Topics in Applied Chemistry. Springer US, 1 edition, 1992.* 11

[103] *H. Y. Chang and C. W. Lin. Proton conducting membranes based on peg/sio2 nanocomposites for direct methanol fuel cells.* Journal of Membrane Science, *218(12):295–306, 2003.* 11

[104] *B. D. Ghosh and J. E. Ritchie. Effect of polymer structure on ion transport in an anhydrous proton conducting electrolyte.* Chemistry of Materials, *22(4):1483–1491, 2010.* 11

[105] *I. Honma, Y. Takeda, and J. M. Bae. Protonic conducting properties of sol-gel derived organic/inorganic nanocomposite membranes doped with acidic functional molecules.* Solid State Ionics, *120(14):255–264, 1999. 11, 12*

[106] *I. Honma, S. Nomura, and H. Nakajima. Protonic conducting organic/inorganic nanocomposites for polymer electrolyte membrane.* Journal of Membrane Science, *185(1):83–94, 2001. 11, 12*

[107] *I. Honma, S. Hirakawa, K. Yamada, and J. M. Bae. Synthesis of organic/inorganic nanocomposites protonic conducting membrane through sol-gel processes.* Solid State Ionics, *118(12):29–36, 1999. 11, 12*

[108] *J. E. Ritchie and J. A. Crisp. A solgel synthesis of polyether-based proton conducting electrolytes.* Analytica Chimica Acta, *496(12):65–71, 2003. 11*

[109] *J. F. Snyder, J. C. Hutchison, M. A. Ratner, and D. F. Shriver. Synthesis of comb polysiloxane polyelectrolytes containing oligoether and perfluoroether side chains.* Chemistry of Materials, *15(22):4223–4230, 2003. 11*

[110] *C. Sun and J. E. Ritchie. Effects of bulky copolymers on ion transport in an anhydrous proton-conducting electrolyte.* Journal of The Electrochemical Society, *157(11):B1549–B1555, 2010. 11*

[111] *C. Sun and J. E. Ritchie. Star-shaped mepegn polymers as h+ conducting electrolytes.* The Journal of Physical Chemistry B, *115(26):8381–8389, 2011. 11*

[112] *C. Sun and J. E. Ritchie. Polyethylene glycol-functionalized polyoctahedral silsesquioxanes as h+-conducting electrolytes.* Journal of Solid State Electrochemistry, *18(6):1735–1742, 2014. 11*

[113] *B. Yancey, J. Jones, and J. E. Ritchie. Volume fraction of ether is a significant factor in controlling conductivity in proton conducting polyether based polymer solgel electrolytes.* The Journal of Physical Chemistry B, *118(45):13002–13010, 2014. 11*

[114] *S. K. Begum, S. A. Ratna, R. J. Clarke, and M. S. Ahmed. Excess molar volumes, refractive indices and transport properties of aqueous solutions of poly(ethylene glycol)s at (303.15323.15) k.* Journal of Molecular Liquids, *202:176–188, 2015. 11*

[115] *O. Borodin, D. Bedrov, and G. D. Smith. A molecular dynamics simulation study of polymer dynamics in aqueous poly(ethylene oxide) solutions.* Macromolecules, *34, 2001. 11*

[116] *B. Hong, F. Escobedo, and A. Z. Panagiotopoulos. Diffusivities and viscosities of poly(ethylene oxide) oligomers.* Journal of Chemical & Engineering Data, *55(10):4273–4280, 2010.* 11

[117] *S. A. Oelmeier, F. Dismer, and J. Hubbuch. Molecular dynamics simulations on aqueous two-phase systems - single peg-molecules in solution.* BMC Biophysics, *5(1):1–13, 2012.* 11

[118] *K. Shimada, H. Kato, T. Saito, S. Matsuyama, and S. Kinugasa. Precise measurement of the self-diffusion coefficient for poly(ethylene glycol) in aqueous solution using uniform oligomers.* The Journal of Chemical Physics, *122(24):244914, 2005.* 11

[119] *Qifei Wang, David J. Keffer, and Donald M. Nicholson. A coarse-grained model for polyethylene glycol polymer.* The Journal of Chemical Physics, *135(21):214903–1 – 214903–10, 2011.* 11

[120] *Q. Xu, J. Mi, and C. Zhong. Structure of poly(ethylene glycol)water mixture studied by polymer reference interaction site model theory.* The Journal of Chemical Physics, *133(17):174104, 2010.* 11

[121] *C. Liu, X. Li, and Z. Jin. Progress in thermoregulated liquid/liquid biphasic catalysis.* Catalysis Today, *247:82–89, 2015.* 11

[122] *J. M. Harris and R. B. Chess. Effect of pegylation on pharmaceuticals.* Nature Reviews Drug Discovery, *2(3):214, 2003.* 11

[123] *A. Kolate, D. Baradia, S. Patil, I. Vhora, G. Kore, and A. Misra. Peg a versatile conjugating ligand for drugs and drug delivery systems.* Journal of Controlled Release, *192:67–81, 2014.* 11

[124] *F. M. Veronese and G. Pasut. Pegylation, successful approach to drug delivery.* Drug Discovery Today, *10(21):1451–1458, 2005.* 11

[125] *D. Gupta and V. Choudhary. Non-fluorinated hybrid composite membranes based on polyethylene glycol functionalized polyhedral oligomeric silsesquioxane [pposs] and sulfonated poly(ether ether ketone) [speek] for fuel cell applications.* Reactive and Functional Polymers, *73(9):1268–1280, 2013.* 11

[126] *F. Capuano, A. Vergara, L. Paduano, O. Annunziata, and R. Sartorio. Electrostatic and excluded volume effects on the transport of electrolytes in poly(ethylene glycol)-water mixed solvents.* The Journal of Physical Chemistry B, *107(44):12363–12369, 2003.* 11

[127] *J. K. Chung and S. Consta. Release mechanisms of poly(ethylene glycol) macroions from aqueous charged nanodroplets.* The Journal of Physical Chemistry B, *116(19):5777–5785, 2012.* 11

[128] *S. Consta and J. K. Chung. Charge-induced conformational changes of peg-(na+)n in a vacuum and aqueous nanodroplets.* The Journal of Physical Chemistry B, *115(35):10447–10455, 2011.* 11

[129] *J. Herranen, J. Kinnunen, B. Mattsson, H. Rinne, F. Sundholm, and L. Torell. Characterisation of poly(ethylene oxide) sulfonic acids.* Solid State Ionics, *80(34):201–212, 1995.* 12, 13

[130] *B. Mattsson, A. Brodin, L. M. Torell, H. Rinne, J. Hamara, F. Sundholm, and P. Jacobsson. Raman scattering investigations of peo and ppo sulphonic acids.* Solid State Ionics, *97(14):309–314, 1997.* 12, 13

[131] *J. Ennari, M. Elomaa, and F. Sundholm. Modelling a polyelectrolyte system in water to estimate the ion-conductivity.* Polymer, *40(18):5035–5041, 1999.* 13

[132] *J. Ennari, I. Neelov, and F. Sundholm. Molecular dynamics simulation of the structure of peo based solid polymer electrolytes.* Polymer, *41(11):4057–4063, 2000.* 13

[133] *J. Ennari, I. Neelov, and F. Sunholm. Modelling of gas transport properties of polymer electrolytes containing various amounts of water.* Polymer, *45(12):4171–4179, 2004.* 13

[134] *J. Ennari, L.-O. Pietil, V. Virkkunen, and F. Sundholm. Molecular dynamics simulation of the structure of an ion-conducting peo-based solid polymer electrolyte.* Polymer, *43(20):5427–5438, 2002.* 13

[135] *J. Ennari, M. Elomaa, I. Neelov, and F. Sundholm. Modeling of water-free and water containing solid polyelectrolytes.* Polymer, *41(3):985–990, 2000.* 13

[136] *J. Ennari, I. Neelov, and F. Sundholm. Estimation of the ion conductivity of a peo-based polyelectrolyte system by molecular modeling.* Polymer, *42(19):8043–8050, 2001.* 13

[137] *A. C. T. van Duin, S. Dasgupta, F. Lorant, and W. A. Goddard. Reaxff: A reactive force field for hydrocarbons.* Journal of Physical Chemistry A, *105(41):9396–9409, 2001.* 15, 29, 104

[138] *Andres Jaramillo-Botero, Saber Naserifar, and William A Goddard III. General multiobjective force field optimization framework, with application to reactive force fields for silicon carbide.* Journal of Chemical Theory and Computation, *10(4):1426–1439, 2014.* 15, 87

[139] *A. Jaramillo-Botero. Garffield website, 2016.* 15, 87

[140] *Pierre Sorlier, Anne Denuzire, Christophe Viton, and Alain Domard. Relation between the degree of acetylation and the electrostatic properties of chitin and chitosan.* Biomacromolecules, *2(3):765–772, 2001.* 17

[141] *W. Damm, A. Frontera, J. TiradoRives, and W. L. Jorgensen. Opls all-atom force field for carbohydrates.* Journal of Computational Chemistry, *18(16):1955–1970, 1997.* 18

[142] *William L. Jorgensen, Jeffry D. Madura, and Carol J. Swenson. Optimized intermolecular potential functions for liquid hydrocarbons.* Journal of the American Chemical Society, *106(22):6638–6646, 1984.* 18, 52

[143] *William L. Jorgensen, David S. Maxwell, and Julian Tirado-Rives. Development and testing of the opls all-atom force field on conformational energetics and properties of organic liquids.* Journal of the American Chemical Society, *118(45):11225–11236, 1996.* 18, 52

[144] *R. C. Rizzo and W. L. Jorgensen. Opls all-atom model for amines: Resolution of the amine hydration problem.* Journal of the American Chemical Society, *121(20):4827–4836, 1999.* 18

[145] *Jeremy C. Smith and Martin Karplus. Empirical force field study of geometries and conformational transitions of some organic molecules.* Journal of the American Chemical Society, *114(3):801–812, 1992.* 18

[146] *H. W. Horn, W. C. Swope, J. W. Pitera, J. D. Madura, T. J. Dick, G. L. Hura, and T. Head-Gordon. Development of an improved four-site water model for biomolecular simulations: Tip4p-ew.* Journal of Chemical Physics, *120(20):9665–9678, 2004.* 18, 20

[147] *William L. Jorgensen, Jayaraman Chandrasekhar, Jeffry D. Madura, Roger W. Impey, and Michael L. Klein. Comparison of simple potential functions for simulating liquid water.* The Journal of Chemical Physics, *79(2):926–935, 1983.* 18, 52

[148] *Collin D. Wick and Liem X. Dang. Investigating hydroxide anion interfacial activity by classical and multistate empirical valence bond molecular dynamics simulations.* The Journal of Physical Chemistry A, *113(22):6356–6364, 2009. PMID: 19391589.* 18

[149] *Niels Hansen, Felix A.B. Agbor, and Frerich J. Keil. New force fields for nitrous oxide and oxygen and their application to phase equilibria simulations.* Fluid Phase Equilibria, *259(2):180 – 188, 2007.* 18

[150] *S. Despond, E. Espuche, N. Cartier, and A. Domard. Hydration mechanism of polysaccharides: A comparative study.* Journal of Polymer Science Part B: Polymer Physics, *43(1):48–58, 2005.* 18

[151] *S. Despond, E. Espuche, and A. Domard. Water sorption and permeation in chitosan films: Relation between gas permeability and relative humidity.* Journal of Polymer Science Part B: Polymer Physics, *39(24):3114–3127, 2001.* 18, 36

[152] *R. W. Hockney and J. W. Eastwood.* Computer simulation using particles. *Taylor & Francis, Inc., 1988.* 18, 52

[153] *S. J. Plimpton. Large-scale atomistic/molecular massively parallel simulator (lammps) website, 2016.* 18, 24, 53, 87

[154] *Steve Plimpton. Fast parallel algorithms for short-range molecular dynamics.* Journal of Computational Physics, *117(1):1 – 19, 1995.* 18, 24, 53, 87

[155] *M. Tuckerman, B. J. Berne, and G. J. Martyna. Reversible multiple time scale molecular dynamics.* The Journal of Chemical Physics, *97(3):1990–2001, 1992.* 18, 53

[156] *H. C. Andersen. Rattle - a velocity version of the shake algorithm for molecular-dynamics calculations.* Journal of Computational Physics, *52(1):24–34, 1983.* 18

[157] *J. P. Ryckaert, G. Ciccotti, and H. J. C. Berendsen. Numerical-integration of cartesian equations of motion of a system with constraints - molecular-dynamics of n-alkanes.* Journal of Computational Physics, *23(3):327–341, 1977.* 18

[158] *H. Kamberaj, R. J. Low, and M. P. Neal. Time reversible and symplectic integrators for molecular dynamics simulations of rigid molecules.* Journal of Chemical Physics, *122(22), 2005.* 18

[159] *W. G. Hoover. Canonical dynamics: Equilibrium phase-space distributions.* Physical Review A, *31(3):1695–1697, 1985.* 18, 53

[160] *S. Nos. A unified formulation of the constant temperature molecular dynamics methods.* The Journal of Chemical Physics, *81(1):511–519, 1984.* 18, 53

[161] *G. J. Martyna, D. J. Tobias, and M. L. Klein. Constant pressure molecular dynamics algorithms.* The Journal of Chemical Physics, *101(5):4177–4189, 1994.* 18, 53

[162] *M. Parrinello and A. Rahman. Polymorphic transitions in single crystals: A new molecular dynamics method.* Journal of Applied Physics, *52(12):7182–7190, 1981.* 18, 53

[163] *W. Shinoda, M. Shiga, and M. Mikami. Rapid estimation of elastic constants by molecular dynamics simulation under constant stress.* Physical Review B, *69(13):134103, 2004.* 18, 53

[164] *M. E. Tuckerman, J. Alejandre, R. Lpez-Rendn, A. L. Jochim, and G. J. Martyna. A liouville-operator derived measure-preserving integrator for molecular dynamics simulations in the isothermalisobaric ensemble.* Journal of Physics A: Mathematical and General, *39(19):5629, 2006.* 18, 53

[165] *R. O. Dror, R. M. Dirks, J. P. Grossman, H. Xu, and D. E. Shaw.* Biomolecular Simulation: A Computational Microscope for Molecular Biology, *volume 41 of* Annual Review of Biophysics, *pages 429–452. 2012.* 19

[166] *T. C. Germann and K. Kadau. Trillion-atom molecular dynamics becomes a reality.* International Journal of Modern Physics C, *19(9):1315–1319, 2008.* 19

[167] *J. Dean and S. Ghemawat. Mapreduce: Simplified data processing on large clusters.* Communications of the Acm, *51(1):107–113, 2008.* 19

[168] *J. Dean and S. Ghemawat. Mapreduce: A flexible data processing tool.* Communications of the Acm, *53(1):72–77, 2010.* 19

[169] *J. Dean, S. Ghemawat, and Usenix.* MapReduce: Simplified data processing on large clusters. *USENIX Association Proceedings of the Sixth Symposium on Operating Systems Design and Implementation. 2004.* 19

[170] *T. Tu, C. A. Rendleman, D. W. Borhani, R. O. Dror, J. Gullingsrud, M. O. Jensen, J. L. Klepeis, P. Maragakis, P. Miller, and K. A.et al. Stafford. A scalable parallel framework for analyzing terascale molecular dynamics simulation trajectories.* International Conference for High Performance Computing, Networking, Storage and Analysis, *pages 432–443, 2008.* 19

[171] *S. J. Plimpton. Mapreduce-mpi library website, 2016.* 19, 20

[172] *S. J. Plimpton and K. D. Devine. Mapreduce in mpi for large-scale graph algorithms.* Parallel Computing, *37(9):610–632, 2011.* 19, 20

[173] *S. J. Plimpton and T. Shead. Streaming data analytics via message passing with application to graph algorithms.* Journal of Parallel and Distributed Computing, *74(8):2687–2698, 2014.* 19, 20

[174] *E. M. Calvo-Munoz, M. E. Selvan, R. Xiong, M. Ojha, D. J. Keffer, D. M. Nicholson, and T. Egami. Applications of a general random-walk theory for confined diffusion.* Physical Review E: Statistical Physics, Plasmas, Fluids, and Related Interdisciplinary Topics, *83(1), 2011.* 20, 40

[175] *Y.-L. Wang, R. S. Lawrence, Z.-Y. Lu, and A. Laaksonen. Molecular dynamics study of aqueous solution of polyethylene oxide: Critical test of force field models.* Soft Materials, *11(4):371–383, 2013.* 20

[176] *C. Chipot and A. Pohorille.* Free Energy Calculations: Theory and Applications in Chemistry and Biology. *Springer Series in Chemical Physics. Springer-Verlag Berlin Heidelberg, 2007.* 21, 35

[177] *D. Frenkel and B. Smit.* Chapter 7 - Free Energy Calculations, *pages 167–200. Academic Press, San Diego, 2002.* 21

[178] *B. Widom. Some topics in the theory of fluids.* The Journal of Chemical Physics, *39(11):2808–2812, 1963.* 21, 23

[179] *G. C. Boulougouris, I. G. Economou, and D. N. Theodorou. On the calculation of the chemical potential using the particle deletion scheme.* Molecular physics, *96(6):905–913, 1999.* 21, 23, 25

[180] *G. C. Boulougouris, I. G. Economou, and D. N. Theodorou. Calculation of the chemical potential of chain molecules using the staged particle deletion scheme.* Journal of Chemical Physics, *115(17):8231–8237, 2001.* 21, 23, 24

[181] *G. C. Boulougouris, E. C. Voutsas, I. G. Economou, D. N. Theodorou, and D. P. Tassios. Henry's constant analysis for water and nonpolar solvents from experimental data, macroscopic models, and molecular simulation.* Journal of Physical Chemistry B, *105(32):7792–7798, 2001.* 21, 23

[182] *M. G. De Angelis, G. C. Boulougouris, and D. N. Theodorou. Prediction of infinite dilution benzene solubility in linear polyethylene melts via the direct particle deletion method.* Journal of Physical Chemistry B, *114(19):6233–6246, 2010.* 21, 23, 25

[183] *K. Shing and K. E. Gubbins. The chemical potential in dense fluids and fluid mixtures via computer simulation.* Molecular Physics, *46(5):1109–1128, 1982.* 21, 23

[184] *T. Spyriouni, G. C. Boulougouris, and D. N. Theodorou. Prediction of sorption of co2 in glassy atactic polystyrene at elevated pressures through a new computational scheme.* Macromolecules, *42(5):1759–1769, 2009.* 21, 23, 25

[185] *G. C. Boulougouris. Calculation of the chemical potential beyond the first-order free-energy perturbation: from deletion to reinsertion.* Journal of Chemical and Engineering Data, *55(10):4140–4146, 2010.* 21

[186] *G. C. Boulougouris. On the estimation of the free energy, from a single equilibrium statistical ensemble, via particle reinsertion.* Journal of Physical Chemistry B, *116(3):997–1006, 2012.* 21

[187] *J. G. Kirkwood. Statistical mechanics of fluid mixtures.* Journal of Chemical Physics, *3(5):300–313, 1935.* 21

[188] *J.G. Kirkwood and B.J. Alder.* Theory of liquids. *Documents on modern physics. Gordon and Breach, 1968.* 21

[189] *R. W. Zwanzig. High-temperature equation of state by a perturbation method. i. nonpolar gases.* Journal of Chemical Physics, *22(8):1420–1426, 1954.* 21

[190] *M. Mezei. The finite difference thermodynamic integration, tested on calculating the hydration free energy difference between acetone and dimethylamine in water.* Journal of Chemical Physics, *86(12):7084–7088, 1987.* 21

[191] *A. Z. Panagiotopoulos. Direct determination of fluid-phase equilibria by simulation in the gibbs ensemble - a review.* Molecular Simulation, *9(1):1–23, 1992.* 21

[192] *A. Z. Panagiotopoulos, N. Quirke, M. Stapleton, and D. J. Tildesley. Phase-equilibria by simulation in the gibbs ensemble - alternative derivation, generalization and application to mixture and membrane equilibria.* Molecular Physics, *63(4):527–545, 1988.* 21

[193] *D. A. Kofke. Gibbs-duhem integration - a new method for direct evaluation of phase coexistence by molecular simulation.* Molecular Physics, *78(6):1331–1336, 1993.* 21

[194] *C. H. Bennett. Efficient estimation of free energy differences from monte carlo data.* Journal of Computational Physics, *22(2):245–268, 1976.* 21

[195] *T. C. Beutler, A. E. Mark, R. C. Vanschaik, P. R. Gerber, and W. F. Vangunsteren. Avoiding singularties and numerical instabilities in free-energy calculations based on molecular simulations.* Chemical Physics Letters, *222(6):529–539, 1994.* 22

[196] *M. R. Shirts and V. S. Pande. Solvation free energies of amino acid side chain analogs for common molecular mechanics water models.* Journal of Chemical Physics, *122(13), 2005.* 22

[197] *D. A. Kofke and P. T. Cummings. Quantitative comparison and optimization of methods for evaluating the chemical potential by molecular simulation.* Molecular Physics, *92(6):973–996, 1997.* 23, 35

[198] *M. R. Siegert, M. Heuchel, and D. Hofmann. A generalized direct-particle-deletion scheme for the calculation of chemical potential and solubilities of small- and medium-sized molecules in amorphous polymers.* Journal of Computational Chemistry, *28(5):877–889, 2007.* 23, 24

[199] *L. R. Dodd and D. N. Theodorou. Analytical treatment of the volume and surface-area of molecules formed by an arbitrary collection of unequal spheres intersected by planes.* Molecular Physics, *72(6):1313–1345, 1991.* 24

[200] *T. P. Senftle, S. Hong, M. M. Islam, S. B. Kylasa, Y. Zheng, Y. K. Shin, C. Junkermeier, R. Engel-Herbert, M. J. Janik, and H. M.et al. Aktulga. The reaxff reactive force-field: development, applications and future directions.* NPJ Computational Materials, *2:15011, 2016.* 29, 85, 86, 87, 104

[201] *M. L. Laury, L.-P. Wang, V. S. Pande, T. Head-Gordon, and J. W. Ponder. Revised parameters for the amoeba polarizable atomic multipole water model.* Journal of Physical Chemistry B, *119(29):9423–9437, 2015.* 29, 37, 104

[202] *J. W. Ponder, C. Wu, P. Ren, V. S. Pande, J. D. Chodera, M. J. Schnieders, I. Haque, D. L. Mobley, D. S. Lambrecht, and Jr.et al. DiStasio, R. A. Current status of the amoeba polarizable force field.* Journal of Physical Chemistry B, *114(8):2549–2564, 2010.* 29, 37, 104

[203] *D. A. Kofke and P. T. Cummings. Precision and accuracy of staged free-energy perturbation methods for computing the chemical potential by molecular simulation.* Fluid Phase Equilibria, *150:41–49, 1998.* 35

[204] *C. T. Lee, J. Comer, C. Herndon, N. Leung, A. Pavlova, R. V. Swift, C. Tung, C. N. Rowley, R. E. Amaro, and C.et al. Chipot. Simulation-based approaches for determining membrane permeability of small compounds.* Journal of Chemical Information and Modeling, *56(4):721–733, 2016.* 35, 37

[205] *N. D. Lu, J. K. Singh, and D. A. Kofke. Appropriate methods to combine forward and reverse free-energy perturbation averages.* Journal of Chemical Physics, *118(7):2977–2984, 2003.* 35

[206] *A. E. Pavlath, D. S. W. Wong, and T. F. Kumosinski. New coatings for cut fruits and vegetables.* Chemtech, *23(2):36–40, 1993.* 36

[207] *N. Gontard, R. Thibault, B. Cuq, and S. Guilbert. Influence of relative humidity and film composition on oxygen and carbon dioxide permeabilities of edible films.* Journal of Agricultural and Food Chemistry, *44(4):1064–1069, 1996.* 36, 37

[208] *R. Xiong, D. J. Keffer, M. Fuentes-Cabrera, D. M. Nicholson, A. Michalkova, T. Petrova, J. Leszczynski, K. Odbadrakh, B. L. Doss, and J. P. Lewis. Effect of charge distribution on rdx adsorption in irmof-10.* Langmuir, *26(8):5942–5950, 2010.* 37

[209] *Scott Kirkpatrick. Percolation and conduction.* Rev. Mod. Phys., *45:574–588, Oct 1973.* 39

[210] *Muhammad Sahimi, Barry D. Hughes, L. E. Scriven, and H. T. Davis. Stochastic transport in disordered systems.* The Journal of Chemical Physics, *78(11):6849–6864, 1983.* 39

[211] *J.O.M. Bockris and A.K.N. Reddy.* Modern Electrochemistry. *Number v. 2, pt. 1 in Modern Electrochemistry. Plenum Press, 1998.* 39

[212] *T. Dippel and K. D. Kreuer. Proton transport mechanism in concentrated aqueous solutions and solid hydrates of acids.* Solid State Ionics, *46:3–9, 1991.* 40

[213] *M. Esai Selvan, D.J. Keffer, S. Cui, and S.J. Paddison. Proton transport in water confined in carbon nanotubes: a reactive molecular dynamics study.* Molecular Simulation, *36(7-8):568–578, 2010. 40, 41, 42, 45*

[214] *J. Liu, N. Suraweera, D. J. Keffer, S. Cui, and S. J. Paddison. On the relationship between polymer electrolyte structure and hydrated morphology of perfluorosulfonic acid membranes.* J. Phys. Chem. C, *114(25):11279–11292, 2010. 40, 48, 50*

[215] *R.A. Robinson and R.H. Stokes.* Electrolyte Solutions: Second Revised Edition. *Dover Books on Chemistry Series. Dover Publications, Incorporated, 2012. 41*

[216] *Manfred Holz, Stefan R. Heil, and Antonio Sacco. Temperature-dependent self-diffusion coefficients of water and six selected molecular liquids for calibration in accurate 1h nmr pfg measurements.* Phys. Chem. Chem. Phys., *2:4740–4742, 2000. 41*

[217] *Myvizhi Esai Selvan, David J. Keffer, and Shengting Cui. Reactive molecular dynamics study of proton transport in polymer electrolyte membranes.* The Journal of Physical Chemistry C, *115(38):18835–18846, 2011. 40, 42, 103*

[218] *C. J. T. Grotthuss. Theory of decomposition of liquids by electrical currents.* Ann. Chim., *58:54–74, 1806. 41*

[219] *Myvizhi Esai Selvan, M.Selvan, David J. Keffer, Shengting Cui, and Stephen J. Paddison. A reactive molecular dynamics algorithm for proton transport in aqueous systems.* The Journal of Physical Chemistry C, *114(27):11965–11976, 2010. 41, 42*

[220] *M. K. Petersen and G. A. Voth. Amphiphilic character of the hydrated proton in methanol-water solutions.* The Journal of Physical Chemistry B, *110(14):7085–7089, 2006. 42, 69*

[221] *B. D. Cornish and R. J. Speedy. Proton conductivity in supercooled aqueous hcl solutions.* J. Phys. Chem. B, *88:1888–1892, 1984. 45*

[222] *C. Dellago, M. M. Naor, and G. Hummer. Proton transport through water-filled carbon nanotubes.* Physical Review Letters, *90(10), 2003. 45*

[223] *Seung Soon Jang, Valeria Molinero, Tahir Cagn, and William A. Goddard. Nanophase-segregation and transport in nafion 117 from molecular dynamics simulations: Effect of monomeric sequence.* The Journal of Physical Chemistry B, *108(10):3149–3157, 2004. 50*

[224] *S. J. Paddison and J. A. Elliott. Molecular modeling of the short-side-chain perfluorosulfonic acid membrane.* J. Phys. Chem. A, *109(33):7583–7593, 2005. 50*

[225] *S. J. Paddison and J. A. Elliott. On the consequences of side chain flexibility and backbone conformation on hydration and proton dissociation in perfluorosulfonic acid membranes.* Phys. Chem. Chem. Phys., *8(18):2193–2203, 2006.* 50

[226] *R. Marschall, I. Bannat, J. Caro, and M. Wark. Proton conductivity of sulfonic acid functionalised mesoporous materials.* Microporous and Mesoporous Materials, *99(1-2):190–196, 2007.* 50

[227] *M. Sharifi, M. Wark, D. Freude, and J. Haase. Highly proton conducting sulfonic acid functionalized mesoporous materials studied by impedance spectroscopy, mas nmr spectroscopy and mas pfg nmr diffusometry.* Microporous and Mesoporous Materials, *156:80–89, 2012.* 50

[228] *K. Burke. Perspective on density functional theory.* The Journal of Chemical Physics, *136(15):150901, 2012.* 52

[229] *G. Paolo, B. Stefano, B. Nicola, C. Matteo, C. Roberto, C. Carlo, C. Davide, L. C. Guido, C. Matteo, and D.et al. Ismaila. Quantum espresso: a modular and open-source software project for quantum simulations of materials.* Journal of Physics: Condensed Matter, *21(39):395502, 2009.* 52

[230] *Dominik Marx, Mark E. Tuckerman, Jrg Hutter, and Michele Parrinello. The nature of the hydrated excess proton in water.* Nature, *397(6720):601, 1999.* 52, 62, 72, 93, 104

[231] *William L. Jorgensen, Jakob P. Ulmschneider, and Julian Tirado-Rives. Free energies of hydration from a generalized born model and an all-atom force field.* The Journal of Physical Chemistry B, *108(41):16264–16270, 2004.* 52

[232] *Eyal Neria, Stefan Fischer, and Martin Karplus. Simulation of activation free energies in molecular systems.* The Journal of Chemical Physics, *105(5):1902–1921, 1996.* 52

[233] *Shingo Urata, Jun Irisawa, Akira Takada, Wataru Shinoda, Seiji Tsuzuki, and Masuhiro Mikami. Molecular dynamics simulation of swollen membrane of perfluorinated ionomer.* The Journal of Physical Chemistry B, *109(9):4269–4278, 2005.* 52

[234] *A. I. Jewett, Z. Zhuang, and J.-E. Shea. Moltemplate a coarse-grained model assembly tool.* Biophysical Journal, *104(2, Supplement 1):169a, 2013.* 53

[235] *S. K. Begum, R. J. Clarke, M. S. Ahmed, S. Begum, and M. A. Saleh. Volumetric, viscosimetric and surface properties of aqueous solutions of triethylene glycol, tetraethylene glycol, and tetraethylene glycol dimethyl ether.* Journal of Molecular Liquids, *177:11–18, 2013.* 53

[236] *J. P. Perdew, J. A. Chevary, S. H. Vosko, K. A. Jackson, M. R. Pederson, D. J. Singh, and C. Fiolhais. Erratum: Atoms, molecules, solids, and surfaces: Applications of the generalized gradient approximation for exchange and correlation.* Physical Review B, *48(7):4978–4978, 1993.* 53

[237] *J. P. Perdew and Y. Wang. Accurate and simple analytic representation of the electron-gas correlation energy.* Physical Review B, *45(23):13244–13249, 1992.* 53

[238] *K. Laasonen, R. Car, C. Lee, and D. Vanderbilt. Implementation of ultrasoft pseudopotentials in ab initio molecular dynamics.* Physical Review B, *43(8):6796–6799, 1991.* 54

[239] *D. Vanderbilt. Soft self-consistent pseudopotentials in a generalized eigenvalue formalism.* Physical Review B, *41(11):7892–7895, 1990.* 54

[240] *J. P. Perdew, K. Burke, and M. Ernzerhof. Generalized gradient approximation made simple.* Physical Review Letters, *77(18):3865–3868, 1996.* 54

[241] *J. P. Perdew, K. Burke, and M. Ernzerhof. Generalized gradient approximation made simple [phys. rev. lett. 77, 3865 (1996)].* Physical Review Letters, *78(7):1396–1396, 1997.* 54

[242] *N. Troullier and J. L. Martins. Efficient pseudopotentials for plane-wave calculations.* Physical Review B, *43(3):1993–2006, 1991.* 54

[243] *A. Tkatchenko, R. A. DiStasio, R. Car, and M. Scheffler. Accurate and efficient method for many-body van der waals interactions.* Physical Review Letters, *108(23):236402, 2012.* 54

[244] *A. Tkatchenko and M. Scheffler. Accurate molecular van der waals interactions from ground-state electron density and free-atom reference data.* Physical Review Letters, *102(7):073005, 2009.* 54

[245] *A. D. Becke. Density-functional exchange-energy approximation with correct asymptotic behavior.* Physical Review A, *38(6):3098–3100, 1988.* 54

[246] *C. Lee, W. Yang, and R. G. Parr. Development of the colle-salvetti correlation-energy formula into a functional of the electron density.* Physical Review B, *37(2):785–789, 1988.* 54

[247] *A. Chandra, M. E. Tuckerman, and D. Marx. Connecting solvation shell structure to proton transport kinetics in hydrogen-bonded networks via population correlation functions.* Physical Review Letters, *99(14):145901, 2007.* 54, 72, 75, 76, 80

[248] *M. E. Tuckerman, A. Chandra, and D. Marx. A statistical mechanical theory of proton transport kinetics in hydrogen-bonded networks based on population correlation functions with applications to acids and bases.* The Journal of Chemical Physics, *133(12):124108, 2010.* 54, 72, 75, 76, 80

[249] *W. Ekardt. Work function of small metal particles: Self-consistent spherical jellium-background model.* Physical Review B, *29(4):1558–1564, 1984.* 54

[250] *R. A. DiStasio, B. Santra, Z. Li, X. Wu, and R. Car. The individual and collective effects of exact exchange and dispersion interactions on the ab initio structure of liquid water.* The Journal of Chemical Physics, *141(8):084502, 2014.* 54, 57

[251] *J. C. Grossman, E. Schwegler, E. W. Draeger, F. Gygi, and G. Galli. Towards an assessment of the accuracy of density functional theory for first principles simulations of water.* The Journal of Chemical Physics, *120(1):300–311, 2004.* 54

[252] *I. F. W. Kuo, C. J. Mundy, M. J. McGrath, J. I. Siepmann, J. VandeVondele, M. Sprik, J. Hutter, B. Chen, M. L. Klein, and F.et al. Mohamed. Liquid water from first principles: Investigation of different sampling approaches.* The Journal of Physical Chemistry B, *108(34):12990–12998, 2004.* 54

[253] *E. Schwegler, J. C. Grossman, F. Gygi, and G. Galli. Towards an assessment of the accuracy of density functional theory for first principles simulations of water.ii.* The Journal of Chemical Physics, *121(11):5400–5409, 2004.* 54

[254] *G. J. Martyna, M. L. Klein, and M. Tuckerman. Noshoover chains: The canonical ensemble via continuous dynamics.* The Journal of Chemical Physics, *97(4):2635–2643, 1992.* 55

[255] *Y. Marcus. Thermodynamic functions of transfer of single ions from water to non-aqueous and mixed solvents (based on an extrathermodynamic assumption): Part 5 - gibbs energies of transfer into aqueous alcohols.* Pure and Applied Chemistry, *62(5):899, 1990.* 62, 88

[256] *Udo W. Schmitt and Gregory A. Voth. The computer simulation of proton transport in water.* Journal of Chemical Physics, *111(20):9361, 1999.* 62

[257] *T. J. F. Day, A. V. Soudackov, M. uma, U. W. Schmitt, and G. A. Voth. A second generation multistate empirical valence bond model for proton transport in aqueous systems.* The Journal of Chemical Physics, *117(12):5839–5849, 2002.* 62

[258] *C. Knight, G. E. Lindberg, and G. A. Voth. Multiscale reactive molecular dynamics.* The Journal of Chemical Physics, *137(22):22A525, 2012.* 62

[259] *Udo W. Schmitt and Gregory A. Voth. Multistate empirical valence bond model for proton transport in water.* The Journal of Physical Chemistry B, *102(29):5547–5551, 1998.* 62

[260] *M. E. Tuckerman and D. Marx. On the quantum nature of the shared proton in hydrogen bonds.* Science, *275(5301):817–820, 1997.* 62

[261] *N. Agmon. Correction.* Journal of Physical Chemistry, *96(4):2020–2020, 1992.* 66

[262] *N. Agmon, D. Huppert, A. Masad, and E. Pines. Excited-state proton transfer to methanol-water mixtures.* The Journal of Physical Chemistry, *95(25):10407–10413, 1991.* 66

[263] *H. Lapid, N. Agmon, M. K. Petersen, and G. A. Voth. A bond-order analysis of the mechanism for hydrated proton mobility in liquid water.* The Journal of Chemical Physics, *122(1):014506, 2005.* 67

[264] *R. Shevchuk, N. Agmon, and F. Rao. Network analysis of proton transfer in liquid water.* The Journal of Chemical Physics, *140(24):244502, 2014.* 67

[265] *S. Iuchi, H. Chen, F. Paesani, and G. A. Voth. Hydrated excess proton at water-hydrophobic interfaces.* The Journal of Physical Chemistry B, *113(13):4017–4030, 2009.* 69

[266] *K. N. Kudin and R. Car. Why are water-hydrophobic interfaces charged?* Journal of the American Chemical Society, *130(12):3915–3919, 2008.* 69

[267] *M. K. Petersen, S. S. Iyengar, T. J. F. Day, and G. A. Voth. The hydrated proton at the water liquid/vapor interface.* The Journal of Physical Chemistry B, *108(39):14804–14806, 2004.* 69

[268] *C. Zhang, D. G. Knyazev, Y. A. Vereshaga, E. Ippoliti, T. H. Nguyen, P. Carloni, and P. Pohl. Water at hydrophobic interfaces delays proton surface-to-bulk transfer and provides a pathway for lateral proton diffusion.* Proceedings of the National Academy of Sciences, *109(25):9744–9749, 2012.* 71, 96

[269] *A. Luzar and D. Chandler. Hydrogen-bond kinetics in liquid water.* Nature, *379(6560):55–57, 1996.* 76

[270] *D. C. Rapaport. Hydrogen bonds in water.* Molecular Physics, *50(5):1151–1162, 1983.* 76

[271] *H. Chen, G. A. Voth, and N. Agmon. Kinetics of proton migration in liquid water.* The Journal of Physical Chemistry B, *114(1):333–339, 2010.* 76, 80

[272] *A. Bankura and A. Chandra. A first principles molecular dynamics study of the solvation structure and migration kinetics of an excess proton and a hydroxide ion in binary water-ammonia mixtures.* The Journal of Chemical Physics, *136(11):114509, 2012.* 76

[273] *M. J. Wiedemair, M. Hitzenberger, and T. S. Hofer. Tuning the reactivity of a dissociative force field: proton transfer properties of aqueous h3o+ and their dependence on the three-body interaction.* Physical Chemistry Chemical Physics, *17(16):10934–10943, 2015.* 76

[274] *M. Valiev, E. J. Bylaska, N. Govind, K. Kowalski, T. P. Straatsma, H. J. J. Van Dam, D. Wang, J. Nieplocha, E. Apra, T. L. Windus, and W. A. de Jong. NWChem: A comprehensive and scalable open-source solution for large scale molecular simulations.* Computer Physics Communications, *181:1477–1489, September 2010.* 86, 97

[275] *S. R. Bahn and K. W. Jacobsen. An object-oriented scripting interface to a legacy electronic structure code.* Comput. Sci. Eng., *4(3):56–66, MAY-JUN 2002.* 86, 97

[276] *Jacobsen K. W. Mortensen J. J. Atomic simulation environment website, 2016.* 86, 97

[277] *Axel D. Becke. Densityfunctional thermochemistry. iii. the role of exact exchange.* The Journal of Chemical Physics, *98(7):5648–5652, 1993.* 86, 97

[278] *R. Ditchfield, W. J. Hehre, and J. A. Pople. Selfconsistent molecularorbital methods. ix. an extended gaussiantype basis for molecularorbital studies of organic molecules.* The Journal of Chemical Physics, *54(2):724–728, 1971.* 86, 97

[279] *Vyacheslav S. Bryantsev, Mamadou S. Diallo, Adri C. T. van Duin, and III William A. Goddard. Evaluation of b3lyp, x3lyp, and m06-class density functionals for predicting the binding energies of neutral, protonated, and deprotonated water clusters.* Journal of Chemical Theory and Computation, *5(4):1016–1026, 2009. PMID: 26609610.* 86

[280] *Adri C. T. van Duin, Jan M. A. Baas, and Bastiaan van de Graaf. Delft molecular mechanics: a new approach to hydrocarbon force fields. inclusion of a geometry-dependent charge calculation.* J. Chem. Soc., Faraday Trans., *90:2881–2895, 1994.* 86

[281] *Henrik R Larsson, Adri CT Duin, and Bernd Hartke. Global optimization of parameters in the reactive force field reaxff for sioh.* Journal of computational chemistry, *34(25):2178–2189, 2013.* 87

[282] *Mark Dittner, Julian Müller, Hasan Metin Aktulga, and Bernd Hartke. Efficient global optimization of reactive force-field parameters.* Journal of computational chemistry, *36(20):1550–1561, 2015.* 87

[283] *Betsy M Rice, James P Larentzos, Edward FC Byrd, and N Scott Weingarten. Parameterizing complex reactive force fields using multiple objective evolutionary strategies (moes): Part 2: Transferability of reaxff models to c–h–n–o energetic materials.* Journal of chemical theory and computation, *11(2):392–405, 2015.* 87

[284] *Murray S. Daw, Stephen M. Foiles, and Michael I. Baskes. The embedded-atom method: a review of theory and applications.* Materials Science Reports, *9(7):251 – 310, 1993.* 87

[285] *Tzu-Ray Shan, Bryce D Devine, Travis W Kemper, Susan B Sinnott, and Simon R Phillpot. Charge-optimized many-body potential for the hafnium/hafnium oxide system.* Physical Review B, *81(12):125328, 2010.* 87

[286] *Susanna Monti, Adri CT van Duin, Sung-Yup Kim, and Vincenzo Barone. Exploration of the conformational and reactive dynamics of glycine and diglycine on tio2: computational investigations in the gas phase and in solution.* The Journal of Physical Chemistry C, *116(8):5141–5150, 2012.* 87

[287] *Leandro Martínez, Ricardo Andrade, Ernesto G Birgin, and José Mario Martínez. Packmol: a package for building initial configurations for molecular dynamics simulations.* Journal of computational chemistry, *30(13):2157–2164, 2009.* 89

[288] *H. J. C. Berendsen, J. P. M. Postma, W. F. v. Gunsteren, A. DiNola, and J. R. Haak. Molecular dynamics with coupling to an external bath.* Journal Chem Phys, *81, 1984.* 90

[289] *N. K. Roberts and H. L. Northey. Proton and deuteron mobility in normal and heavy water solutions of electrolytes.* Journal of the Chemical Society, Faraday Transactions 1: Physical Chemistry in Condensed Phases, *70(0):253–262, 1974.* 95

[290] *Yun Kyung Shin, Hyunwook Kwak, Alex V. Vasenkov, Debasis Sengupta, and Adri C.T. van Duin. Development of a reaxff reactive force field for fe/cr/o/s and application to oxidation of butane over a pyrite-covered cr2o3 catalyst.* ACS Catalysis, *5(12):7226–7236, 2015.* 97

[291] *S. J. Hamrock and M. A. Yandrasits. Proton exchange membranes for fuel cell applications.* Polymer Reviews, *46(3):219–244, 2006.* 102

Appendix

Appendix A

Distribution of lifetimes in TEG-water mixtures

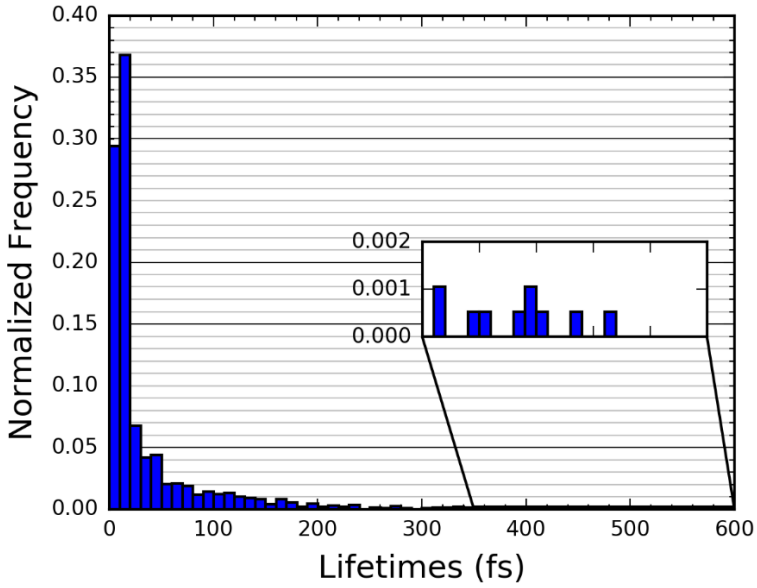


Figure A.1: Normalized distribution of H_3O^+lifetimes in TEG-water mixture for PW91 XC functional.

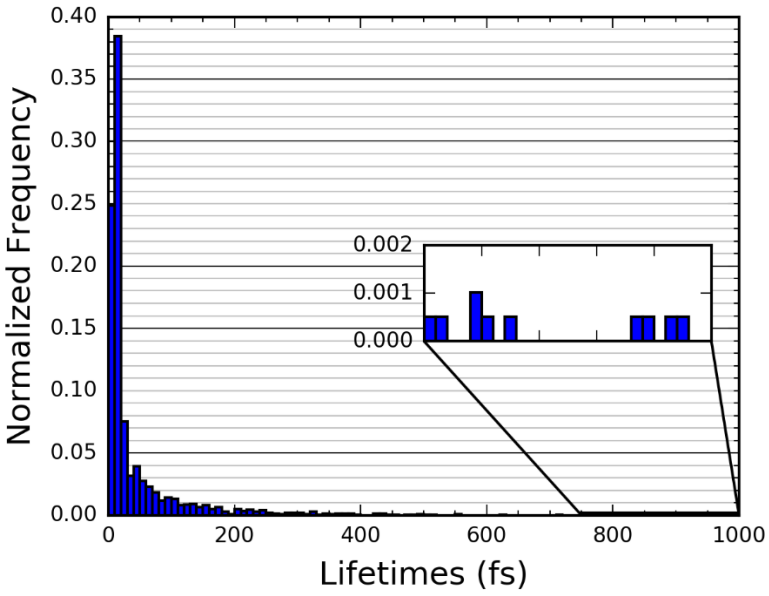


Figure A.2: Normalized distribution of H_3O^+lifetimes in TEG-water mixture for PBE XC functional.

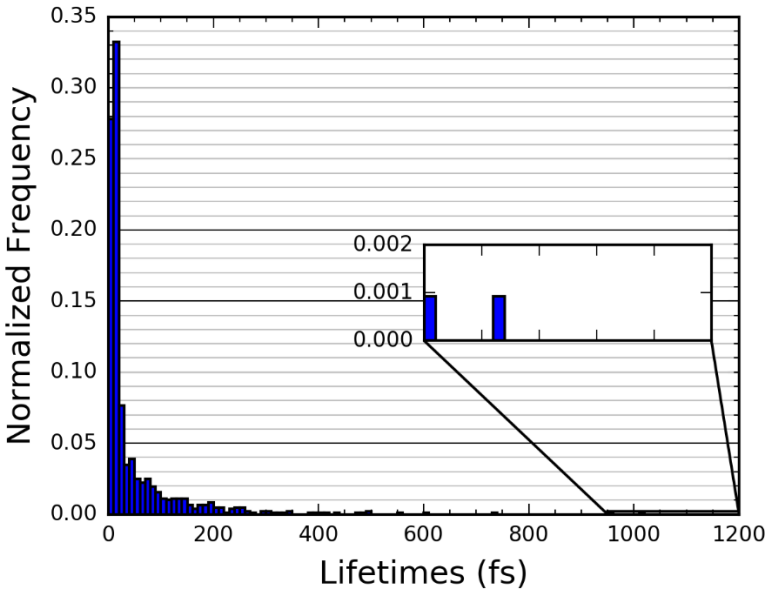


Figure A.3: Normalized distribution of H_3O^+lifetimes in TEG-water mixture for PBE+TS-vdW XC functional.

Appendix B

Free energy change for H^+ to transfer from water to hydroxyl groups of TEG.

Given that we have an excess proton as our ion, H^+, in a solution of water, W, and alcohol, S, we annotate the change in the free energy of transfer for H^+ to be transferred from water (W) to the solvent alcohol S to be $\Delta G(H^+, W \rightarrow S)$. Given the following proton transfer reaction:

$S + WH^+ \leftrightarrow SH^+ + W$

We assume that we can calculate the change in free energy of reaction, ΔG, using the concentration equilibrium constant, K_c, implying we substitute concentrations in place of activities of species. Then, $\Delta G(H^+, W \rightarrow S)$ is given as:

$\Delta G(H^+, W \rightarrow S = G(H^+, S) - G(H^+, W) = -RT\ln\{K_c\} = -RT\ln\left\{\frac{[W][SH^+]}{[S][WH^+]}\right\}$

where R is the gas constant, and T is temperature

Table B.1: The occurrence of water, W, alcohol, S, water with the excess proton ion, WH^+, and the alcohol with the excess proton, SH^+ used to calculate the change in free energy of transfer of H^+, $\Delta G(H^+, W \rightarrow S)$, for all three XC functionals and the average over all three different functionals.

Functional	SH^+	WH^+	W	S	$\Delta G(H^+, W \rightarrow S)$ (kJ/mol)
PW91	0.0043	0.9957	26.0043	1.9957	7.2
PBE	0.0013	0.9987	26.0013	1.9987	10.2
PBE+TS-vdW	0.0003	0.9997	26.0003	1.9997	13.8
					10.4[a]

[a] Average over all three functionals in this work.

Appendix C

Special pairs for TEG-water mixtures with proton rattling included

Table C.1: The occurrences and lifetimes of special pairs made up of the protonated species ($Z_{protonated}$) and the special partner of the protonated species (Z_{shared}) found in aqueous H^+ and triethylene glycol (TEG) systems. Proton rattling effects are included.

Functional	$Z_{protonated}$	Z_{shared}	%	$\sum$ %	Lifetime (fs)
PW91	H_3O^+	H_2O	97.15	97.15	12.3(±12.6)
	H_3O^+	ROH	2.18	99.33	9.1(±9.3)
	ROH_2^+	H_2O	0.53	99.87	10.9(±11.4)
	H_3O^+	OH^-	0.09	99.96	15.6(±13.4)
	H_3O^+	RO^-	0.04	100	7.6(±3.9)
PBE	H_3O^+	H_2O	98.76	98.76	13.5(±14.7)
	H_3O^+	ROH	1.07	99.83	13.0(±14.6)
	ROH_2^+	H_2O	0.14	99.97	12.2(±8.6)
	H_3O^+	OH^-	0.01	99.98	14.8(±12.8)
	H_3O^+	RO^-	0.01	99.99	6.7(±5.8)
	H_3O^+	ROR	0.01	100	20.5 [a]
PBE+TS-vdW	H_3O^+	H_2O	99.49	99.49	12.9(±13.0)
	H_3O^+	ROH	0.46	99.95	10.9(±8.8)
	ROH_2^+	H_2O	0.03	99.98	8.2(±1.5)
	H_3O^+	ROR	0.01	99.99	7.9(±0.8)
	H_3O^+	OH^-	~0.00	100	1.60 [a]

Appendix D

Solvation shells for TEG-water mixture with proton rattling included

Table D.1: The occurrences and lifetimes of solvating shell species ($H_{A,1\text{-}3}$)around the protonated species ($Z_{protonated}$) found in aqueous H^+ and triethylene glycol (TEG) systems. Proton rattling effects are included.

Functional	$Z_{protonated}$	$H_{A,1}$	$H_{A,2}$	$H_{A,3}$	%	$\sum$%	Lifetime (fs)
PW91[a]	H_3O^+	H_2O	H_2O	H_2O	86.21	86.21	22.4(±38.6)
	H_3O^+	ROH	H_2O	H_2O	9.74	95.95	17.4(±26.5)
	H_3O^+	H_2O	H_2O	...	3.05	99.0	33.0(±46.6)
	H_3O^+	ROH	H_2O	...	0.50	99.50	23.8(±36.4)
	$ROH_2{}^+$	H_2O	H_2O	...	0.50	100	18.3(±24.5)
PBE [b]	H_3O^+	H_2O	H_2O	H_2O	85.53	85.53	24.8(±51.4)
	H_3O^+	ROH	H_2O	H_2O	7.98	93.51	27.4(±46.6)
	H_3O^+	H_2O	H_2O	...	6.10	99.61	38.2(±66.9)
	H_3O^+	ROR	H_2O	H_2O	0.21	99.82	13.8(±33.1)
	H_3O^+	H_2O	H_2O	CH_2	0.18	100	25.1(±37.0)
PBE+TS-vdW [c]	H_3O^+	H_2O	H_2O	H_2O	88.51	88.51	21.3(±45.2)
	H_3O^+	H_2O	H_2O	...	5.85	94.36	36.5(±70.8)
	H_3O^+	ROH	H_2O	H_2O	2.17	96.53	22.7(±29.6)
	H_3O^+	ROR	H_2O	H_2O	1.80	98.33	30.2(±49.2)
	H_3O^+	H_2O	H_2O	CH_2	1.67	100	24.7(±51.5)

[a] 12 different solvation shells found

[b] 12 different solvation shells found

[c] 13 different solvation shells found

Appendix E

Probability union relation for determining concentration-dependent site occupation probabilities

There are three ligand/solvation shell sites for the hydronium ion. The probability to occupy one of these sites is not simply the probability to sit on one site but a probability that at least one of the sites is occupied by the species of interest. For our case of hydroxyl occupying one of these sites as an example, we have 2 hydroxyl groups, 36 molecular groups to chose from, and 3 sites to possibly occupy. The probability to occupy just one site is simply 2 (hydroxyls) / 36 (total choices). Yet, if a water molecule sits on one of the sites, then the probability for a hydroxyl to sit on the next site is not 2/36 but 2/35 since one water already occupies a site and is no longer available in the total number of molecular groups to pick from. We therefore used a probability union $P(1 \cup 2 \cup 3)$ relation for occupation of the ligand sites, namely, the probability to occupy site 1 OR site 2 OR site 3, given as $P(1 \cap 2 \cap 3)$

The equation for this probability relation that a given species occupies a site is:

$P(1 \cup 2 \cup 3) = P(1) + P(2) + P(3) - (P(1 \cap 2) - P(1 \cap 3) - P(2 \cap 3) + P(1 \cap 2 \cap 3)$

where $P(X)$ indicates the probability to occupy site X, $P(X \cap Y)$ indicates the probability intersection of both X and Y being occupied, and similar for $P(1 \cap 2 \cap 3)$ We know $P(X) = \frac{2}{36}$. We also know from the definition of the conditional probability, rearranged for the intersection, $P(X \cap Y) = P(X)P(Y|X) = \frac{2}{36} * \frac{1}{35}$. There are only two hydroxyl groups so $P(1 \cap 2 \cap 3) = 0$. We have:

$P(1 \cup 2 \cup 3) = 3 * \frac{2}{36} - 3 * \frac{2}{36} * \frac{1}{35} = 16.2\%$

Neglecting the fact that each hydronium ion has three bond acceptor sites in the first solvation shell underestimates this concentration-dependent probability to occupy ligand/solvation shell sites.

We generalized the probability union equation used for the solvation shell to determine what the probability would be to occupy hydrogen bond network sites. This generalization determines what the probability to occupy any S sites/number of union relations, given N_{total} total species, with $N_species$ for the number of the specific species (ROH in the solvation shell discussion and CH_2 in the hydrogen bond network discussion). This is given as:

$P(S, N_{total}, N_{species} = \sum_{i=1}^{S} (-1)^{i+1} * P_i(i, N_{total}, N_{species} * C_i(i, S)$

Where $P_i(i, N_{total}, N_{species}$ is the probability for the i^{th}-level of intersections and $C_i(i, S)$ gives the combination of i^{th}-level of intersections, both given below as:

$$P_i(i, N_{total}, N_{species} = \frac{N_{species!}}{(N_{species}-i)!} \frac{(N_{total}-i)!}{N_{total}!}$$
$$C_i(i, S) = \frac{S!}{i!*(S-i)!}$$

Appendix F

Hydrogen-bond networks with proton rattling excluded

F.1 Hydrogen-bond networks with proton rattling excluded for TEG-water mixtures

Table F.1: The occurrences and lifetimes of hydrogen-bond networks around protonated species found in TEG-water for PW91. The table lists the protonated species ($Z_{protonated}$), the atom (Z_{shared}) hydrogen bonded to the most active proton, the solvating atoms of the protonated species (HBX,p where x=A or D for accepting or donating a hydrogen bond), and the solvating atoms of Zshared (HBX,s with the same definitions of x). Figure 4.4 provides the illustration to match these labels. Proton rattling effects are excluded.

$Z_{protonated}$	Z_{shared}	$HB_{A,p}$	$HB_{A,p}$	$HB_{D,p}$	$HB_{A,s}$	$HB_{A,s}$	$HB_{D,s}$	%	$\sum$%	Lifetime (ps)
H_3O^+	H_2O	H_2O	H_2O	...	H_2O	H_2O	H_2O	22.87	22.87	2283.12±1101.06
H_3O^+	H_2O	H_2O	H_2O	CH_2	H_2O	H_2O	...	20.98	43.85	618.26±0.00
H_3O^+	H_2O	H_2O	H_2O	...	H_2O	H_2O	...	20.29	64.14	320.46±0.00
H_3O^+	H_2O	H_2O	H_2O	CH_2	H_2O	H_2O	H_2O	8.47	72.62	14.16±4.11
H_3O^+	H_2O	H_2O	H_2O	...	H_2O	H_2O	CH_2	8.18	80.80	1367.45±1343.68
H_3O^+	H_2O	ROH	H_2O	...	H_2O	H_2O	H_2O	5.54	86.34	1092.29±1554.93
H_3O^+	H_2O	H_2O	H_2O	...	ROH	H_2O	...	2.77	89.11	253.81±0.00
H_3O^+	H_2O	ROH	H_2O	...	H_2O	H_2O	CH_2	2.66	91.77	56.48±0.00
H_3O^+	H_2O	H_2O	H_2O	CH_2	ROH	H_2O	H_2O	2.64	94.41	397.12±0.00
H_3O^+	H_2O	H_2O	H_2O	H_2O	H_2O	H_2O	H_2O	2.47	96.88	566.17±241.39
H_3O^+	H_2O	ROH	H_2O	CH_2	H_2O	H_2O	...	1.42	98.30	8083.86±0.00
H_3O^+	H_2O	H_2O	...	...	H_2O	H_2O	H_2O	0.79	99.09	1.45±0.00
H_3O^+	H_2O	H_2O	H_2O	H_2O	ROR	H_2O	H_2O	0.25	99.34	529.40±0.00
H_3O^+	H_2O	H_2O	...	H_2O	H_2O	H_2O	...	0.18	99.52	87.70±0.00
H_3O^+	H_2O	H_2O	H_2O	...	H_2O	CH_2	H_2O	0.14	99.66	4069.67±0.00
H_3O^+	H_2O	H_2O	...	...	ROH	H_2O	...	0.12	99.78	1180.33±0.00
H_3O^+	H_2O	H_2O	...	...	H_2O	...	...	0.08	99.86	756.06±0.00
H_3O^+	H_2O	H_2O	H_2O	H_2O	H_2O	...	H_2O	0.05	99.91	8857.93±0.00
H_3O^+	H_2O	ROH	H_2O	CH_2	H_2O	...	H_2O	0.04	99.95	13.79±0.00
OH^-	H_2O	...	...	H_2O	H_2O	H_2O	H_2O	0.03	99.98	0.87±0.00
H_3O^+	OH^-	H_2O	H_2O	H_2O	H_2O	...	H_2O	0.01	99.99	1902.85±0.00
H_3O^+	H_2O	H_2O	...	...	H_2O	...	H_2O	0.01	~100	1309.56±0.00
OH^-	H_2O	...	...	H_2O	H_2O	H_2O	...	~0.00	100	3.63±0.00

Table F.2: The occurrences and lifetimes of hydrogen-bond networks around protonated species found in TEG-water for PBE. The table lists the protonated species ($Z_{protonated}$), the atom (Z_{shared}) hydrogen bonded to the most active proton, the solvating atoms of the protonated species (HBX,p where x=A or D for accepting or donating a hydrogen bond), and the solvating atoms of Zshared (HBX,s with the same definitions of x). Figure 4.4 provides the illustration to match these labels. Proton rattling effects are excluded.

$Z_{protonated}$	Z_{shared}	$HB_{A,p}$	$HB_{A,p}$	$HB_{D,p}$	$HB_{A,s}$	$HB_{A,s}$	$HB_{D,s}$	%	$\sum$%	Lifetime (ps)
H_3O^+	H_2O	H_2O	H_2O	...	H_2O	H_2O	H_2O	28.04	28.04	1295.47±2548.96
H_3O^+	H_2O	H_2O	H_2O	...	H_2O	H_2O	...	25.89	53.93	473.76±404.90
H_3O^+	H_2O	H_2O	H_2O	...	H_2O	H_2O	CH_2	8.47	62.40	1778.85±0.00
H_3O^+	H_2O	H_2O	H_2O	...	ROH	H_2O	...	6.91	69.31	109.92±0.00
H_3O^+	H_2O	H_2O	H_2O	...	ROH	H_2O	H_2O	6.37	75.68	680.26±0.00
H_3O^+	H_2O	H_2O	H_2O	CH_2	H_2O	H_2O	...	5.38	81.06	523.88±0.00
H_3O^+	H_2O	H_2O	H_2O	...	H_2O	H_2O	ROH	3.95	85.01	2382.51±898.59
H_3O^+	H_2O	H_2O	...	...	H_2O	H_2O	...	2.98	87.99	7258.69±5693.18
H_3O^+	H_2O	H_2O	H_2O	H_2O	H_2O	H_2O	H_2O	2.47	90.46	2893.45±1396.32
H_3O^+	H_2O	H_2O	H_2O	H_2O	H_2O	H_2O	CH_2	2.09	92.55	337.59±0.00
H_3O^+	H_2O	H_2O	...	...	H_2O	H_2O	H_2O	1.80	94.35	7698.21±0.00
H_3O^+	H_2O	H_2O	H_2O	...	H_2O	...	H_2O	1.46	95.81	10.74±0.00
H_3O^+	H_2O	H_2O	H_2O	H_2O	ROH	H_2O	...	1.23	97.04	304.92±249.63
H_3O^+	H_2O	H_2O	...	H_2O	H_2O	H_2O	...	1.13	98.17	1439.51±0.00
H_3O^+	H_2O	ROH	H_2O	...	H_2O	H_2O	H_2O	0.97	99.14	2339.17±0.00
H_3O^+	ROH	H_2O	H_2O	H_2O	H_2O	...	CH_2	0.31	99.45	151.30±79.95
H_3O^+	H_2O	H_2O	H_2O	ROH	H_2O	H_2O	CH_2	0.26	99.71	1993.16±0.00
H_3O^+	ROH	H_2O	H_2O	H_2O	H_2O	...	...	0.21	99.92	50.67±0.00
H_3O^+	ROH	H_2O	H_2O	CH_2	H_2O	...	H_2O	0.08	100	376.79±0.00

Table F.3: The occurrences and lifetimes of hydrogen-bond networks around protonated species found in TEG-water for PBE+TS-vdW. The table lists the protonated species ($Z_{protonated}$), the atom (Z_{shared}) hydrogen bonded to the most active proton, the solvating atoms of the protonated species (HBX,p where x=A or D for accepting or donating a hydrogen bond), and the solvating atoms of Zshared (HBX,s with the same definitions of x). Figure 4.4 provides the illustration to match these labels. Proton rattling effects are excluded.

$Z_{protonated}$	Z_{shared}	$HB_{A,p}$	$HB_{A,p}$	$HB_{D,p}$	$HB_{A,s}$	$HB_{A,s}$	$HB_{D,s}$	%	$\sum$%	Lifetime (ps)
H_3O^+	H_2O	H_2O	H_2O	...	H_2O	H_2O	H_2O	35.61	35.61	813.99±35.43
H_3O^+	H_2O	H_2O	H_2O	...	H_2O	H_2O	...	24.40	60.01	754.39±109.12
H_3O^+	H_2O	H_2O	H_2O	CH_2	H_2O	H_2O	H_2O	10.77	70.78	49.22±0.00
H_3O^+	H_2O	H_2O	H_2O	...	H_2O	H_2O	CH_2	8.00	78.78	4335.24±0.00
H_3O^+	H_2O	H_2O	H_2O	H_2O	H_2O	H_2O	H_2O	6.74	85.52	2371.91±4013.46
H_3O^+	H_2O	H_2O	H_2O	...	ROR	H_2O	H_2O	4.61	90.13	930.30±0.00
H_3O^+	H_2O	H_2O	H_2O	...	H_2O	...	...	4.10	94.23	250.25±117.46
H_3O^+	H_2O	H_2O	H_2O	H_2O	H_2O	...	...	1.79	96.02	1216.49±0.00
H_3O^+	H_2O	ROH	H_2O	...	H_2O	H_2O	H_2O	1.23	97.25	960.21±0.00
H_3O^+	H_2O	H_2O	H_2O	...	H_2O	H_2O	ROH	1.04	98.29	950.19±0.00
H_3O^+	H_2O	H_2O	H_2O	CH_2	H_2O	...	H_2O	1.00	99.29	2613.55±2177.64
H_3O^+	ROH	H_2O	H_2O	...	H_2O	...	...	0.31	99.60	11.33±0.00
H_3O^+	H_2O	H_2O	...	...	H_2O	H_2O	ROH	0.26	99.86	163.64±0.00
H_3O^+	H_2O	H_2O	...	...	H_2O	CH_2	H_2O	0.07	99.93	1363.28±0.00
H_3O^+	ROH	H_2O	H_2O	H_2O	H_2O	...	CH_2	0.04	99.97	127.34±0.00
H_3O^+	H_2O	H_2O	...	...	ROH	H_2O	H_2O	0.03	100	431.53±0.00

Appendix G

Hydrogen-bond networks with proton rattling excluded for bulk water

Table G.1: The occurrences and lifetimes of hydrogen-bond networks around protonated species found in bulk water for PW91. The table lists the protonated species (Z_{prot}), the atom (Z_{shared}) hydrogen bonded to the most active proton, the solvating atoms of the protonated species (HBX,p where x=A or D for accepting or donating a hydrogen bond), and the solvating atoms of Zshared (HBX,s with the same definitions of x). Figure 4.4 provides the illustration to match these labels. Proton rattling effects are excluded.

Z_{prot}	Z_{shared}	$HB_{A,p}$	$HB_{A,p}$	$HB_{D,p}$	$HB_{A,s}$	$HB_{A,s}$	$HB_{D,s}$	%	$\sum$%	Lifetime (ps)
H_3O^+	H_2O	H_2O	H_2O	...	H_2O	H_2O	H_2O	59.96	59.96	974.62±1638.26
H_3O^+	H_2O	H_2O	H_2O	H_2O	H_2O	H_2O	H_2O	30.12	90.08	462.61±939.45
H_3O^+	H_2O	H_2O	H_2O	...	H_2O	H_2O	...	7.21	97.29	1972.40±1842.76
H_3O^+	H_2O	H_2O	H_2O	...	H_2O	...	H_2O	1.39	98.68	21.39±14.93
H_3O^+	H_2O	H_2O	H_2O	H_2O	H_2O	...	H_2O	1.23	99.94	10384.34±10368.24
OH^-	H_2O	...	...	H_2O	H_2O	H_2O	H_2O	0.05	99.99	585.81±292.32
OH^-	H_3O^+	...	...	H_2O	H_2O	H_2O	H_2O	0.01	100	0.44±0.00

Table G.2: The occurrences and lifetimes of hydrogen-bond networks around protonated species found in bulk water for BLYP. The table lists the protonated species (Z_{prot}), the atom (Z_{shared}) hydrogen bonded to the most active proton, the solvating atoms of the protonated species (HBX,p where x=A or D for accepting or donating a hydrogen bond), and the solvating atoms of Zshared (HBX,s with the same definitions of x). Figure 4.4 provides the illustration to match these labels. Proton rattling effects are excluded.

Z_{prot}	Z_{shared}	$HB_{A,p}$	$HB_{A,p}$	$HB_{D,p}$	$HB_{A,s}$	$HB_{A,s}$	$HB_{D,s}$	%	$\sum$%	Lifetime (ps)
H_3O^+	H_2O	H_2O	H_2O	...	H_2O	H_2O	H_2O	49.31	49.31	4118.40±5977.15
H_3O^+	H_2O	H_2O	H_2O	...	H_2O	H_2O	...	31.40	80.71	1126.97±1106.77
H_3O^+	H_2O	H_2O	H_2O	H_2O	H_2O	H_2O	H_2O	10.50	91.21	1417.06±1536.98
H_3O^+	H_2O	H_2O	H_2O	...	H_2O	...	...	5.59	96.80	2116.00±0.00
H_3O^+	H_2O	H_2O	H_2O	...	H_2O	...	H_2O	3.20	100	300.56±0.00

Table G.3: The occurrences and lifetimes of hydrogen-bond networks around protonated species found in bulk water for PBE. The table lists the protonated species (Z_{prot}), the atom (Z_{shared}) hydrogen bonded to the most active proton, the solvating atoms of the protonated species (HBX,p where x=A or D for accepting or donating a hydrogen bond), and the solvating atoms of Zshared (HBX,s with the same definitions of x). Figure 4.4 provides the illustration to match these labels. Proton rattling effects are excluded.

Z_{prot}	Z_{shared}	$HB_{A,p}$	$HB_{A,p}$	$HB_{D,p}$	$HB_{A,s}$	$HB_{A,s}$	$HB_{D,s}$	%	$\sum$%	Lifetime (ps)
H_3O^+	H_2O	H_2O	H_2O	...	H_2O	H_2O	H_2O	56.55	56.55	1961.56±2648.58
H_3O^+	H_2O	H_2O	H_2O	...	H_2O	H_2O	...	19.27	75.82	1222.98±1670.95
H_3O^+	H_2O	H_2O	H_2O	H_2O	H_2O	H_2O	H_2O	18.44	94.26	1252.52±2491.43
H_3O^+	H_2O	H_2O	H_2O	...	H_2O	...	H_2O	4.04	98.30	87.12±0.00
H_3O^+	H_2O	H_2O	H_2O	H_2O	H_2O	...	H_2O	1.70	100	67.81±0.00

Table G.4: The occurrences and lifetimes of hydrogen-bond networks around protonated species found in bulk water for PBE+TS-vdW. The table lists the protonated species (Z_{prot}), the atom (Z_{shared}) hydrogen bonded to the most active proton, the solvating atoms of the protonated species (HBX,p where x=A or D for accepting or donating a hydrogen bond), and the solvating atoms of Zshared (HBX,s with the same definitions of x). Figure 4.4 provides the illustration to match these labels. Proton rattling effects are excluded.

Z_{prot}	Z_{shared}	$HB_{A,p}$	$HB_{A,p}$	$HB_{D,p}$	$HB_{A,s}$	$HB_{A,s}$	$HB_{D,s}$	%	$\sum$%	Lifetime (ps)
H_3O^+	H_2O	H_2O	H_2O	...	H_2O	H_2O	H_2O	47.18	47.18	826.41±795.25
H_3O^+	H_2O	H_2O	H_2O	...	H_2O	H_2O	...	42.10	89.28	6676.21±4148.56
H_3O^+	H_2O	H_2O	H_2O	H_2O	H_2O	H_2O	H_2O	9.71	98.99	2848.58±2786.24
H_3O^+	H_2O	H_2O	H_2O	H_2O	H_2O	...	H_2O	1.01	100	362.95±62.28

Appendix H

Mechanistic picture for proton transfer among water molecules.

H.1 Time evolution of radial distribution functions leading up to proton transfer events for bulk water

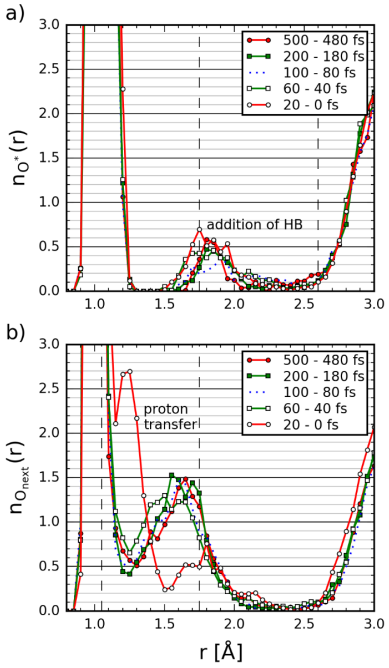


Figure H.1: The RDFs for bulk water using the PW91 XC functional for protonated oxygen in water (O* in (a)) and the next water oxygen to be protonated (O_{next} in (b)) averaged over 20 fs intervals long before proton transfer (500-480 fs) and leading up to proton transfer (200-180 fs, 100-80 fs, 60-40 fs, and 20-0 fs) at 300 K . Specific regions are marked for the proton transfer process and the change in the HB network. Proton rattling events are excluded.

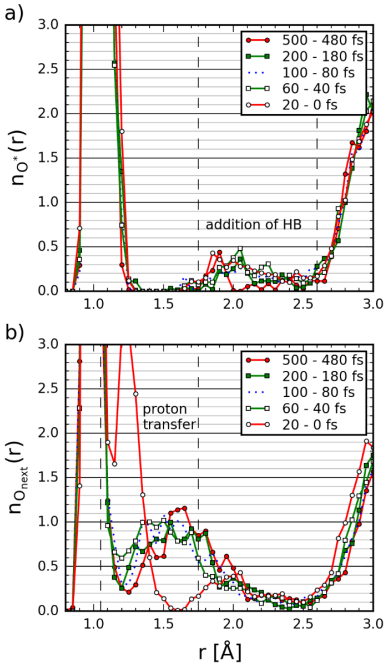


Figure H.2: The RDFs for bulk water using the BLYP XC functional for protonated oxygen in water (O* in (a)) and the next water oxygen to be protonated (O_{next} in (b)) averaged over 20 fs intervals long before proton transfer (500-480 fs) and leading up to proton transfer (200-180 fs, 100-80 fs, 60-40 fs, and 20-0 fs) at 300 K . Specific regions are marked for the proton transfer process and the change in the HB network. Proton rattling events are excluded.

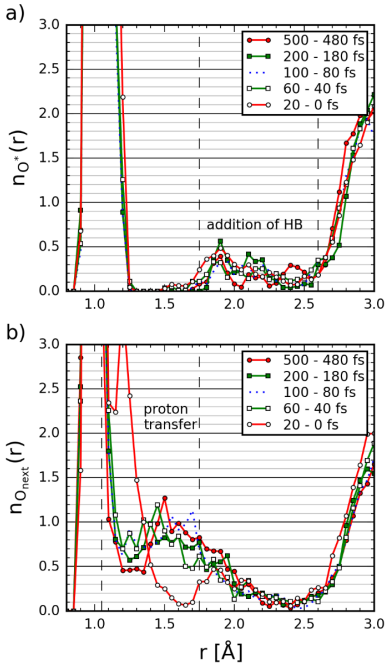


Figure H.3: The RDFs for bulk water using the PBE XC functional for protonated oxygen in water (O* in (a)) and the next water oxygen to be protonated (O_{next} in (b)) averaged over 20 fs intervals long before proton transfer (500-480 fs) and leading up to proton transfer (200-180 fs, 100-80 fs, 60-40 fs, and 20-0 fs) at 300 K . Specific regions are marked for the proton transfer process and the change in the HB network. Proton rattling events are excluded.

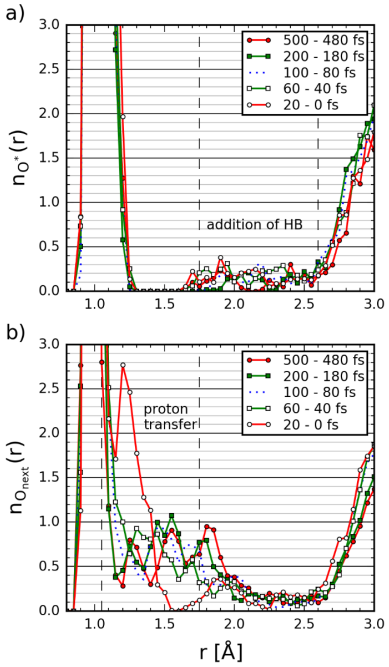


Figure H.4: The RDFs for bulk water using the PBE+TS-vdW XC functional for protonated oxygen in water (O* in (a)) and the next water oxygen to be protonated (O_{next} in (b)) averaged over 20 fs intervals long before proton transfer (500-480 fs) and leading up to proton transfer (200-180 fs, 100-80 fs, 60-40 fs, and 20-0 fs) at 300 K . Specific regions are marked for the proton transfer process and the change in the HB network. Proton rattling events are excluded

H.2 Time evolution of integrated coordination numbers leading up to proton transfer events for water-water proton transfer for bulk water

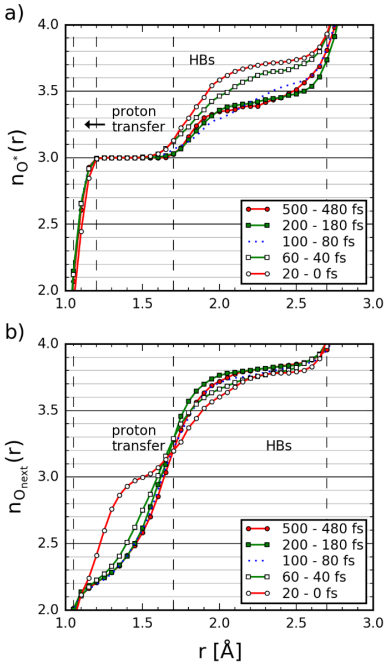


Figure H.5: The ICNs for bulk water using the PW91 XC functional for protonated oxygen in water (O* in (a)) and the next water oxygen to be protonated (O_{next} in (b)) averaged over 20 fs intervals long before proton transfer (500-480 fs) and leading up to proton transfer (200-180 fs, 100-80 fs, 60-40 fs, and 20-0 fs) at 300 K . The integration is over the RDF in Figure S5. Specific regions are marked for the proton transfer process and the change in the HB network. Proton rattling events are excluded.

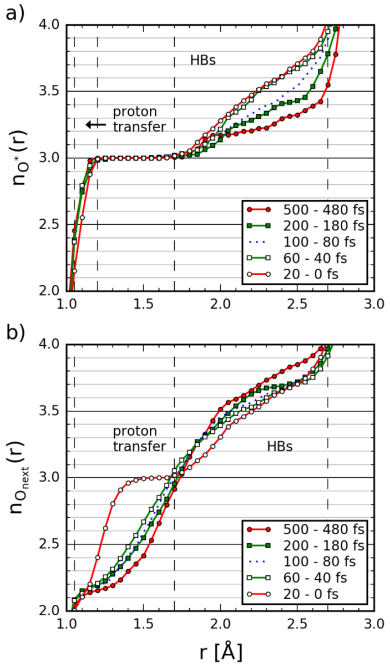


Figure H.6: The ICNs for bulk water using the BLYP XC functional for protonated oxygen in water (O* in (a)) and the next water oxygen to be protonated (O_{next} in (b)) averaged over 20 fs intervals long before proton transfer (500-480 fs) and leading up to proton transfer (200-180 fs, 100-80 fs, 60-40 fs, and 20-0 fs) at 300 K . The integration is over the RDF in Figure S6. Specific regions are marked for the proton transfer process and the change in the HB network. Proton rattling events are excluded.

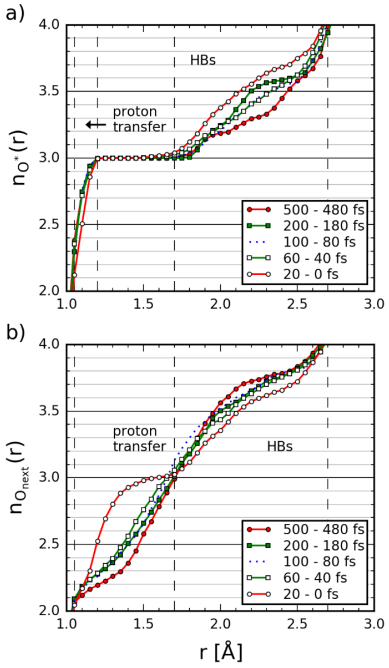


Figure H.7: The ICNs for bulk water using the PBE XC functional for protonated oxygen in water (O* in (a)) and the next water oxygen to be protonated (O_{next} in (b)) averaged over 20 fs intervals long before proton transfer (500-480 fs) and leading up to proton transfer (200-180 fs, 100-80 fs, 60-40 fs, and 20-0 fs) at 300 K . The integration is over the RDF in Figure S7. Specific regions are marked for the proton transfer process and the change in the HB network. Proton rattling events are excluded.

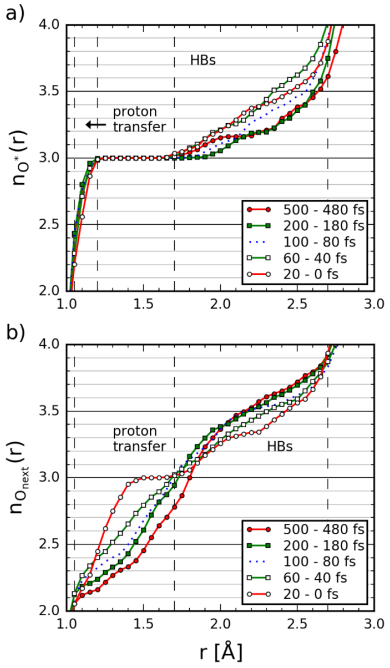


Figure H.8: The ICNs for bulk water using the PBE+TS-vdW XC functional for protonated oxygen in water (O* in (a)) and the next water oxygen to be protonated (O_{next} in (b)) averaged over 20 fs intervals long before proton transfer (500-480 fs) and leading up to proton transfer (200-180 fs, 100-80 fs, 60-40 fs, and 20-0 fs) at 300 K. The integration is over the RDF in Figure S8. Specific regions are marked for the proton transfer process and the change in the HB network. Proton rattling events are excluded.

H.3 Time evolution of radial distribution functions leading up to proton transfer events for water-water proton transfer for TEG-water mixtures

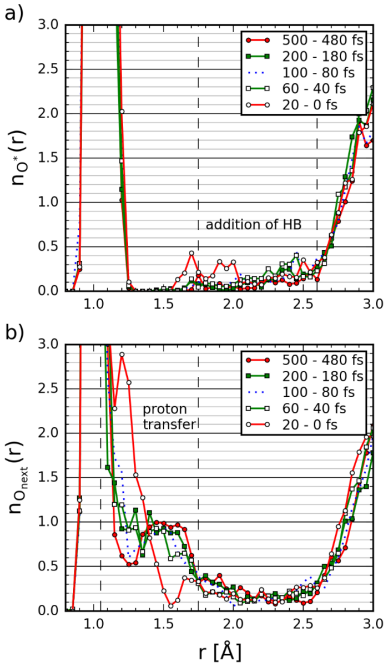


Figure H.9: The RDFs for TEG-water mixtures using the PW91 XC functional for protonated oxygen in water (O* in (a)) and the next water oxygen to be protonated (O_{next} in (b)) averaged over 20 fs intervals long before proton transfer (500-480 fs) and leading up to proton transfer (200-180 fs, 100-80 fs, 60-40 fs, and 20-0 fs) at 300 K . Specific regions are marked for the proton transfer process and the change in the HB network. Proton rattling events are excluded.

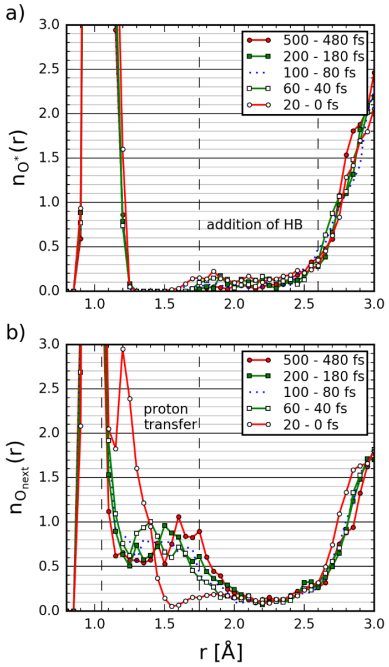


Figure H.10: The RDFs for TEG-water using the PBE XC functional for protonated oxygen in water (O* in (a)) and the next water oxygen to be protonated (O_{next} in (b)) averaged over 20 fs intervals long before proton transfer (500-480 fs) and leading up to proton transfer (200-180 fs, 100-80 fs, 60-40 fs, and 20-0 fs) at 300 K . Specific regions are marked for the proton transfer process and the change in the HB network. Proton rattling events are excluded.

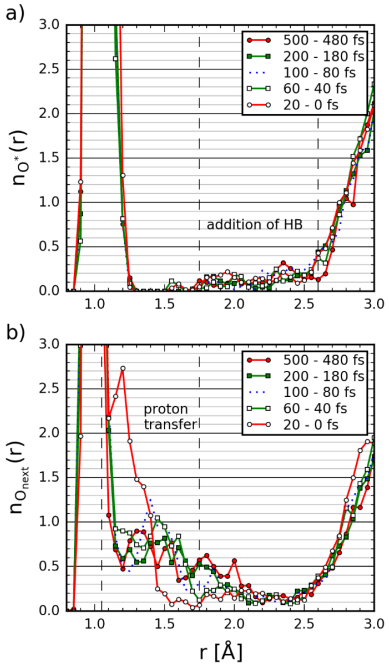


Figure H.11: The RDFs for TEG-water using the PBE+TS-vdW XC functional for protonated oxygen in water (O* in (a)) and the next water oxygen to be protonated (O_{next} in (b)) averaged over 20 fs intervals long before proton transfer (500-480 fs) and leading up to proton transfer (200-180 fs, 100-80 fs, 60-40 fs, and 20-0 fs) at 300 K . Specific regions are marked for the proton transfer process and the change in the HB network. Proton rattling events are excluded.

H.4 Time evolution of integrated coordination numbers leading up to proton transfer events for water-water proton transfer for TEG-water mixtures

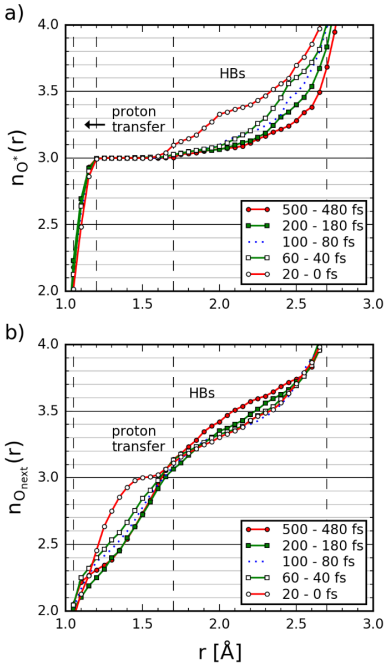


Figure H.12: The ICNs using the PW91 XC functional for protonated oxygen in water (O* in (a)) and the next water oxygen to be protonated (O_{next} in (b)) averaged over 20 fs intervals long before proton transfer (500-480 fs) and leading up to proton transfer (200-180 fs, 100-80 fs, 60-40 fs, and 20-0 fs) at 300 K . The integration is over the RDF in Figure S13. Specific regions are marked for the proton transfer process and the change in the HB network. Proton rattling events are excluded.

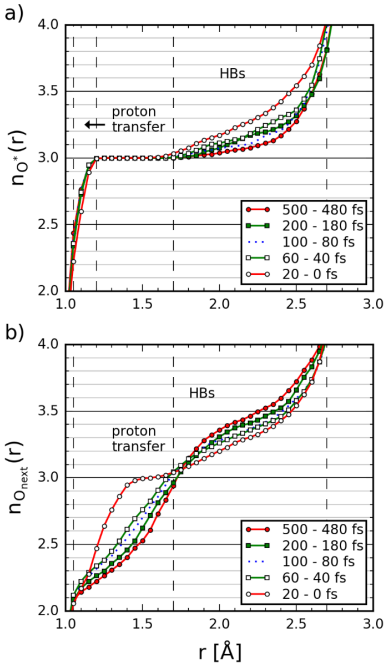


Figure H.13: The ICNs using the PBE XC functional for protonated oxygen in water (O* in (a)) and the next water oxygen to be protonated (O_{next} in (b)) averaged over 20 fs intervals long before proton transfer (500-480 fs) and leading up to proton transfer (200-180 fs, 100-80 fs, 60-40 fs, and 20-0 fs) at 300 K . The integration is over the RDF in Figure S14. Specific regions are marked for the proton transfer process and the change in the HB network. Proton rattling events are excluded.

H.5 Time evolution of integrated coordination numbers leading up to proton transfer events for water-hydroxyl proton transfer for TEG-water mixtures

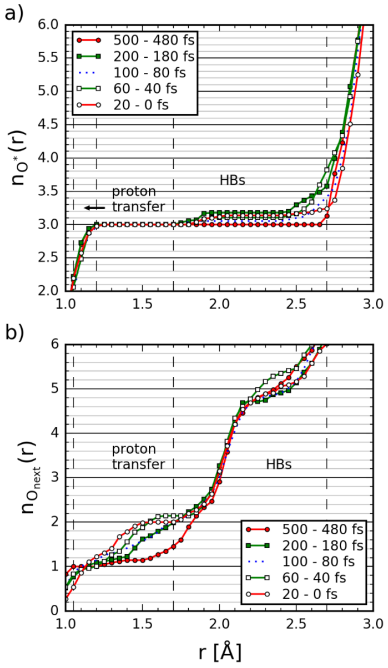


Figure H.14: The ICNs for TEG-water mixtures using the PW91 XC functional for protonated oxygen in water (O* in (a)) and the next hydroxyl oxygen of TEG to be protonated (O_{next} in (b)) averaged over 20 fs intervals leading up to proton transfer (60-40 fs, and 20-0 fs) at 300 K. Specific regions are marked for the proton transfer process and the change in the HB network. Proton rattling events are included.

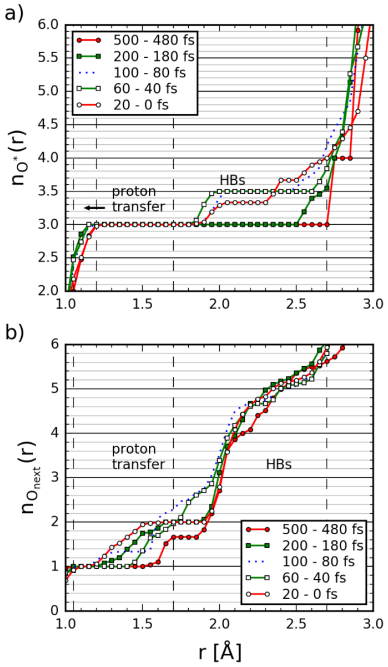


Figure H.15: The ICNs for TEG-water mixtures using the PBE XC functional for protonated oxygen in water (O* in (a)) and the next hydroxyl oxygen of TEG to be protonated (O_{next} in (b)) averaged over 20 fs intervals leading up to proton transfer (100-80 fs, 60-40 fs, and 20-0 fs) at 300 K . Specific regions are marked for the proton transfer process and the change in the HB network. Proton rattling events are included.

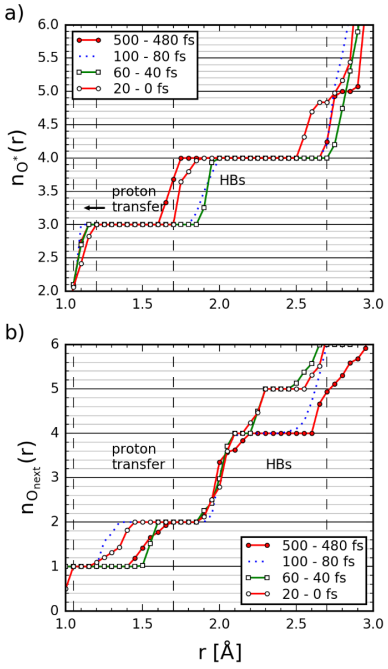


Figure H.16: The ICNs for TEG-water mixtures using the PBE+TS-vdW XC functional for protonated oxygen in water (O* in (a)) and the next hydroxyl oxygen of TEG to be protonated (O_{next} in (b)) averaged over 20 fs intervals long before proton transfer (500-480 fs) and leading up to proton transfer (200-180 fs, 100-80 fs, 60-40 fs, and 20-0 fs) at 300 K. Specific regions are marked for the proton transfer process and the change in the HB network. Proton rattling events are included.

H.6 Time evolution of integrated coordination numbers leading up to proton transfer events for hydroxyl-water proton transfer for TEG-water mixtures

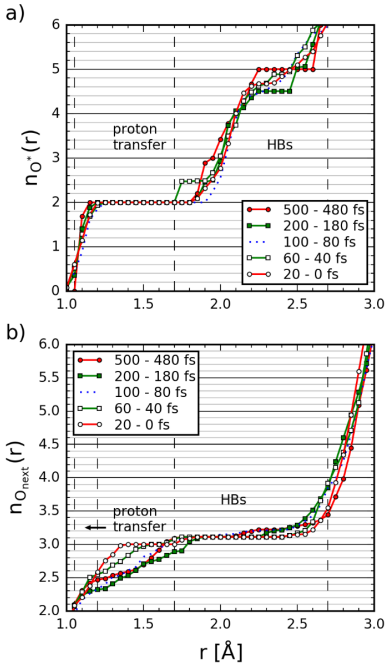


Figure H.17: The ICNs for TEG-water mixtures using the PW91 XC functional for protonated oxygen in the hydroxyl group of TEG (O* in (a)) and the next water oxygen to be protonated (O_{next} in (b)) averaged over 20 fs intervals leading up to proton transfer (100-80 fs, 60-40 fs, and 20-0 fs) at 300 K . Specific regions are marked for the proton transfer process and the change in the HB network. Proton rattling events are included.

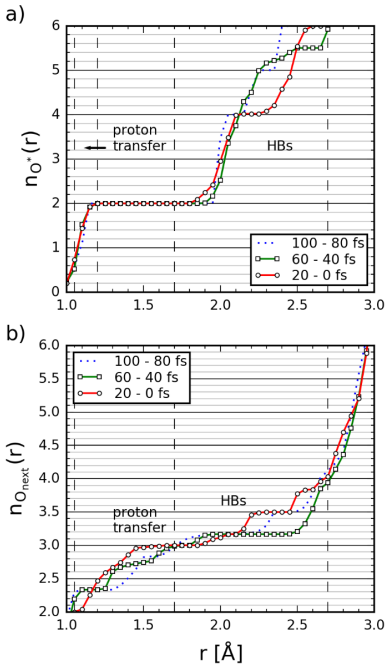


Figure H.18: The ICNs for TEG-water mixtures using the PBE XC functional for protonated oxygen in the hydroxyl group of TEG (O* in (a)) and the next water oxygen to be protonated (O_{next} in (b)) averaged over 20 fs intervals leading up to proton transfer (100-80 fs, 60-40 fs, and 20-0 fs) at 300 K . Specific regions are marked for the proton transfer process and the change in the HB network. Proton rattling events are included.

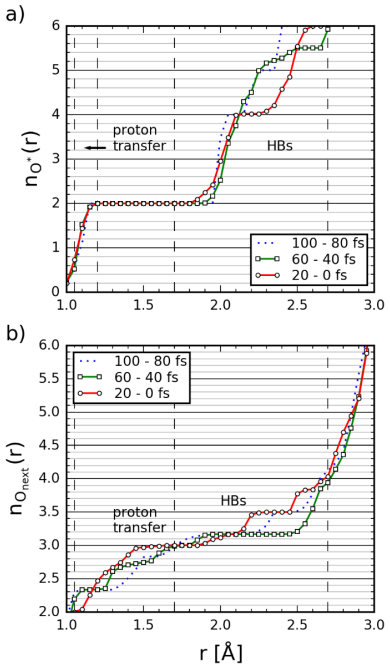


Figure H.19: The ICNs for TEG-water mixtures using the PBE+TS-vdW XC functional for protonated oxygen in the hydroxyl group of TEG (O* in (a)) and the next water oxygen to be protonated (O_{next} in (b)) averaged over 20 fs intervals leading up to proton transfer (200-180 fs, 100-80 fs, 60-40 fs, and 20-0 fs) at 300 K . Specific regions are marked for the proton transfer process and the change in the HB network. Proton rattling events are included.

H.7 Integrated coordination numbers during water-water proton transfer for all XC functionals

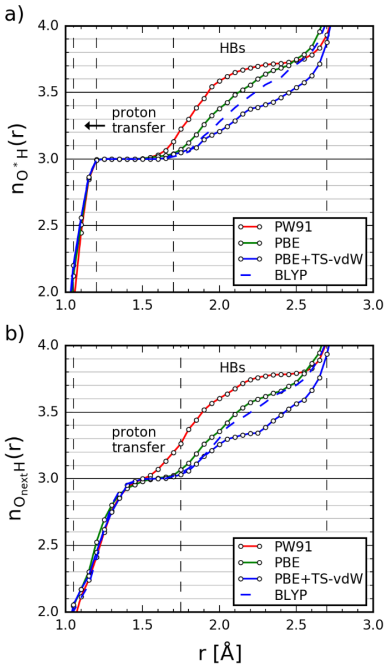


Figure H.20: The ICNs for all four XC functionals in bulk water for protonated oxygen in water (O* in (a)) and the next water oxygen to be protonated (O_{next} in (b)) averaged over 20 fs intervals leading up to proton transfer at 300 K. Specific regions are marked for the proton transfer process and the HBs. Proton rattling events are excluded.

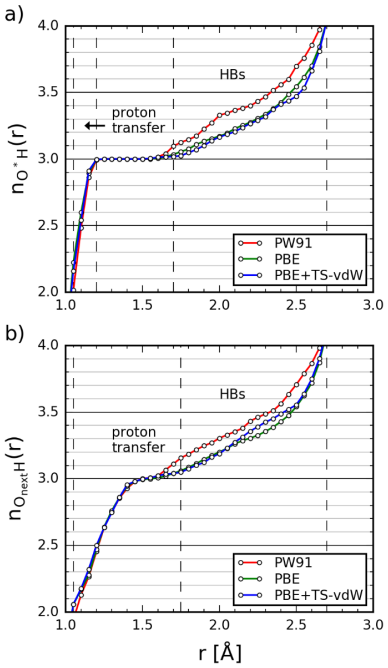


Figure H.21: The ICNs for all three XC functionals in TEG-water mixtures for protonated oxygen in water (O* in (a)) and the next water oxygen to be protonated (O_{next} in (b)) averaged over 20 fs intervals leading up to proton transfer at 300 K. Specific regions are marked for the proton transfer process and the HBs. Proton rattling events are excluded.

Appendix I

Probability density functions

I.1 Probability density functions for bulk water

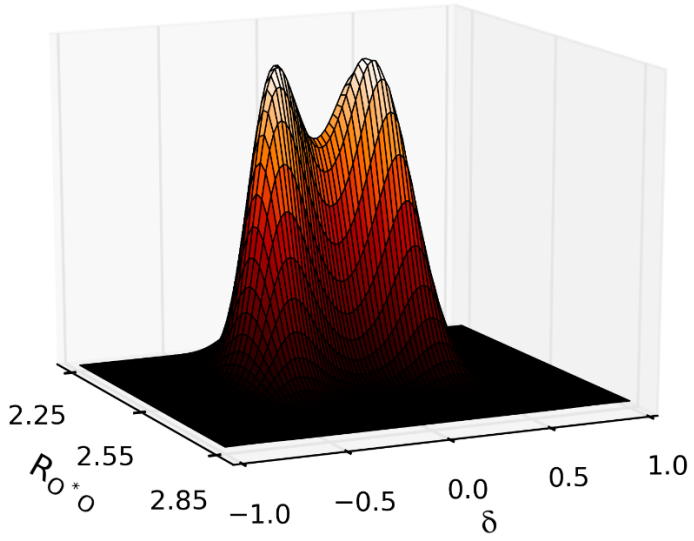


Figure I.1: Probability density function of proton transfer between water molecules in bulk water for the PW91 XC functional simulations at 300 K. The reaction coordinate δ is the difference of the HB distances for the shared proton (H^*) between the two oxygen atoms of the water molecules and R_{O^*O} is the oxygen-oxygen distance. The surface has been smoothed and z-axis made arbitrary.

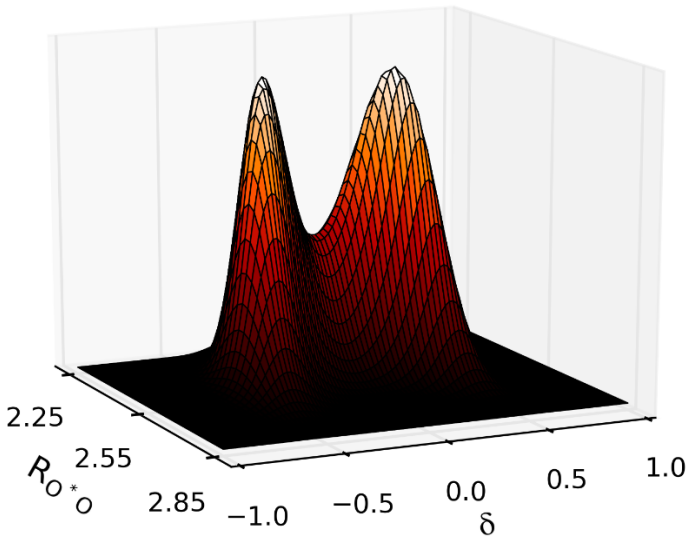


Figure I.2: Probability density function of proton transfer between water molecules in bulk water for the BLYP XC functional simulations at 300 K. The reaction coordinate δ is the difference of the HB distances for the shared proton (H^*) between the two oxygen atoms of the water molecules and R_{O^*O} is the oxygen-oxygen distance. The surface has been smoothed and z-axis made arbitrary.

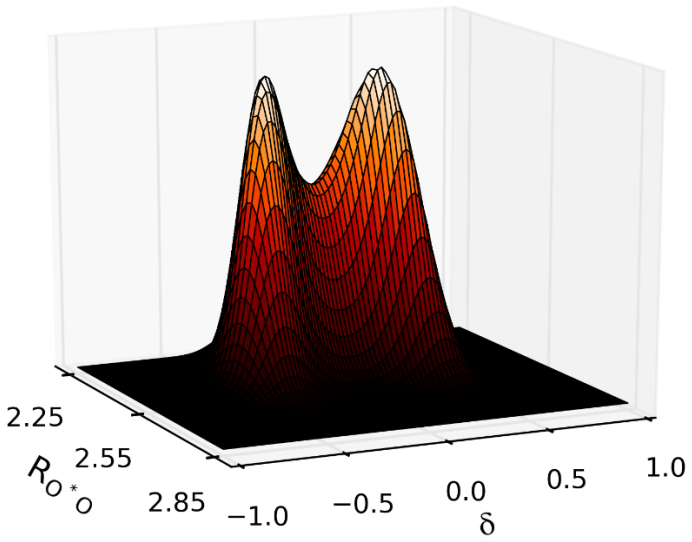


Figure I.3: Probability density function of proton transfer between water molecules in bulk water for the PBE XC functional simulations at 300 K. The reaction coordinate δ is the difference of the HB distances for the shared proton (H^*) between the two oxygen atoms of the water molecules and R_{O^*O} is the oxygen-oxygen distance. The surface has been smoothed and z-axis made arbitrary.

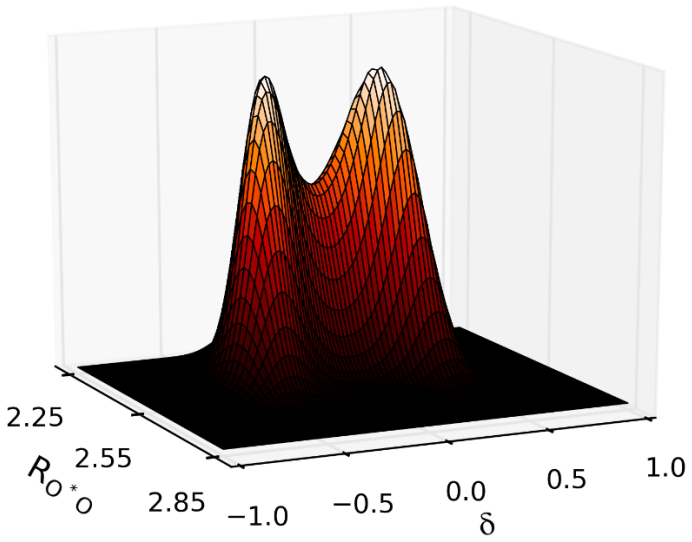


Figure I.4: Probability density function of proton transfer between water molecules in bulk water for the PBE+TS-vdW XC functional simulations at 300 K. The reaction coordinate δ is the difference of the HB distances for the shared proton (H^*) between the two oxygen atoms of the water molecules and R_{O^*O} is the oxygen-oxygen distance. The surface has been smoothed and z-axis made arbitrary.

I.2 Probability density functions for water-water proton transfer in TEG-water mixtures.

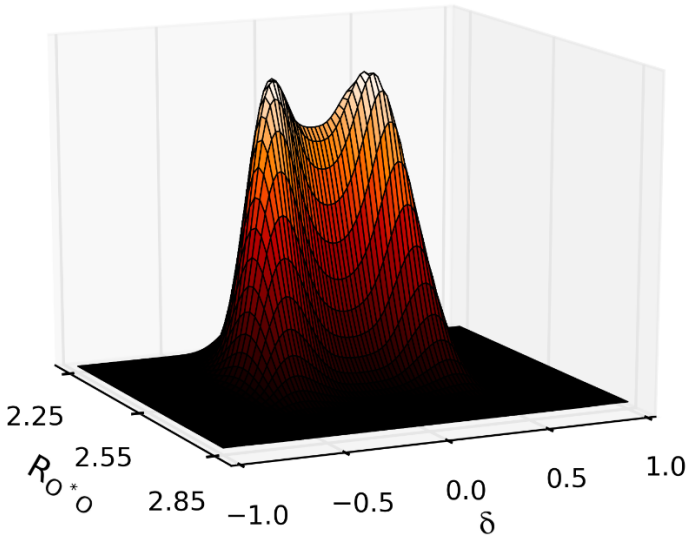


Figure I.5: Probability density function of proton transfer between water molecules for the TEG-water mixture for one of the PW91 functional simulations at 300 K. The reaction coordinate δ is the difference of the HB distances for the shared proton (H^*) between the two oxygen atoms of the water molecules and R_{O^*O} is the oxygen-oxygen distance. The surface has been smoothed and z-axis made arbitrary.

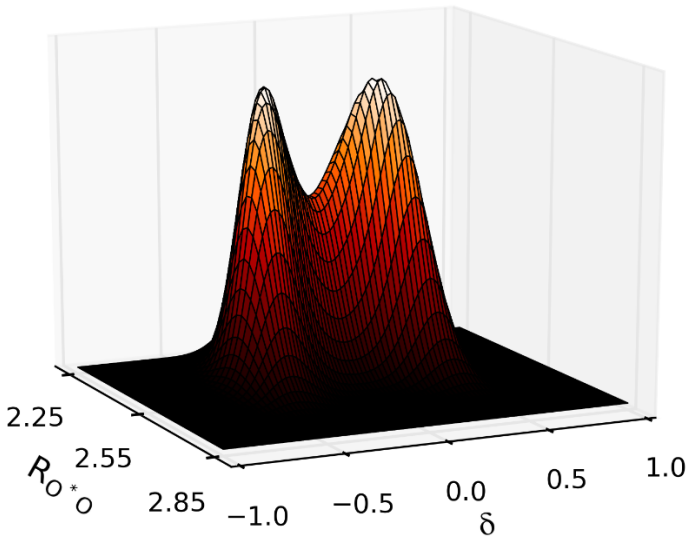


Figure I.6: Probability density function of proton transfer between water molecules for the TEG-water mixture for one of the PBE functional simulations at 300 K. The reaction coordinate δ is the difference of the HB distances for the shared proton (H^*) between the two oxygen atoms of the water molecules and R_{O^*O} is the oxygen-oxygen distance. The surface has been smoothed and z-axis made arbitrary.

Appendix J

Hopping dynamics and mean square displacements

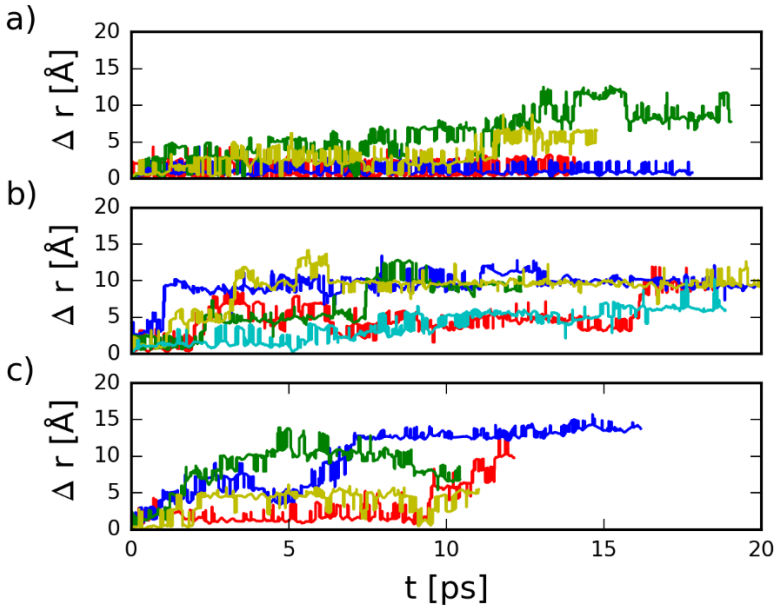


Figure J.1: The distance for the protonated atom (O*) that has the excess proton H^+ relative to the initial position of the first protonated atom in TEG-water mixture for all individual simulation trajectories for each of the XC functionals (a) PW91, (b) PBE, and (c) PBE+TS-vdW.

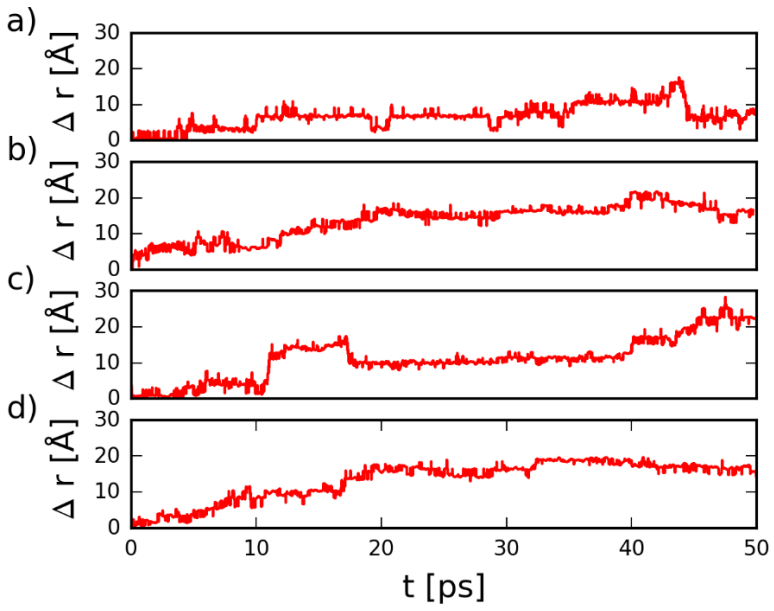


Figure J.2: The distance for the hydronium oxygen (O*) relative to the initial position vs. time in bulk water for the XC functionals (a) PW91, (b) BLYP, (c) PBE, and (d) PBE+TS-vdW.

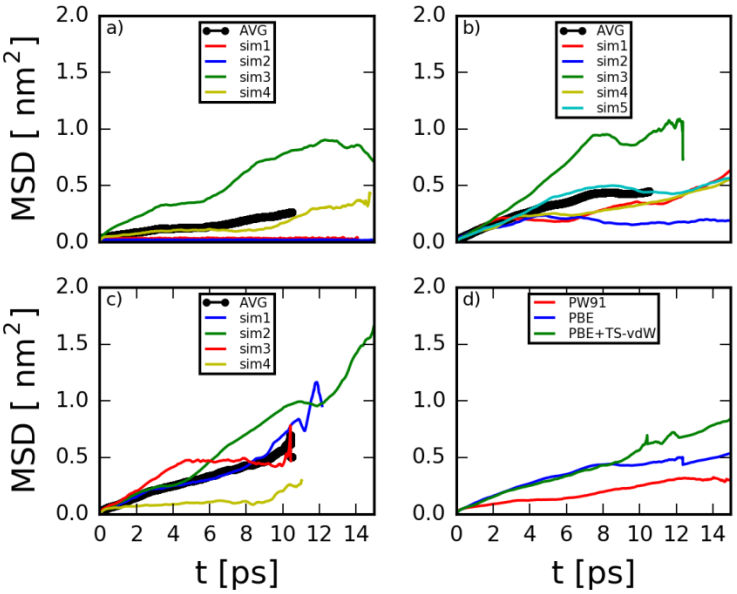


Figure J.3: The mean squared displacements (MSDs) of the protonated atom (O*) versus time in TEG-water mixture for each individual trajectory and their average (a-c) and the average MSDs for each XC functional (d). The graphs show the XC functionals (a) PW91, (b) PBE, and (c) PBE+TS-vdW and then the average for all three XC functionals in in graph (d). The average MSDs in (a-c) were truncated at 10 ps where the MSDs in (d) were averaged out to the longest time length but with averaging over only a subset of all MSDs.

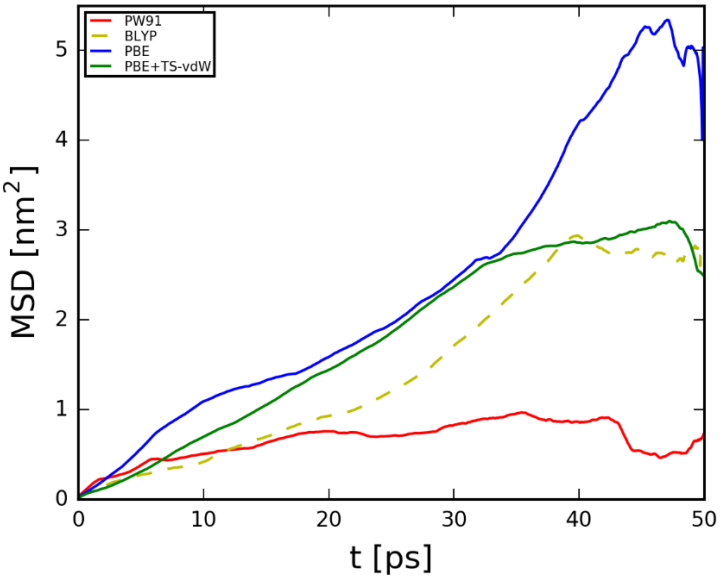


Figure J.4: The mean squared displacements of the hydronium oxygen (O*) versus time in bulk water for all XC functionals.

Appendix K

Hydrogen-bond networks with proton rattling included

K.1 Hydrogen-bond networks with proton rattling included for bulk water

Table K.1: The occurrences and lifetimes of hydrogen-bond networks around protonated species found in bulk water for PW91. The table lists the protonated species ($Z_{protonated}$), the atom (Z_{shared}) hydrogen bonded to the most active proton, the solvating atoms of the protonated species (HBX,p where x=A or D for accepting or donating a hydrogen bond), and the solvating atoms of Zshared (HBX,s with the same definitions of x). Figure 4.4 provides the illustration to match these labels. Proton rattling effects are included.

$Z_{protonated}$	Z_{shared}	$HB_{A,p}$	$HB_{A,p}$	$HB_{D,p}$	$HB_{A,s}$	$HB_{A,s}$	$HB_{D,s}$	%	$\sum$%	Lifetime (fs)
H_3O^+	H_2O	H_2O	H_2O	...	H_2O	H_2O	H_2O	58.62	58.62	8.34±9.30
H_3O^+	H_2O	H_2O	H_2O	H_2O	H_2O	H_2O	H_2O	29.45	88.08	8.91±10.99
H_3O^+	H_2O	H_2O	H_2O	...	H_2O	H_2O	...	7.05	95.13	10.43±12.65
H_3O^+	H_2O	H_2O	...	...	H_2O	H_2O	H_2O	1.72	96.85	10.26±11.95
H_3O^+	H_2O	H_2O	H_2O	...	H_2O	...	H_2O	1.36	98.21	8.72±13.23
H_3O^+	H_2O	H_2O	H_2O	H_2O	H_2O	...	H_2O	1.23	99.43	7.22±8.56
H_3O^+	H_2O	H_2O	...	...	H_2O	H_2O	...	0.44	99.87	6.42±6.64
OH^-	H_2O	...	...	H_2O	H_2O	H_2O	H_2O	0.05	99.92	4.76±2.44
H_3O^+	H_2O	H_2O	...	...	H_2O	...	H_2O	0.04	99.96	3.65±2.08
OH^-	H_2O	...	...	H_2O	H_2O	H_2O	...	0.01	99.97	1.60±0.00
OH^-	H_2O	...	...	H_2O	H_2O	...	H_2O	0.01	99.99	2.61±0.00
OH^-	H_3O^+	...	...	H_2O	H_2O	H_2O	H_2O	0.01	99.99	0.44±0.00
H_3O^+	H_2O	H_2O	...	H_2O	H_2O	...	H_2O	0.01	100.00	8.78±5.88

Table K.2: The occurrences and lifetimes of hydrogen-bond networks around protonated species found in bulk water for PBE. The table lists the protonated species ($Z_{protonated}$), the atom (Z_{shared}) hydrogen bonded to the most active proton, the solvating atoms of the protonated species ($HB_{X,p}$ where x=A or D for accepting or donating a hydrogen bond), and the solvating atoms of Z_{shared} ($HB_{X,s}$ with the same definitions of x). Figure 4.4 provides the illustration to match these labels. Proton rattling effects are included.

$Z_{protonated}$	Z_{shared}	$HB_{A,p}$	$HB_{A,p}$	$HB_{D,p}$	$HB_{A,s}$	$HB_{A,s}$	$HB_{D,s}$	%	$\sum$%	Lifetime (ps)
H_3O^+	H_2O	H_2O	H_2O	...	H_2O	H_2O	H_2O	53.89	53.89	8.02±9.10
H_3O^+	H_2O	H_2O	H_2O	...	H_2O	H_2O	...	18.36	72.25	8.59±10.02
H_3O^+	H_2O	H_2O	H_2O	H_2O	H_2O	H_2O	H_2O	17.58	89.83	7.86±8.90
H_3O^+	H_2O	H_2O	H_2O	...	H_2O	...	H_2O	3.85	93.68	7.82±8.99
H_3O^+	H_2O	H_2O	H_2O	...	H_2O	...	...	2.42	96.10	7.46±8.17
H_3O^+	H_2O	H_2O	...	...	H_2O	H_2O	H_2O	2.10	98.20	8.06±10.38
H_3O^+	H_2O	H_2O	H_2O	H_2O	H_2O	...	H_2O	1.62	99.82	6.93±7.75
H_3O^+	H_2O	H_2O	...	H_2O	H_2O	...	...	0.10	99.92	4.00±3.09
H_3O^+	H_2O	H_2O	...	...	H_2O	...	...	0.06	99.98	5.05±4.06
H_3O^+	H_2O	H_2O	...	H_2O	H_2O	...	H_2O	0.01	99.99	6.10±6.81
H_3O^+	H_2O	...	...	H_2O	H_2O	H_2O	H_2O	0.01	100.00	4.14±2.83

Table K.3: The occurrences and lifetimes of hydrogen-bond networks around protonated species found in bulk water for BLYP. The table lists the protonated species ($Z_{protonated}$), the atom (Z_{shared}) hydrogen bonded to the most active proton, the solvating atoms of the protonated species ($HB_{X,p}$ where x=A or D for accepting or donating a hydrogen bond), and the solvating atoms of Z_{shared} ($HB_{X,s}$ with the same definitions of x). Figure 4.4 provides the illustration to match these labels. Proton rattling effects are included.

$Z_{protonated}$	Z_{shared}	$HB_{A,p}$	$HB_{A,p}$	$HB_{D,p}$	$HB_{A,s}$	$HB_{A,s}$	$HB_{D,s}$	%	$\sum$%	Lifetime (ps)
H_3O^+	H_2O	H_2O	H_2O	...	H_2O	H_2O	H_2O	47.47	47.47	8.46±10.16
H_3O^+	H_2O	H_2O	H_2O	...	H_2O	H_2O	...	30.23	77.70	8.58±10.73
H_3O^+	H_2O	H_2O	H_2O	H_2O	H_2O	H_2O	H_2O	10.10	87.80	8.58±9.87
H_3O^+	H_2O	H_2O	H_2O	...	H_2O	...	...	5.38	93.18	9.43±12.20
H_3O^+	H_2O	H_2O	H_2O	...	H_2O	...	H_2O	3.08	96.27	8.61±10.96
H_3O^+	H_2O	H_2O	...	...	H_2O	H_2O	H_2O	2.50	98.76	6.73±6.40
H_3O^+	H_2O	H_2O	H_2O	H_2O	H_2O	...	H_2O	0.80	99.56	6.07±6.18
H_3O^+	H_2O	H_2O	...	...	H_2O	...	...	0.20	99.77	3.96±4.18
H_3O^+	H_2O	H_2O	...	...	H_2O	...	H_2O	0.15	99.91	3.43±3.98
H_3O^+	H_2O	...	...	...	H_2O	H_2O	...	0.04	99.96	6.53±6.99
H_3O^+	H_2O	...	...	...	H_2O	H_2O	H_2O	0.03	99.98	10.12±5.59
H_3O^+	H_2O	H_2O	...	H_2O	H_2O	...	H_2O	0.02	100.00	4.50±1.99

Table K.4: The occurrences and lifetimes of hydrogen-bond networks around protonated species found in bulk water for PBE+TS-vdW. The table lists the protonated species ($Z_{protonated}$), the atom (Z_{shared}) hydrogen bonded to the most active proton, the solvating atoms of the protonated species ($HB_{X,p}$ where x=A or D for accepting or donating a hydrogen bond), and the solvating atoms of Z_{shared} ($HB_{X,s}$ with the same definitions of x). Figure 4.4 provides the illustration to match these labels. Proton rattling effects are included.

$Z_{protonated}$	Z_{shared}	$HB_{A,p}$	$HB_{A,p}$	$HB_{D,p}$	$HB_{A,s}$	$HB_{A,s}$	$HB_{D,s}$	%	$\sum$%	Lifetime (ps)
H_3O^+	H_2O	H_2O	H_2O	...	H_2O	H_2O	H_2O	41.34	41.34	7.99±10.30
H_3O^+	H_2O	H_2O	H_2O	...	H_2O	H_2O	...	36.89	78.23	7.92±9.98
H_3O^+	H_2O	H_2O	H_2O	H_2O	H_2O	H_2O	H_2O	8.51	86.75	7.31±8.06
H_3O^+	H_2O	H_2O	...	...	H_2O	H_2O	...	6.20	92.95	9.34±12.05
H_3O^+	H_2O	H_2O	H_2O	...	H_2O	...	H_2O	3.19	96.14	7.67±9.94
H_3O^+	H_2O	H_2O	...	...	H_2O	H_2O	H_2O	2.48	98.63	7.43±8.83
H_3O^+	H_2O	H_2O	H_2O	H_2O	H_2O	...	H_2O	0.89	99.51	6.80±8.17
H_3O^+	H_2O	H_2O	...	...	H_2O	...	H_2O	0.25	99.76	3.23±3.44
H_3O^+	H_2O	H_2O	...	...	H_2O	...	...	0.16	99.92	4.90±5.20
H_3O^+	H_2O	H_2O	...	H_2O	H_2O	...	H_2O	0.05	99.97	3.89±2.93
H_3O^+	H_2O	...	...	...	H_2O	H_2O	...	0.01	99.99	4.14±2.04
H_3O^+	H_2O	...	...	H_2O	H_2O	...	...	0.01	99.99	2.76±0.00
H_3O^+	H_2O	...	...	H_2O	H_2O	H_2O	H_2O	0.01	100.00	1.45±0.58
H_3O^+	H_2O	...	...	...	H_2O	H_2O	H_2O	0.00	100.00	0.87±0.00

K.2 Hydrogen-bond networks with proton rattling included for TEG-water mixtures

Table K.5: The occurrences and lifetimes of all hydrogen-bond networks around protonated species found in TEG-water mixture for PW91. The table lists the protonated species (Z_{prot}), the atom (Z_{shared}) hydrogen bonded to the most active proton, the solvating atoms of the protonated species ($HB_{X,p}$ where x=A or D for accepting or donating a hydrogen bond and y = 1 or 2), and the solvating atoms of Z_{shared} ($HB_{X,s}$with the same definitions of x). Figure 4.4 provides the illustration to match these labels. Proton rattling effects are included.

Z_{prot}	Z_{shared}	$HB_{A,p}$	$HB_{A,p}$	$HB_{D,p}$	$HB_{A,s}$	$HB_{A,s}$	$HB_{D,s}$	%	$\sum$ %	Lifetime (fs)
H_3O^+	H_2O	H_2O	H_2O	...	H_2O	H_2O	H_2O	17.60	17.60	8.23±10.65
H_3O^+	H_2O	H_2O	H_2O	CH_2	H_2O	H_2O	...	16.14	33.75	7.94±8.78
H_3O^+	H_2O	H_2O	H_2O	...	H_2O	H_2O	...	15.61	49.36	7.70±9.06
H_3O^+	H_2O	H_2O	H_2O	CH_2	H_2O	H_2O	H_2O	6.52	55.87	8.45±11.00
H_3O^+	H_2O	H_2O	H_2O	...	H_2O	H_2O	CH_2	6.29	62.16	6.55±6.59
H_3O^+	H_2O	ROH	H_2O	...	H_2O	H_2O	H_2O	4.27	66.43	6.40±6.99
H_3O^+	H_2O	H_2O	H_2O	...	ROH	H_2O	H_2O	3.66	70.09	8.56±10.04
H_3O^+	H_2O	H_2O	H_2O	H_2O	H_2O	H_2O	CH_2	3.50	73.58	6.61±7.05
H_3O^+	H_2O	H_2O	H_2O	...	ROH	H_2O	...	2.13	75.72	7.70±9.40
H_3O^+	H_2O	ROH	H_2O	...	H_2O	H_2O	CH_2	2.05	77.77	6.50±6.49
H_3O^+	H_2O	H_2O	H_2O	CH_2	ROH	H_2O	H_2O	2.03	79.80	6.96±7.36
H_3O^+	H_2O	H_2O	H_2O	H_2O	H_2O	H_2O	H_2O	1.90	81.70	8.00±8.73
H_3O^+	H_2O	H_2O	H_2O	CH_2	H_2O	...	...	1.38	83.08	10.39±14.70
H_3O^+	H_2O	ROH	H_2O	CH_2	H_2O	H_2O	H_2O	1.26	84.34	7.13±7.75
H_3O^+	H_2O	H_2O	H_2O	CH_2	H_2O	H_2O	CH_2	1.17	85.51	7.74±8.13
H_3O^+	H_2O	ROH	H_2O	CH_2	H_2O	H_2O	...	1.09	86.60	7.36±7.83
H_3O^+	H_2O	H_2O	...	CH_2	H_2O	H_2O	...	0.96	87.56	7.69±10.21
H_3O^+	H_2O	H_2O	H_2O	...	H_2O	...	...	0.88	88.45	13.70±19.08
H_3O^+	H_2O	H_2O	H_2O	...	ROR	H_2O	H_2O	0.69	89.14	7.65±7.38
H_3O^+	H_2O	H_2O	...	...	H_2O	H_2O	...	0.67	89.80	8.97±11.17
H_3O^+	H_2O	H_2O	...	...	H_2O	H_2O	H_2O	0.61	90.41	6.74±9.30
H_3O^+	H_2O	H_2O	H_2O	...	H_2O	...	H_2O	0.57	90.98	7.07±7.40
H_3O^+	ROH	H_2O	H_2O	...	H_2O	...	H_2O	0.54	91.52	6.15±7.56
H_3O^+	H_2O	H_2O	H_2O	H_2O	ROH	H_2O	H_2O	0.49	92.02	6.05±5.37
H_3O^+	ROH	H_2O	H_2O	...	H_2O	...	CH_2	0.44	92.46	5.95±5.09
H_3O^+	ROH	H_2O	H_2O	...	H_2O	...	...	0.39	92.85	5.70±5.52
H_3O^+	H_2O	ROH	H_2O	CH_2	H_2O	H_2O	CH_2	0.35	93.19	6.50±7.47
H_3O^+	H_2O	H_2O	...	...	H_2O	H_2O	CH_2	0.33	93.52	6.14±8.18
H_3O^+	H_2O	H_2O	H_2O	H_2O	H_2O	...	...	0.33	93.85	6.25±6.93
H_3O^+	ROH	H_2O	H_2O	CH_2	H_2O	...	...	0.32	94.17	7.32±7.28
H_3O^+	H_2O	ROH	H_2O	...	ROH	H_2O	H_2O	0.20	94.37	6.08±5.76
H_3O^+	H_2O	H_2O	H_2O	CH_2	H_2O	...	H_2O	0.20	94.57	5.72±6.02
H_3O^+	H_2O	H_2O	H_2O	H_2O	ROR	H_2O	H_2O	0.19	94.76	6.00±4.74
H_3O^+	H_2O	H_2O	...	CH_2	H_2O	H_2O	H_2O	0.19	94.95	5.71±6.27
H_3O^+	H_2O	H_2O	...	H_2O	H_2O	H_2O	H_2O	0.17	95.12	5.65±4.85
H_3O^+	H_2O	H_2O	H_2O	H_2O	ROR	H_2O	...	0.17	95.29	5.17±2.86
H_3O^+	ROH	H_2O	H_2O	CH_2	H_2O	...	H_2O	0.17	95.46	4.80±4.04
H_3O^+	H_2O	H_2O	...	H_2O	H_2O	H_2O	CH_2	0.16	95.62	5.70±5.95
H_3O^+	H_2O	H_2O	H_2O	...	ROR	H_2O	...	0.14	95.76	6.63±5.81
H_3O^+	H_2O	H_2O	...	...	ROH	H_2O	H_2O	0.14	95.90	5.23±4.16
H_3O^+	H_2O	H_2O	...	H_2O	H_2O	H_2O	...	0.14	96.03	5.14±5.94
H_3O^+	H_2O	H_2O	CH_2	...	ROH	H_2O	H_2O	0.12	96.16	4.55±3.52
H_3O^+	H_2O	H_2O	H_2O	H_2O	ROH	...	...	0.12	96.28	5.86±7.45
ROH_2^+	H_2O	H_2O	...	...	H_2O	H_2O	H_2O	0.12	96.40	5.38±3.71
H_3O^+	H_2O	H_2O	H_2O	...	H_2O	CH_2	H_2O	0.11	96.51	8.76±5.54
H_3O^+	ROH	H_2O	...	...	H_2O	...	H_2O	0.11	96.63	8.05±5.92
H_3O^+	H_2O	H_2O	CH_2	...	H_2O	H_2O	H_2O	0.10	96.73	6.65±6.66
H_3O^+	H_2O	ROH	H_2O	H_2O	H_2O	H_2O	H_2O	0.10	96.84	7.51±3.53
H_3O^+	H_2O	H_2O	H_2O	H_2O	H_2O	CH_2	H_2O	0.10	96.94	6.31±4.73
H_3O^+	H_2O	H_2O	H_2O	CH_2	ROR	H_2O	...	0.10	97.04	4.97±3.94
H_3O^+	H_2O	H_2O	...	CH_2	ROH	H_2O	...	0.10	97.13	6.11±6.12
H_3O^+	H_2O	H_2O	H_2O	...	ROR	H_2O	ROH	0.10	97.23	15.37±15.65
H_3O^+	ROH	H_2O	...	...	H_2O	...	...	0.09	97.32	6.67±5.00
H_3O^+	ROH	H_2O	...	...	H_2O	...	CH_2	0.09	97.42	4.93±3.48
H_3O^+	H_2O	ROH	H_2O	H_2O	H_2O	H_2O	CH_2	0.09	97.50	7.06±7.93
H_3O^+	H_2O	H_2O	H_2O	...	ROH	...	H_2O	0.09	97.59	3.73±3.13

Table K.5 Continued.

Z_{prot}	Z_{shared}	$HB_{A,p}$	$HB_{A,p}$	$HB_{D,p}$	$HB_{A,s}$	$HB_{A,s}$	$HB_{D,s}$	%	$\sum$ %	Lifetime (fs)
H_3O^+	OH^-	ROH	H_2O	...	H_2O	...	H_2O	0.09	97.68	7.64±11.71
H_3O^+	H_2O	H_2O	...	...	ROH	H_2O	...	0.09	97.77	9.20±8.55
H_3O^+	H_2O	H_2O	H_2O	CH_2	ROR	H_2O	H_2O	0.08	97.85	8.33±6.54
H_3O^+	H_2O	H_2O	H_2O	H_2O	ROH	H_2O	...	0.08	97.93	5.48±6.85
H_3O^+	H_2O	ROH	H_2O	CH_2	ROH	H_2O	H_2O	0.07	98.01	3.57±2.03
H_3O^+	H_2O	ROH	H_2O	...	ROH	H_2O	...	0.07	98.08	3.24±1.91
H_3O^+	H_2O	ROR	H_2O	H_2O	H_2O	H_2O	H_2O	0.07	98.15	10.16±5.47
H_3O^+	H_2O	H_2O	CH_2	CH_2	H_2O	H_2O	H_2O	0.07	98.22	4.02±2.95
H_3O^+	ROH	H_2O	...	CH_2	H_2O	...	H_2O	0.06	98.28	4.48±3.56
H_3O^+	H_2O	ROH	H_2O	CH_2	H_2O	...	CH_2	0.06	98.34	8.41±6.66
H_3O^+	H_2O	H_2O	...	...	H_2O	...	...	0.06	98.40	2.43±2.15
H_3O^+	ROH	H_2O	H_2O	CH_2	H_2O	...	ROH	0.06	98.45	5.70±3.76
H_3O^+	H_2O	H_2O	H_2O	H_2O	ROR	H_2O	ROH	0.05	98.50	6.13±2.84
H_3O^+	H_2O	H_2O	...	...	ROH	H_2O	CH_2	0.05	98.56	12.02±10.46
H_3O^+	H_2O	H_2O	H_2O	H_2O	H_2O	...	CH_2	0.05	98.61	6.75±7.75
H_3O^+	ROH	H_2O	H_2O	H_2O	H_2O	...	CH_2	0.05	98.65	11.45±9.87
H_3O^+	ROH	H_2O	H_2O	H_2O	H_2O	...	H_2O	0.05	98.70	7.28±6.07
H_3O^+	ROH	H_2O	H_2O	...	H_2O	...	ROH	0.05	98.75	8.69±11.11
H_3O^+	H_2O	H_2O	...	CH_2	ROH	H_2O	H_2O	0.05	98.79	7.15±5.16
H_3O^+	H_2O	H_2O	...	...	H_2O	...	CH_2	0.05	98.84	3.44±2.61
H_3O^+	H_2O	H_2O	H_2O	CH_2	ROH	...	...	0.04	98.89	13.36±12.87
H_3O^+	H_2O	H_2O	H_2O	...	ROH	...	...	0.04	98.93	8.74±7.27
ROH_2^+	H_2O	H_2O	...	...	H_2O	...	CH_2	0.04	98.97	4.17±2.81
H_3O^+	H_2O	H_2O	H_2O	H_2O	H_2O	...	H_2O	0.04	99.01	3.17±2.04
H_3O^+	H_2O	H_2O	H_2O	CH_2	H_2O	CH_2	H_2O	0.04	99.05	4.40±1.95
H_3O^+	H_2O	H_2O	...	CH_2	H_2O	H_2O	CH_2	0.04	99.09	3.35±2.97
H_3O^+	H_2O	ROH	...	CH_2	H_2O	H_2O	H_2O	0.04	99.13	5.54±4.51
H_3O^+	ROH	H_2O	H_2O	H_2O	H_2O	...	ROH	0.04	99.17	16.12±5.59
H_3O^+	ROH-	H_2O	H_2O	...	...	...	H_2O	0.04	99.21	5.63±4.95
H_3O^+	H_2O	H_2O	H_2O	ROH	H_2O	H_2O	CH_2	0.03	99.24	7.11±6.26
H_3O^+	H_2O	H_2O	H_2O	CH_2	ROH	H_2O	...	0.03	99.27	9.79±10.95
H_3O^+	H_2O	H_2O	H_2O	...	H_2O	H_2O	ROH	0.03	99.30	15.83±16.40
H_3O^+	H_2O	ROH	H_2O	H_2O	ROH	H_2O	H_2O	0.03	99.33	2.95±2.09
H_3O^+	H_2O	H_2O	H_2O	...	ROH	...	CH_2	0.03	99.36	7.89±11.26
H_3O^+	H_2O	ROH	H_2O	CH_2	H_2O	...	H_2O	0.03	99.39	13.29±21.66
H_3O^+	H_2O	H_2O	H_2O	CH_2	H_2O	...	CH_2	0.03	99.42	3.24±2.96
H_3O^+	H_2O	ROH	H_2O	H_2O	H_2O	...	H_2O	0.03	99.44	3.97±3.06
H_3O^+	H_2O	ROH	H_2O	H_2O	H_2O	...	...	0.02	99.47	8.42±12.73
H_3O^+	H_2O	H_2O	CH_2	...	H_2O	H_2O	...	0.02	99.49	17.17±20.70
H_3O^+	H_2O	H_2O	CH_2	...	ROH	H_2O	...	0.02	99.51	9.44±4.65
H_3O^+	H_2O	H_2O	...	CH_2	H_2O	...	H_2O	0.02	99.53	2.03±2.19
OH^-	H_2O	...	...	H_2O	H_2O	H_2O	H_2O	0.02	99.55	0.56±0.20
H_3O^+	H_2O	H_2O	H_2O	H_2O	H_2O	...	ROH	0.02	99.57	10.45±9.87
H_3O^+	H_2O	H_2O	H_2O	...	ROR	...	...	0.02	99.58	1.92±1.60
H_3O^+	H_2O	ROH	H_2O	CH_2	ROH	H_2O	...	0.02	99.60	5.75±5.89
H_3O^+	H_2O	ROH	H_2O	...	ROH	...	H_2O	0.02	99.62	9.22±5.31
H_3O^+	H_2O	H_2O	H_2O	H_2O	ROH	...	H_2O	0.02	99.63	1.81±0.36
H_3O^+	H_2O	ROH	...	CH_2	H_2O	H_2O	CH_2	0.01	99.65	4.50±1.02
H_3O^+	OH^-	H_2O	H_2O	H_2O	H_2O	...	H_2O	0.01	99.66	8.57±2.76
H_3O^+	H_2O	H_2O	H_2O	...	H_2O	...	ROH	0.01	99.67	13.29±5.30
H_3O^+	H_2O	ROH	H_2O	...	H_2O	...	H_2O	0.01	99.69	6.45±5.12
H_3O^+	H_2O	H_2O	...	...	H_2O	...	H_2O	0.01	99.70	3.82±4.01
H_3O^+	H_2O	H_2O	...	...	ROR	H_2O	ROH	0.01	99.71	2.42±1.08
H_3O^+	H_2O	H_2O	H_2O	CH_2	ROH	...	H_2O	0.01	99.72	1.88±0.63
H_3O^+	H_2O	H_2O	...	...	ROR	H_2O	H_2O	0.01	99.74	3.99±2.54
ROH_2^+	H_2O	H_2O	...	...	H_2O	...	H_2O	0.01	99.75	2.76±2.18
ROH-	H_3O^+	...	...	...	H_2O	H_2O	...	0.01	99.76	1.31±0.00
H_3O^+	H_2O	H_2O	H_2O	H_2O	ROR	H_2O	CH_2	0.01	99.77	13.46±12.15
H_3O^+	H_2O	H_2O	CH_2	CH_2	ROH	H_2O	H_2O	0.01	99.78	1.16±0.00
H_3O^+	H_2O	H_2O	...	CH_2	H_2O	...	...	0.01	99.79	5.86±7.92
H_3O^+	H_2O	ROH	ROH	...	H_2O	H_2O	H_2O	0.01	99.80	1.45±1.31
H_3O^+	H_2O	H_2O	...	CH_2	ROR	H_2O	H_2O	0.01	99.81	1.09±0.36
ROH_2^+	H_2O	H_2O	...	CH_2	H_2O	H_2O	CH_2	0.01	99.82	2.76±0.73
OH^-	H_2O	...	...	H_2O	H_2O	...	H_2O	0.01	99.82	0.73±0.00
H_3O^+	H_2O	H_2O	CH_2	...	H_2O	H_2O	CH_2	0.01	99.83	3.48±0.00
H_3O^+	H_2O	H_2O	H_2O	...	ROR	ROR	H_2O	0.01	99.84	3.12±1.38
H_3O^+	H_2O	H_2O	H_2O	ROH	H_2O	H_2O	H_2O	0.01	99.85	6.53±0.00
H_3O^+	H_2O	H_2O	...	...	ROR	H_2O	...	0.01	99.85	2.23±1.19
H_3O^+	H_2O	ROH	...	CH_2	H_2O	H_2O	...	0.01	99.86	2.61±1.45
H_3O^+	H_2O	H_2O	H_2O	...	H_2O	CH_2	...	0.01	99.87	12.20±8.28
H_3O^+	H_2O	ROH	H_2O	H_2O	H_2O	CH_2	H_2O	0.01	99.87	1.89±0.00
ROH_2^+	H_2O	H_2O	...	...	ROH	H_2O	CH_2	0.01	99.88	1.74±0.00
H_3O^+	H_2O	H_2O	H_2O	CH_2	H_2O	CH_2	...	0.01	99.89	0.58±0.00

Table K.5 Continued.

Z_{prot}	Z_{shared}	$HB_{A,p}$	$HB_{A,p}$	$HB_{D,p}$	$HB_{A,s}$	$HB_{A,s}$	$HB_{D,s}$	%	$\sum$ %	Lifetime (fs)
H_3O^+	H_2O	H_2O	...	H_2O	ROH	H_2O	...	0.01	99.89	8.86±0.00
H_3O^+	H_2O	H_2O	H_2O	CH_2	CH_2	...	...	0.01	99.90	4.94±4.36
H_3O^+	H_2O	H_2O	H_2O	...	ROR	CH_2	H_2O	0.01	99.90	5.08±0.00
H_3O^+	H_2O	H_2O	...	CH_2	ROH	...	...	0.01	99.91	1.16±0.00
H_3O^+	H_2O	ROH	H_2O	...	ROH	...	...	0.00	99.91	4.36±1.60
H_3O^+	H_2O	H_2O	H_2O	ROH	ROR	H_2O	...	0.00	99.92	11.04±0.00
H_3O^+	H_2O	H_2O	...	...	ROH	...	CH_2	0.00	99.92	0.58±0.00
H_3O^+	H_2O	ROH	...	H_2O	H_2O	...	H_2O	0.00	99.93	0.58±0.00
OH^-	H_2O	...	...	H_2O	ROR	H_2O	H_2O	0.00	99.93	9.44±0.00
H_3O^+	H_2O	CH_2	...	...	H_2O	H_2O	H_2O	0.00	99.94	1.60±0.00
H_3O^+	ROH	ROH	H_2O	...	H_2O	...	H_2O	0.00	99.94	0.87±0.00
H_3O^+	H_2O	H_2O	H_2O	...	CH_2	...	...	0.00	99.94	1.60±0.00
H_3O^+	H_2O	H_2O	H_2O	...	ROR	H_2O	CH_2	0.00	99.95	2.40±0.22
OH^-	ROH	...	...	H_2O	H_2O	...	ROH	0.00	99.95	0.29±0.00
H_3O^+	H_2O	ROH	...	H_2O	H_2O	H_2O	H_2O	0.00	99.95	1.02±0.29
H_3O^+	H_2O	ROH	...	H_2O	H_2O	H_2O	CH_2	0.00	99.96	0.15±0.00
H_3O^+	ROH	ROH	H_2O	...	H_2O	...	...	0.00	99.96	2.61±0.00
H_3O^+	H_2O	H_2O	H_2O	...	ROR	...	H_2O	0.00	99.96	1.74±0.00
H_3O^+	H_2O	...	...	...	H_2O	H_2O	H_2O	0.00	99.96	1.74±0.00
H_3O^+	H_2O	H_2O	CH_2	...	ROH	...	H_2O	0.00	99.97	6.24±0.00
H_3O^+	H_2O	ROH	H_2O	H_2O	H_2O	...	CH_2	0.00	99.97	0.29±0.00
H_3O^+	H_2O	H_2O	H_2O	CH_2	ROH	H_2O	ROH	0.00	99.97	38.19±0.00
H_3O^+	H_2O	ROH	H_2O	CH_2	ROH	...	H_2O	0.00	99.97	5.23±0.00
OH^-	H_2O	...	...	H_2O	H_2O	H_2O	...	0.00	99.97	3.63±0.00
H_3O^+	H_2O	H_2O	...	...	H_2O	CH_2	H_2O	0.00	99.98	0.29±0.00
H_3O^+	H_2O	H_2O	H_2O	ROH	ROR	H_2O	H_2O	0.00	99.98	3.19±0.00
H_3O^+	H_2O	ROH	...	...	H_2O	...	H_2O	0.00	99.99	3.05±0.00
H_3O^+	H_2O	H_2O	...	CH_2	ROH	...	CH_2	0.00	99.99	2.90±0.00
H_3O^+	H_2O	...	...	H_2O	H_2O	H_2O	CH_2	0.00	99.99	2.32±0.00
H_3O^+	H_2O	H_2O	H_2O	CH_2	ROR	...	...	0.00	99.99	18.30±0.00
H_3O^+	H_2O	H_2O	H_2O	H_2O	H_2O	CH_2	...	0.00	100	0.73±0.00

Table K.6: The occurrences and lifetimes of all hydrogen-bond networks around protonated species found in TEG-water mixture for PBE. The table lists the protonated species (Z_{prot}), the atom (Z_{shared}) hydrogen bonded to the most active proton, the solvating atoms of the protonated species ($HB_{X,p}$ where x=A or D for accepting or donating a hydrogen bond and y = 1 or 2), and the solvating atoms of Z_{shared} ($HB_{X,s}$ with the same definitions of x). Figure 4.4 provides the illustration to match these labels. Proton rattling effects are included.

Z_{prot}	Z_{shared}	$HB_{A,p}$	$HB_{A,p}$	$HB_{D,p}$	$HB_{A,s}$	$HB_{A,s}$	$HB_{D,s}$	%	$\sum$ %	Lifetime (fs)
H_3O^+	H_2O	H_2O	H_2O	...	H_2O	H_2O	H_2O	21.35	21.35	7.98±10.79
H_3O^+	H_2O	H_2O	H_2O	...	H_2O	H_2O	...	19.71	41.06	7.62±9.39
H_3O^+	H_2O	H_2O	H_2O	...	H_2O	H_2O	CH_2	6.45	47.51	7.23±8.06
H_3O^+	H_2O	H_2O	H_2O	...	ROH	H_2O	...	5.26	52.78	8.10±9.60
H_3O^+	H_2O	H_2O	H_2O	...	ROH	H_2O	H_2O	4.85	57.63	7.48±8.44
H_3O^+	H_2O	H_2O	H_2O	CH_2	H_2O	H_2O	...	4.10	61.73	7.26±11.29
H_3O^+	H_2O	H_2O	H_2O	CH_2	H_2O	H_2O	H_2O	4.07	65.80	6.72±8.67
H_3O^+	H_2O	H_2O	H_2O	...	H_2O	H_2O	ROH	3.01	68.81	7.09±6.73
H_3O^+	H_2O	H_2O	...	...	H_2O	H_2O	...	2.27	71.09	8.07±13.09
H_3O^+	H_2O	H_2O	H_2O	...	H_2O	...	...	2.04	73.12	9.62±12.87
H_3O^+	H_2O	H_2O	H_2O	H_2O	H_2O	H_2O	H_2O	1.88	75.00	7.20±8.22
H_3O^+	H_2O	H_2O	H_2O	CH_2	ROH	H_2O	...	1.73	76.74	7.05±8.83
H_3O^+	H_2O	H_2O	H_2O	H_2O	H_2O	H_2O	CH_2	1.59	78.33	7.52±10.54
H_3O^+	H_2O	H_2O	...	...	H_2O	H_2O	H_2O	1.37	79.70	7.65±9.08
H_3O^+	H_2O	H_2O	H_2O	CH_2	H_2O	H_2O	CH_2	1.25	80.95	6.90±7.74
H_3O^+	H_2O	H_2O	H_2O	...	ROH	H_2O	CH_2	1.18	82.13	6.62±8.28
H_3O^+	H_2O	H_2O	H_2O	...	H_2O	...	H_2O	1.11	83.24	6.96±7.97
H_3O^+	H_2O	H_2O	H_2O	...	H_2O	...	CH_2	1.02	84.26	6.52±7.03
H_3O^+	H_2O	ROH	H_2O	...	H_2O	H_2O	...	0.97	85.23	9.12±9.96
H_3O^+	H_2O	H_2O	H_2O	H_2O	ROH	H_2O	...	0.94	86.16	6.58±8.55
H_3O^+	H_2O	H_2O	...	H_2O	H_2O	H_2O	...	0.86	87.02	8.34±10.68
H_3O^+	H_2O	H_2O	H_2O	CH_2	H_2O	...	...	0.78	87.80	7.68±9.65
H_3O^+	H_2O	ROH	H_2O	...	H_2O	H_2O	H_2O	0.74	88.54	9.12±8.92
H_3O^+	H_2O	ROH	H_2O	H_2O	H_2O	H_2O	H_2O	0.73	89.27	7.80±11.99
H_3O^+	H_2O	ROH	H_2O	H_2O	H_2O	H_2O	CH_2	0.51	89.78	6.23±5.20
H_3O^+	H_2O	H_2O	H_2O	H_2O	ROH	H_2O	H_2O	0.49	90.27	9.82±11.13
H_3O^+	H_2O	H_2O	...	CH_2	H_2O	H_2O	...	0.45	90.72	5.76±6.97

Table K.6. Continued.

Z_{prot}	Z_{shared}	$HB_{A,p}$	$HB_{A,p}$	$HB_{D,p}$	$HB_{A,s}$	$HB_{A,s}$	$HB_{D,s}$	%	$\sum$ %	Lifetime (fs)
H_3O^+	H_2O	H_2O	...	...	ROH	H_2O	...	0.41	91.13	9.38±15.42
H_3O^+	H_2O	H_2O	...	...	H_2O	H_2O	CH_2	0.36	91.49	5.93±7.21
H_3O^+	H_2O	ROH	H_2O	...	H_2O	...	...	0.33	91.82	9.14±9.02
H_3O^+	H_2O	H_2O	H_2O	CH_2	H_2O	...	H_2O	0.32	92.13	5.48±7.32
H_3O^+	ROH	H_2O	H_2O	...	H_2O	...	H_2O	0.32	92.45	9.91±9.01
H_3O^+	H_2O	H_2O	H_2O	H_2O	H_2O	...	...	0.30	92.75	9.39±12.74
H_3O^+	H_2O	H_2O	H_2O	...	H_2O	...	ROH	0.29	93.05	11.28±13.43
H_3O^+	H_2O	H_2O	...	CH_2	H_2O	H_2O	H_2O	0.29	93.33	6.18±6.95
H_3O^+	H_2O	H_2O	...	...	H_2O	...	...	0.27	93.60	5.33±6.18
H_3O^+	H_2O	H_2O	H_2O	H_2O	ROH	H_2O	CH_2	0.25	93.85	7.68±8.76
H_3O^+	H_2O	H_2O	...	CH_2	H_2O	H_2O	CH_2	0.25	94.10	4.68±5.16
H_3O^+	H_2O	H_2O	H_2O	CH_2	ROH	H_2O	H_2O	0.24	94.34	8.88±12.93
H_3O^+	ROH	H_2O	H_2O	H_2O	H_2O	...	CH_2	0.23	94.57	10.57±10.72
H_3O^+	H_2O	H_2O	H_2O	ROH	H_2O	H_2O	H_2O	0.21	94.77	8.12±8.42
H_3O^+	H_2O	H_2O	H_2O	...	ROH	...	...	0.21	94.98	11.85±19.12
H_3O^+	H_2O	H_2O	H_2O	ROH	H_2O	H_2O	CH_2	0.20	95.17	6.75±5.69
H_3O^+	H_2O	H_2O	H_2O	H_2O	H_2O	...	CH_2	0.19	95.37	5.04±6.13
H_3O^+	H_2O	H_2O	...	...	ROH	H_2O	H_2O	0.19	95.56	6.86±7.19
H_3O^+	H_2O	H_2O	...	...	H_2O	...	H_2O	0.18	95.74	4.90±5.77
H_3O^+	H_2O	H_2O	H_2O	H_2O	H_2O	...	H_2O	0.17	95.91	5.01±4.92
H_3O^+	ROH	H_2O	H_2O	H_2O	H_2O	...	...	0.16	96.07	5.70±3.55
H_3O^+	H_2O	H_2O	H_2O	CH_2	ROR	H_2O	H_2O	0.14	96.21	8.08±8.59
H_3O^+	H_2O	H_2O	...	H_2O	H_2O	H_2O	CH_2	0.14	96.35	6.83±6.68
H_3O^+	H_2O	H_2O	H_2O	...	ROR	H_2O	...	0.14	96.49	5.55±3.57
H_3O^+	H_2O	H_2O	H_2O	CH_2	H_2O	...	CH_2	0.13	96.62	7.00±11.40
H_3O^+	H_2O	H_2O	...	...	H_2O	H_2O	ROH	0.12	96.74	5.45±5.82
H_3O^+	H_2O	H_2O	CH_2	...	H_2O	H_2O	...	0.12	96.85	8.49±18.94
ROH_2^+	H_2O	H_2O	...	H_2O	H_2O	H_2O	H_2O	0.12	96.97	8.13±6.02
H_3O^+	H_2O	ROH	H_2O	H_2O	H_2O	...	...	0.12	97.09	8.67±11.16
H_3O^+	H_2O	H_2O	H_2O	...	ROR	H_2O	H_2O	0.11	97.20	5.97±5.96
H_3O^+	ROH	H_2O	H_2O	...	H_2O	...	...	0.11	97.30	13.18±21.72
H_3O^+	H_2O	H_2O	H_2O	H_2O	H_2O	H_2O	ROH	0.10	97.40	5.78±6.18
H_3O^+	H_2O	ROH	H_2O	...	H_2O	...	CH_2	0.09	97.49	15.13±16.10
H_3O^+	H_2O	H_2O	H_2O	...	H_2O	CH_2	H_2O	0.09	97.58	8.53±8.26
H_3O^+	H_2O	H_2O	...	...	ROR	H_2O	...	0.08	97.67	5.03±3.62
H_3O^+	H_2O	H_2O	H_2O	...	ROH	...	H_2O	0.08	97.75	9.05±11.44
H_3O^+	H_2O	H_2O	...	...	ROH	H_2O	CH_2	0.08	97.83	7.49±6.19
H_3O^+	H_2O	H_2O	...	CH_2	H_2O	...	...	0.08	97.90	4.28±5.43
H_3O^+	H_2O	H_2O	CH_2	CH_2	H_2O	H_2O	...	0.07	97.97	6.62±5.87
H_3O^+	H_2O	H_2O	H_2O	H_2O	H_2O	CH_2	...	0.06	98.04	4.99±4.27
H_3O^+	ROH	H_2O	H_2O	CH_2	H_2O	...	H_2O	0.06	98.10	6.75±8.56
H_3O^+	H_2O	H_2O	H_2O	ROH	H_2O	...	...	0.06	98.16	7.97±4.81
H_3O^+	H_2O	ROH	H_2O	...	H_2O	H_2O	CH_2	0.06	98.22	6.58±3.96
H_3O^+	H_2O	H_2O	H_2O	CH_2	ROH	H_2O	CH_2	0.06	98.28	8.10±6.18
H_3O^+	H_2O	H_2O	H_2O	...	ROH	...	CH_2	0.05	98.33	8.96±7.69
H_3O^+	H_2O	H_2O	H_2O	CH_2	ROR	H_2O	...	0.05	98.39	2.62±2.77
H_3O^+	H_2O	H_2O	...	...	H_2O	...	ROH	0.05	98.44	1.67±1.05
H_3O^+	H_2O	ROH	H_2O	CH_2	H_2O	...	...	0.05	98.49	7.10±5.13
H_3O^+	H_2O	ROH	...	...	H_2O	H_2O	CH_2	0.05	98.54	9.76±14.25
H_3O^+	H_2O	H_2O	...	CH_2	ROH	H_2O	...	0.05	98.58	11.22±19.82
H_3O^+	H_2O	H_2O	...	H_2O	ROR	H_2O	...	0.05	98.63	4.79±3.46
H_3O^+	H_2O	H_2O	H_2O	H_2O	ROR	H_2O	...	0.04	98.67	5.94±3.98
ROH_2^+	H_2O	H_2O	...	CH_2	H_2O	H_2O	...	0.04	98.71	14.48±15.43
H_3O^+	H_2O	ROH	H_2O	CH_2	H_2O	H_2O	CH_2	0.04	98.75	5.18±4.64
H_3O^+	H_2O	H_2O	...	H_2O	ROH	H_2O	...	0.04	98.79	3.86±1.95
H_3O^+	H_2O	H_2O	CH_2	H_2O	H_2O	H_2O	...	0.04	98.83	5.14±3.08
H_3O^+	H_2O	H_2O	...	CH_2	H_2O	...	H_2O	0.04	98.87	6.31±8.77
H_3O^+	ROH	H_2O	H_2O	CH_2	H_2O	...	...	0.04	98.90	3.94±2.74
H_3O^+	H_2O	ROH	...	...	H_2O	H_2O	H_2O	0.04	98.94	4.68±5.69
H_3O^+	H_2O	H_2O	H_2O	...	H_2O	CH_2	...	0.03	98.98	6.11±2.85
H_3O^+	ROH	H_2O	H_2O	H_2O	H_2O	...	H_2O	0.03	99.01	18.93±15.74
H_3O^+	H_2O	ROH	H_2O	H_2O	H_2O	H_2O	ROH	0.03	99.04	7.91±6.61
H_3O^+	H_2O	H_2O	...	H_2O	H_2O	H_2O	H_2O	0.03	99.06	3.81±2.27
H_3O^+	ROH	H_2O	H_2O	H_2O	CH_2	...	...	0.02	99.09	3.01±2.26
H_3O^+	H_2O	H_2O	CH_2	...	H_2O	...	...	0.02	99.11	2.87±2.40
H_3O^+	H_2O	ROH	H_2O	H_2O	H_2O	...	H_2O	0.02	99.13	7.07±7.73
H_3O^+	H_2O	ROR	H_2O	...	H_2O	H_2O	CH_2	0.02	99.15	3.00±1.48
H_3O^+	H_2O	H_2O	H_2O	CH_2	ROH	...	H_2O	0.02	99.17	2.29±1.84
H_3O^+	H_2O	...	...	...	H_2O	H_2O	...	0.02	99.19	5.19±6.01
H_3O^+	H_2O	CH_2	...	...	H_2O	H_2O	H_2O	0.02	99.22	4.36±0.52
H_3O^+	H_2O	H_2O	...	...	H_2O	...	CH_2	0.02	99.24	5.84±4.05
H_3O^+	ROH	H_2O	...	...	H_2O	...	H_2O	0.02	99.26	5.21±7.88
H_3O^+	H_2O	ROR	...	...	H_2O	H_2O	...	0.02	99.27	1.02±0.15
H_3O^+	H_2O	H_2O	...	ROH	H_2O	H_2O	CH_2	0.02	99.29	2.32±1.05
H_3O^+	H_2O	H_2O	...	ROH	H_2O	H_2O	H_2O	0.02	99.31	6.26±2.45

Table K.6. Continued.

Z_{prot}	Z_{shared}	$HB_{A,p}$	$HB_{A,p}$	$HB_{D,p}$	$HB_{A,s}$	$HB_{A,s}$	$HB_{D,s}$	%	$\sum$ %	Lifetime (fs)
H_3O^+	H_2O	H_2O	H_2O	H_2O	H_2O	CH_2	H_2O	0.02	99.33	6.48±2.91
H_3O^+	H_2O	H_2O	CH_2	...	H_2O	H_2O	CH_2	0.02	99.35	5.52±4.22
H_3O^+	H_2O	ROH	...	H_2O	H_2O	H_2O	...	0.02	99.37	14.70±15.20
H_3O^+	ROH	H_2O	H_2O	...	CH_2	...	...	0.02	99.38	5.90±6.54
H_3O^+	H_2O	H_2O	...	CH_2	ROR	H_2O	...	0.02	99.40	2.09±0.49
H_3O^+	H_2O	ROH	H_2O	CH_2	H_2O	H_2O	...	0.02	99.42	10.65±12.30
H_3O^+	H_2O	ROH	H_2O	H_2O	ROR	H_2O	...	0.02	99.43	11.12±15.32
H_3O^+	H_2O	H_2O	...	H_2O	ROH	H_2O	H_2O	0.02	99.45	4.16±6.08
H_3O^+	H_2O	...	...	...	H_2O	H_2O	CH_2	0.02	99.46	2.62±2.36
H_3O^+	H_2O	H_2O	H_2O	H_2O	ROH	...	H_2O	0.01	99.48	1.55±1.60
H_3O^+	H_2O	H_2O	H_2O	CH_2	ROH	CH_2	...	0.01	99.49	2.25±0.80
H_3O^+	H_2O	H_2O	...	CH_2	ROH	H_2O	H_2O	0.01	99.51	2.94±2.00
H_3O^+	ROH	H_2O	H_2O	CH_2	H_2O	...	CH_2	0.01	99.52	9.66±7.48
H_3O^+	H_2O	H_2O	H_2O	CH_2	ROH	...	...	0.01	99.54	4.64±5.11
H_3O^+	H_2O	H_2O	H_2O	ROH	ROH	H_2O	...	0.01	99.55	12.05±8.57
H_3O^+	H_2O	H_2O	H_2O	H_2O	ROH	...	...	0.01	99.56	8.04±5.52
H_3O^+	H_2O	H_2O	...	CH_2	H_2O	...	CH_2	0.01	99.57	4.55±4.08
H_3O^+	OH^-	ROH	H_2O	H_2O	H_2O	...	H_2O	0.01	99.59	12.63±0.29
H_3O^+	H_2O	ROR	H_2O	H_2O	H_2O	...	...	0.01	99.60	5.15±4.01
H_3O^+	H_2O	ROH	H_2O	...	H_2O	...	H_2O	0.01	99.61	16.46±11.44
H_3O^+	H_2O	H_2O	...	...	H_2O	CH_2	H_2O	0.01	99.62	0.58±0.21
H_3O^+	H_2O	ROR	...	...	H_2O	...	CH_2	0.01	99.63	0.29±0.00
H_3O^+	H_2O	H_2O	H_2O	ROH	ROR	H_2O	H_2O	0.01	99.64	5.51±3.38
H_3O^+	H_2O	H_2O	H_2O	CH_2	H_2O	...	ROH	0.01	99.65	4.36±3.05
H_3O^+	H_2O	H_2O	H_2O	CH_2	H_2O	CH_2	CH_2	0.01	99.66	13.58±8.58
H_3O^+	H_2O	ROH	H_2O	H_2O	H_2O	...	CH_2	0.01	99.67	4.79±0.00
H_3O^+	H_2O	H_2O	H_2O	CH_2	H_2O	CH_2	...	0.01	99.68	3.29±0.78
H_3O^+	H_2O	...	...	CH_2	H_2O	H_2O	H_2O	0.01	99.70	13.72±10.53
H_3O^+	H_2O	ROH	H_2O	CH_2	H_2O	H_2O	H_2O	0.01	99.70	1.96±1.52
H_3O^+	H_2O	ROR	H_2O	H_2O	H_2O	...	H_2O	0.01	99.71	4.72±1.09
H_3O^+	H_2O	ROH	H_2O	CH_2	H_2O	...	H_2O	0.01	99.72	10.20±14.30
H_3O^+	H_2O	H_2O	CH_2	...	H_2O	H_2O	H_2O	0.01	99.73	7.77±4.57
H_3O^+	ROH	H_2O	H_2O	...	H_2O	...	CH_2	0.01	99.74	6.75±4.14
H_3O^+	H_2O	ROH	...	...	H_2O	...	...	0.01	99.75	0.58±0.29
H_3O^+	H_2O	H_2O	...	...	ROH	...	...	0.01	99.76	4.84±5.72
H_3O^+	H_2O	H_2O	CH_2	CH_2	H_2O	...	...	0.01	99.76	2.25±0.65
H_3O^+	ROH	H_2O	H_2O	CH_2	CH_2	...	...	0.01	99.77	5.11±3.33
H_3O^+	H_2O	H_2O	...	CH_2	ROR	H_2O	H_2O	0.01	99.78	8.23±6.81
H_3O^+	H_2O	H_2O	...	H_2O	H_2O	H_2O	ROH	0.01	99.79	5.71±3.77
H_3O^+	H_2O	H_2O	H_2O	H_2O	ROR	H_2O	H_2O	0.01	99.79	4.86±1.96
H_3O^+	H_2O	ROH	H_2O	H_2O	ROR	H_2O	H_2O	0.01	99.80	2.62±1.60
H_3O^+	H_2O	H_2O	H_2O	...	ROR	...	H_2O	0.01	99.81	6.32±3.27
H_3O^+	H_2O	ROH	...	CH_2	H_2O	H_2O	H_2O	0.01	99.82	5.52±0.29
H_3O^+	ROH	H_2O	...	H_2O	H_2O	...	CH_2	0.01	99.82	2.61±0.87
H_3O^+	H_2O	ROR	...	...	H_2O	...	...	0.01	99.83	7.65±3.97
H_3O^+	H_2O	H_2O	...	H_2O	ROH	...	...	0.01	99.84	19.17±0.00
H_3O^+	H_2O	...	...	...	H_2O	...	CH_2	0.01	99.84	1.45±0.00
H_3O^+	H_2O	ROR	H_2O	...	H_2O	H_2O	...	0.01	99.85	4.57±0.36
H_3O^+	H_2O	ROH	...	CH_2	H_2O	H_2O	CH_2	0.01	99.86	5.45±0.36
H_3O^+	ROH	H_2O	...	CH_2	H_2O	...	...	0.01	99.86	4.79±0.00
H_3O^+	H_2O	ROR	H_2O	...	H_2O	...	...	0.01	99.87	0.73±0.00
H_3O^+	H_2O	ROH	...	CH_2	H_2O	...	...	0.01	99.87	0.15±0.00
H_3O^+	H_2O	ROR	H_2O	CH_2	H_2O	H_2O	...	0.01	99.88	4.94±0.00
H_3O^+	ROR	H_2O	H_2O	...	...	...	...	0.01	99.88	0.29±0.00
H_3O^+	H_2O	H_2O	H_2O	ROH	H_2O	...	CH_2	0.00	99.89	18.22±18.08
H_3O^+	H_2O	...	...	H_2O	H_2O	H_2O	H_2O	0.00	99.89	2.11±0.07
H_3O^+	H_2O	H_2O	...	H_2O	H_2O	CH_2	...	0.00	99.90	0.87±0.00
H_3O^+	H_2O	H_2O	...	CH_2	ROH	H_2O	CH_2	0.00	99.90	9.17±3.97
H_3O^+	H_2O	ROH	H_2O	...	ROR	H_2O	H_2O	0.00	99.91	3.48±0.00
H_3O^+	H_2O	H_2O	H_2O	ROH	ROH	H_2O	H_2O	0.00	99.91	6.82±3.49
H_3O^+	H_2O	...	...	H_2O	H_2O	H_2O	...	0.00	99.92	3.15±2.81
H_3O^+	H_2O	H_2O	H_2O	H_2O	ROH	...	CH_2	0.00	99.92	0.22±0.07
H_3O^+	H_2O	ROR	...	H_2O	H_2O	...	...	0.00	99.92	2.76±0.00
H_3O^+	H_2O	H_2O	...	...	H_2O	CH_2	...	0.00	99.93	15.25±0.00
H_3O^+	H_2O	H_2O	CH_2	H_2O	H_2O	H_2O	CH_2	0.00	99.93	0.44±0.00
H_3O^+	H_2O	H_2O	H_2O	ROH	ROR	H_2O	...	0.00	99.94	2.76±0.00
H_3O^+	ROH-	H_2O	H_2O	...	...	...	H_2O	0.00	99.94	6.90±6.03
H_3O^+	H_2O	ROH	H_2O	CH_2	H_2O	...	CH_2	0.00	99.94	1.02±0.00
H_3O^+	H_2O	H_2O	H_2O	CH_2	ROR	...	H_2O	0.00	99.95	24.97±0.00
H_3O^+	H_2O	H_2O	...	CH_2	ROH	CH_2	...	0.00	99.95	6.97±0.00
H_3O^+	H_2O	H_2O	H_2O	...	H_2O	CH_2	CH_2	0.00	99.95	8.13±0.00
H_3O^+	H_2O	...	...	...	H_2O	H_2O	H_2O	0.00	99.96	5.77±2.74
H_3O^+	H_2O	H_2O	H_2O	H_2O	H_2O	CH_2	CH_2	0.00	99.96	2.18±0.00
H_3O^+	H_2O	H_2O	H_2O	H_2O	ROH	ROR	H_2O	0.00	99.96	8.13±0.00

Table K.6. Continued.

Z_{prot}	Z_{shared}	$HB_{A,p}$	$HB_{A,p}$	$HB_{D,p}$	$HB_{A,s}$	$HB_{A,s}$	$HB_{D,s}$	%	$\sum$ %	Lifetime (fs)
H_3O^+	H_2O	H_2O	...	H_2O	H_2O	...	CH_2	0.00	99.96	1.02±0.00
H_3O^+	H_2O	H_2O	...	ROH	H_2O	...	...	0.00	99.97	4.57±0.80
H_3O^+	H_2O	H_2O	...	ROH	H_2O	...	H_2O	0.00	99.97	10.31±0.00
H_3O^+	H_2O	ROH	...	CH_2	H_2O	H_2O	...	0.00	99.97	17.86±0.00
H_3O^+	H_2O	ROR	...	...	H_2O	H_2O	CH_2	0.00	99.97	6.17±4.72
H_3O^+	H_2O	H_2O	...	...	ROH	...	CH_2	0.00	99.97	5.15±0.94
H_3O^+	H_2O	ROH	...	H_2O	H_2O	H_2O	H_2O	0.00	99.98	10.16±0.00
H_3O^+	H_2O	...	...	...	H_2O	...	H_2O	0.00	99.98	5.52±3.34
H_3O^+	H_2O	H_2O	...	CH_2	H_2O	CH_2	CH_2	0.00	99.98	3.78±0.00
H_3O^+	H_2O	ROH	H_2O	...	ROR	H_2O	...	0.00	99.98	4.07±0.00
H_3O^+	H_2O	H_2O	...	ROH	ROH	H_2O	H_2O	0.00	99.98	26.43±0.00
H_3O^+	ROR	H_2O	H_2O	H_2O	...	...	...	0.00	99.98	3.12±1.82
H_3O^+	H_2O	H_2O	H_2O	CH_2	H_2O	CH_2	H_2O	0.00	99.99	0.73±0.00
H_3O^+	H_2O	...	...	H_2O	H_2O	H_2O	CH_2	0.00	99.99	1.89±0.00
ROH-	H_3O^+	...	...	...	H_2O	H_2O	...	0.00	99.99	0.58±0.00
H_3O^+	ROH	H_2O	H_2O	...	CH_2	...	H_2O	0.00	99.99	2.47±0.00
H_3O^+	H_2O	ROH	CH_2	CH_2	H_2O	H_2O	...	0.00	99.99	7.11±0.00
H_3O^+	H_2O	ROH	...	...	H_2O	...	H_2O	0.00	99.99	0.15±0.00
H_3O^+	ROH	H_2O	...	...	H_2O	...	...	0.00	99.99	2.61±0.00
H_3O^+	H_2O	ROH	CH_2	CH_2	H_2O	...	...	0.00	100	0.58±0.00

Table K.7: The occurrences and lifetimes of all hydrogen-bond networks around protonated species found in TEG-water mixture for PBE+TS-vdW. The table lists the protonated species (Z_{prot}), the atom (Z_{shared}) hydrogen bonded to the most active proton, the solvating atoms of the protonated species ($HB_{X,p}$ where x=A or D for accepting or donating a hydrogen bond and y = 1 or 2), and the solvating atoms of Z_{shared} ($HB_{X,s}$ with the same definitions of x). Figure 4.4 provides the illustration to match these labels. Proton rattling effects are included.

Z_{prot}	Z_{shared}	$HB_{A,p}$	$HB_{A,p}$	$HB_{D,p}$	$HB_{A,s}$	$HB_{A,s}$	$HB_{D,s}$	%	$\sum$ %	Lifetime (fs)
H_3O^+	H_2O	H_2O	H_2O	...	H_2O	H_2O	H_2O	20.56	20.56	6.91±7.77
H_3O^+	H_2O	H_2O	H_2O	...	H_2O	H_2O	...	14.09	34.65	7.12±7.52
H_3O^+	H_2O	H_2O	H_2O	...	ROR	H_2O	...	6.67	41.33	6.60±7.19
H_3O^+	H_2O	H_2O	H_2O	CH_2	H_2O	H_2O	...	6.66	47.98	6.27±6.28
H_3O^+	H_2O	H_2O	H_2O	CH_2	H_2O	H_2O	H_2O	6.22	54.21	6.55±6.92
H_3O^+	H_2O	H_2O	H_2O	...	H_2O	H_2O	CH_2	4.62	58.82	7.33±8.90
H_3O^+	H_2O	H_2O	H_2O	H_2O	H_2O	H_2O	H_2O	3.89	62.71	7.05±7.75
H_3O^+	H_2O	H_2O	H_2O	...	ROR	H_2O	H_2O	2.66	65.38	7.04±6.99
H_3O^+	H_2O	H_2O	H_2O	...	H_2O	...	...	2.37	67.74	6.40±6.64
H_3O^+	H_2O	H_2O	H_2O	...	ROH	H_2O	...	2.37	70.11	5.88±5.03
H_3O^+	H_2O	H_2O	H_2O	CH_2	ROR	H_2O	...	2.06	72.17	5.88±6.05
H_3O^+	H_2O	H_2O	H_2O	...	H_2O	...	H_2O	1.62	73.79	5.87±6.81
H_3O^+	H_2O	H_2O	H_2O	...	ROH	H_2O	H_2O	1.35	75.14	6.13±6.36
H_3O^+	H_2O	H_2O	H_2O	...	H_2O	CH_2	...	1.30	76.45	6.87±7.02
H_3O^+	H_2O	H_2O	H_2O	...	ROH	ROR	H_2O	1.06	77.51	6.99±8.87
H_3O^+	H_2O	H_2O	H_2O	H_2O	H_2O	...	...	1.03	78.53	7.60±8.76
H_3O^+	H_2O	H_2O	H_2O	H_2O	ROR	H_2O	...	1.00	79.54	6.61±8.73
H_3O^+	H_2O	H_2O	H_2O	...	ROH	ROR	...	0.86	80.40	6.71±6.36
H_3O^+	H_2O	H_2O	H_2O	CH_2	H_2O	H_2O	CH_2	0.79	81.19	4.62±4.23
H_3O^+	H_2O	H_2O	H_2O	...	ROH	...	...	0.79	81.98	8.50±9.04
H_3O^+	H_2O	H_2O	...	CH_2	H_2O	H_2O	...	0.78	82.76	4.59±5.08
H_3O^+	H_2O	H_2O	H_2O	CH_2	H_2O	...	...	0.71	83.47	6.11±7.91
H_3O^+	H_2O	ROH	H_2O	...	H_2O	H_2O	H_2O	0.71	84.18	6.15±5.95
H_3O^+	H_2O	H_2O	H_2O	...	H_2O	...	CH_2	0.69	84.87	6.94±7.94
H_3O^+	H_2O	ROR	H_2O	...	H_2O	H_2O	H_2O	0.68	85.55	7.70±6.24
H_3O^+	H_2O	H_2O	H_2O	...	H_2O	H_2O	ROH	0.60	86.15	9.46±10.36
H_3O^+	H_2O	H_2O	H_2O	CH_2	H_2O	...	H_2O	0.58	86.73	4.66±4.74
H_3O^+	H_2O	H_2O	...	...	ROR	H_2O	...	0.57	87.30	8.15±10.38
H_3O^+	H_2O	H_2O	H_2O	...	ROR	...	...	0.57	87.87	6.83±5.58
H_3O^+	H_2O	H_2O	...	...	H_2O	H_2O	...	0.56	88.43	6.56±8.96
H_3O^+	H_2O	H_2O	H_2O	...	ROR	H_2O	CH_2	0.55	88.98	6.49±7.81
H_3O^+	H_2O	H_2O	H_2O	ROH	H_2O	H_2O	CH_2	0.52	89.50	6.77±7.46
H_3O^+	H_2O	H_2O	...	...	H_2O	H_2O	H_2O	0.50	89.99	4.75±4.93
H_3O^+	H_2O	H_2O	H_2O	H_2O	H_2O	...	H_2O	0.49	90.49	6.15±5.80
H_3O^+	H_2O	H_2O	H_2O	...	H_2O	CH_2	H_2O	0.49	90.97	7.57±9.31
H_3O^+	H_2O	H_2O	H_2O	CH_2	ROR	H_2O	H_2O	0.47	91.44	5.52±3.96
H_3O^+	H_2O	H_2O	...	CH_2	H_2O	H_2O	H_2O	0.42	91.86	5.32±6.53

Table K.7. Continued.

Z_{prot}	Z_{shared}	$HB_{A,p}$	$HB_{A,p}$	$HB_{D,p}$	$HB_{A,s}$	$HB_{A,s}$	$HB_{D,s}$	%	$\sum$ %	Lifetime (fs)
H_3O^+	H_2O	H_2O	...	...	H_2O	H_2O	CH_2	0.38	92.24	7.23±10.66
H_3O^+	H_2O	H_2O	H_2O	...	ROH	...	H_2O	0.33	92.57	4.58±3.36
H_3O^+	H_2O	ROH	...	...	H_2O	H_2O	H_2O	0.32	92.90	7.08±4.77
H_3O^+	H_2O	H_2O	H_2O	...	ROH	H_2O	CH_2	0.27	93.17	5.64±5.51
H_3O^+	H_2O	ROH	H_2O	H_2O	H_2O	H_2O	H_2O	0.26	93.43	7.41±7.32
H_3O^+	H_2O	H_2O	H_2O	H_2O	ROH	ROR	H_2O	0.23	93.66	7.14±4.32
H_3O^+	H_2O	H_2O	H_2O	...	ROH	CH_2	H_2O	0.22	93.88	8.67±12.48
H_3O^+	H_2O	H_2O	CH_2	...	H_2O	...	...	0.21	94.09	4.63±4.15
H_3O^+	H_2O	H_2O	H_2O	H_2O	ROR	H_2O	H_2O	0.19	94.28	4.66±4.53
H_3O^+	H_2O	H_2O	H_2O	CH_2	H_2O	CH_2	...	0.19	94.47	5.90±9.92
H_3O^+	H_2O	H_2O	H_2O	CH_2	ROH	ROR	H_2O	0.19	94.65	4.93±3.80
H_3O^+	H_2O	H_2O	H_2O	ROH	H_2O	H_2O	...	0.18	94.83	4.89±2.63
H_3O^+	ROH	H_2O	H_2O	...	H_2O	...	...	0.18	95.01	9.50±9.14
H_3O^+	H_2O	H_2O	H_2O	CH_2	ROR	...	...	0.16	95.17	5.99±4.02
H_3O^+	H_2O	H_2O	H_2O	CH_2	ROH	H_2O	...	0.16	95.33	6.61±8.31
H_3O^+	H_2O	H_2O	...	...	H_2O	...	H_2O	0.16	95.49	4.12±4.10
H_3O^+	H_2O	H_2O	H_2O	H_2O	H_2O	...	CH_2	0.15	95.64	9.31±16.84
H_3O^+	H_2O	H_2O	...	...	H_2O	H_2O	ROH	0.15	95.79	8.91±10.22
H_3O^+	H_2O	ROH	...	H_2O	H_2O	H_2O	H_2O	0.14	95.93	4.90±3.33
H_3O^+	H_2O	H_2O	H_2O	H_2O	H_2O	H_2O	ROH	0.14	96.07	5.87±4.49
H_3O^+	H_2O	H_2O	CH_2	...	H_2O	H_2O	ROH	0.14	96.21	5.06±5.68
H_3O^+	H_2O	H_2O	H_2O	CH_2	H_2O	...	ROH	0.14	96.35	6.83±5.92
H_3O^+	H_2O	H_2O	...	...	H_2O	...	...	0.13	96.48	5.78±4.28
H_3O^+	H_2O	H_2O	H_2O	CH_2	H_2O	...	CH_2	0.13	96.61	4.93±4.48
H_3O^+	H_2O	H_2O	H_2O	H_2O	ROH	ROR	...	0.12	96.73	5.98±4.99
H_3O^+	ROH	H_2O	H_2O	H_2O	H_2O	...	...	0.12	96.85	5.69±4.13
H_3O^+	H_2O	H_2O	H_2O	CH_2	ROH	ROR	...	0.12	96.97	10.56±9.92
H_3O^+	H_2O	H_2O	H_2O	...	ROR	...	CH_2	0.11	97.08	6.94±5.31
H_3O^+	H_2O	H_2O	H_2O	H_2O	ROR	...	...	0.11	97.19	5.25±5.73
H_3O^+	H_2O	H_2O	H_2O	CH_2	ROR	H_2O	CH_2	0.11	97.30	5.10±3.54
H_3O^+	H_2O	ROR	H_2O	...	H_2O	...	CH_2	0.10	97.40	6.27±6.81
H_3O^+	H_2O	H_2O	H_2O	H_2O	H_2O	CH_2	...	0.10	97.50	4.62±4.02
H_3O^+	H_2O	ROR	H_2O	...	H_2O	H_2O	ROH	0.09	97.59	5.45±4.23
H_3O^+	ROH	H_2O	H_2O	...	H_2O	...	CH_2	0.08	97.68	7.84±3.23
H_3O^+	H_2O	H_2O	...	...	H_2O	...	CH_2	0.08	97.75	2.95±2.82
H_3O^+	H_2O	H_2O	...	CH_2	H_2O	H_2O	CH_2	0.07	97.82	6.93±8.80
H_3O^+	H_2O	H_2O	H_2O	CH_2	ROH	H_2O	H_2O	0.07	97.89	2.89±1.93
H_3O^+	H_2O	ROR	H_2O	H_2O	H_2O	H_2O	ROH	0.07	97.96	6.28±3.78
H_3O^+	H_2O	H_2O	H_2O	...	ROR	...	H_2O	0.07	98.03	4.27±4.83
H_3O^+	H_2O	H_2O	H_2O	...	H_2O	...	ROH	0.07	98.09	5.26±5.92
H_3O^+	H_2O	H_2O	H_2O	H_2O	ROH	H_2O	H_2O	0.06	98.15	6.76±4.63
H_3O^+	H_2O	ROH	CH_2	...	H_2O	H_2O	H_2O	0.06	98.22	4.03±2.28
H_3O^+	H_2O	H_2O	CH_2	H_2O	H_2O	H_2O	ROH	0.06	98.28	3.05±2.34
H_3O^+	H_2O	H_2O	H_2O	H_2O	ROH	CH_2	H_2O	0.06	98.33	5.25±3.82
H_3O^+	H_2O	H_2O	...	CH_2	H_2O	H_2O	ROH	0.06	98.39	10.09±9.18
H_3O^+	H_2O	H_2O	...	H_2O	ROR	H_2O	...	0.06	98.45	6.87±7.19
H_3O^+	H_2O	ROH	H_2O	H_2O	H_2O	...	...	0.05	98.50	4.17±3.33
H_3O^+	H_2O	H_2O	H_2O	ROH	H_2O	H_2O	H_2O	0.05	98.55	6.82±4.92
H_3O^+	H_2O	H_2O	H_2O	H_2O	ROR	H_2O	CH_2	0.05	98.60	2.53±2.00
H_3O^+	H_2O	H_2O	...	...	ROR	H_2O	H_2O	0.05	98.65	6.94±6.51
H_3O^+	H_2O	H_2O	H_2O	H_2O	H_2O	CH_2	H_2O	0.05	98.70	5.36±2.92
H_3O^+	H_2O	...	...	CH_2	H_2O	H_2O	...	0.05	98.75	3.39±0.54
H_3O^+	H_2O	ROH	H_2O	...	H_2O	...	H_2O	0.05	98.80	7.03±4.01
H_3O^+	H_2O	H_2O	...	CH_2	ROR	H_2O	CH_2	0.05	98.85	1.78±1.61
H_3O^+	H_2O	H_2O	H_2O	CH_2	ROH	...	H_2O	0.05	98.90	7.74±7.82
H_3O^+	H_2O	H_2O	H_2O	CH_2	H_2O	CH_2	H_2O	0.04	98.94	5.49±2.94
H_3O^+	H_2O	H_2O	H_2O	CH_2	ROR	...	CH_2	0.04	98.98	2.85±1.23
H_3O^+	H_2O	H_2O	H_2O	...	ROH	CH_2	...	0.04	99.03	6.10±4.54
H_3O^+	H_2O	H_2O	...	...	H_2O	CH_2	H_2O	0.04	99.07	4.53±4.20
H_3O^+	H_2O	H_2O	...	CH_2	H_2O	...	H_2O	0.03	99.10	1.59±0.43
H_3O^+	H_2O	H_2O	H_2O	CH_2	ROR	...	H_2O	0.03	99.13	3.58±3.50
H_3O^+	H_2O	...	...	CH_2	H_2O	H_2O	CH_2	0.03	99.16	1.52±0.22
H_3O^+	H_2O	H_2O	H_2O	H_2O	ROH	H_2O	...	0.03	99.19	7.11±4.57
H_3O^+	H_2O	H_2O	H_2O	H_2O	ROH	H_2O	CH_2	0.03	99.22	5.81±4.17
H_3O^+	H_2O	ROR	...	H_2O	H_2O	H_2O	ROH	0.03	99.25	2.27±2.19
H_3O^+	H_2O	H_2O	...	...	ROR	...	...	0.03	99.27	4.66±3.74
H_3O^+	H_2O	H_2O	...	...	ROR	H_2O	CH_2	0.03	99.30	7.75±5.23
H_3O^+	ROH	H_2O	H_2O	...	CH_2	...	...	0.02	99.32	32.04±30.56
H_3O^+	H_2O	...	...	...	H_2O	H_2O	...	0.02	99.34	3.94±1.79
H_3O^+	H_2O	H_2O	H_2O	H_2O	H_2O	...	ROH	0.02	99.37	7.89±3.81
H_3O^+	ROH	H_2O	H_2O	H_2O	H_2O	...	CH_2	0.02	99.39	5.08±0.00
H_3O^+	H_2O	ROH	...	...	H_2O	H_2O	...	0.02	99.41	5.18±2.97
H_3O^+	H_2O	H_2O	...	...	ROH	H_2O	H_2O	0.02	99.43	33.83±25.01
H_3O^+	H_2O	...	...	...	H_2O	H_2O	CH_2	0.02	99.45	3.21±2.87
H_3O^+	H_2O	ROH	H_2O	CH_2	H_2O	H_2O	CH_2	0.02	99.47	2.76±0.00

Table K.7. Continued.

Z_{prot}	Z_{shared}	$HB_{A,p}$	$HB_{A,p}$	$HB_{D,p}$	$HB_{A,s}$	$HB_{A,s}$	$HB_{D,s}$	%	$\sum$ %	Lifetime (fs)
H_3O^+	H_2O	ROR	...	...	H_2O	H_2O	ROH	0.02	99.49	6.46±0.07
H_3O^+	H_2O	H_2O	...	...	ROH	H_2O	CH_2	0.02	99.50	5.11±5.49
H_3O^+	H_2O	H_2O	...	H_2O	H_2O	...	H_2O	0.02	99.52	3.92±3.80
H_3O^+	H_2O	ROR	H_2O	...	H_2O	...	ROH	0.02	99.54	8.35±4.57
H_3O^+	ROH	H_2O	...	...	H_2O	...	...	0.02	99.56	3.58±3.05
H_3O^+	H_2O	H_2O	H_2O	ROH	ROH	H_2O	...	0.02	99.57	13.79±13.65
H_3O^+	H_2O	H_2O	H_2O	CH_2	ROH	H_2O	CH_2	0.02	99.59	3.18±1.34
H_3O^+	H_2O	H_2O	H_2O	ROH	H_2O	CH_2	CH_2	0.02	99.61	5.59±1.96
H_3O^+	H_2O	H_2O	...	...	ROH	H_2O	...	0.01	99.62	5.49±1.26
H_3O^+	H_2O	H_2O	H_2O	...	H_2O	CH_2	CH_2	0.01	99.63	4.60±5.38
H_3O^+	H_2O	H_2O	...	CH_2	ROR	H_2O	...	0.01	99.65	1.45±0.00
H_3O^+	H_2O	H_2O	H_2O	...	ROR	ROR	...	0.01	99.66	6.82±0.00
H_3O^+	ROH	ROR	H_2O	H_2O	H_2O	...	...	0.01	99.68	6.53±0.00
H_3O^+	H_2O	H_2O	...	CH_2	ROR	H_2O	H_2O	0.01	99.69	1.50±1.13
H_3O^+	H_2O	H_2O	...	CH_2	ROR	...	CH_2	0.01	99.70	1.02±0.87
H_3O^+	H_2O	H_2O	...	...	ROH	CH_2	H_2O	0.01	99.72	1.89±0.00
H_3O^+	H_2O	H_2O	...	H_2O	ROH	H_2O	CH_2	0.01	99.73	0.44±0.00
H_3O^+	H_2O	H_2O	...	ROH	H_2O	H_2O	...	0.01	99.74	6.97±0.00
H_3O^+	ROH	H_2O	H_2O	CH_2	H_2O	...	...	0.01	99.76	4.43±3.56
H_3O^+	H_2O	H_2O	...	H_2O	ROR	...	...	0.01	99.77	1.08±0.07
H_3O^+	H_2O	H_2O	...	H_2O	ROH	H_2O	...	0.01	99.78	7.26±0.00
H_3O^+	ROH	H_2O	...	...	H_2O	...	H_2O	0.01	99.79	5.15±0.65
H_3O^+	H_2O	...	...	...	H_2O	H_2O	H_2O	0.01	99.80	13.79±5.95
H_3O^+	H_2O	H_2O	...	CH_2	H_2O	...	ROH	0.01	99.81	4.65±2.90
H_3O^+	H_2O	H_2O	...	ROH	H_2O	...	...	0.01	99.82	10.31±0.00
H_3O^+	H_2O	H_2O	H_2O	CH_2	ROR	ROR	...	0.01	99.83	8.86±1.60
H_3O^+	ROR	H_2O	H_2O	H_2O	...	...	...	0.01	99.84	1.60±0.00
H_3O^+	H_2O	H_2O	...	...	ROH	ROR	H_2O	0.01	99.85	21.20±0.00
H_3O^+	H_2O	ROH	H_2O	CH_2	H_2O	H_2O	ROH	0.01	99.86	3.05±0.00
H_3O^+	H_2O	H_2O	...	ROH	H_2O	H_2O	H_2O	0.01	99.87	23.09±0.00
H_3O^+	H_2O	H_2O	CH_2	H_2O	H_2O	...	CH_2	0.01	99.88	1.45±0.00
H_3O^+	ROH	...	...	...	H_2O	...	...	0.01	99.88	14.81±0.00
H_3O^+	H_2O	H_2O	...	CH_2	ROR	...	...	0.01	99.89	2.18±0.00
H_3O^+	H_2O	H_2O	...	...	ROH	ROR	...	0.01	99.90	3.78±0.00
H_3O^+	H_2O	H_2O	...	H_2O	ROH	ROR	H_2O	0.01	99.91	16.41±0.00
H_3O^+	H_2O	H_2O	...	...	H_2O	CH_2	...	0.01	99.91	4.07±0.15
H_3O^+	ROH	H_2O	...	H_2O	H_2O	...	...	0.01	99.92	3.92±0.00
H_3O^+	H_2O	H_2O	...	H_2O	ROH	ROR	...	0.01	99.93	3.05±0.00
H_3O^+	H_2O	H_2O	H_2O	ROH	H_2O	...	H_2O	0.01	99.93	3.00±1.58
H_3O^+	H_2O	H_2O	...	H_2O	H_2O	CH_2	...	0.01	99.94	0.44±0.00
H_3O^+	H_2O	H_2O	...	CH_2	H_2O	CH_2	...	0.00	99.94	2.03±0.00
H_3O^+	H_2O	H_2O	...	H_2O	ROR	...	CH_2	0.00	99.95	0.58±0.00
H_3O^+	H_2O	H_2O	...	CH_2	H_2O	...	CH_2	0.00	99.95	3.48±0.00
H_3O^+	H_2O	CH_2	...	...	H_2O	H_2O	...	0.00	99.96	3.00±0.36
H_3O^+	H_2O	...	...	...	ROR	H_2O	H_2O	0.00	99.96	0.15±0.00
H_3O^+	H_2O	ROH	...	...	H_2O	...	H_2O	0.00	99.96	3.05±0.00
H_3O^+	ROH	H_2O	H_2O	...	H_2O	...	H_2O	0.00	99.97	0.44±0.00
H_3O^+	H_2O	H_2O	...	...	ROH	...	...	0.00	99.97	0.15±0.00
H_3O^+	ROR	H_2O	...	H_2O	...	...	...	0.00	99.97	1.31±0.00
H_3O^+	H_2O	H_2O	...	CH_2	ROH	ROR	...	0.00	99.98	5.08±0.00
H_3O^+	H_2O	H_2O	CH_2	...	H_2O	...	CH_2	0.00	99.98	4.21±0.00
H_3O^+	H_2O	H_2O	...	H_2O	ROH	...	H_2O	0.00	99.98	3.05±0.00
H_3O^+	H_2O	CH_2	...	...	H_2O	H_2O	H_2O	0.00	99.98	0.29±0.00
H_3O^+	H_2O	...	...	H_2O	H_2O	H_2O	CH_2	0.00	99.99	5.23±0.00
H_3O^+	H_2O	H_2O	CH_2	...	H_2O	...	ROH	0.00	99.99	2.61±0.00
H_3O^+	H_2O	CH_2	...	H_2O	H_2O	H_2O	ROH	0.00	99.99	9.15±0.00
H_3O^+	H_2O	CH_2	...	H_2O	H_2O	H_2O	...	0.00	99.99	10.60±0.00
H_3O^+	ROR	ROH	H_2O	H_2O	...	...	...	0.00	99.99	7.26±0.00
H_3O^+	ROH	H_2O	...	...	CH_2	...	H_2O	0.00	99.99	3.19±0.00
H_3O^+	H_2O	...	...	CH_2	H_2O	H_2O	H_2O	0.00	99.99	18.00±0.00
H_3O^+	H_2O	H_2O	...	H_2O	H_2O	...	CH_2	0.00	99.99	8.86±0.00
H_3O^+	H_2O	ROH	H_2O	H_2O	H_2O	...	H_2O	0.00	99.99	7.41±0.00
H_3O^+	H_2O	H_2O	...	...	ROH	...	H_2O	0.00	99.99	6.68±0.00
H_3O^+	H_2O	H_2O	...	...	ROR	...	CH_2	0.00	100	4.36±0.00

Appendix L

Hydrogen-bond networks found during proton transfer events

L.1 Hydrogen-bond networks found during proton transfer events for bulk water

Table L.1: The occurrences and lifetimes of hydrogen-bond networks around the reactant and product during proton transfer found in bulk water for PW91. The table lists the protonated species (Z_{prot}), the previously protonated species (Z_{prev}), the hydrogen-bond atoms of the protonated species ($HB_{X,p}$ where x=A or D for accepting or donating a hydrogen bond), and the solvating atoms of Z_{prev} ($HB_{X,r}$ with the same definitions of x). Figure 4.4 gives an illustration for these labels. Proton rattling effects are included.

Z_{prot}	Z_{prev}	$HB_{A,p}$	$HB_{A,p}$	$HB_{D,p}$	$HB_{A,r}$	$HB_{A,r}$	$HB_{D,r}$	%	$\sum$ %
H_3O^+	H_2O	H_2O	H_2O	H_2O	H_2O	H_2O	...	52.92	52.92
H_3O^+	H_2O	H_2O	H_2O	H_2O	H_2O	H_2O	H_2O	35.54	88.46
H_3O^+	H_2O	H_2O	H_2O	...	H_2O	H_2O	...	7.06	95.52
H_3O^+	H_2O	H_2O	...	...	H_2O	H_2O	H_2O	1.59	97.11
H_3O^+	OH^-	H_2O	H_2O	H_2O	H_2O	...	H_2O	1.44	98.56
H_3O^+	OH^-	H_2O	H_2O	...	H_2O	...	H_2O	0.99	99.54
H_3O^+	H_2O	H_2O	H_2O	...	H_2O	...	...	0.38	99.92
H_3O^+	OH^-	H_2O	...	...	H_2O	...	H_2O	0.08	100.00

Table L.2: The occurrences and lifetimes of hydrogen-bond networks around the reactant and product during proton transfer found in bulk water for PBE. The table lists the protonated species (Z_{prot}), the previously protonated species (Z_{prev}), the hydrogen-bond atoms of the protonated species ($HB_{X,p}$ where x=A or D for accepting or donating a hydrogen bond), and the solvating atoms of Z_{prev} ($HB_{X,r}$ with the same definitions of x). Figure 4.4 gives an illustration for these labels. Proton rattling effects are included.

Z_{prot}	Z_{prev}	$HB_{A,p}$	$HB_{A,p}$	$HB_{D,p}$	$HB_{A,r}$	$HB_{A,r}$	$HB_{D,r}$	%	$\sum$ %
H_3O^+	H_2O	H_2O	H_2O	H_2O	H_2O	H_2O	...	48.35	48.35
H_3O^+	H_2O	H_2O	H_2O	H_2O	H_2O	H_2O	H_2O	22.33	70.69
H_3O^+	H_2O	H_2O	H_2O	...	H_2O	H_2O	...	20.24	90.93
H_3O^+	H_2O	H_2O	H_2O	H_2O	H_2O	...	...	2.99	93.92
H_3O^+	H_2O	H_2O	...	...	H_2O	H_2O	...	2.79	96.71
H_3O^+	H_2O	H_2O	...	H_2O	H_2O	H_2O	...	1.50	98.21
H_3O^+	H_2O	H_2O	H_2O	H_2O	H_2O	...	H_2O	1.40	99.60
H_3O^+	H_2O	H_2O	...	...	H_2O	...	...	0.30	99.90
H_3O^+	H_2O	...	...	H_2O	H_2O	H_2O	H_2O	0.10	100.00

Table L.3: The occurrences and lifetimes of hydrogen-bond networks around the reactant and product during proton transfer found in bulk water for BLYP. The table lists the protonated species (Z_{prot}), the previously protonated species (Z_{prev}), the hydrogen-bond atoms of the protonated species ($HB_{X,p}$ where x=A or D for accepting or donating a hydrogen bond), and the solvating atoms of Z_{prev} ($HB_{X,r}$ with the same definitions of x). Figure 4.4 gives an illustration for these labels. Proton rattling effects are included.

Z_{prot}	Z_{prev}	$HB_{A,p}$	$HB_{A,p}$	$HB_{D,p}$	$HB_{A,r}$	$HB_{A,r}$	$HB_{D,r}$	%	$\sum$ %
H_3O^+	H_2O	H_2O	H_2O	H_2O	H_2O	H_2O	...	40.33	40.33
H_3O^+	H_2O	H_2O	H_2O	...	H_2O	H_2O	...	36.76	77.09
H_3O^+	H_2O	H_2O	H_2O	H_2O	H_2O	H_2O	H_2O	14.40	91.50
H_3O^+	H_2O	H_2O	...	...	H_2O	H_2O	...	4.53	96.02
H_3O^+	H_2O	H_2O	H_2O	...	H_2O	...	H_2O	1.92	97.94
H_3O^+	H_2O	H_2O	H_2O	H_2O	H_2O	...	...	1.23	99.18
H_3O^+	H_2O	H_2O	...	H_2O	H_2O	H_2O	H_2O	0.55	99.73
H_3O^+	H_2O	...	...	...	H_2O	H_2O	H_2O	0.14	99.86
H_3O^+	H_2O	...	...	...	H_2O	H_2O	...	0.14	100.00

Table L.4: The occurrences and lifetimes of hydrogen-bond networks around the reactant and product during proton transfer found in bulk water for PBE+TS-vdW. The table lists the protonated species (Z_{prot}), the previously protonated species (Z_{prev}), the hydrogen-bond atoms of the protonated species ($HB_{X,p}$ where x=A or D for accepting or donating a hydrogen bond), and the solvating atoms of Z_{prev} ($HB_{X,r}$ with the same definitions of x). Figure 4.4 gives an illustration for these labels. Proton rattling effects are included.

Z_{prot}	Z_{prev}	$HB_{A,p}$	$HB_{A,p}$	$HB_{D,p}$	$HB_{A,r}$	$HB_{A,r}$	$HB_{D,r}$	%	$\sum$ %
H_3O^+	H_2O	H_2O	H_2O	...	H_2O	H_2O	...	38.73	38.73
H_3O^+	H_2O	H_2O	H_2O	H_2O	H_2O	H_2O	...	37.76	76.49
H_3O^+	H_2O	H_2O	H_2O	H_2O	H_2O	H_2O	H_2O	10.24	86.72
H_3O^+	H_2O	H_2O	H_2O	...	H_2O	...	...	6.64	93.36
H_3O^+	H_2O	H_2O	...	...	H_2O	H_2O	H_2O	2.49	95.85
H_3O^+	H_2O	H_2O	H_2O	...	H_2O	...	H_2O	2.35	98.20
H_3O^+	H_2O	H_2O	...	H_2O	H_2O	H_2O	H_2O	1.11	99.31
H_3O^+	H_2O	H_2O	...	...	H_2O	...	...	0.28	99.59
H_3O^+	H_2O	H_2O	...	...	H_2O	...	H_2O	0.28	99.86
H_3O^+	H_2O	...	...	...	H_2O	H_2O	...	0.14	100.00

L.2 Hydrogen-bond networks found during proton transfer events for TEG-water mixtures

Table L.5: The occurrences and lifetimes of hydrogen-bond networks around the reactant and product during proton transfer found in TEG-water mixture for PW91. The table lists the protonated species (Z_{prot}), the previously protonated species (Z_{prev}), the hydrogen-bond atoms of the protonated species ($HB_{X,p}$ where x=A or D for accepting or donating a hydrogen bond), and the solvating atoms of Z_{prev} ($HB_{X,r}$ with the same definitions of x). Figure 4.4 gives an illustration for these labels. Proton rattling effects are included.

Z_{prot}	Z_{shared}	$HB_{A,p}$	$HB_{A,p}$	$HB_{D,p}$	$HB_{A,s}$	$HB_{A,s}$	$HB_{D,s}$	%	$\sum$ %
H_3O^+	H_2O	H_2O	H_2O	...	H_2O	H_2O	...	15.19	15.19
H_3O^+	H_2O	H_2O	H_2O	...	H_2O	H_2O	CH_2	14.82	30.02
H_3O^+	H_2O	H_2O	H_2O	H_2O	H_2O	H_2O	...	14.25	44.26
H_3O^+	H_2O	H_2O	H_2O	CH_2	H_2O	H_2O	...	11.52	55.79
H_3O^+	H_2O	H_2O	H_2O	CH_2	H_2O	H_2O	H_2O	4.45	60.24
H_3O^+	H_2O	H_2O	H_2O	H_2O	ROH	H_2O	...	4.24	64.48
H_3O^+	H_2O	H_2O	H_2O	H_2O	H_2O	H_2O	CH_2	4.14	68.62
H_3O^+	H_2O	ROH	H_2O	...	H_2O	H_2O	...	2.88	71.50
H_3O^+	H_2O	ROH	H_2O	H_2O	H_2O	H_2O	...	2.41	73.91
H_3O^+	H_2O	H_2O	H_2O	H_2O	H_2O	H_2O	H_2O	2.30	76.22
H_3O^+	H_2O	H_2O	...	...	H_2O	H_2O	...	1.73	77.95
H_3O^+	H_2O	ROH	H_2O	...	H_2O	H_2O	CH_2	1.73	79.68
H_3O^+	H_2O	H_2O	H_2O	CH_2	H_2O	H_2O	CH_2	1.68	81.35
H_3O^+	H_2O	H_2O	...	...	H_2O	H_2O	CH_2	1.47	82.82
H_3O^+	H_2O	ROH	H_2O	H_2O	H_2O	H_2O	CH_2	1.36	84.18
H_3O^+	H_2O	H_2O	H_2O	H_2O	ROH	H_2O	CH_2	1.26	85.44
H_3O^+	H_2O	H_2O	...	...	H_2O	H_2O	H_2O	1.20	86.64
H_3O^+	H_2O	H_2O	H_2O	...	ROH	H_2O	CH_2	1.20	87.85
H_3O^+	H_2O	H_2O	...	CH_2	H_2O	H_2O	...	0.73	88.58
H_3O^+	H_2O	H_2O	H_2O	H_2O	ROH	H_2O	H_2O	0.73	89.31
H_3O^+	H_2O	H_2O	H_2O	H_2O	H_2O	...	H_2O	0.52	89.84
H_3O^+	H_2O	ROH	H_2O	...	H_2O	H_2O	H_2O	0.52	90.36
H_3O^+	H_2O	H_2O	H_2O	CH_2	ROH	H_2O	CH_2	0.47	90.83
H_3O^+	H_2O	H_2O	H_2O	...	ROH	H_2O	H_2O	0.42	91.25
ROH_2^+	H_2O	H_2O	...	CH_2	H_2O	H_2O	...	0.42	91.67
H_3O^+	ROH	H_2O	H_2O	...	H_2O	...	...	0.31	91.99
H_3O^+	ROH	H_2O	H_2O	CH_2	H_2O	...	...	0.31	92.30
H_3O^+	H_2O	H_2O	H_2O	...	H_2O	...	H_2O	0.31	92.61
H_3O^+	H_2O	H_2O	H_2O	...	H_2O	...	CH_2	0.31	92.93
H_3O^+	H_2O	H_2O	...	H_2O	H_2O	H_2O	CH_2	0.26	93.19
H_3O^+	H_2O	ROH	H_2O	H_2O	ROH	H_2O	...	0.26	93.45
H_3O^+	H_2O	H_2O	CH_2	H_2O	H_2O	H_2O	...	0.26	93.71
H_3O^+	ROH	H_2O	H_2O	...	H_2O	...	H_2O	0.26	93.98
H_3O^+	H_2O	H_2O	H_2O	CH_2	H_2O	...	...	0.21	94.19
H_3O^+	H_2O	H_2O	...	...	ROH	H_2O	...	0.21	94.39
ROH_2^+	H_2O	H_2O	...	...	H_2O	H_2O	...	0.21	94.60
H_3O^+	H_2O	H_2O	H_2O	...	ROR	H_2O	H_2O	0.21	94.81
ROH_2^+	H_2O	H_2O	...	H_2O	H_2O	H_2O	...	0.21	95.02
H_3O^+	H_2O	ROH	H_2O	H_2O	H_2O	H_2O	H_2O	0.21	95.23
ROH_2^+	H_2O	H_2O	...	H_2O	H_2O	...	...	0.21	95.44
H_3O^+	H_2O	ROH	...	...	H_2O	H_2O	H_2O	0.21	95.65
H_3O^+	H_2O	H_2O	H_2O	H_2O	ROR	H_2O	H_2O	0.21	95.86
ROH_2^+	H_2O	H_2O	...	...	H_2O	H_2O	CH_2	0.16	96.02
H_3O^+	H_2O	H_2O	H_2O	H_2O	H_2O	...	...	0.16	96.18
H_3O^+	H_2O	H_2O	H_2O	CH_2	H_2O	...	CH_2	0.16	96.33
H_3O^+	H_2O	H_2O	H_2O	H_2O	H_2O	CH_2	H_2O	0.16	96.49
H_3O^+	H_2O	H_2O	CH_2	...	ROH	H_2O	H_2O	0.16	96.65
H_3O^+	ROH	H_2O	H_2O	H_2O	H_2O	...	...	0.16	96.80
H_3O^+	ROH	H_2O	...	...	H_2O	...	...	0.16	96.96
H_3O^+	H_2O	H_2O	...	CH_2	H_2O	H_2O	H_2O	0.16	97.12
H_3O^+	ROH-	H_2O	H_2O	...	...	...	H_2O	0.16	97.28
ROH_2^+	H_2O	H_2O	...	CH_2	H_2O	...	...	0.10	97.38
ROH_2^+	H_2O	H_2O	...	H_2O	H_2O	H_2O	CH_2	0.10	97.49
H_3O^+	OH^-	H_2O	H_2O	H_2O	H_2O	...	H_2O	0.10	97.59

Table L.5. Continued.

Z_{prot}	Z_{shared}	$HB_{A,p}$	$HB_{A,p}$	$HB_{D,p}$	$HB_{A,s}$	$HB_{A,s}$	$HB_{D,s}$	%	$\sum$ %
H_3O^+	H_2O	H_2O	H_2O	H_2O	H_2O	...	CH_2	0.10	97.70
H_3O^+	H_2O	H_2O	...	H_2O	ROH	H_2O	H_2O	0.10	97.80
H_3O^+	H_2O	H_2O	...	...	H_2O	...	...	0.10	97.90
H_3O^+	OH^-	H_2O	H_2O	...	ROH	...	H_2O	0.10	98.01
H_3O^+	ROH	H_2O	H_2O	CH_2	H_2O	...	H_2O	0.10	98.11
H_3O^+	H_2O	ROH	H_2O	...	H_2O	CH_2	...	0.10	98.22
ROH_2^+	H_2O	H_2O	...	...	H_2O	H_2O	H_2O	0.10	98.32
H_3O^+	ROH	H_2O	H_2O	...	H_2O	...	CH_2	0.10	98.43
H_3O^+	H_2O	H_2O	H_2O	...	H_2O	H_2O	ROH	0.10	98.53
H_3O^+	ROH	H_2O	H_2O	CH_2	H_2O	...	CH_2	0.10	98.64
H_3O^+	H_2O	ROH	...	CH_2	H_2O	H_2O	H_2O	0.05	98.69
H_3O^+	H_2O	H_2O	...	...	H_2O	...	CH_2	0.05	98.74
H_3O^+	H_2O	ROR	H_2O	...	H_2O	H_2O	CH_2	0.05	98.80
H_3O^+	ROH	H_2O	...	CH_2	H_2O	...	H_2O	0.05	98.85
H_3O^+	ROH	H_2O	...	...	H_2O	...	H_2O	0.05	98.90
H_3O^+	OH^-	H_2O	H_2O	CH_2	H_2O	...	H_2O	0.05	98.95
H_3O^+	H_2O	H_2O	...	...	ROR	H_2O	ROH	0.05	99.00
ROH_2^+	H_2O	H_2O	...	H_2O	H_2O	...	CH_2	0.05	99.06
H_3O^+	H_2O	ROH	H_2O	CH_2	H_2O	H_2O	H_2O	0.05	99.11
H_3O^+	H_2O	H_2O	...	ROH	H_2O	H_2O	...	0.05	99.16
H_3O^+	H_2O	H_2O	...	CH_2	H_2O	H_2O	CH_2	0.05	99.21
H_3O^+	H_2O	H_2O	H_2O	CH_2	ROH	...	...	0.05	99.27
H_3O^+	H_2O	ROR	H_2O	H_2O	H_2O	H_2O	...	0.05	99.32
H_3O^+	H_2O	ROH	...	H_2O	H_2O	H_2O	...	0.05	99.37
H_3O^+	H_2O	H_2O	H_2O	H_2O	H_2O	CH_2	CH_2	0.05	99.42
ROH_2^+	H_2O	H_2O	...	...	ROH	H_2O	...	0.05	99.48
H_3O^+	H_2O	H_2O	H_2O	H_2O	H_2O	CH_2	...	0.05	99.53
H_3O^+	H_2O	H_2O	...	H_2O	ROH	H_2O	CH_2	0.05	99.58
H_3O^+	ROH	H_2O	...	H_2O	H_2O	...	...	0.05	99.63
H_3O^+	H_2O	H_2O	H_2O	H_2O	ROR	H_2O	...	0.05	99.69
H_3O^+	H_2O	H_2O	H_2O	CH_2	ROH	H_2O	...	0.05	99.74
H_3O^+	H_2O	H_2O	H_2O	CH_2	ROR	H_2O	H_2O	0.05	99.79
H_3O^+	H_2O	ROR	H_2O	...	H_2O	H_2O	...	0.05	99.84
ROH_2^+	H_2O	H_2O	...	H_2O	H_2O	H_2O	H_2O	0.05	99.90
H_3O^+	H_2O	H_2O	H_2O	CH_2	ROH	...	CH_2	0.05	99.95
H_3O^+	H_2O	H_2O	...	...	ROH	H_2O	CH_2	0.05	100

Table L.6: The occurrences and lifetimes of hydrogen-bond networks around the reactant and product during proton transfer found in TEG-water mixture for PBE. The table lists the protonated species (Z_{prot}), the previously protonated species (Z_{prev}), the hydrogen-bond atoms of the protonated species ($HB_{X,p}$ where x=A or D for accepting or donating a hydrogen bond), and the solvating atoms of Z_{prev} ($HB_{X,r}$ with the same definitions of x). Figure 4.4 gives an illustration for these labels. Proton rattling effects are included.

Z_{prot}	Z_{shared}	$HB_{A,p}$	$HB_{A,p}$	$HB_{D,p}$	$HB_{A,s}$	$HB_{A,s}$	$HB_{D,s}$	%	$\sum$ %
H_3O^+	H_2O	H_2O	H_2O	...	H_2O	H_2O	...	21.12	21.12
H_3O^+	H_2O	H_2O	H_2O	H_2O	H_2O	H_2O	...	15.96	37.08
H_3O^+	H_2O	H_2O	H_2O	...	H_2O	H_2O	CH_2	7.55	44.63
H_3O^+	H_2O	ROH	H_2O	...	H_2O	H_2O	...	7.40	52.03
H_3O^+	H_2O	ROH	H_2O	H_2O	H_2O	H_2O	...	4.36	56.38
H_3O^+	H_2O	H_2O	H_2O	CH_2	H_2O	H_2O	...	3.90	60.28
H_3O^+	H_2O	H_2O	H_2O	H_2O	H_2O	H_2O	CH_2	3.75	64.03
H_3O^+	H_2O	H_2O	H_2O	ROH	H_2O	H_2O	...	3.50	67.53
H_3O^+	H_2O	H_2O	H_2O	...	H_2O	...	...	2.43	69.96
H_3O^+	H_2O	H_2O	...	...	H_2O	H_2O	...	1.77	71.73
H_3O^+	H_2O	H_2O	H_2O	H_2O	ROH	H_2O	H_2O	1.72	73.45
H_3O^+	H_2O	H_2O	H_2O	H_2O	H_2O	...	...	1.67	75.13
H_3O^+	H_2O	ROH	H_2O	...	H_2O	H_2O	CH_2	1.52	76.65
H_3O^+	H_2O	H_2O	...	H_2O	H_2O	H_2O	...	1.47	78.12
H_3O^+	H_2O	H_2O	H_2O	...	ROH	H_2O	H_2O	1.32	79.43
H_3O^+	H_2O	ROH	H_2O	...	H_2O	H_2O	H_2O	1.32	80.75
H_3O^+	H_2O	H_2O	H_2O	H_2O	H_2O	H_2O	H_2O	1.32	82.07
H_3O^+	H_2O	H_2O	H_2O	CH_2	H_2O	H_2O	CH_2	1.32	83.38
H_3O^+	H_2O	H_2O	H_2O	CH_2	H_2O	H_2O	H_2O	1.27	84.65
H_3O^+	H_2O	ROH	H_2O	CH_2	H_2O	H_2O	...	1.22	85.87
H_3O^+	H_2O	H_2O	...	...	H_2O	H_2O	CH_2	1.17	87.03

Table L.6. Continued.

Z_{prot}	Z_{shared}	$HB_{A,p}$	$HB_{A,p}$	$HB_{D,p}$	$HB_{A,s}$	$HB_{A,s}$	$HB_{D,s}$	%	$\sum$ %
H_3O^+	H_2O	H_2O	H_2O	...	H_2O	...	CH_2	1.17	88.20
H_3O^+	H_2O	H_2O	...	...	ROH	H_2O	...	0.91	89.11
H_3O^+	H_2O	H_2O	H_2O	...	H_2O	H_2O	H_2O	0.86	89.97
H_3O^+	H_2O	H_2O	H_2O	CH_2	ROH	H_2O	...	0.86	90.83
H_3O^+	H_2O	H_2O	...	H_2O	H_2O	H_2O	CH_2	0.51	91.34
H_3O^+	H_2O	H_2O	...	CH_2	H_2O	H_2O	H_2O	0.51	91.84
H_3O^+	H_2O	ROH	H_2O	H_2O	H_2O	H_2O	CH_2	0.41	92.25
H_3O^+	H_2O	ROH	H_2O	H_2O	H_2O	...	...	0.35	92.60
H_3O^+	H_2O	H_2O	H_2O	H_2O	ROH	H_2O	...	0.35	92.96
H_3O^+	H_2O	H_2O	H_2O	H_2O	H_2O	H_2O	ROH	0.30	93.26
H_3O^+	H_2O	ROH	H_2O	...	H_2O	...	...	0.30	93.57
H_3O^+	H_2O	H_2O	...	...	ROR	H_2O	...	0.25	93.82
H_3O^+	H_2O	ROH	H_2O	CH_2	H_2O	...	...	0.20	94.02
H_3O^+	H_2O	H_2O	...	CH_2	H_2O	H_2O	CH_2	0.20	94.22
H_3O^+	H_2O	H_2O	H_2O	CH_2	H_2O	...	...	0.20	94.43
H_3O^+	H_2O	H_2O	...	...	H_2O	...	...	0.20	94.63
H_3O^+	H_2O	H_2O	H_2O	...	ROR	H_2O	...	0.20	94.83
ROH_2^+	H_2O	H_2O	...	H_2O	H_2O	H_2O	CH_2	0.15	94.98
H_3O^+	H_2O	H_2O	H_2O	...	H_2O	CH_2	H_2O	0.15	95.14
H_3O^+	ROH	H_2O	H_2O	H_2O	H_2O	...	CH_2	0.15	95.29
H_3O^+	H_2O	H_2O	...	CH_2	H_2O	H_2O	...	0.15	95.44
H_3O^+	H_2O	ROH	H_2O	CH_2	H_2O	H_2O	H_2O	0.15	95.59
H_3O^+	H_2O	H_2O	...	ROH	H_2O	H_2O	...	0.15	95.74
H_3O^+	H_2O	H_2O	CH_2	CH_2	H_2O	H_2O	...	0.15	95.90
H_3O^+	H_2O	H_2O	H_2O	ROH	ROH	H_2O	H_2O	0.15	96.05
H_3O^+	H_2O	H_2O	H_2O	H_2O	ROH	H_2O	CH_2	0.15	96.20
H_3O^+	H_2O	...	...	...	H_2O	H_2O	...	0.15	96.35
H_3O^+	H_2O	H_2O	H_2O	CH_2	ROR	H_2O	...	0.15	96.50
H_3O^+	H_2O	H_2O	CH_2	...	H_2O	H_2O	...	0.15	96.66
ROH_2^+	H_2O	H_2O	...	CH_2	H_2O	H_2O	H_2O	0.15	96.81
H_3O^+	H_2O	H_2O	...	...	H_2O	H_2O	ROH	0.10	96.91
H_3O^+	H_2O	H_2O	...	...	H_2O	...	CH_2	0.10	97.01
H_3O^+	H_2O	H_2O	...	CH_2	ROH	H_2O	...	0.10	97.11
H_3O^+	H_2O	H_2O	H_2O	...	ROH	...	...	0.10	97.21
H_3O^+	H_2O	H_2O	H_2O	...	ROH	...	CH_2	0.10	97.32
H_3O^+	H_2O	H_2O	H_2O	CH_2	H_2O	...	CH_2	0.10	97.42
H_3O^+	H_2O	H_2O	H_2O	CH_2	H_2O	...	H_2O	0.10	97.52
H_3O^+	H_2O	H_2O	H_2O	...	ROR	H_2O	H_2O	0.10	97.62
H_3O^+	H_2O	H_2O	H_2O	CH_2	ROH	H_2O	CH_2	0.10	97.72
H_3O^+	H_2O	H_2O	H_2O	ROH	H_2O	H_2O	H_2O	0.10	97.82
ROH_2^+	H_2O	H_2O	...	H_2O	H_2O	H_2O	...	0.10	97.92
H_3O^+	H_2O	...	...	H_2O	H_2O	H_2O	...	0.10	98.02
H_3O^+	ROH	H_2O	H_2O	...	H_2O	...	CH_2	0.10	98.13
H_3O^+	H_2O	H_2O	H_2O	CH_2	H_2O	H_2O	ROH	0.10	98.23
H_3O^+	ROH	H_2O	H_2O	...	H_2O	...	H_2O	0.10	98.33
H_3O^+	H_2O	H_2O	...	...	H_2O	...	ROH	0.05	98.38
H_3O^+	H_2O	H_2O	H_2O	CH_2	ROH	...	...	0.05	98.43
H_3O^+	H_2O	H_2O	CH_2	...	H_2O	H_2O	CH_2	0.05	98.48
H_3O^+	H_2O	H_2O	H_2O	H_2O	ROH	...	...	0.05	98.53
H_3O^+	H_2O	ROH	H_2O	...	H_2O	...	CH_2	0.05	98.58
H_3O^+	H_2O	H_2O	...	H_2O	H_2O	...	...	0.05	98.63
H_3O^+	H_2O	H_2O	H_2O	...	ROH	H_2O	CH_2	0.05	98.68
H_3O^+	H_2O	H_2O	...	...	H_2O	CH_2	...	0.05	98.73
H_3O^+	ROH-	H_2O	H_2O	CH_2	...	...	H_2O	0.05	98.78
H_3O^+	H_2O	H_2O	H_2O	H_2O	H_2O	...	CH_2	0.05	98.83
H_3O^+	ROH	H_2O	H_2O	H_2O	H_2O	...	H_2O	0.05	98.89
H_3O^+	H_2O	ROH	...	H_2O	H_2O	H_2O	...	0.05	98.94
H_3O^+	H_2O	ROH	CH_2	CH_2	H_2O	H_2O	...	0.05	98.99
H_3O^+	H_2O	H_2O	...	CH_2	ROH	H_2O	CH_2	0.05	99.04
H_3O^+	H_2O	ROR	H_2O	...	H_2O	H_2O	H_2O	0.05	99.09
H_3O^+	H_2O	H_2O	...	H_2O	ROH	H_2O	H_2O	0.05	99.14
H_3O^+	H_2O	...	...	H_2O	H_2O	H_2O	H_2O	0.05	99.19
H_3O^+	H_2O	H_2O	H_2O	...	H_2O	CH_2	CH_2	0.05	99.24
H_3O^+	H_2O	ROR	...	...	H_2O	H_2O	...	0.05	99.29
H_3O^+	ROH	H_2O	H_2O	H_2O	H_2O	...	...	0.05	99.34
H_3O^+	ROH	H_2O	H_2O	CH_2	H_2O	...	H_2O	0.05	99.39
H_3O^+	OH^-	H_2O	...	...	H_2O	...	H_2O	0.05	99.44
H_3O^+	H_2O	H_2O	CH_2	...	H_2O	H_2O	H_2O	0.05	99.49
H_3O^+	ROH	H_2O	...	...	H_2O	...	H_2O	0.05	99.54
H_3O^+	H_2O	ROR	H_2O	...	H_2O	...	CH_2	0.05	99.59
H_3O^+	H_2O	H_2O	CH_2	H_2O	H_2O	H_2O	...	0.05	99.65
H_3O^+	H_2O	H_2O	H_2O	ROH	H_2O	...	...	0.05	99.70
ROH_2^+	H_2O	H_2O	...	CH_2	H_2O	H_2O	CH_2	0.05	99.75

Table L.6. Continued.

Z_{prot}	Z_{shared}	$HB_{A,p}$	$HB_{A,p}$	$HB_{D,p}$	$HB_{A,s}$	$HB_{A,s}$	$HB_{D,s}$	%	$\sum$ %
ROH_2^+	H_2O	H_2O	...	...	H_2O	H_2O	H_2O	0.05	99.80
H_3O^+	H_2O	H_2O	...	...	ROH	H_2O	CH_2	0.05	99.85
H_3O^+	H_2O	ROH	...	...	H_2O	...	H_2O	0.05	99.90
ROH_2^+	H_2O	H_2O	...	CH_2	H_2O	H_2O	...	0.05	99.95
H_3O^+	H_2O	ROH	...	CH_2	H_2O	H_2O	...	0.05	100.00

Table L.7: The occurrences and lifetimes of hydrogen-bond networks around the reactant and product during proton transfer found in TEG-water mixture for PBE+TS-vdW. The table lists the protonated species (Z_{prot}), the previously protonated species (Z_{prev}), the hydrogen-bond atoms of the protonated species ($HB_{X,p}$ where x=A or D for accepting or donating a hydrogen bond), and the solvating atoms of Z_{prev} ($HB_{X,r}$ with the same definitions of x). Figure 4.4 gives an illustration for these labels. Proton rattling effects are included.

Z_{prot}	Z_{shared}	$HB_{A,p}$	$HB_{A,p}$	$HB_{D,p}$	$HB_{A,s}$	$HB_{A,s}$	$HB_{D,s}$	%	$\sum$ %
H_3O^+	H_2O	H_2O	H_2O	...	H_2O	H_2O	...	16.07	16.07
H_3O^+	H_2O	H_2O	H_2O	H_2O	H_2O	H_2O	...	11.36	27.42
H_3O^+	H_2O	H_2O	H_2O	CH_2	H_2O	H_2O	...	7.94	35.36
H_3O^+	H_2O	ROR	H_2O	...	H_2O	H_2O	...	6.37	41.74
H_3O^+	H_2O	H_2O	H_2O	...	H_2O	H_2O	H_2O	6.00	47.74
H_3O^+	H_2O	H_2O	H_2O	...	H_2O	H_2O	CH_2	4.71	52.45
H_3O^+	H_2O	H_2O	H_2O	H_2O	H_2O	H_2O	H_2O	3.60	56.05
H_3O^+	H_2O	H_2O	H_2O	CH_2	H_2O	H_2O	H_2O	3.14	59.19
H_3O^+	H_2O	H_2O	H_2O	H_2O	H_2O	H_2O	CH_2	2.68	61.87
H_3O^+	H_2O	H_2O	H_2O	...	ROH	H_2O	...	2.59	64.45
H_3O^+	H_2O	H_2O	...	...	H_2O	H_2O	...	2.22	66.67
H_3O^+	H_2O	H_2O	...	...	H_2O	H_2O	CH_2	2.22	68.88
H_3O^+	H_2O	H_2O	CH_2	...	H_2O	H_2O	...	2.12	71.01
H_3O^+	H_2O	H_2O	H_2O	H_2O	H_2O	...	...	1.48	72.48
H_3O^+	H_2O	ROR	H_2O	H_2O	H_2O	H_2O	...	1.48	73.96
H_3O^+	H_2O	ROH	H_2O	H_2O	H_2O	H_2O	...	1.48	75.44
H_3O^+	H_2O	H_2O	H_2O	...	H_2O	...	...	1.20	76.64
H_3O^+	H_2O	H_2O	H_2O	CH_2	H_2O	H_2O	ROH	1.20	77.84
H_3O^+	H_2O	H_2O	H_2O	H_2O	ROH	H_2O	...	1.20	79.04
H_3O^+	H_2O	ROR	H_2O	...	H_2O	H_2O	CH_2	1.11	80.15
H_3O^+	H_2O	H_2O	H_2O	...	ROH	ROR	...	1.02	81.16
H_3O^+	H_2O	ROR	H_2O	...	H_2O	H_2O	H_2O	1.02	82.18
H_3O^+	H_2O	H_2O	H_2O	CH_2	H_2O	H_2O	CH_2	0.92	83.10
H_3O^+	H_2O	H_2O	H_2O	...	H_2O	...	H_2O	0.92	84.03
H_3O^+	H_2O	ROH	...	...	H_2O	H_2O	...	0.83	84.86
H_3O^+	H_2O	H_2O	...	...	H_2O	H_2O	H_2O	0.74	85.60
H_3O^+	H_2O	H_2O	H_2O	...	H_2O	...	CH_2	0.65	86.24
H_3O^+	H_2O	H_2O	H_2O	...	H_2O	H_2O	ROH	0.65	86.89
H_3O^+	H_2O	H_2O	...	CH_2	H_2O	H_2O	CH_2	0.55	87.44
H_3O^+	H_2O	H_2O	H_2O	H_2O	ROH	H_2O	H_2O	0.55	88.00
H_3O^+	H_2O	ROH	ROR	H_2O	H_2O	H_2O	...	0.55	88.55
H_3O^+	H_2O	H_2O	CH_2	H_2O	H_2O	H_2O	...	0.55	89.10
H_3O^+	H_2O	H_2O	...	H_2O	H_2O	H_2O	CH_2	0.46	89.57
H_3O^+	H_2O	H_2O	...	CH_2	H_2O	H_2O	...	0.46	90.03
H_3O^+	H_2O	H_2O	...	...	ROR	H_2O	...	0.46	90.49
H_3O^+	H_2O	ROR	H_2O	H_2O	H_2O	H_2O	CH_2	0.37	90.86
H_3O^+	H_2O	H_2O	H_2O	...	ROH	CH_2	H_2O	0.37	91.23
H_3O^+	H_2O	H_2O	...	H_2O	H_2O	H_2O	...	0.37	91.60
H_3O^+	H_2O	H_2O	CH_2	...	H_2O	H_2O	CH_2	0.37	91.97
H_3O^+	H_2O	ROR	H_2O	CH_2	H_2O	H_2O	...	0.37	92.34
H_3O^+	H_2O	H_2O	...	...	H_2O	...	...	0.37	92.71
H_3O^+	H_2O	H_2O	H_2O	H_2O	ROR	H_2O	...	0.37	93.07
H_3O^+	H_2O	H_2O	H_2O	ROH	ROR	H_2O	...	0.37	93.44
H_3O^+	H_2O	H_2O	H_2O	ROH	H_2O	...	...	0.37	93.81
H_3O^+	H_2O	ROH	...	...	H_2O	H_2O	H_2O	0.37	94.18
H_3O^+	H_2O	ROR	H_2O	H_2O	H_2O	H_2O	ROH	0.28	94.46
H_3O^+	H_2O	ROR	H_2O	...	H_2O	...	...	0.28	94.74
H_3O^+	H_2O	H_2O	...	CH_2	ROR	H_2O	...	0.28	95.01
H_3O^+	H_2O	H_2O	H_2O	H_2O	H_2O	...	H_2O	0.28	95.29
H_3O^+	H_2O	H_2O	H_2O	ROH	H_2O	H_2O	H_2O	0.28	95.57
H_3O^+	H_2O	H_2O	H_2O	...	H_2O	CH_2	...	0.18	95.75
H_3O^+	OH^-	H_2O	H_2O	CH_2	H_2O	...	H_2O	0.18	95.94
H_3O^+	H_2O	ROH	ROR	H_2O	H_2O	H_2O	H_2O	0.18	96.12

Table L.7. Continued.

Z_{prot}	Z_{shared}	$HB_{A,p}$	$HB_{A,p}$	$HB_{D,p}$	$HB_{A,s}$	$HB_{A,s}$	$HB_{D,s}$	%	$\sum$ %
H_3O^+	H_2O	ROH	...	H_2O	H_2O	H_2O	...	0.18	96.31
H_3O^+	H_2O	H_2O	...	H_2O	H_2O	H_2O	H_2O	0.18	96.49
H_3O^+	H_2O	H_2O	H_2O	CH_2	ROH	ROR	...	0.18	96.68
H_3O^+	H_2O	ROR	...	...	H_2O	H_2O	...	0.18	96.86
H_3O^+	H_2O	H_2O	H_2O	H_2O	ROH	CH_2	...	0.18	97.05
H_3O^+	H_2O	H_2O	H_2O	...	ROR	...	...	0.18	97.23
H_3O^+	H_2O	H_2O	...	CH_2	H_2O	H_2O	H_2O	0.18	97.41
H_3O^+	H_2O	H_2O	H_2O	ROH	H_2O	...	CH_2	0.18	97.60
H_3O^+	H_2O	ROR	...	...	H_2O	H_2O	CH_2	0.09	97.69
H_3O^+	ROH	H_2O	H_2O	...	H_2O	...	...	0.09	97.78
H_3O^+	H_2O	ROR	...	H_2O	H_2O	H_2O	ROH	0.09	97.88
H_3O^+	H_2O	ROH	ROR	H_2O	H_2O	H_2O	CH_2	0.09	97.97
H_3O^+	H_2O	H_2O	H_2O	...	ROR	...	H_2O	0.09	98.06
H_3O^+	H_2O	H_2O	H_2O	ROH	ROH	H_2O	CH_2	0.09	98.15
H_3O^+	H_2O	H_2O	...	...	ROR	H_2O	H_2O	0.09	98.25
H_3O^+	H_2O	...	...	H_2O	H_2O	H_2O	CH_2	0.09	98.34
H_3O^+	H_2O	H_2O	H_2O	CH_2	ROH	H_2O	CH_2	0.09	98.43
H_3O^+	H_2O	H_2O	H_2O	H_2O	H_2O	CH_2	H_2O	0.09	98.52
H_3O^+	H_2O	H_2O	H_2O	CH_2	ROR	...	H_2O	0.09	98.61
H_3O^+	H_2O	ROH	H_2O	...	H_2O	H_2O	...	0.09	98.71
H_3O^+	H_2O	H_2O	H_2O	H_2O	ROH	...	H_2O	0.09	98.80
H_3O^+	H_2O	H_2O	H_2O	H_2O	H_2O	CH_2	...	0.09	98.89
H_3O^+	H_2O	H_2O	H_2O	CH_2	ROH	H_2O	...	0.09	98.98
H_3O^+	H_2O	H_2O	CH_2	...	H_2O	...	...	0.09	99.08
H_3O^+	H_2O	...	...	CH_2	H_2O	H_2O	...	0.09	99.17
H_3O^+	H_2O	H_2O	...	H_2O	H_2O	...	H_2O	0.09	99.26
H_3O^+	H_2O	H_2O	...	ROH	H_2O	H_2O	CH_2	0.09	99.35
H_3O^+	H_2O	ROH	H_2O	...	H_2O	H_2O	ROH	0.09	99.45
H_3O^+	H_2O	H_2O	H_2O	H_2O	ROR	H_2O	H_2O	0.09	99.54
H_3O^+	H_2O	H_2O	...	ROH	H_2O	H_2O	H_2O	0.09	99.63
ROH_2^+	H_2O	H_2O	...	CH_2	H_2O	H_2O	H_2O	0.09	99.72
H_3O^+	H_2O	H_2O	CH_2	H_2O	H_2O	...	...	0.09	99.82
H_3O^+	H_2O	H_2O	CH_2	...	H_2O	H_2O	H_2O	0.09	99.91
H_3O^+	H_2O	ROH	H_2O	H_2O	H_2O	...	...	0.09	100

Vita

Marshall McDonnell was born in St. Louis, MO on December 4, 1985. After finishing high school in 2004, he joined the U.S. Army Reserves and began military occupation training. He was deployed to Kuwait and Southern Iraq from December 2004 to December 2005. After returning, he began his B.S. in chemistry and mathematics at Lincoln Memerial University in January 2006. He deployed again to Central Iraq in April 2009 and return in April 2010, where upon he graduated in May 2010. Following his undergraduate education, Marshall was accepted to graduate studies at the University of Tennessee and joined Dr. David Keffer's research group. He was granted a National Science Foundation (NSF) Integrative Education and Research Traineeship (IGERT) in the Sustainable Technology through Advanced Disciplinary Research (STAIR) graduate program in May 2012. In Dr. Keffer's group, he primarily focused on multiscale molecular modeling of proton transfer in proton exchange membranes for fuel cell applications and permeability in chitosan food packaging films. By the end of his Ph.D. studies, his work resulted in three publications with an additional two submitted. Marshall intends to apply and expand on his skills gained during his graduate studies towards a career as a postdoctoral researcher in an academic or government laboratory position.